UNIVERSIDAD NACIONAL AUTÓNOMA DE MÉXICO
PROGRAMA DE MAESTRÍA Y DOCTORADO EN INGENIERÍA
INGENIERÍA MECÁNICA – TERMOFLUIDOS

EXPERIMENTAL STUDY OF A DROP IMMERSED IN AN ELONGATIONAL FLOW WITH
VORTICITY

TESIS
QUE PARA OPTAR POR EL GRADO DE:
DOCTOR EN INGENIERÍA

PRESENTA:
M.I. ISRAEL ROSAS YESCAS

TUTOR PRINCIPAL
DR. ENRIQUE GEFFROY AGUILARÁ

MÉXICO, D. F. AGOSTO 2013

JURADO ASIGNADO:

Presidente: Dr. Minzoni Alessio Antonmaria

Secretario: Dr. Solorio Ordaz Francisco Javier

Vocal: Dr. Geffroy Aguilar Enrique

1 er Suplente: Dr. Mendez Lavielle Federico

2 do Suplente: Dr. Reyes Huesca Marco Antonio

Lugar donde se realizó la tesis:

INSTITUTO DE INVESTIGACIONES EN MATERIALES, UNAM

TUTOR DE TESIS:

Dr. Enrique Geffroy Aguilar

FIRMA

A mis padres Hilda y Ubaldo

A mis hermanos Jesús, Ixchel y Erandi

A mis abuelos María, Jesús e Irene

Abstract

Fluids formed by small drops of one fluid immersed into a second immiscible fluid are found in countless important industrial operations. This class of problems is highly complex given that the interface of liquids depends on the stress field of the complete flow. This thesis presents the study of the dynamics of a drop immersed in an elongational flow that differs significantly from previous studies by Taylor (Taylor 1934), Leal and coworkers (Bentley and Leal 1986a and b), or the Italians (Guido and Villone 1998; Guido et al. 1999, 2000; Guido and Greco 2001), or Moldenaers (Boonen et al.2010; Vananroye 2006, 2007, 2008). The experimental device used to generate these flow is the Two Roll Mill (TRM), developed for the study of *the dynamics of deformation of drops in elongational flow fields with vorticity* and with several features not available for flow cells with simple shear, eccentric cylinders or pure elongational flow fields. In that way the TRM serves as complement to those devices in the performance of studies that improve the current understanding of the effects of vorticity on drop dynamics in well characterized two-dimensional strong flow fields. The TRM can generate an ample range of planar flow, with kinematics close to simple shear flow up to deformation rates characteristic of pure elongational flows.

Like other extensional (or elongational) flow fields, the drop is placed at the stagnation point — where is subjected to deformation with a saddle-point stability environment. Contrary to the standard technique, maintaining the drop at the unstable stagnation point for extended periods of time requires a different type of control scheme. For the TRM a novel nonlinear procedure is used that is robust, and makes possible a large set of experiments.

Chapter 1 to 4 of this work describe the elements of the experimental device and a characterization of the experimental values of the flow type parameters obtained with the geometries available for the TRM flow cell. As well, the performance of the flow cell is also evaluated, in particular the instantaneous velocities obtained on the cylinders, which are critical parameters in the control strategy implemented. The implementation of this control is done by applying a non-linear scheme —based on the Poincaré-Bendixson theorem— that has not previously been used. It requires a process based on real-time image analysis of the drop and real-time non-periodic updating of the velocities of the motors. Those features are incorporated in the computer program that controls the experimental device, developed in visual C++ and which coordinates the data provided by the image analysis and the control of the motors, all in real-time. This control was experimentally tested to find the most appropriate parameters, to evaluate its robustness and to corroborate that it does not affect the dynamics of drop deformation.

Chapter 5 and 6 present experimental results obtained with the device for different flow type parameters and for two viscosities ratios systems. The results for the low viscosities ratios include the determination of the critical capillary number for that viscosities ratio studied as a function of the flow field type, as well as the observation of the breakup process. For the high viscosities ratio, the experimental results show the highly complex behavior present in the transient stages and how this behavior is modified by the flow field. For this case, the flow device allows the study of the response of the drop to start up flows. For very low capillary numbers, the time evolution of the deformation is characterized by a simple monotonically increasing function to a steady form. For large Capillary numbers the steady form is reached after a multi-damped oscillations evolution. Effects by near walls on the deformation of the drop were also studied, for both viscosities ratios, being more evident and studied with more detail in the high viscosities ratio system. For this latter system and for the flow filed closest to simple shear flow, it was possible to observe the confinement effect on the drop deformation during transient and steady states. This confinement experiments show that there are similar effects in to reduce the vorticity in the flow fields and to inhibit its effects by increasing the confinement of the drop.

Resumen

Los fluidos formados por pequeñas gotas de un fluido inmersas en un Segundo fluido inmiscible se encuentran en incontables operaciones industriales. Esta clase de problemas es altamente complejo dado que la interface de los líquidos depende de de los esfuerzos del campo de flujo completo. Esta tesis presenta el estudio de la dinámica de una gota inmersa en un flujo elongacional que difiere significativamente de los estudios previos de Taylor (Taylor 1934), Leal y colaboradores (Bentley and Leal 1986a and b), o de los italianos Guido y Villone (Guido and Villone 1998; Guido et al. 1999, 2000; Guido and Greco 2001), o Moldenaers (Boonen et al.2010; Vananroye 2006, 2007, 2008). El dispositivo experimental usado para generar estos tipos de flujo es el Molino de dos Rodillos TRM, (por sus siglas en inglés Two Roll Mill), desarrollado para el *estudio de la dinámica de deformación de gotas en campos de flujo elongacional con vorticidad* y con diversas características no disponibles en celdas de campos de flujo de cortante simple, cilindros concéntricos o flujo puramente elongacional. De esta forma el Molino de Dos Rodillos funciona como complemento de estos dispositivos en desarrollo de estudios que mejoren el conocimiento actual de los efectos de la vorticidad en la dinámica de gotas en campos de flujo fuertes bidimensionales bien caracterizados. El Molino de Dos Rodillos puede generar un amplio rango de flujos planos con una cinemática cercana al flujo en cortante simple con velocidades de deformación características de flujos puramente elongacionales.

Al igual que otros campos de flujo extensionales (o elongacionales) la gota es colocada en el punto de estancamiento –donde está sujeta a deformación en un ambiente de estabilidad del tipo punto-silla. Contrario a las técnicas estándar, mantener a la gota en el punto de estancamiento inestable por largos periodos de tiempo requiere un esquema de control diferente. Para el Molino de Dos Rodillos se usa un novedoso procedimiento no lineal que es robusto y hace posible el desarrollo de experimentos de larga duración.

Del capítulo 1 al 4 de este trabajo se describen los elementos del dispositivo experimental además de la caracterización de los valores experimentales del tipo de flujo que se tiene con las geometrías disponibles para la celda de flujo del Molino de Dos Rodillos. También se evalúa el desempeño de la celda de flujo, en particular las velocidades instantáneas obtenidas en los cilindros, las cuales son parámetros críticos en la estrategia de control implementada. La implementación de este control se hace aplicando un esquema no lineal –basado en el teorema de Poincaré-Bendixson– que no ha sido usado previamente. Este control requiere de un proceso basado en un análisis de imágenes en tiempo real y en un ajuste de las velocidades de los motores también en tiempo real. Estas características están incorporadas en un programa de computadora que controla el dispositivo experimental, desarrollado en

Visual C++ y que coordina los datos provistos por el análisis de imágenes y el control de los motores en tiempo real. Este control fue probado experimentalmente para encontrar los parámetros más apropiados, para evaluar su robustez y corroborar que el control no afecta la dinámica de deformación de la gota.

Los capítulos 5 y 6 presentan los resultados experimentales obtenidos con el dispositivo para diferentes parámetros del tipo de flujo y para dos sistemas de relaciones de viscosidad. Los resultados para la relación de viscosidades baja incluye la determinación de los números capilares críticos para esa relación de viscosidades como función del tipo de flujo asi como la observación del proceso de ruptura. Para la relación de viscosidades alta, los resultados experimentales muestran el comportamiento altamente complejo presente en los estados transitorios y como este comportamiento es modificado por el flujo. Para este caso el dispositivo de flujo permite el estudio de la respuesta de la gota al inicio súbito de un flujo. Para números capilares muy bajos, la evolución temporal de la deformación es caracterizada por una función de incremento monótono simple hacia un estado permanente. Para números capilares grandes el estado permanente se alcanza después de una evolución oscilatoria multi-amortiguada. Efectos de fronteras cercanas en la deformación de la gota también fueron estudiadas, para ambas relaciones de viscosidad, siendo más evidentes y estudiadas con mas detalles en el sistema con una alta relación de viscosidades. Para este ultimo sistema y con el campo de flujo más cercano a cortante simple, fue posible observar el efecto de confinamiento en la deformación durante los estados transitorio y permanente. Los experimentos de confinamiento muestran que hay efectos similares en reducir la vorticidad en el campo de flujo y en inhibir sus efectos incrementando el grado de confinamiento de la gota.

Índice

Introduction

Fluids formed by small drops of one fluid immersed into a second continuous immiscible fluid are found in countless important industrial operations. Food and pharmaceutical emulsions, paint manufacturing, polymer processes, are some examples. Also, enhanced oil recovery and soil and groundwater remediation often involve the use of multiphase fluids. Because the structure of the two-phase fluid depends on the history of flow stresses, the processing of these fluids plays a fundamental roll in their manufacturing processes. That is, their properties are due to a dynamic microstructure, which can be easily modified or disrupted by the presence of external stress fields. Hence, engineering applications of these complex fluids require developing the capacity of prediction and control of its dynamic behavior. That is, its rheology must be based upon the knowledge of its microstructure evolution and stability.

It is well known that the basic knowledge of the deformation, break-up and coalescence of one single drop is an useful benchmark to understand the physical phenomena involve, which can be extrapolated to a better qualitative understanding of more concentrated systems. Many researchers have contributed to this knowledge, beginning with the pioneering of Taylor (1934). The flow of these substances shows a rheological behavior that depends on the viscosities ratio, the surface tension, surfactants, flow-type parameter and the coupled effects of the fluid structure and the kinematics properties of the flow. The coupling of structure and flow occurs in the non-linear regimen, being an area of current scientific research.

Earlier studies of the dynamics of drops have been summarized in excellent reviews by Acrivos (1983), Rallison (1984), Stone (1994) and Briscoe et al. (1999). Until now, the bulk of theoretical and experimental studies with strong flows have addressed the fluid dynamics of pure extensional flows or simple shear flows (Rallison 1984; Stone 1994). Four-Roll Mills (pure extensional flows) and Parallel Band (simple shear flows) cover a wide interval in the *flow-type* parameter. More recently, Moldenaers

and collaborators have used an eccentric Couette cell to study the drop deformation dynamics in a combination of simple shear and elongational flow in a periodic time dependent environment.

However, there is a gap between these flow fields and those generated by co-rotating Two-Roll Mill geometries. The TRM flows cover a range of flow parameters not accessible with any of the previous devices. In this Thesis, the methodology for study the dynamic of drops using the Two Roll Mill device will be presented. This device is particularly effective for flows with values of the flow type parameter α between $0.03 \leq \alpha \leq 0.3$ (Reyes and Geffroy 2000b). The smallest value implies a flow very close to the kinematic of simple shear while the largest values provide a deformation rate typical of elongational flow. With this setup, drop deformations can be studied under varied and well characterized kinematic conditions. Thus, this flow cell is capable of providing detailed experimental information about drop dynamics under conditions that include the effects of elongation with significant vorticity, nearby walls, and the presence of surfactants or other polymeric additives; conditions not amenable to study with the earlier flow devices. From the point of view of applicable boundary conditions, drop phenomena analyzed with this experimental setup have similar kinematics, as well as dynamically to the slow flow hydrodynamics of two-phase flows through pores and fractures.

Chapter 1 presents the parameters that rule the drop deformation (the flow type parameter among them) and a brief background about related previous works. Chapter 2 exposes the concept of the Two-Roll Mill geometry, how it produces the different flow fields and the parameter that characterizes those flow fields as the angle that defines the parameter of type of flow. Chapter 3 presents the components of the experimental device and the characterization of the different geometries used in this work, it is to say, the measure of the precise flow type parameter values corresponding to each one of the geometries available.

Chapter 4 presents the implementation of the control scheme used to keep the drop in the region of study, it contains the parameters of the control and the test carried out to ensure that it does not affect the drop deformation results and that is robust enough to carry out long time experiments. In chapter 5 the results of the experiments of drop deformation performed with this flow cell are presented, Those results show the effect of the flow type parameters in the dynamics of deformation for two viscosities ration and the confinement effect for the flow filed closest to simple shear. Chapter 6 present the measure of the interfacial tension for the two viscosities ration using the data provided by the experimental device.

1 General aspects on drop deformation

1.1 Drop deformation parameters

Many problems in fluid mechanics involve the flow of a drop of one fluid embedded in another immiscible fluid. This problem exhibits many complex phenomena and is especially difficult to solve the basic equations, because the position and shape of the drop changes in response to the second fluid in movement. Figure 1.1 shows the basic description of the problem as a drop of radius r_0, viscosity μ_0 and density ρ_0, freely suspended in a second immiscible fluid with viscosity μ_1 and density ρ_1. Assuming that both fluids are Newtonian and incompressible, and that the flow is slow enough such as that Re $\ll$ 1, then the inertial effects may be neglected and the governing equations are only the Stokes and continuity equations.
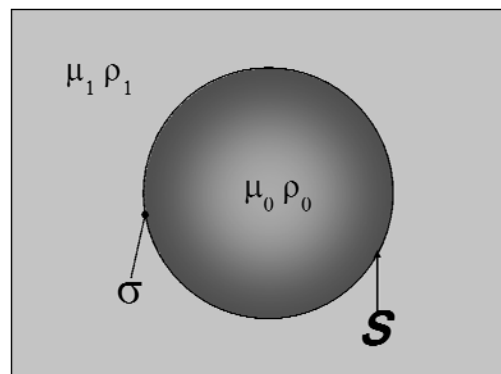

Figure 1.1. Schematic representation of a drop suspended in a second immiscible fluid.

$$\nabla \cdot \boldsymbol{u}_1 = 0 \qquad \nabla p_1 = \mu_1 \nabla^2 \boldsymbol{u}_1 \ , \tag{1.1}$$

$$\nabla \cdot \boldsymbol{u}_0 = 0 \qquad \nabla p_0 = \mu_0 \nabla^2 \boldsymbol{u}_0 \ . \tag{1.2}$$

1.1.1 Boundary Conditions

From a dynamical point of view the interface S between the drop and the external fluid is a singular surface of concentrated forces; i.e., the forces acting on both sides of the interface have different values, which creates a discontinuity on the surface force Δf that basically depends on the surface tension σ. Under flow, when Δf is different from zero and has a finite value, may deform, while $\Delta f = 0$, means that the interface in simply advected by the flow and is has no important role in the deformation dynamics. Considering that the governing equations are valid in the two fluids, there are boundary conditions that must be satisfied at the drop interface in order to determinate completely a solution of these governing equations. Those conditions are: the continuity of the velocity field across the interface, the kinematic condition on the flow device and the local balance of stresses across the interfaces **S.**

Continuity of the velocity

The continuity of the velocity at the interface S corresponding to the *no-slip boundary condition* implies that

$$\mathbf{u_1} = \mathbf{u_0} \text{ on } \boldsymbol{S}, \tag{1.3}$$

where the velocity in the external fluid is $\mathbf{u}_1$ and the velocity of the drop fluid is $\mathbf{u}_0$.

Kinematic condition

The kinematic condition, which comes from the *principle of mass conservation,* is based upon the assumption that the interface is neither a source nor a sink of mass. Accordingly, the normal component of the velocity at S, in both fluids, must be equal to the normal velocity of the surface itself. As the surface S may translate and deform into new shapes as a function of time, the kinematic condition can be expressed in the form of a relationship between $\mathbf{u}_1 \cdot \mathbf{n}$ or $\mathbf{u}_0 \cdot \mathbf{n}$ and the time rate of change of the interface shape (where $\mathbf{n}$ is the unit normal vector to S, see Fig.1.2). To express this relationship in mathematical form, consider that $F(\boldsymbol{x}; t)$ represents the interface shape as the set of points $\boldsymbol{x}$ where $F(\boldsymbol{x}; t) = 0$. Then, the unit normal vector $\mathbf{n}$ to S can be defined in terms of $F(\boldsymbol{x}; t)$ as

$$\mathbf{n} = \pm \frac{\nabla F}{\|\nabla F\|} \ , \tag{1.4}$$

where the sign is chosen by convention so that $\mathbf{n}$ is a positive unit vector when it points into the exterior fluid 1. Now, since F is a scalar function which is always equal to zero at any point on the fluid interface, its time derivative following any material point on the interface is equal to zero, that is

$$\frac{\partial F}{\partial t} + \mathbf{u} \cdot \boldsymbol{\nabla} F = 0 \,, \qquad \text{for any point on } \boldsymbol{S}. \tag{1.5}$$

Replacing Eq. 1.4 into Eq. 1.5, the kinematic condition is given as

$$\frac{1}{\|\boldsymbol{\nabla} F\|} \frac{\partial F}{\partial t} + \mathbf{u} \cdot \mathbf{n} = 0 \,, \qquad \text{on } \boldsymbol{S}. \tag{1.6}$$
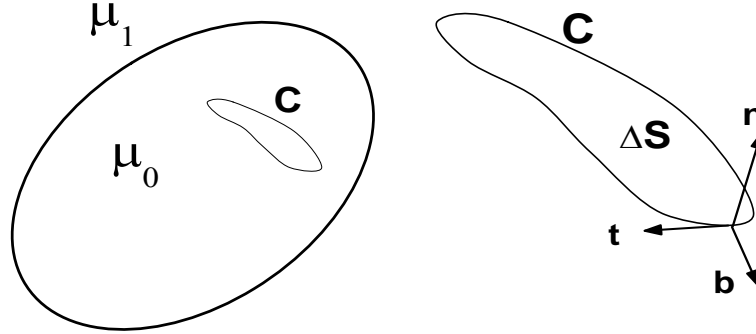

Figure 1.2. Schematic representation of the section of the interface between the drop and the external fluid.

Stress conditions

If the interface is characterized by an isotropic surface tension, σ, acting in the plane of the interface, there are only two forces on any element of the interface: (a) The stresses **T** acting on the faces of the interface element which are proportional to the surface area, and (b) the tensile force, due to the interfacial tension, acting on the plane of the surface at the edges of the interface element. To obtain a relation between σ and Δf, consider an element of surface area at the interface ΔS that is enclosed by the contour **C** —see Fig. 1.2— then, the force balance has the form

$$\iint_{\Delta A} (\mathbf{T} - \hat{\mathbf{T}}) \cdot \mathbf{n} \, dS + \oint_C \sigma \, \mathbf{b} \, dl = 0 \,, \tag{1.7}$$

where the unit vector **b** lies on the plane tangent to the interface and is normal to **C**, see Fig. 1.2. Using the identity $\mathbf{b} = \mathbf{t} \times \mathbf{n}$, Eq. 1.7 can be rewritten in the equivalent form:

$$\iint_{\Delta A} (\mathbf{T} - \hat{\mathbf{T}}) \cdot \mathbf{n} \, dS = \oint_C \sigma \, \mathbf{n} \times \mathbf{t} \, dl \,, \tag{1.8}$$

where **n** and **t** are unit vectors normal to the interface and tangential to **C**, respectively. To convert the contour integral of Eq. 1.8 into an area integral, a variation of the Stokes' theorem can be used; thus,

$$\oint_C \mathbf{F} \times \mathbf{t}\, dl \iint_{\Delta A} (\mathbf{n}\, \nabla \cdot \mathbf{F} - \nabla \mathbf{F} \cdot \mathbf{n})\, dS \, , \tag{1.9}$$

where $\mathbf{F}$ is a differentiable function defined over the whole space. Extending the domain of definition of the normal vector $\mathbf{n}$ and of the surface tension σ away from the interface into the whole space, setting $\mathbf{F} = \sigma\, \mathbf{n}$, and using Eq. 1.9, the following equation is obtained:

$$\oint_C \sigma\, \mathbf{n} \times \mathbf{t}\, dl \iint_{\Delta A} (\mathbf{n}\, \nabla \cdot (\sigma \mathbf{n}) - \nabla(\sigma \mathbf{n}) \cdot \mathbf{n})\, dS \, . \tag{1.10}$$

Substituting Eq. 1.10 into Eq. 1.8, and noting that $\nabla \mathbf{n} \cdot \mathbf{n} = \frac{1}{2}\nabla(\mathbf{n} \cdot \mathbf{n}) = 0$, thus

$$\iint_{\Delta A} [(\mathbf{T} - \widehat{\mathbf{T}}) \cdot \mathbf{n} - \mathbf{n}\, \nabla \cdot (\sigma \mathbf{n}) + \nabla(\sigma \mathbf{n}) \cdot \mathbf{n}]\, dS =$$

$$= \iint_{\Delta A} [(\mathbf{T} - \widehat{\mathbf{T}}) \cdot \mathbf{n} - \sigma \mathbf{n}\, \nabla \cdot \mathbf{n} + (\mathbf{I} - \mathbf{nn}) \cdot \nabla \sigma]\, dS = 0 \, . \tag{1.11}$$

Given that the last equation is true for any arbitrary surface element, and the surface tension is uniform then

$$(\mathbf{T} - \widehat{\mathbf{T}}) \cdot \mathbf{n} = \sigma \mathbf{n}\, \nabla \cdot \mathbf{n} \, . \tag{1.12}$$

If we take the inner product of Eq. 1.6 with $\mathbf{n}$, and recalling that $\mathbf{T} = -p\mathbf{I} + \tau = -p\mathbf{I} + 2\mu\mathbf{E}$, this gives

$$\hat{p} - p + [(\tau - \hat{\tau}) \cdot \mathbf{n}] \cdot \mathbf{n} = \sigma\, \nabla \cdot \mathbf{n} \, . \tag{1.13}$$

The non-dimensionalization of the last equation with the characteristic length the drop radius $l_c = r_0$, the characteristic velocity as the translational velocity of the drop $u_c = \mathbf{U}$ and $p_c = \mu U/a$ for the characteristic pressure (valid for low Reynolds number). The result is

$$\frac{\mu\, \mathbf{U}}{r_0} (\lambda \hat{p} - p) + \frac{\mu\, \mathbf{U}}{r_0} [(2\mathbf{e} - 2\lambda \hat{\mathbf{e}}) \cdot \mathbf{n}] \cdot \mathbf{n} = \frac{\sigma}{r_0} \nabla \cdot \mathbf{n}. \tag{1.14}$$

Or

$$(\lambda \hat{p} - p) + \underbrace{[(\mathbf{e} - \lambda \hat{\mathbf{e}}) \cdot \mathbf{n}] \cdot \mathbf{n}}_{Flow\ Field\ stress} = \frac{1}{Ca} \underbrace{\nabla \cdot \mathbf{n}}_{Drop\ shape} \, . \tag{1.15}$$

Where $\mathbf{e} = (r_0/\mathbf{U})\, \mathbf{E}$, is the dimensionless rate of deformation tensor, $\lambda = \mu_0/\mu_1$ is the viscosity ratio and the dimensionless parameter Ca is the capillary number.

The first and the second terms on the right side of Eq. 1.15 express discontinuities of the stress field in the normal directions. When the drop is subjected to a flow field, the pressure and stress differences at the interface do not have a uniform distribution. In this case, the normal stress balance is satisfied by a deformation on the drop, where the interface curvature $(\nabla \cdot \mathbf{n})$ varies in the same way as the normal-stress variations over the surface.

From the dimensionless form of the stress condition we can observe that the three governing parameters for drop deformation are:

- The viscosities ratio $\lambda = \mu_0/\mu_1$

- The capillary number $Ca \equiv r_0\, \mu_1 \sqrt[2]{|\mathbf{II_{2E}}|}/\sigma \equiv r_0\, \mu_1\, \dot{\gamma}\, /\sigma$

  Where $\mathbf{II_{2E}}$ is the second invariant of $2\mathbf{E} = \nabla\mathbf{u} + \nabla\mathbf{u}^T$. For simple shear rate flows, $\sqrt[2]{|\mathbf{II_{2E}}|} = \dot{\gamma}$

- And the tensorial character of $\nabla\mathbf{u}$.

  Where the tensorial character of $\nabla\mathbf{u}$ gives the *Flow-Type parameter* α

1.1.2 Flow-Type Parameter

The flow-type parameter characterizes the form of the velocity gradient tensor and specifies the ratio of the magnitude of the rate of deformation tensor to that of the vorticity

$$\frac{magnitude\ of\ deformation}{magnitude\ of\ vorticity} = \frac{1+\alpha}{1-\alpha}.$$ (1.16)

Thus α is given by

$$\alpha = \frac{\|\mathbf{E}\| - \|\overline{\mathbf{w}}\|}{\|\mathbf{E}\| + \|\overline{\mathbf{w}}\|}.$$ (1.17)

Where $\mathbf{E} = \frac{1}{2}\left(\nabla\mathbf{u} + \nabla\mathbf{u}^T\right)$ is the rate of deformation tensor and $\overline{\mathbf{w}}$ is the objective vorticity tensor (Astarita 1979), which measures the rate of rotation of a material point with respect to the rate of deformation's principal axes at that point.

The case of $\alpha = -1$ corresponds to pure rotational flow, $\alpha = 0$ to simple shear flow and $\alpha = 1$ describes a pure extensional flow (see Fig.1.3). Figure 1.4 shows the streamlines for different values of α between simple shear and pure extensional flows.
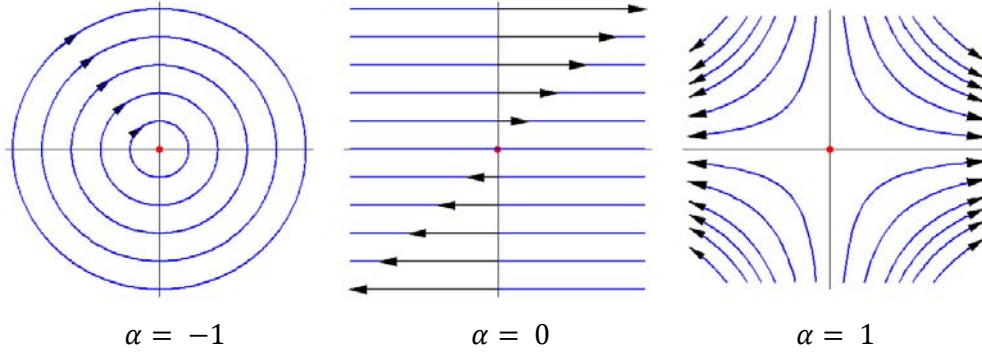
$$\alpha = -1 \qquad\qquad \alpha = 0 \qquad\qquad \alpha = 1$$

Figure 1.3.   stream lines for some flow type parameter.

$\alpha = 1.0 \qquad\qquad \alpha = 0.8 \qquad\qquad \alpha = 0.6$

$\alpha = 0.4 \qquad\qquad \alpha = 0.2 \qquad\qquad \alpha = 0.0$
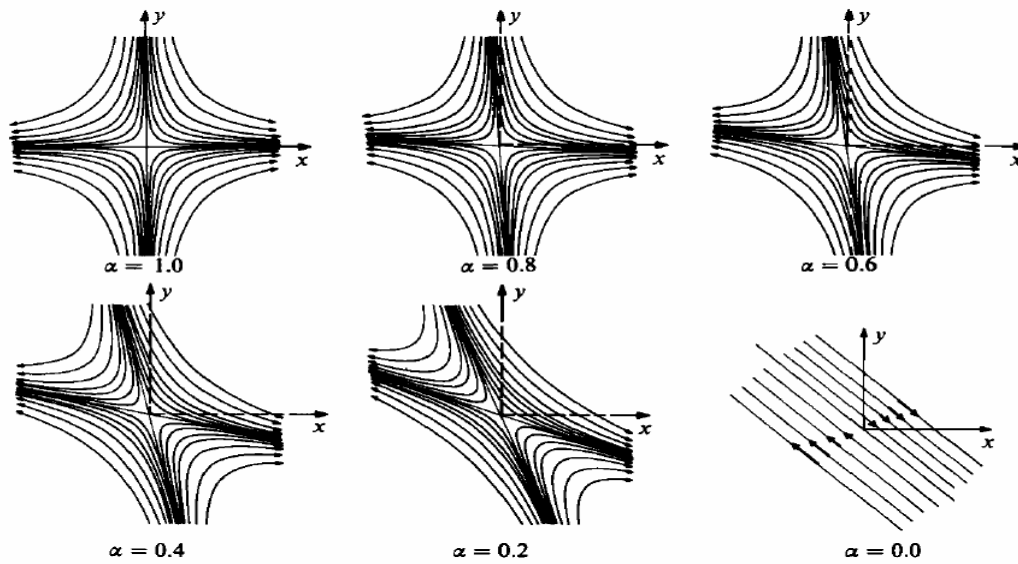
Figure 1.4.   Streamlines for different values of the Flow-Type parameter (Bentley & Leal 1986b). The TRM attains flow fields similar to those of the lower plots.

1.1.3 Deformation Parameter

To characterize the deformation of the drop under a flow field, a first approximation assumes ellipsoidal deformed shape and the dimensionless measure of the magnitude of the deformation is the *Taylor Deformation Parameter* $\boldsymbol{D_T}$, defined in terms of the major semi axis L and the minor semi axis B of the ellipsoidal drop cross section proyected in the *x-y* plane Fig 1.5. The cross section proyected in the *z-y* plane is considered to be almost circular or $W = B$.

$$D_T = \frac{L-B}{L+B}\,, \tag{1.18}$$

The angle between the major semi axis L of the deformed drop and the *x*-axis, correspond to the the orientation angle θ of the drop.
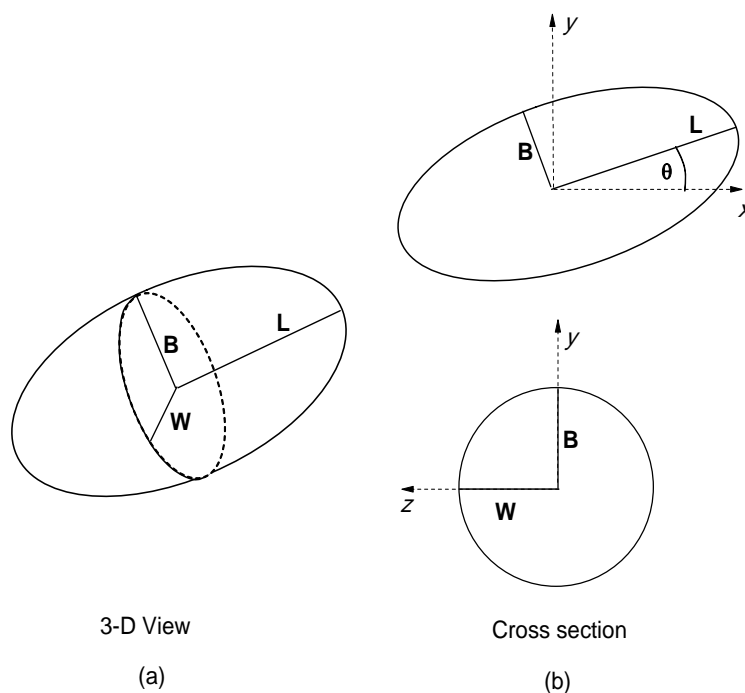
Figure 1.5. Semi-axes of the ellipsoidal deformed drop and the orientation angle θ.

1.2 Historical Background

When a drop is suddenly subjected to flow, it will deform, orient and possibly break up. As it was mentioned before, the drop response is determined by its viscosities ratio, the capillary number, and the nature of the flow. For capillary numbers lower than a critical value, the stresses upon the drop due to the flow field are equilibrated by the interfacial tension and the drop reaches a final steady state shape and orientation. For capillary numbers above the critical value, the surface tension is not strong enough to balance the flow field stresses and the drop eventually breaks up. A high level of research activity, focused on the relationship between flow and drop deformation, has been carried out since the work done by Taylor (1932, 1934). This work includes, both theoretical analysis (based on the small deformation and negligible inertia forces assumptions) and experimental observations, focused on the deformation of single drops suspended in a second liquid to which either a simple shear or a planar elongational flow is applied. In order to generate these flows experimentally Taylor used the Parallel Band apparatus (PB for simple shear flow) and Four-Roll Mill apparatus (FRM for planar elongation). In general, at small deformations Taylor's theory agrees well with experimental observations.

Some major improvements of Taylor's theoretical work include better drop shape description (Chaffey and Brenner 1967), covering a wider range of viscosities ratios (Cox 1969), and the description of their transient behavior (Cox 1969; Barthès-Biesel and Acrivos 1973; Rallison 1980). Furthermore, in

order to study highly extended drops, slender body theory has been applied by Acrivos and Lo (1978), Rallison and Acrivos (1978) and Hinch and Acrivos (1979, 1980).

Major experimental contributions are due to Rumscheidt and Mason (1961), Torza et al. (1972), Grace (1982), Bentley and Leal (1986a,b), Stone et al. (1986) and more recently by Guido and Villone (1998), Guido et al. (1999, 2000), Guido and Greco (2001), Birkhofer et al. (2005) and Megias-Alguacil et al. (2005). These include measurements of the critical capillary number over a wide range of viscosities ratio, both in simple shear and planar elongation flows (Grace 1982), and computer controlled versions of Taylor's four roll mill (Bentley and Leal 1986a) and shear band apparatus (Guido and Villone 1998; Birkhofer et al. 2005). These computer-controlled versions of the Taylor's setup take advantage of modern camera technology in that they use real-time monitoring of the drop position as input in their control algorithms.

The bulk of theoretical and experimental studies (except that of Bentley and Leal 1986a, b), have only addressed the fluid dynamics of two flow field types: simple shear flows (where the magnitudes of the vorticity and the strain rate are equal, $\alpha = 0$), and pure extensional flows (with no vorticity, $\alpha = 1$), whereas actual dispersing devices generally create highly complex flows and the behavior of drop deformations have a strong dependence on the flow type. As it was mentioned before, the three main aspects that domain the behavior of the drop are: the capillary number Ca, the viscosities ratio λ and the nature of the flow field α. The first one can be easily modified by changing the strain rate for fixed viscosities ratio and flow type. With respect to the others, Grace (1982) carried out an investigation for the critical capillary number as a function of the viscosities ratio for single Newtonian drops in both simple shear and planar elongation flows and later, Bentley and Leal (1986b) carried out these studies for some intermediate flow types. Figure 1.6 shows the experimental data for these experiments. The continuous line in the figure is an empirical fit to Grace's data made by de Bruijin (1989) for simple shear flow that summarizes the results indicating that no break up is possible when $\lambda > 3.5$, which agrees well with the results found by Taylor. For pure extensional flow, although qualitatively different, both Grace (1982) and Bentley and Leal (1986b), results show that this flow-type can break up the drop regardless of the viscosities ratio. As to intermediate flow types, Bentley and Leal founded that for flow fields with $\alpha < 0.4$, there is a limit of viscosities ratio that depends on the flow type, for $\alpha = 0.2$ the limits is $\lambda = 27$ and for $\alpha = 0.4$ the corresponding limit is $\lambda = 57$. Flow fields with $\alpha = 0.6$ or higher, always can achieve the breakup of the drop as in pure extensional flows. More recently, Moldenaers and collaborators have used a time combination of simple shear and elongational flows in an eccentric Couette device (Boonen et al. 2010).
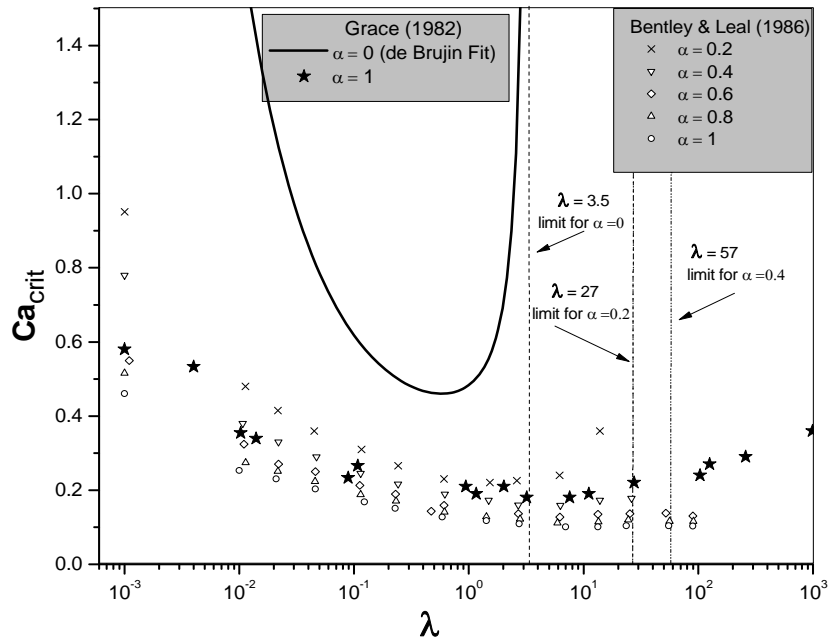
Figure 1.6. **Critical capillary numbers for different values of flow type parameters as function of the viscosities ratio. The continuous line is a curve fitted to the experimental data of Grace (1982) done by de Brujin (1989).**

Figure 1.6 shows that the amount of vorticity plays a critical role in drop deformation. It determines the critical capillary number needed for drop breakup; even more, if the drop will breakup or not for a given viscosity ratio. The breakup condition of a drop depends on the flow type because the vorticity present in the flow field will tend to inhibit the deformation applied for the flow. That's why the breakup of a drop is always possible in flow fields with $\alpha = 1$ or closer values, where the vorticity is too small or even inexistent to counteract the deformation. In general, for the same capillary number and viscosities ratio, as the amount of vorticity present in the flow field is increased (α approaching zero), the possibility to breakup the drop is reduced.

There are many devices which can generate flows with values of $\alpha = 0$ and the computerized version of the four roll mill of Bentley and Leal (1986a) allows the generation of flow fields in which the flow type parameter can achieve different values ranging from $0.2 < \alpha \leq 1$. Thus, four-roll mills and simple shear flow devices cover a wide interval in the flow-type parameter space. However, there is a gap in the flow type values still not reported. As can be seen in Fig. 1.6; the qualitative behavior for flows with $\alpha \geq 0.6$ is very similar, and is close to that for $\alpha = 0.2$, the figure shows that the drop behavior for flow fields with values of $\alpha = 0$, differs greatly from those with values of α higher than 0.2. In order to fill this gap in understanding, which is worth to investigate, the co-rotating Two-Roll Mill (TRM) can be used. Different geometries for this device can generate flow fields with an effective interval for α of $0.03 \leq \alpha \leq 0.3$ (Reyes and Geffroy 2000b). And for the Newtonian-fluid Stokes flow, there is an analytical

solution for the TRM that can be used as benchmark for the underlying studies of the accuracy of the flow device, *not available* for FRM configurations.

2 Flows generated by Two-Roll Mills

The use of laminar flows capable of inducing significant deformation on the fluid microstructure on embedded objects is an essential tool for studies in fluid mechanics of non-Newtonian fluids (Geffroy and Leal 1992, Singh and Leal 1996), chaotic advection (Jana et al. 1996, Atobe 1997), drop and bubble dynamics (Stone 1994, Bentley and Leal 1986 b), and in general in many industrial applications. These flows have proven advantageous for studies of fluid systems that show a marked nonlinear, hysteretic behavior due to its dynamic microstructure. Simple viscometric flows and purely extensional flows (Huilgol and Phan Thien) are among the two most frequently used flow fields that have different kinematics. However, on one hand viscometric flows have significant amounts of vorticity and are expected not to produce large deformations on an embedded object. The observed behavior in viscometric steady flows is understood by parcels of fluid that at any given time separate linearly in time; i. e., at most, the separation can only grow algebraically. Hence, these flows produce only a moderate change on the fluid structure, and thus are classified as weak flows. On the other hand, for steady extensional flows there is no vorticity, and two neighboring elements of fluid will separate in time exponentially. Given enough time, the flow will induce significant changes on the microstructure of the fluid regardless of its relaxation mechanisms; therefore, these are classified as strong flows (Olbricht et al. 1992, Chong et al. 1990).

2.1 The Two-Roll Mill geometry

A schematic of the Two-Roll Mill device is shown in Fig. 2.1. It consists of two cylinders of radius R with collinear axes separated by a small distance de and rotating in the same direction, while immersed in a fluid bath. The flow fields generated by a co-rotating TRM contain a stagnation point on the line between the cylinders axes, with well known local kinematic conditions and characterized by a given value of the flow parameter α.

Some of the features of the flow fields generated by these mills are as follows:

(a)   The value of the flow parameter α is determined only by the geometrical characteristics of the TRM; i.e., the cylinders radii and the axes separation.

(b)   Although these flows belong to the family of *strong flows*, simple shear flows behavior can be approached as closely as needed, by increasing monotonically the vorticity.

(c)   There exists an analytical solution for Stokes flow that takes into account the presence of the cylinders' boundaries, in contrast with other strong flows used to study long-term effects in embedded objects, such as four-roll mills.

In a TRM, the strength of vorticity and the shear rate can be easily varied, although with less flexibility than with a FRM (Bentley and Leal 1986a). Compared to Four-Roll Mills, the Two-Roll Mill requires a change of geometry for different values of α. In contrast and for a given geometry, the shear rate, $\dot{\gamma} = \sqrt{|\mathbf{II_{2E}}|}$, at the stagnation point is a simple function of the speed of the cylinders.

For TRM geometries with equal radii, the flow-type parameter at the stagnation point has a maximum value when the angular velocity is the same on each cylinder, and the ratio of deformation rates to vorticity associated to the flow-type parameter α, it is given as

$$\alpha = tan^2(\phi), \tag{2.1}$$

where ϕ is half the angle of the incoming and outgoing axes in the stagnation point (see Fig. 2.1). This angle is a function of the geometry of the TRM, and is independent of the angular velocity of the cylinders (Reyes and Geffroy 2000a, Reyes 2005). Fig. 2.2 shows the streamlines for symmetric co-rotating Two Roll Mills for several ratios between the cylinder's radius and their axes separation distance *de*.

For large α values, say $\alpha > 0.3$, the maximum shear rate accessible at the stagnation point is small, requiring a high angular velocity of the cylinders in order to achieve moderate shear rates at the central region. Under these conditions, a high shear rate always exists near the cylinders, consequently generating a poor condition for a low Reynolds number flow fields. This is the main limitation for generating strong flows using devices based on Two-Roll Mill geometries. When using Four-Roll Mills, the smaller values of the flow field parameter are achieved by rotating a set of two cylinders very slowly compared to the other two. Thus, Four-Roll Mill flow fields with small values are intrinsically unstable, and the control scheme becomes less reliable, contrary to what is expected for flows generated by TRMs. Consequently, Two-Roll and Four-Roll Mills are adequate flow field complements to each other.
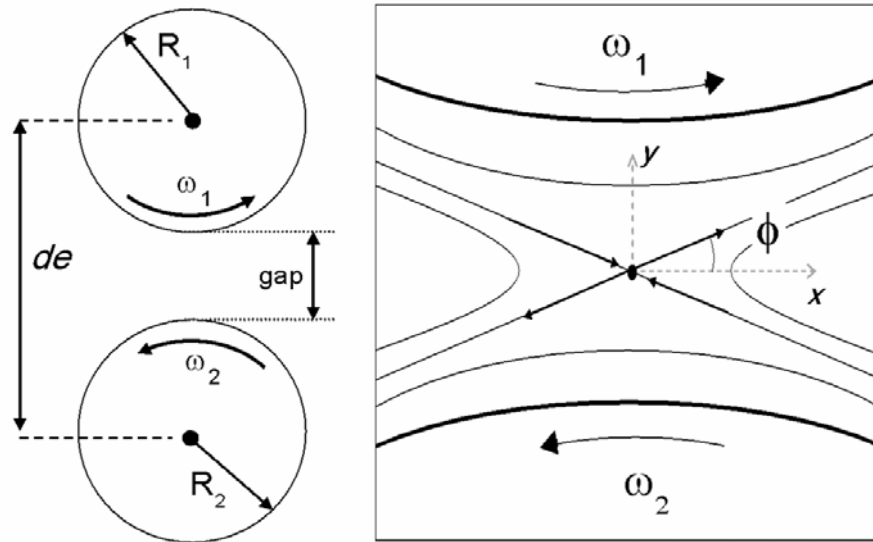
Figure 2.1. (a) The Two-Roll Mill device consist in two co-rotating cylinders of equal radius, with collinear axes separated by a small distance; (b) Stream lines for a flow field generated by a Two Roll Mill device. The stagnation point is located on the line between the cylinders' axes and the angle ϕ between the incoming and outgoing stream lines.

$\alpha = 0.03$
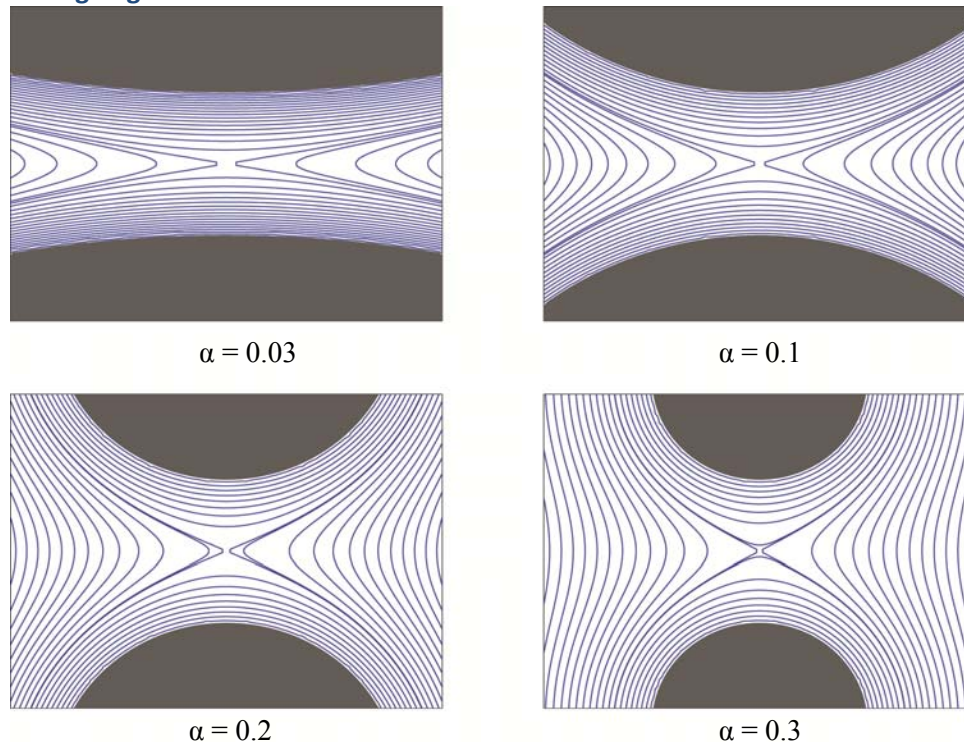
$\alpha = 0.1$

$\alpha = 0.2$

$\alpha = 0.3$

Fig. 2.2. Streamlines for symmetric co-rotating Two-Roll Mills for several ratios between the cylinders' radius and their axes distance. These figures are obtained from the analytical solution (Reyes 2005). This solution is used to calculate all flow parameters and is valid for an extended central region.

3 The experimental device

This chapter presents the elements that constitute the computer-controlled Two Roll Mill flow cell experimental device. It is divided in two parts. The first part describes the characteristics of the elements of the apparatus and the second part describes the characteristics of its operation to produce the required flow field parameters.

3.1 Main elements of the experimental device

Figure 3.1 (a) shows some of the principal components of the experimental device mounted on a pneumatically levitated workstation by Newport Research. In the Figure can be seen the optical system, the Two-Roll Mill flow cell and the pair of motors. The figure 3.1 (b) is a scheme of the experimental arrangement.

The experimental device components are the:

- Optical System.
- Two Roll Mill flow cell.
- Interface system and motors.
- Illumination and thermal bath.

3.1.1 The optical system

The optical train is made up with:

- A motorized Navitar telecentric zoom, with a maximum magnification of 12X,
- An optical adapter Navitar 1-61390 with a magnification of 2X,
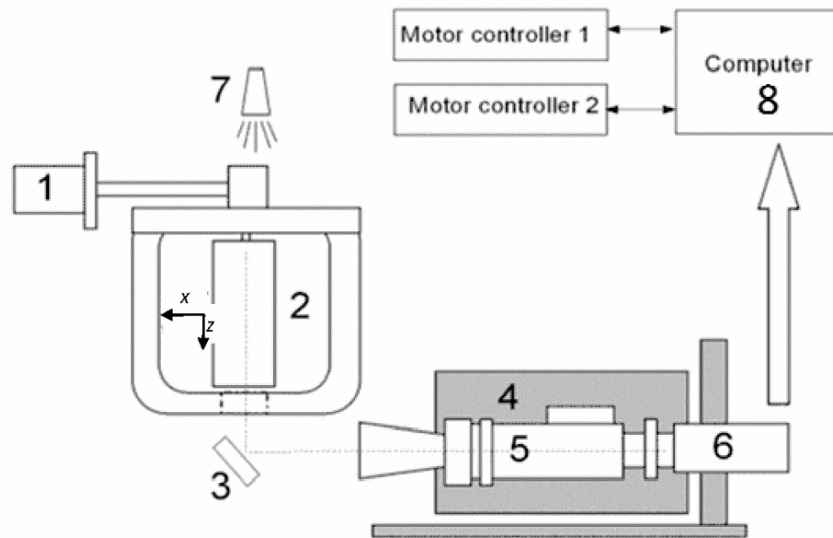- An IEEE 1394 CCD Sony camera, model XCD-X700.
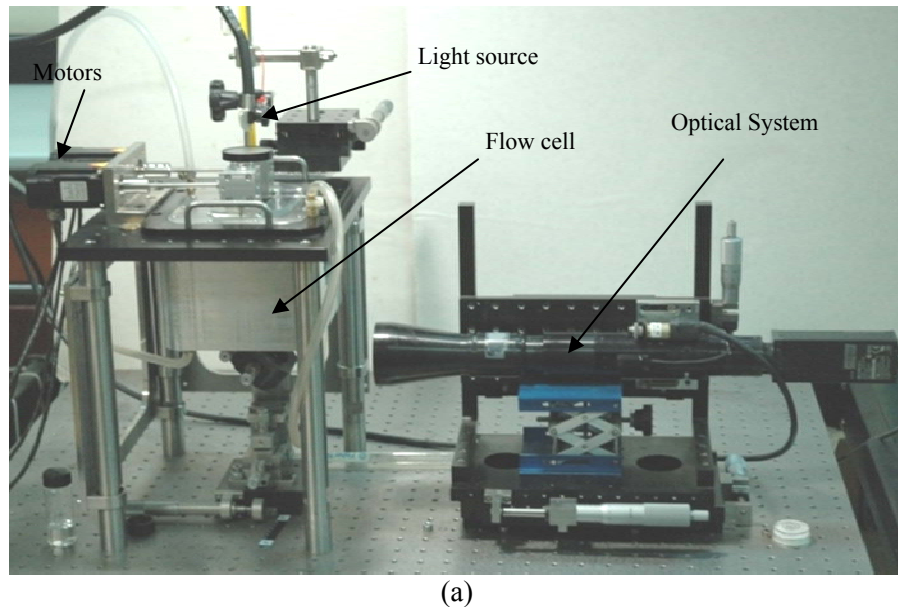
Figure 3.1. **Photo of the Experimental setup (top) and principal components: (1) Each cylinder is driven independently by a high resolution servomotor, (2) Flow cell container, (3) Mirror, (4) 3-axes displacement mount for optical system, (5) Motorized zoom and focus lens, (6) CCD Camera, (7) Fiber optic light source, and (8) Computer operating in real-time processes images and sets the motors speeds.**

The experiment is mounted to a base fixed to the levitated workstation. The optical assembly is mounted on a base that allows precise movements in all three axes by means of precision ground slides and micrometric screws manually operated, see Fig. 3.2. The visual field-of-view is covered with 1024 by 768 pixels is on the x-y plane of the flow field, which is accessible through the bottom glass window using a 45 degrees mirror (with the reflective coating on the front surface) located underneath the flow cell.
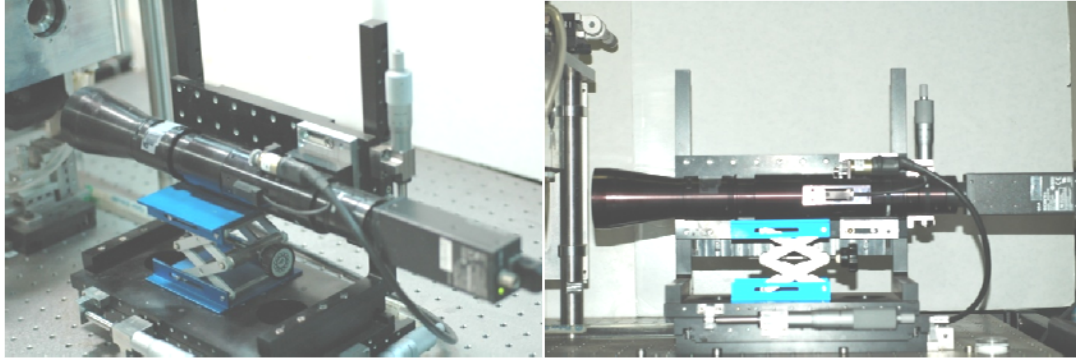
Figure 3.2. The optical system consists mainly of the camera and the motorized zoom is mounted in a rigid base that allows precise movements by means of precision ground slides and micrometric screws.

The optical system has two main purposes: (a) to monitor the position of the center of mass of the drop during the experiments, providing a sequence of images in real time to the control scheme in order to keep the drop in the stagnation point region, and (b) once the experiment is running, the system captures and saves the images of the deformation process for a posterior analysis of the dynamics. In order to carry out those tasks, it is necessary to know the capabilities and characteristics of the system, i.e., the resolution, focal distance, and the pixel/mm ratio for the optical train mounted.

The maximum optical resolution of the full assembly was determined using a 1951 USAF glass slide resolution test target by Edmund Optics. With this target, the resolution of any imaging system can be determined by viewing the clarity of the horizontal and vertical lines in the image of the target acquired by the system. The largest set of non-distinguishable horizontal and vertical lines determines the resolving power of the imaging system. Fig. 3.3 shows the structure of the target and Table 3.1 lists the resolution in number of line pairs per millimeter for a given element within a group. With our optical system, the maximum resolution is 64 line pairs per millimeter, which equates to roughly 8 μm corresponding to that of the element 1 in the group 6, Fig. 3.4.
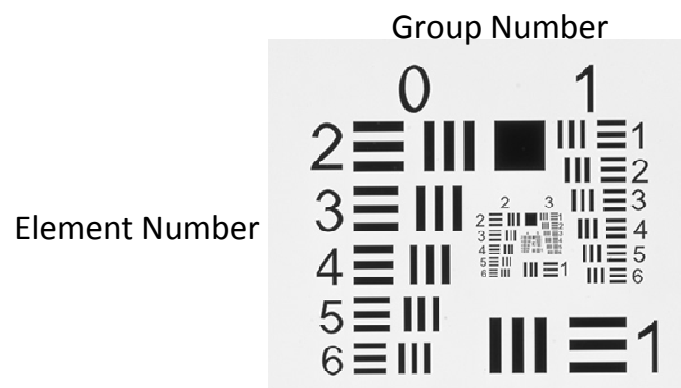

Figure 3.3 Structure of the USAF 1951 target showing the elements and groups numbers.

Table 3.1. Resolution of the system in number of line-pairs in function of the element and group number.

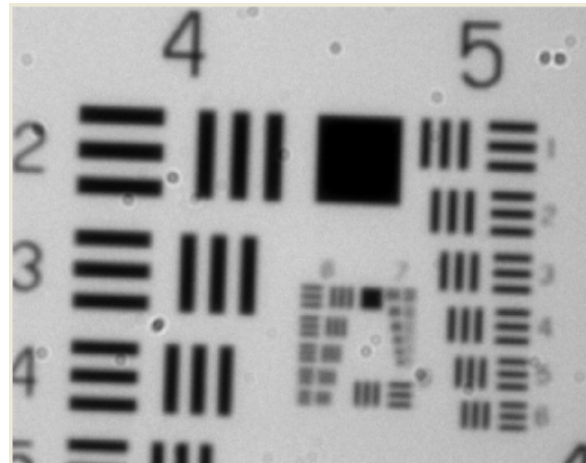| Element	Group Number									
	-2	-1	0	1	2	3	4	5	6	7
1	0.250	0.500	1.00	2.00	4.00	8.00	16.00	32.00	64.0	128.0
2	0.280	0.561	1.12	2.24	4.49	8.98	17.95	36.0	71.8	144.0
3	0.315	0.630	1.26	2.52	5.04	10.10	20.16	40.3	80.6	161.0
4	0.353	0.707	1.41	2.83	5.66	11.30	22.62	45.3	90.5	181.0
5	0.397	0.793	1.59	3.17	6.35	12.70	25.39	50.8	102.0	203.0
6	0.445	0.891	1.78	3.56	7.13	14.30	28.50	57.0	114.0	228.0

Figure 3.4. Image of the maximum resolution possible in the optical system. In this picture the element taken for the calibration is the first element of the sixth group corresponding to a resolution of 64 line pairs per millimeter.

It is necessary to obtain the real size of the objects in the images and given that the image analysis provides the dimension in pixels, then, a relation between pixels and millimeters is needed. This relation was determined using an Image Analysis Micrometer test target by Edmund Optics. The calibration was done by measuring a distance in the image of the target in pixels and relating that distance with the corresponding indicated for the target in micrometers. Fig. 3.5 shows an example of the image of the target obtained with the maximum magnification in the optical system. The procedure was repeated for different magnifications of the zoom and given that a change in the zoom requires an adjustment of the focal distance, this was done by translating the optical system along the optical axis with the micrometric screws. Table 3.2 summarizes the results of the calibration providing the relation of pixels and millimeters as well as the focal distance and the visual field dimensions for different zoom positions.
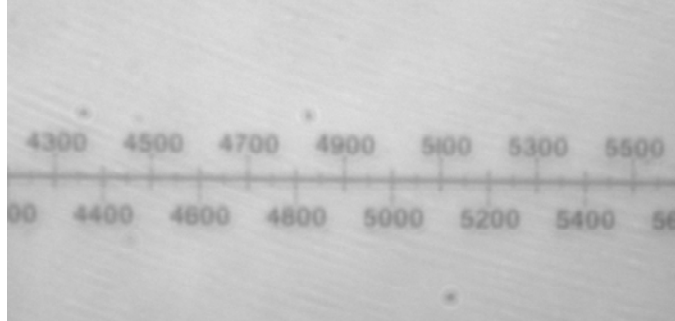
Figure 3.5. Image of the micrometer target test used for determine the relation of pixels and millimeters. This picture corresponds to maximum zoom and a relation of 700 pixels per each millimeter.

Table 3.2 Characteristics of the visual field of the optical system for different magnification grades.

Zoom position	Focal distance [mm]	pixels/mm ratio	Visual field size [mm]
12300	34.5	700	1.46 x 1.09
12000	34.8	658	1.55 x 1.16
11000	34.9	537.5	1.90 x 1.42
10000	35.2	438.4	2.33 x 1.75
9000	37.0	356.5	2.87 x 2.1
8000	39.5	288.8	3.54 x 2.65
7000	41.4	234.9	4.36 x 3.27
6000	42.4	191.5	5.34 x 4.01

3.1.2 The Two-Roll Mill flow cell

The TRM flow cell consists in two cylinders, a support for the two cylinders and an enclosure. To minimize the external wall effects on the flow field, the interior contour of the container matches a selected streamline around the cylinders. It is made of black anodized aluminum to minimize internal optical reflections (see Fig. 3.6). This main body has a cooling loop around the vertical walls of the body designed to maintain stable the temperature of the fluids. The cell has three optical quality windows, two on the side and one at the bottom. The cell is covered with a strong stainless steel lid where the cylinder supports —the housing for the worm-gear mechanism and bearing— are fastened. The lid has a large detachable acrylic window to facilitate illuminating from the top. Each cylinder inside of the flow cell is held in position by a set of three bearings, with worm-gear and bearing preloaded for tighter operation on the radial and axial directions. The cylinders are made of two pieces, an internal shaft of small diameter made of stainless steel, (which is in contact with all bearings, bolts and gears) and the outer shell —larger in diameter— made of black-anodized aluminum. The shafts were attached permanently —by previously cryo-shrinking the shafts— inside hollowed aluminum cylinders, and subsequently machining the ensemble to the exact required external dimensions. This low-mass design reduces the rotational inertia

of the cylinder while maintaining the required rigidity. The top and bottom end of the cylinder have conical shapes, with an angle that guarantees that the shear rate at the top and bottom gap is smaller than the values observed within the flow field. There is a 1mm gap between the top and bottom of the flow cell and the conical portion of the cylinders. These gaps can be filled with air (at the top) or a heavy fluid (for the bottom) of low viscosity in order to reduce the component of the velocity gradient normal to the extensional flow field.

Table 3.3. Dimension of the cylinders for each geometries and the corresponding analytical value of the flow type parameter α for each one of them.

Geometry	Cylinder	Diameter [mm]	Gap [mm]	Analytical value of the flow type parameter α
A	1	41.037	10.9	0.12
A	2	41.035	10.9	0.12
B	1	42.909	9.1	0.1
B	2	42.905	9.1	0.1
C	1	47.17	4.8	0.05
C	2	47.18	4.8	0.05
D	1	49.03	3	0.03
D	2	49.02	3	0.03

Given that the distance between the cylinder axes is fixed by the cell design, pairs of cylinders of different size are needed to generate flow fields with different values of α. In order to attain the highest accuracy generating flows, the most important criterion are the machining tolerances required for the geometry of flow cell. In particular, the value of α depends strongly on the size and shape of the cylinders and the separation and parallelism between its axes, while the steadiness of the shear rate depends on the tolerances of the coupling mechanism and motor performance driving each cylinder. For the actual geometry used in the laboratory, three physical length scales are critical: the exact diameter of cylinders, the concentricity of all cylindrical surfaces and the parallelism and exact distance between the cylinders axes. Assuming a fixed distance for the cylinder axes, *de,* and good concentricity of surfaces, then cylinders with a machining accuracy of ±0.005 mm will generate a flow field with an uncertainty of less than ±0.4% of the nominal value of α. The configuration of the flow cell used in these experiments has a fixed distance between cylinder axes of 52.000 mm. Table 3.3 presents the measured dimensions of the set of cylinders and its corresponding analytical value of the flow type parameter α. The parallelism of the cylinder axes is maintained by preloaded bearings. These bearing housings were all machined with the cell rigidly set on the milling machine, which guarantee a parallelism for the cylinders axes within 5 arc-seconds. The position of the lid is pin down to the flow cell by a pair of pegs, the latter maintaining a

reproducible top-to-bottom alignment. The cell is mounted on a rigid base to assure that this support provides the highest rigidity to shear displacement with respect to the imaging systems base.

Fig. 3.6 shows the channels and the connectors of the cooling loop, the top transparent cover for illumination, the housing for the gears, worms and top bearings, the lateral window housing. The flow cell is placed on a rigid base where the motors that drive the cylinders are attached. Given that the cylinder axes position is fixed for the TRM geometry, different sizes of the cylinders are needed to generate flow with different values of the flow type parameter.
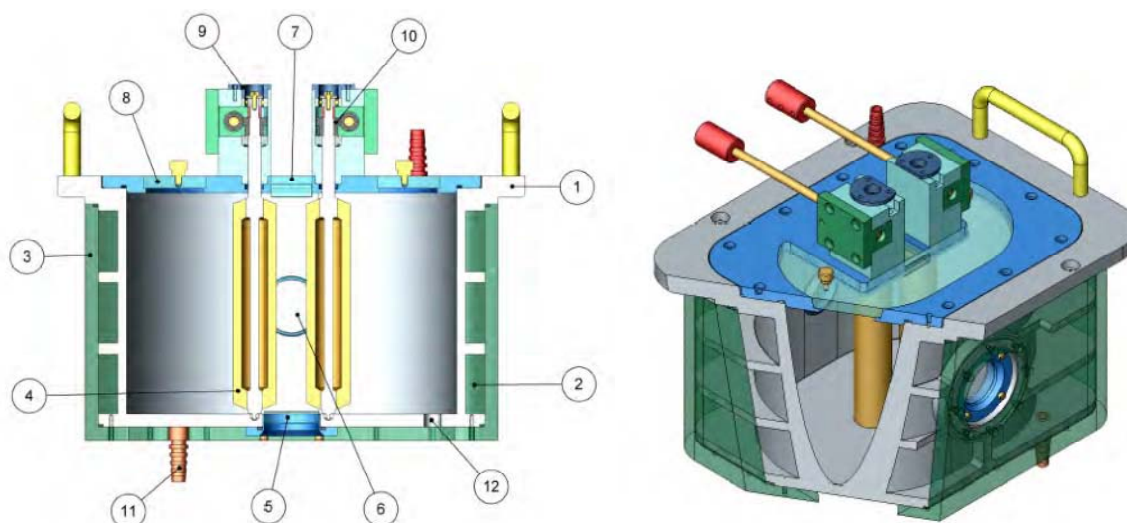

Figure 3.6. Components of the flow cell TRM–B: (1) Main body of the flow cell; (2) Channels of the cooling loop; (3) Exterior jacket of the cooling loop; (4) Hollowed cylinders, with steel shaft and external black anodized cylinders; (5) Bottom window assembly; (6) Lateral window assembly; (7) Top window assembly; (8) Lid of the cell body, with top acrylic window; (9) bearings and worm-gear support of a cylinder; (10) Worm-Gear mechanism; (11) Connector to the cooling loop; (12) Drainage hole.

3.1.3 Interface system and motors

The data acquisition system consists of a computer Workstation HP XW4300 with a PCI SERCOS expansion card for the motors, and a Firewire interface for the imaging system. The SERCOS communicates via optical fibers with the controllers of the motors, and permits addressing the motion controllers individually. Each cylinder is driven by a servomotor coupled with a precision and preloaded worm-gear mechanism. The Kollmorgen motors AKM-11B have a rating of 125W —with very small inertia— and are driven by Controller SERCOS Servostar 300. Communication by the motion controllers to the computer is through the dedicated PCI interface card. The steadiness to establish a given shear rate is

better than 0.2% and depends primarily on the precision of the motors systems to generate the corresponding velocity of rotation. The control of the motors can be done using the software BASIC Moves Development Studio, provided by Kollmorgen or using the API (Application Programming Interface) files incorporated in the Visual C++ program that was developed for this experiment. The software BASIC Moves was used only for the correct configuration of the motors and controllers or for testing purposes.

3.1.4 Illumination and thermal bath

Illumination

The illumination is done from the top using an optical-fiber bundle to guide the light from the lamp to the flow cell. The fiber optics is placed above the flow cell as is shown in Fig. 3.1. The light source is a Fiber-Lite metal halide fiber optic illuminator with intensity control via manual iris, model MH 100 by Dolan-Jenner.

Thermal bath

The control of the temperature of the fluids in the experiment was done using a RM6 LAUDA thermal bath. The inlet and outlet of the bath were connected to the inlets and outlets of the cooling loop in the flow cell. The temperature is maintained within ±0.01K.

3.2 Experimental parameters

In order to have reliable results with the experiments it is necessary to know the precise value of the parameters that characterize the dynamic of the drop deformation, it is to say: the viscosities ratio λ — that depends on the properties of the fluids—, the value of the flow type parameter α —that depends on the geometry of the cylinders— and the shear rate applied —that depends on the angular velocity of the cylinders ω. Besides, an essential aspect in the experiments is the control of the drop position whose fundamental parameter is the stagnation point location given by the intersection of the outgoing and incoming axis. Consequently, it is necessary to characterize the uncertainties of the experimental device in three aspects: (1) the real value of the flow type parameter α, (2) the velocities of the cylinders and (3) the stagnation point location, related with both the geometry and velocity of the cylinders.

3.2.1 Experimental values of the flow type parameter

The value of the flow type parameter α depends basically on the diameters of the cylinders used in the flow cell. However, the accuracy of the generated flow depends on the accuracy of machining. In

order to determine experimentally the value of α for each pair of cylinders we can use Eq. (2.1) that relates this value with ϕ —the angle between the incoming and outgoing axes in the flow field.

During, the calibration procedure, the exact location of the stagnation point—with respect to the optical image—is sought, as well as determining experimentally the precise value of the flow-type parameter α. Obtaining this information does not require visualization of all streamlines, but knowing only the location of the incoming and outgoing axes suffices. Their intersection will provide the exact position of the stagnation point and the angle between them will give the flow-type parameter value.

A small amount of very small air bubbles are injected in the region about the stagnation point, with the sole purpose of being use as flow tracer particles. The high viscosity of the silicon fluid and the very small size of the bubbles allow using them for a sufficiently long period of time. With the bubbles in place, the cylinders are rotated slowly with the same angular velocity, Figs. 3.7a and 3.7b. The bubbles drift away from the central region following the outgoing streamlines. Eventually; bubbles on the outgoing axis remain only, as shown in Figs. 3.7c and 3.7d. Then, the cylinders are spun in the opposite direction converting the outgoing axis into the incoming one. Now the bubbles drift back towards the central region and after a short time, as before, then drift away making it possible to visualize the line corresponding to the outgoing axis: Figs. 3.7e to 3.7h. The overlap of both pictures in Fig. 3.7d and 3.7h, allows the determination of the angle of orientation, ϕ —an experimental value for the flow-type parameter— and the actual position of the stagnation point. This process was carried out for each pair of cylinders in order to have the value of α for all the geometries. Table 3.4 shows the overlapped pictures of each geometry as well as the flow type parameter value for each one of them.
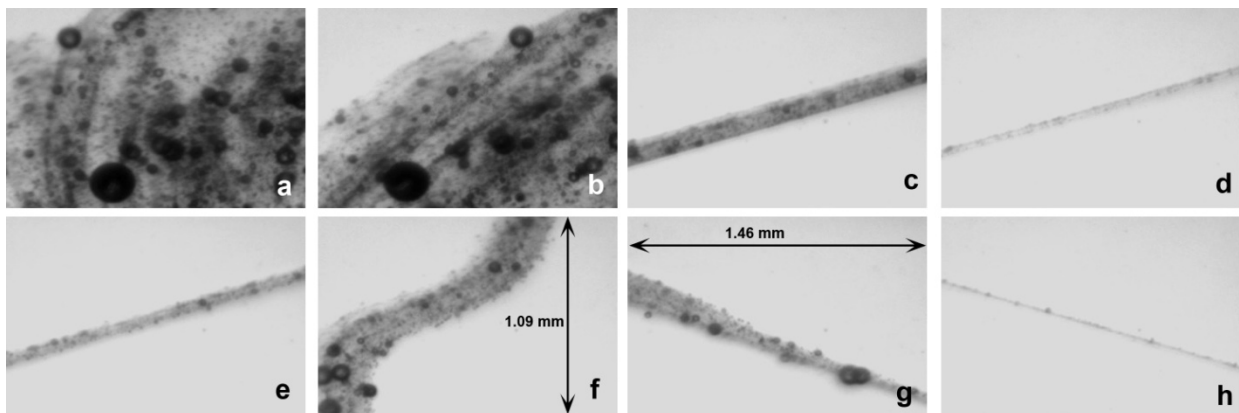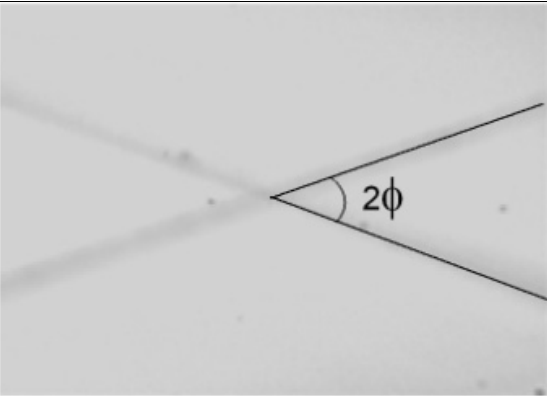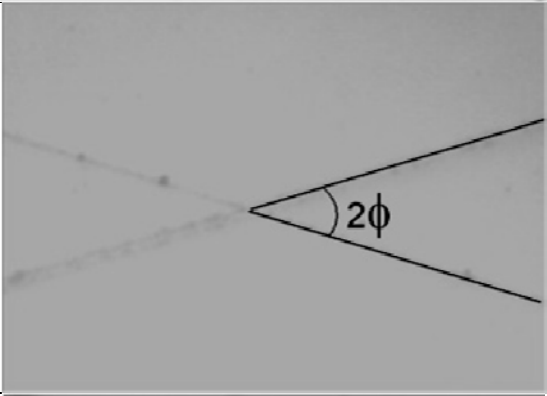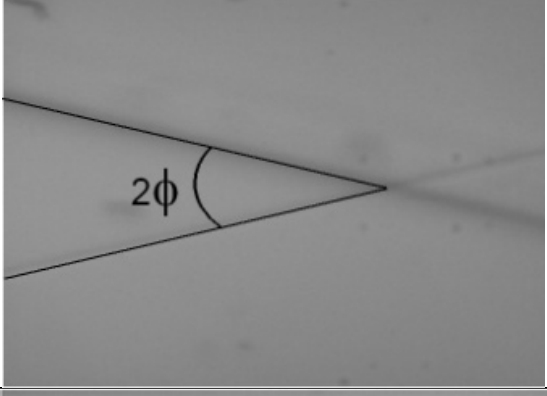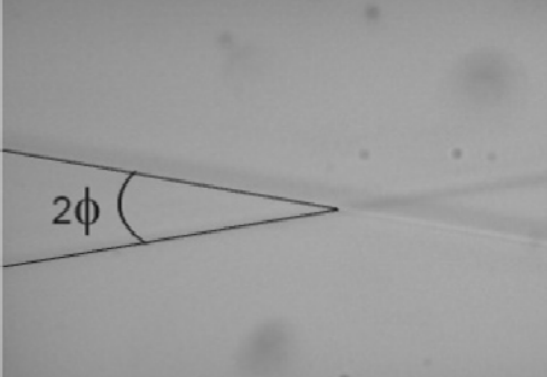

Figure 3.7. Sequence of images for the determination of the type of flow. From *a* to *d*, the cylinders are rotating clockwise with the same angular velocity and counterclockwise from *e-h*. The dark line corresponds to the outgoing axis. The pictures correspond to the geometry A and the experimental value of the type of flow is as determined by the angle sustained in images *d* and *h* is $\alpha = 0.13$.

Table 3.4. Experimental value of the flow type parameter α for the different geometries.

Geometry	Overlapped pictures	Angle ϕ [degrees]	Flow Type α
A		19.9	0.13
B		17.5	0.01
C		13.1	0.05
D		10.04	0.03

3.2.2 Angular velocity of the cylinders

The angular velocity of the cylinders, ω, depends on the velocity of the motors and is a fundamental parameter for two aspects in the experiment: (1) the shear rate about the stagnation point, that is directly proportional to it, and (2) controlling the position of the drop, that is based on small variations —around 4%— of these velocities. The angular velocity of the motors is set at the computer using the software developed for the experiment and transfer from the motors to the cylinders using a worm-gear mechanism. Due to this transmission arrangement, the motor rotates five times faster than the required angular velocity on the cylinder. To ensure that the velocity programmed through software is the correct one on the cylinders, these latter were measured. First, a velocity was set via the program and then the actual velocities of the motors and the cylinders were measured. Because of the control scheme, during an experiment a cylinder can have one of three possible velocities: (1) the nominal velocity, ω^{nom}, that depends on the required shear rate, (2) a maximum velocity ω^+ (4% faster than the nominal value), and (3) a minimum velocity ω^- (4% slower than ω^{nom}). The measured velocities during the test phase are those corresponding to a nominal velocity for a shear rate of $1s^{-1}$, using the cell with geometry B and its corresponding maximum and minimum velocities. Table 3.5 shows the results for the motors and the cylinders. Even though there are small differences between the velocities programmed for the motors and the real ones, these differences seems to disappear due to the reduction in the transmission resulting in a perfect match in the velocities of the cylinders and therefore in the shear rate value.

Table 3.5. Comparison between the velocities ω^+, ω^{nom} and ω^-, programmed and measured, both in the motors and in the cylinders. The nominal velocity value correspond to that necessary for having a shear rate of $\dot{\gamma} =1s^{-1}$ with the cell geometry B.

		Programmed Angular Velocity [rad/seg]	Measured Angular Velocity [rad/seg]	
M O T O R S	Maxima ω^+	1.19075	1.1922	Motor 1
			1.1922	Motor 2
	Nominal ω^{nom}	1.1491	1.1497	Motor 1
			1.1485	Motor 2
	Minimal ω^-	1.1045	1.1090	Motor 1
			1.1069	Motor 2
C Y L I N D E R S	Maxima ω^+	0.23815	0.2382	Cylinder 1
			0.2382	Cylinder 2
	Nominal ω^{nom}	0.22982	0.22985	Cylinder 1
			0.22985	Cylinder 2
	Minimal ω^-	0.22090	0.22098	Cylinder 1
			0.22098	Cylinder 2

3.2.3 Fluctuation of the stagnation point location

During the execution of an experiment, the exact position of the stagnation point is not fixed, it could only be fixed if the cylinders had a perfect geometry with no eccentricities and were rotating with exactly the same angular velocity all the time. Given that those conditions are practically impossible to achieve under laboratory conditions, the actual, instantaneous location of the stagnation point is continuously changing. These changes are mainly because of two factors: (1), the small variations in the instantaneous velocity of the cylinders and (2), the eccentricities of each cylinder with respect to its rotational axes.

3.2.3.1 Instantaneous velocity

According to the Table 3.4, the angular velocities in the cylinders are in excellent agreement with those programmed in the software which means that the shear rate in the stagnation point is the correct one. However, those velocities are the time-average values. But for determining the instantaneous stagnation point location, those measures are not enough. The instantaneous position of the stagnation point depends (among other things) on the instantaneous *relative* tangential velocities of the cylinders; i.e., if the velocity of a cylinder changes, the stagnation point position will be displaced, moving toward the cylinder rotating slower. In order to determine the fluctuation of the position of the stagnation point due to variations of the instantaneous velocities of the cylinders, the variations of velocities were measured to determine how important these are. To carry this out, a band of paper —with a series of equally spaced lines printed on it— was attached to the surface of each cylinder, Fig.3.8 (a). The paper band image was recorded while the cylinder was rotating at a specific velocity; in this way, the instantaneous velocity of the cylinder is be determined by analyzing the video, and measuring the time taken for each line to travel a certain distance, Figure 3.8 (b).
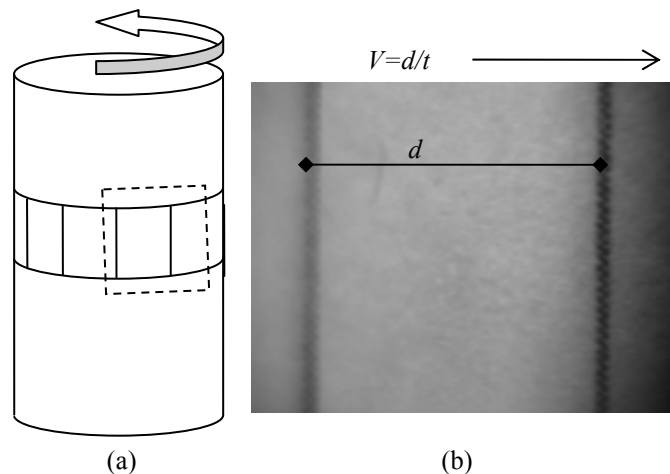

$V=d/t$

(a)   (b)

Figure 3.8. Configuration used to measure the instantaneous velocity in the cylinder.

Figure 3.9 presents the instantaneous angular velocities, ω^+, ω^{nom} and ω^-, measured on cylinder 2 of geometry B, as a function of time. The total time interval for determining the maximum and nominal velocities corresponds to approximately 2 revolutions of the cylinder, and one revolution for the minimum speed. By observing the graphic it can be noted that even when there are fluctuations in the velocities there is a certain similarity in the plots of those variations and that the pattern is repeated in each velocity curve. Thus, instead of plotting the speed data as a function of time, in Fig. 3.10 speeds are presented as a function of the angular position of the cylinder. The same data of the maximum and nominal velocities are plotted in polar form in Fig. 3.11. In this plot, it is clear that the variations repeat each revolution and are the same regardless the velocity of the cylinders. Figs. 3.12 and 3.13 correspond to the instantaneous velocities of cylinder 1, with these figures showing the same behavior than those corresponding to cylinder 2. Fig. 3.12 is the polar plot corresponding to the maximum velocity of the cylinder 1 and figure 3.13 is the plot of the velocities ω^+, ω^{nom} and ω^- for cylinder 1 as a function of the position and as the same as the cylinder 2 the pattern in the plot is repeated in all three velocities curves.
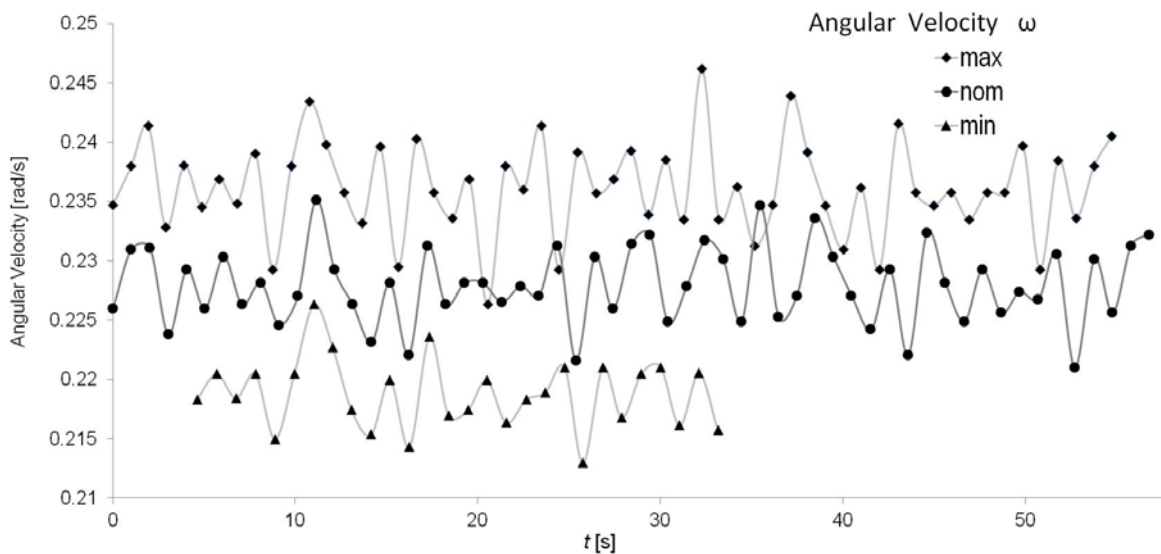

Figure 3.9. Variation of the three different instantaneous velocities programmed for the cylinder 2 of the geometry B as a function of the time.
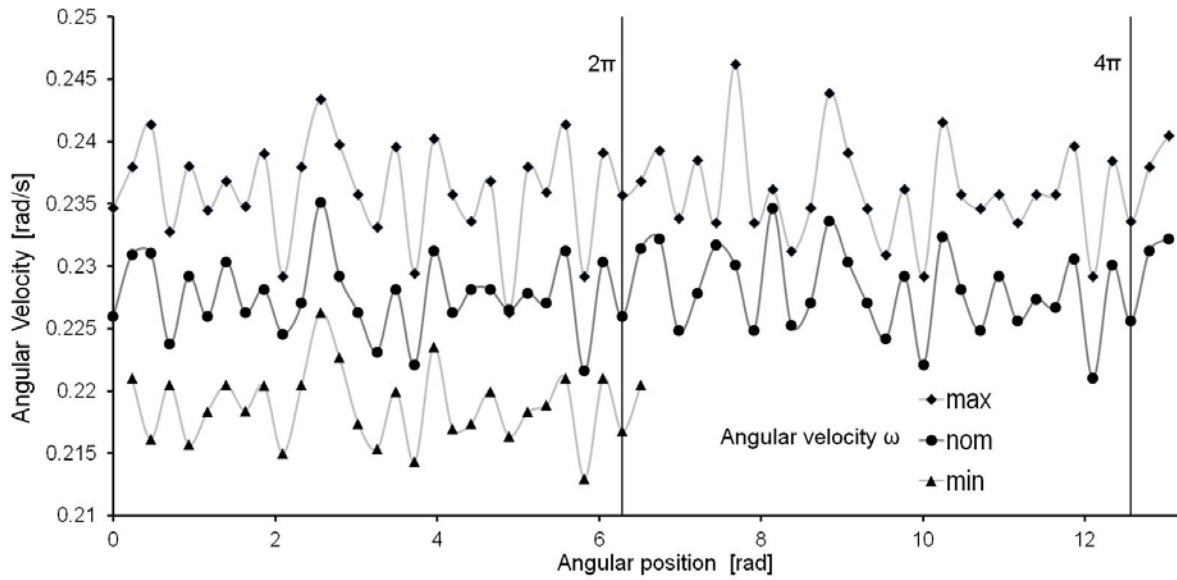
 Figure 3.10.   Variation of the three different instantaneous velocities programmed for the cylinder 2 of the geometry B as a function of the cylinder position.
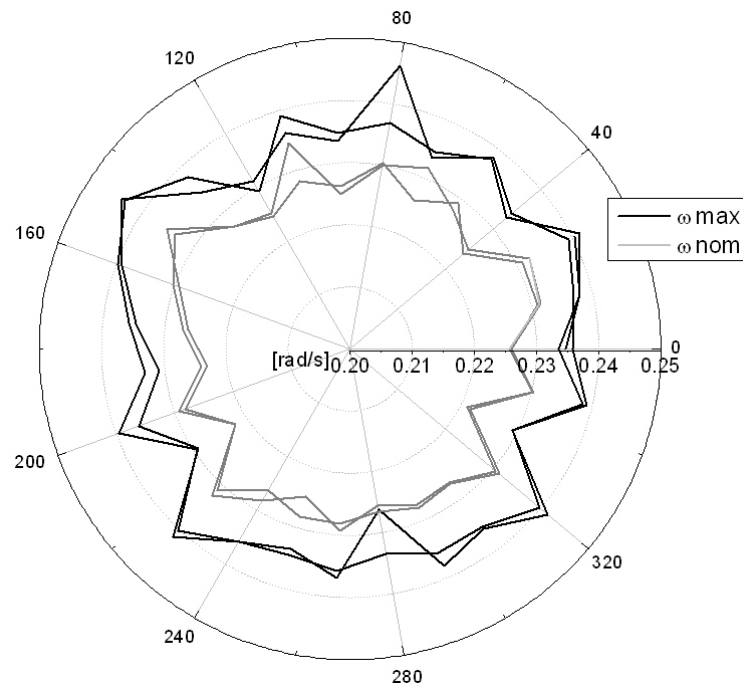

Figure 3.11.   Polar plot of the maximum and nominal velocities measured in the cylinder 2 of geometry B. The data corresponds to the measures of two revolutions.
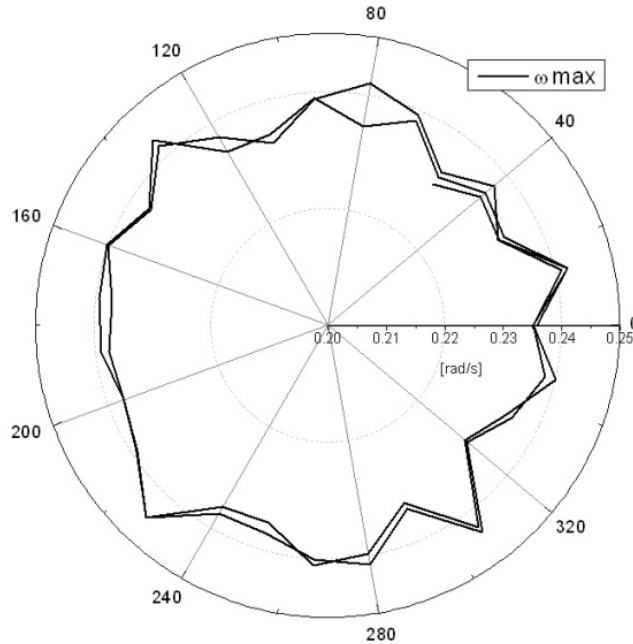
Figure 3.12. Polar plot of the maximum velocity measured in the cylinder 1 of the geometry B. The data corresponds to the measures of two complete revolutions and the beginning of a third.
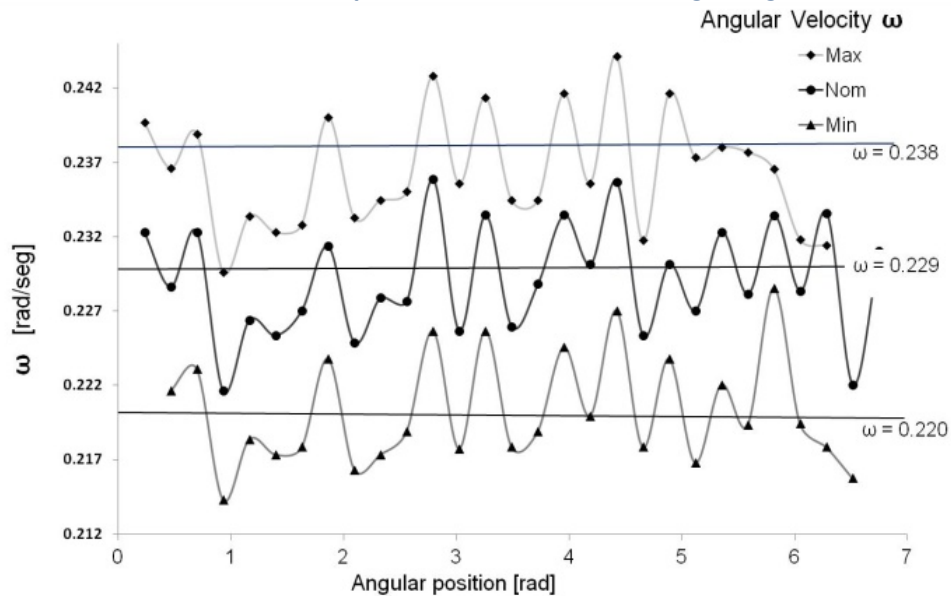

Figure 3.13. Variation of the three different instantaneous velocities programmed for the cylinder 1 of the geometry B as a function of the cylinder position.

The previous plots show that variations of the instantaneous velocities of each cylinder are less than 3% of the average value. Furthermore, these variations depend mainly on the angular position of the cylinders and are independent of the set velocities value. A possible cause for the variations can be the transmission connecting the motors and the cylinders. The mechanism accelerates and decelerates the cylinders depending on the position of the worm respect to the gear and every time they are in the same

position, they have the same variations and the cylinder has the same velocity. Even when the average velocity for each revolution is correct, the instantaneous velocity is continuously changing due to the minimal irregularities in the contact between the worm and gear surfaces. Given that the shape of these pieces are fixed so are the irregularities and in consequence the changes in the velocities. In order to confirm that, the mechanism was disassembled and the relative position of the gear respect to the worm was changed. Fig.3.14 shows the nominal instantaneous velocity of cylinder 1 in geometry B after this change was done. Even when this was carried out for one velocity only, it can be seen that, as expected, the pattern of fluctuations changed but is still periodic for each revolution. Consequently, the position of the stagnation point will be changing due to the variations of the instantaneous velocity of the cylinders and even when the changes are not expected to be important, they are significant so that the stagnation point location will not be fixed, but also fluctuate.
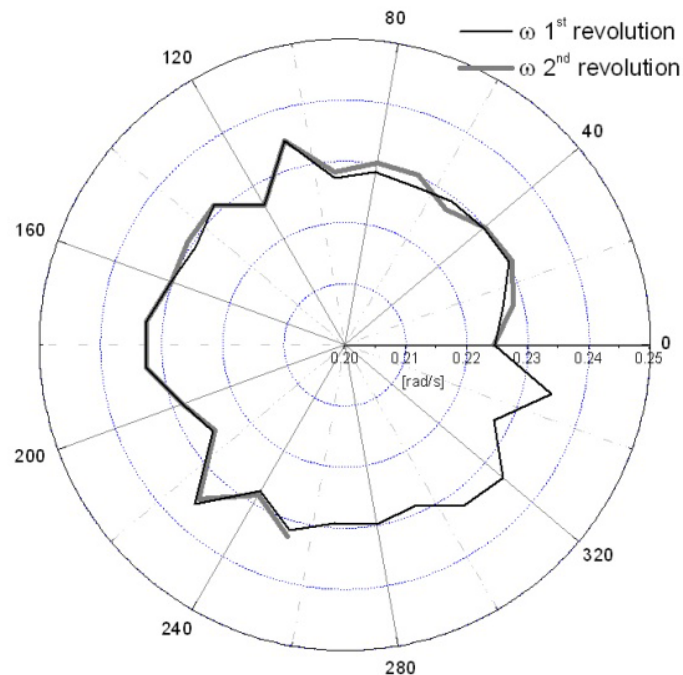

Figure 3.14. Polar plot of the nominal velocity measured in the cylinder 1 of the geometry B once that the relative positions of the worm and gear have been changed. The data corresponds to the measures of one complete revolutions and the beginning of a second.
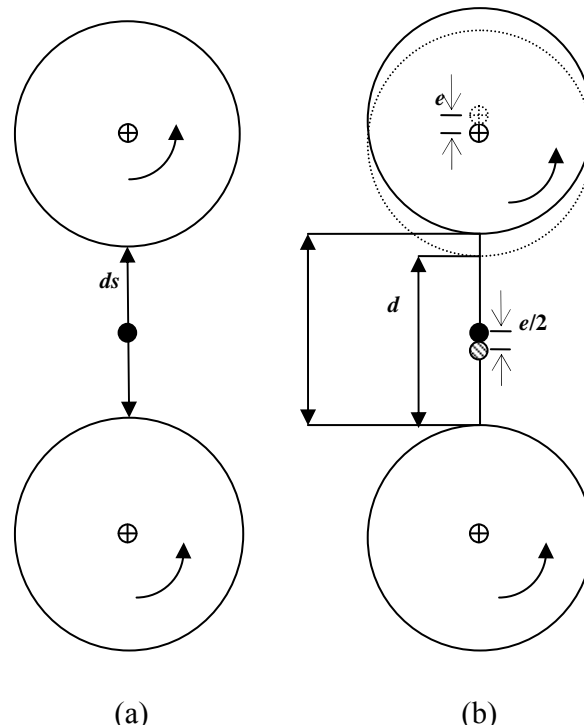
Figure 3.15. Schematic representation of the effect of the eccentricity in the stagnation point position. (a) cylinders rotating with no eccentricities and (b) movement of the stagnation point due to the eccentricity present in the upper cylinder. The same behavior is expected for a cylinder with an eccentric outer surface.

3.2.3.2 Cylinders geometry

Along with the diameter, the eccentricity of the cylinders, *e*, and the distance separating their axes, *de*, are of major importance. In the best of cases, if the cylinders had no eccentricities and with the distance *de* fixed, the length of the line *ds*, indicated in Fig. 3.15 (a), would remain constant, And if the cylinders were rotating with the same velocity ω, the position of the stagnation point would be at the middle of that line and would also remain unmoved. But, any eccentricity *e* present on one cylinder (or both of them), Fig.3.15 (b), the distance *ds* will be instantaneously changing between *ds* and *ds'*; because of that, the position of the stagnation point will be displaced by the distance *e/2*.

In order to know if the stagnation point will be displaced due to the eccentricities of the cylinders, these were measured for all geometries. The measurements were carried out using a Mitutoyo dial indicator (±0.0001" resolution) placed at the top, in the middle and at the bottom of the cylinder, as Fig. 3.16 shows, with the eccentricity *e* given by the total displacement of the dial indicator. Fig. 3.17 is a plot of the dial indicator displacements for cylinders of geometries A and B, as a function of the angular

position of the cylinder. All curves in the graphic resemble those produced for a circle rotating eccentrically and only differ in amplitude.
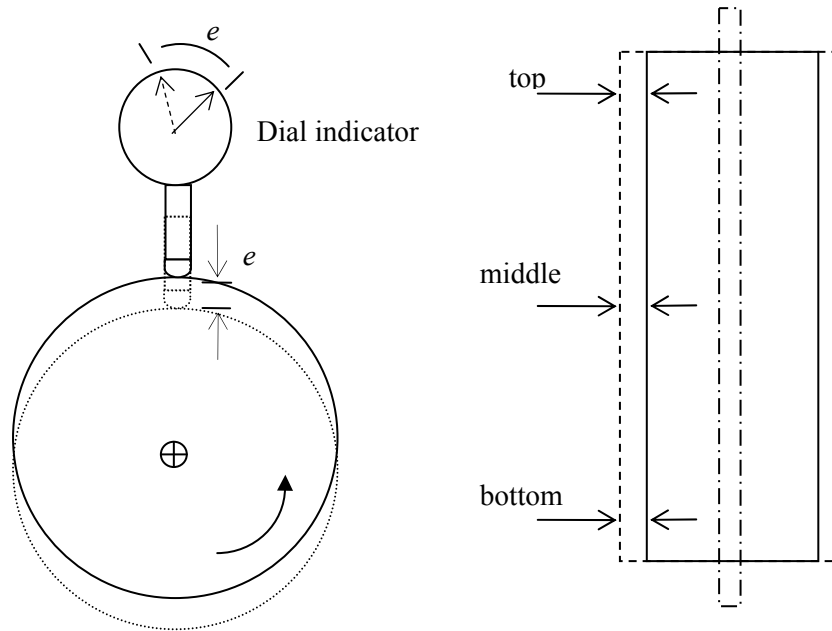

Figure 3.16. Schematic representation of the measures of the eccentricities in the cylinders with the dial indicator.
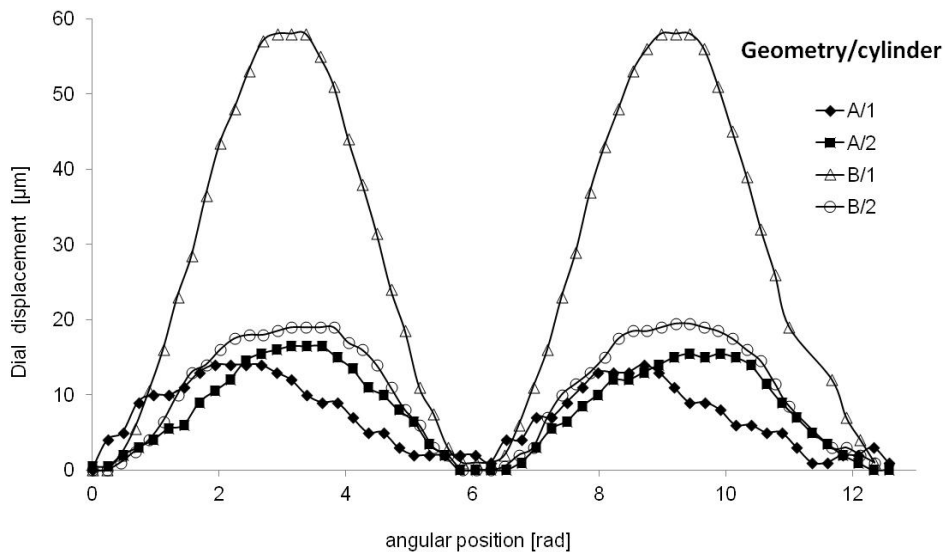

Figure 3.17. Displacement of the dial indicator as a function of the angular position in the cylinder.

It can be seen that the eccentricity of the cylinder 1 of the geometry B is much bigger than the corresponding to the other cylinders, whose eccentricities have the same order. These eccentricities will

cause a change in the stagnation point position but this change can be reduced if the cylinders are placed in such a way that the maximum and minimum displacements of each cylinder coincides in the line where is formed the stagnation point; with that the distance *"ds"* will change symmetrically and in that way the effect of the eccentricities can be eliminated or at least reduced. Table 3.6 shows the results for the measure of the eccentricities in all the cylinders. The geometry B will be discarded because of its eccentricities being too large. All other pairs of cylinders have total eccentricities less than 20μm resulting in a displacement of the stagnation point less than 10μm and if they are placed correctly, the displacement can be reduced even more.

Table 3.6. Measured eccentricities of the cylinders.

Geometry/Cylinder	Eccentricities [μm]		
	Top	Middle	Bottom
A/1	13	12	10
A/2	16	11	9
B/1	58	28	13
B/2	19	18	18
C/1	4	6	9
C/2	22	18	20
D/1	10	10	20
D/2	24	18	10

3.2.2.3 Total displacement of the stagnation point

As it was mentioned before, the information about the exact position of the stagnation point is of importance for carrying out the experiments. During an experiment, that position cannot be determined and is supposed to be known, under nominal conditions (both cylinders rotating with the same angular velocity ω^{nom}) the program that controls the experiment assumes that the stagnation point is located at the center of the image acquired by the camera.

So, in order to ensure that this assumption is correct, it is necessary to find the location of the stagnation point and adjust the position of the camera in such a way that the center of the image coincides with the actual stagnation position. It is to say, once the software has fixed the angular velocities for each cylinder, the stagnation point will not have a static position, but instead there is a region where it wanders about due to the combined effects of the fluctuations in the instantaneous velocities and the shape parameters of the geometry. This small region is delimited by a lower and a upper position will depend on

36

these combined causes. Figure 3.18 (a) is a composition of two time-lapse frames with the lines of the outgoing axes for both extreme positions remarked. This Figure shown the range of fluctuations of the position of the stagnation point during execution of an experiment; thus, the *stagnation region limits* can be determined.

Center of the image in the video camera

Region of the displacement of the stagnation point

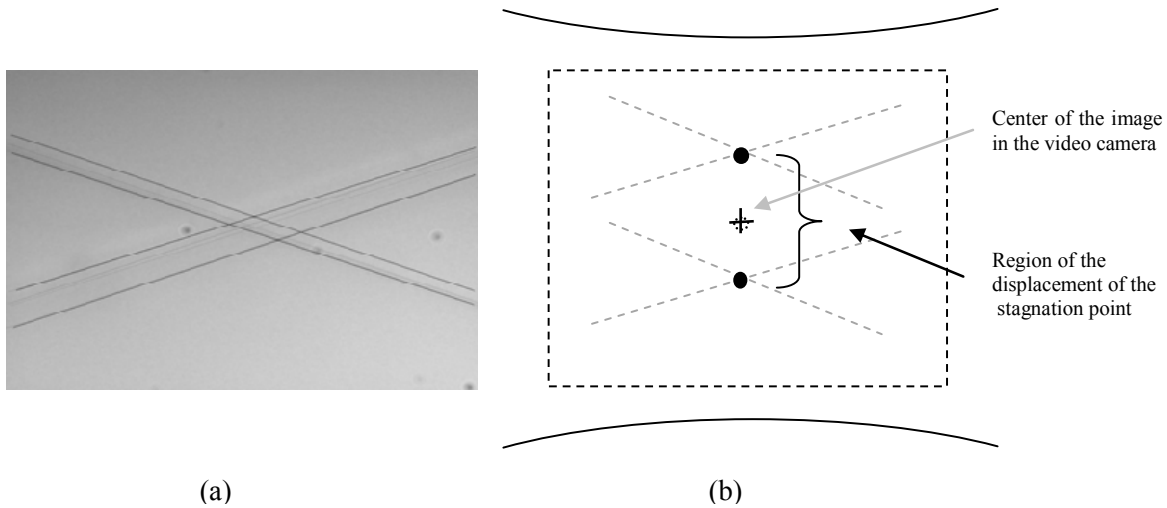(a)   (b)

Figure 3.18. (a) Lines marking the extreme positions of the outgoing axes and delimiting the region of displacement of the stagnation point. (b) the camera is positioned in the middle of the extreme positions of the stagnation point.

This composite picture gives a clearer idea of the continuous movement of the stagnation point. Thus, more than adjusting the position of the video camera to make the center of the image coincide with it, the best option is to place the camera to match the center of the image with the center of the region about the trace of the instantaneous stagnation point, Figure 3.18 (b).   Figure 3.19 shows the determination of the limits of the displacement of the stagnation point for three possible combinations of the angular velocities in the experiment. The superior configuration corresponds to that for the upper cylinder (cylinder 2) rotating with ω^- and the cylinder 1 below rotating with ω^+. The central region, or the nominal, corresponds with both cylinders rotating with the same nominal velocity ω^{nom}, and the inferior configuration correspond to cylinder 2 rotating with ω^+ and cylinder 1 rotating with ω^-. Now with that information available, it is possible to implement the control scheme for maintain the drop in the region of interest and in that way to perform the experiments of drop deformation.
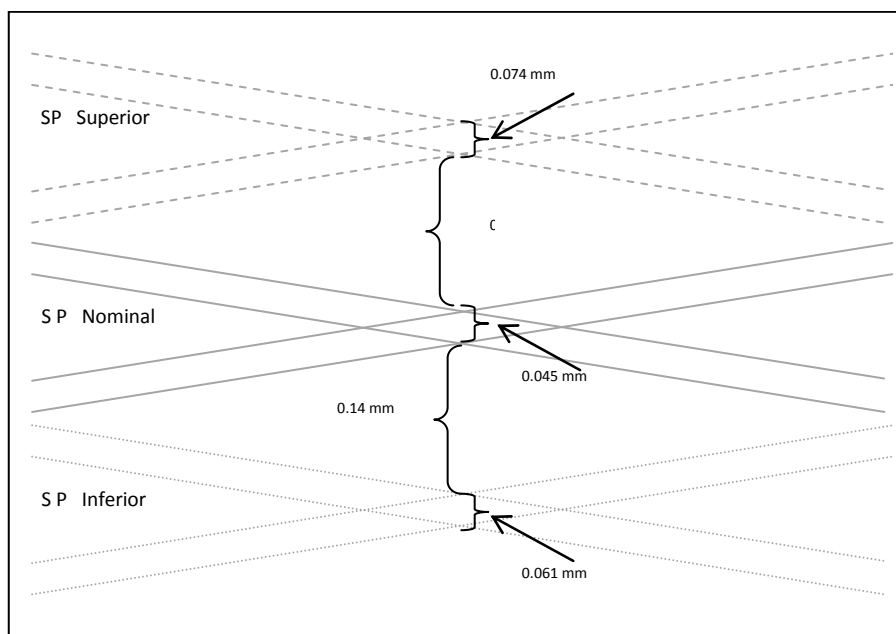
Figure 3.19. Lines delimiting the regions of displacement of the stagnation point for the combination of the three possible velocities in the cylinders. The measures correspond to velocities for a shear rate of 1s^{-1} in the geometry A.

4 Control scheme for the drop position

In this chapter, the implementation of a control scheme for the position of a drop around the stagnation point of the flow generated by the Two-Roll Mill is presented. The control is based on the Poincaré-Bendixson theorem for two-dimensional ordinary differential equations (Reyes et al. 2011). Namely, when a particle moves within a closed region containing inside a saddle point, and the vector field of the equation points inwards at the boundary of the region, the particle undergoes a stable attractive periodic motion. Given a prescribed tolerance region, around the unstable stagnation point, an incoming flow field can always be generated when the centre of mass of the drop reaches the boundary of the tolerance region. This corrective flow field is produced by adjusting the angular velocity of the cylinders, which are calculated using the analytical solution for the flow. The variation of the velocities needed by the control does not imply a significant change in the flow parameters. That is, the velocity corrections are small and these apply for a small period of time. This scheme gives the time dependent analogue of the Poincaré-Bendixson situation just described.

The drop is controlled in a perturbed-attracting non-periodic and closed trajectory about the stagnation point, while being confined to a prescribed tolerance area. This mechanism is very different from the one used for the proportional control which modifies the unstable nature of the saddle point by adjusting the angular velocities of the cylinder to project the motion along the stable direction only. In this implemented control, the effect of the unstable direction combined with the flow readjustment produces the periodic motion. The control scheme is capable of relocating the stagnation point on a time scale much shorter than the time scale of the drop's evolution and the influence of this control scheme on the drop's parameters is small with respect to the nominal flow (around 1%) Reyes et al. (2011). Moreover, the control would remain effective during times much longer than the internal time scales for the drop evolution.

Reyes made numerically studies on the influence of the control scheme upon the drop's forms. He studied the influence of this control on the motion of a two dimensional drop by solving the Stokes equations in a container subjected to the appropriate boundary conditions on the cylinders and the free surface of the drop. These equations are solved for a variety of flows and drop parameters in order to study the perturbation effects introduced by the application of the control scheme and to provide the appropriate parameters for experimental studies.

The control scheme is simple. As the drop evolves under flow conditions, its center of mass is tracked. When the drop drifts away from the stagnation point and its center of mass overtakes the prescribed domain, the flow is modified by adjusting the angular velocity of the cylinders according to the values obtained from the approximate solution for flows generated by TRMs. Essentially, by adjusting the angular velocities of the cylinders, the outgoing streamline environment is changed into an incoming one, reversing the direction of motion of the drop, which is now towards the nominal stagnation point along a stable direction. The important feature for studies of deformation of drops is that the reversal of direction does not alter significantly the deformation rates applied upon the drop; thus, the drop's deformation dynamics is essentially undisturbed. The process is repeated as needed and the drop is confined for long times under steady and known flow conditions

4.1 Formulation of the control problem

As already demonstrated by Bentley and Leal (1986a), the only way to maintain fixed the position of the drop with respect to the flow field is by changing the location of the stagnation point via adjustments of the angular velocities of the cylinders, with the constraint that these changes must avoid significant modifications of the flow field. Consequently, a useful control scheme for flows by TRMs or FRMs has to maintain the drop as close as possible to the stagnation point for a sufficiently long time, making possible studies of the drop dynamics. From now on, the selected flow field conditions of a TRM are called *nominal*, and its properties such as the shear rate, flow-type parameter and the position of the stagnation point will be denoted by the subscript *Nom*.

Figure 4.1 shows the streamlines around the stagnation point of the *nominal flow field*. When a drop or rigid particle is placed around the stagnation point, eventually, it drifts along the direction of the outgoing streamlines. The objective of the control is to maintain a drop around the stagnation point under nominal flow conditions. In Fig. 4.2a, a rectangle is shown about the stagnation point of the flow field; the boundaries of this rectangle serve as the limits where the position of the center of mass of the drop is

allowed to stay at nominal flow conditions. This tolerance area is quite small for the experimental set up, being a small fraction of the diameter of the drop.

The dark lines in Fig. 4.2(a) correspond to the streamlines of the nominal flow field with the outgoing and incoming axes marked with arrows over the tolerance area. In Fig. 4.2(a), the dashed flow lines correspond to the streamlines of the *corrective flow* with its stagnation point at y_{SS}. The flow lines which correspond to the corrective stagnation point in the lower half of the tolerance are, at $-y_{SS}$ (not shown), are similar although located in a mirror-symmetric manner relative to the tolerance area. Fig. 4.2b shows a detailed sketch of the tolerance area above the nominal stagnation point with the nominal and corrective stagnation points marked.
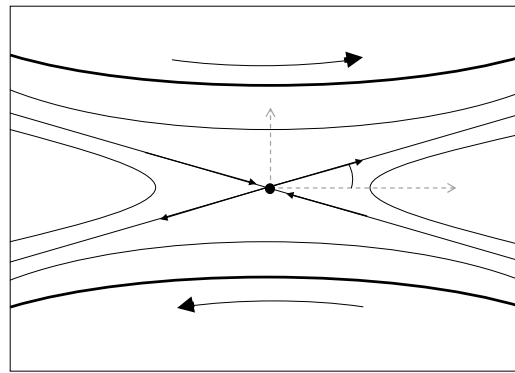

Figure. 4.1. Streamlines generated by the Two-Roll Mill, showing the stagnation point in the gap between the rollers. The position of the stagnation point along the vertical can be moved changing the angular velocities of the rollers.

(a)   **(b)**
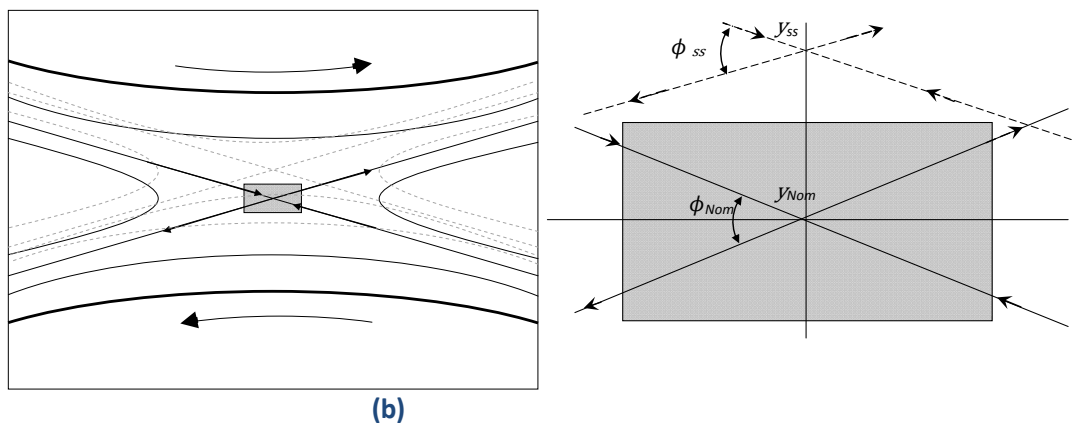
Figure 4. 2. Streamlines around the stagnation point of the unperturbed flow field (dark lines) and the corrective flow (dashed lines) generated by the TRM. The angle between the incoming and outgoing streamlines at the nominal stagnation point θ_{Nom} and the angle at the corrective flow θ_{ss} have essentially the same values Reyes et al. (2011).

When a drop is placed near the nominal stagnation point and the flow is started, the particle center of mass drifts away from that point. Assume the center of mass initially at the position A —at time $t = 0$— located inside the tolerance area shown in Fig. 4.3(a). At this position, the flow corresponds to the nominal conditions, and the center of mass is subsequently advected along the outgoing direction reaching B at $t = t_{on}$ when the control is applied. The effect of the control is to displace the stagnation point to y_{SS}, switching the flow field to one where the stream lines at B are towards the *corrected stagnation point*. As a result, the center of mass follows the flow lines along the path BC, arriving at C at time $t = t_{off}$ that depends on the limit established by l_{in}; see Fig. 4.3(b). At C, the flow is reset to the nominal conditions and the stagnation point is moved back to the y_{Nom} position; thus, the center of mass follows the path CD, as in Fig. 4.(c). At D the situation is repeated but now shifting the stagnation point to $-y_{SS}$, until the center of mass reaches E, in Fig. 4.3(d), where the stagnation point is shifted back to the nominal value and the center of mass moves towards F where the process is repeated Fig. 4.3(e). Now, the line l_{in} is very important, and as can be seen it works as the boundary that determines when the corrective flow is turned off and the experiment go back to the nominal conditions. *The slope of l_{in} can be modified in order to adjust the time lag associated to the characteristic time scale of the fluid when the flow is reset to the nominal conditions.*
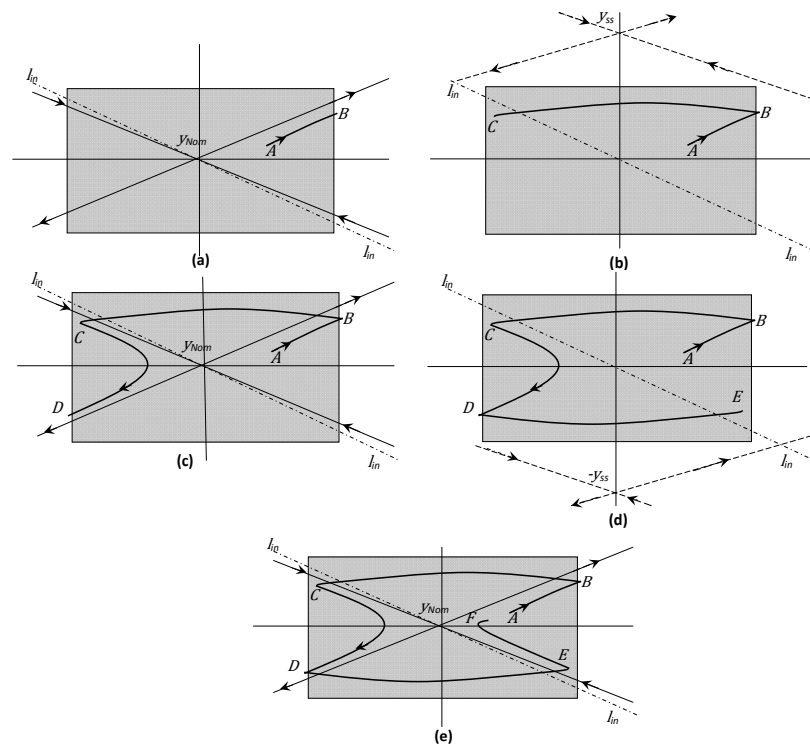

Figure 4.3. Trajectory followed by the center of mass of a drop immersed in the controlled flow field. The control area is shown in grey. The nominal flow corresponds to the darker continuous lines, and the dashed lines show the relative displacement of the flow field during the controlled portion of the cycle.

Thus, the purpose of the implemented control scheme is to produce always an incoming flow for the drop at the boundary of the tolerance area. In this way, the centre of mass is effectively moved as a dynamical system with an unstable rest point (the stagnation point) but with an incoming vector field in an area surrounding the box. In this case, since the incoming vector field is time dependent, a bounded trajectory is obtained that is approximately recursive. This nonlinear procedure of balancing the repulsion at the critical point with the correction of the boundary of the tolerance region always produces a very robust bounded trajectory inside any prescribed area. Furthermore, the main parameters of the flow, $\dot{\gamma}$ and α, remain quasi-constant values.

All displacements of the stagnation point are assumed to be carried out on a time scale small compared to the dynamics of the drop. In the theoretical description above, both the center of mass of the drop and the streamlines are adjusted instantaneously. For a laboratory experiment this is not the case: the exact position of the center of mass is determined after processing the images, so, the determination of the position of the center of mass of the drop and then the modification of the velocity of the driving motors accordingly to the flow field required is done within a finite response time.

The relevant times involved are τ_1, associated to the velocity of the video system, the time of capture and processing of all images, the finite response time τ_2, the time taken by the cylinders to readjust their velocity as a consequence of the control, and τ_3, the time of response of the fluid around the drop to the adjustment in the velocity of the TRM. The total response time $\tau_1 + \tau_2 + \tau_3 = \tau_c$ must be smaller than the characteristic time τ_d of the internal motion of the drop which is a function of the capillary number and the viscosity ratio.

To determine the adjusted velocity field —i.e., the position of the stagnation point position y_{SS} (or $- y_{SS}$)— it is necessary to ensure an incoming flow field at this position on the boundary. This requirement gives y_{SS} as a function of the size of the tolerance area. So, the required values of ω^+ and ω^- to relocate the stagnation point to y_{SS} can be calculated using the analytical solution. It is remarked that the present control takes advantage of the knowledge of the local flow field and balances the unstable motion at the stagnation point with a time dependent incoming flow at the boundary, giving an effective dynamical system with a periodic or quasi-periodic orbit for the center of mass. As well, during the control steps, $\mathbf{II_{2D}}$ (related to the applied shear rate) remains constant while all changes of α are less than 0.5% for all cases Reyes et al. (2011).

44

4.2 Experimental Scheme

Fig. 4.4 shows the schematic block diagram of the experimental setup. A drop is initially placed as close as possible to the nominal stagnation point in the flow field and its position is monitored with the optical system that provides the images used to calculate the coordinates of the center of mass of the drop. With this information, the program selects the appropriate angular velocity for the cylinders, in order to maintain the drop in the desired position (which is the nearest to the nominal stagnation point location). Once these velocities are selected, the velocities of the motors are updated and this cycle is repeated.
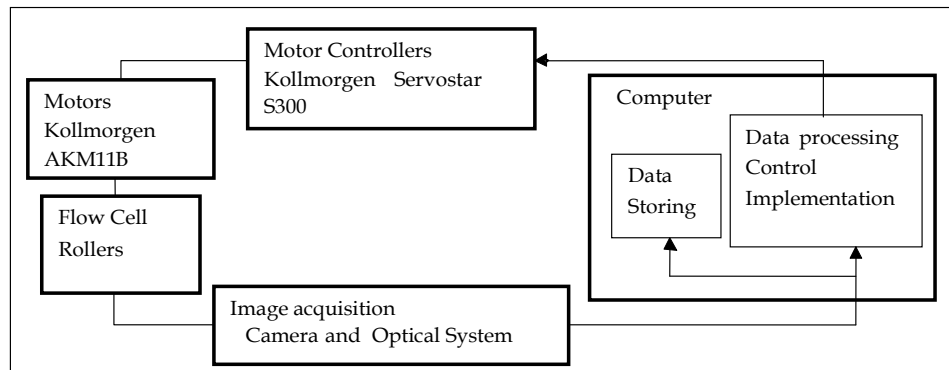

Figure 4.4. Experimental set up block diagram.

The control software is written in Visual C++, for execution in real-time mode. A Graphical User Interface (GUI) provides access to the application; see Fig. 4.5. It incorporates the tools to adjust the video and the parameters of the motors. For the video signals, the GUI window has two displays. One is for the raw video input, which shows in real time the frame acquired by the camera. The other display shows processed images made up of the contour of the drop and the location of its calculated center of mass, along with the tolerance area (fixed with the slide bar in the window, during execution of the experiments) and the lines corresponding to the ingoing and outgoing streamlines of the nominal stagnation point.

For the control of the motors, the GUI has a manual and an automatic control options. The manual control is use prior to the execution of an experiment, to position the drop near the nominal stagnation point inside the tolerance area. It consists of the GUI window slide bars that allow controlling the velocities of each cylinder as well as their direction of rotation. In this way, achieving an initial drop position is quite simple, requiring a few attempts by the experimentalist. Once the drop is in the starting location (i.e., inside the tolerance area), the automatic control is activated and an experiment is initiated. The monitoring section in the window allows us to watch the instantaneous velocities of the motors, the coordinates of the center of mass, the size of the tolerance area, and the number of images that have been saved and processed.
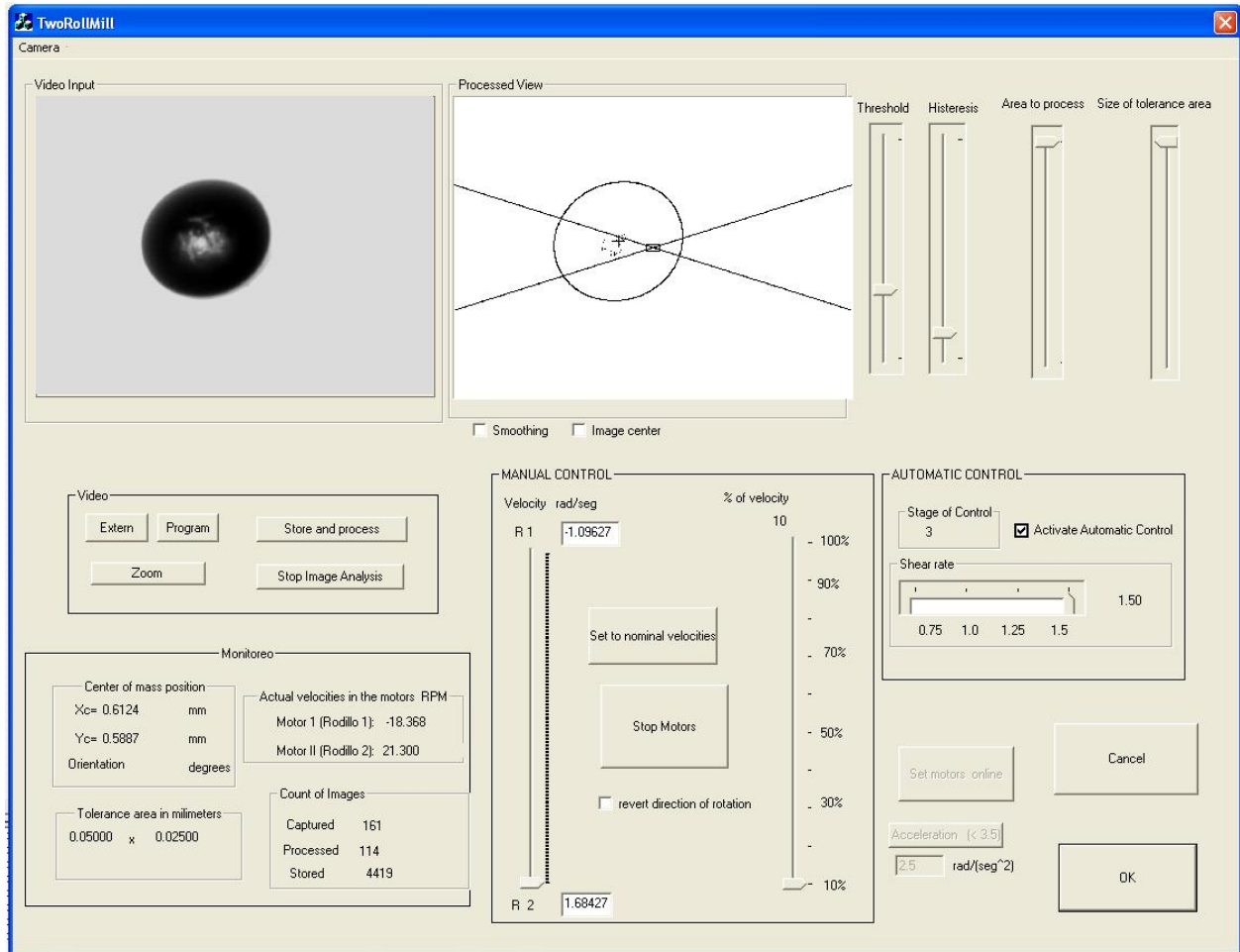
Figure 4.5. Graphical User Interface (GUI) of the Two-Roll Mill Experiment. It incorporates two displays. One is for the raw video input the other display shows processed images made up of the contour of the drop and the location of its calculated center of mass, along with the tolerance area, the lines corresponding to the ingoing and outgoing streamlines of the nominal stagnation point.

4.2.1 Control implementation

The typically observed response time for the computer interface, motor power electronics and cylinders inertia is less than 0.01 seconds, for changes of rotational speeds less than 5% of the preset values. The flow parameters and the position of the stagnation point are adjusted simultaneously by varying the angular velocities of both cylinders ω_1 and ω_2 keeping $\mathbf{II_{2D}}$ constant.

The automatic control operates under a real-time environment and the program has three data feeds: (*i*) The image acquisition (*ii*) Image analysis (*iii*) Adjustment of the velocities of the motors. The diagram of the control scheme is shown in Fig. 4.6.
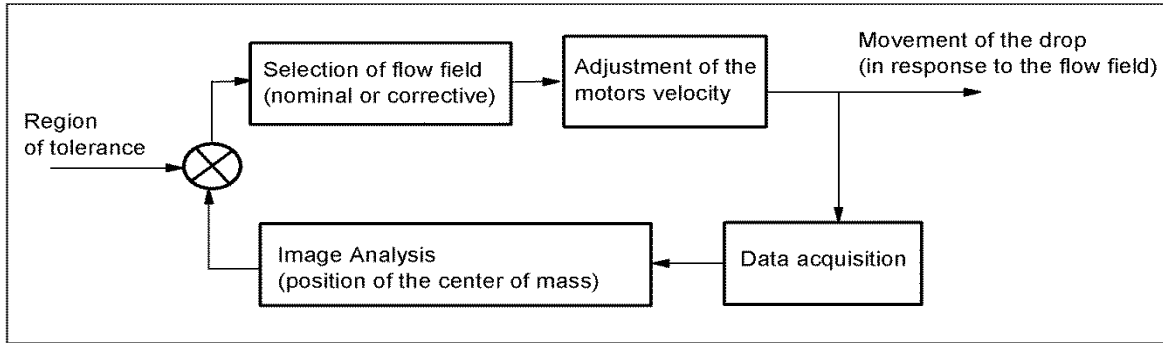
Figure 4.6. Diagram of the control scheme. The program monitors the drop position and adjust the velocity of the cylinders to keep the drop near to the nominal stagnation point.

Image acquisition

The images acquired by the CCD camera are handled using the Instrumental and Industrial Digital Camera Application Programming Interface (*IIDCAPI*) written in the C++ language, by Sony. The image acquisition consists of two simultaneous processes, taking the photo and storing it in a file, along with the nominal parameters in the experiment at that time (shear rate, control stage, tolerance area size and drop position coordinates), and the other one is creating a temporary archive of images. The archive is a short FIFO list with a fixed number of elements and with the last image acquired by the camera available for analysis as well as a few previous ones in case of delays in processing data.

Image analysis

The image analysis evaluates the instantaneous position of the drop in real-time, which is the input variable for the control scheme. The Open Source Computer Vision Library (OpenCV) from http://opencv.org/ is used to process the raw images. Firstly, an image frame is loaded from the list to define the drop contour. Since the drop contour looks dark on a bright background, the appropriate range goes from a gray level corresponding to black to the upper threshold value selected; an appropriate value of such a threshold must satisfy the condition of generating an image with a closed drop contour. Then, a simple standard algorithm (gray-level thresholding) is applied to remove and clean the image of all pixels having a gray level outside a certain range (from 0 to 255 in a gray-scale). In this way, most of all spurious objects in the image having pixel values below a pre-set threshold are filtered out and the process leads to a binary (black & white) image containing only the drop. For each binary image, the contour of the drop is found using the Canny algorithm (Canny 1986), a function available in the OpenCV libraries, and then the center of mass is computed using the corresponding discrete integral. The analysis is carried out in a 1/100 of a second, regardless of the drop size, and the resolution for the position of the drop centroid is a fraction of a pixel for the smallest drops studied.

Adjustment of the velocities of the motors

Once the program has the coordinates of the center of mass of the drop, the algorithm next evaluates whether the centroid is inside the tolerance area. If it is not, the program executes de P-B control algorithm and modifies the velocities of the motors depending on the position of the center of mass of the drop; otherwise the algorithm carries on under nominal flow field conditions. Also, in this section of the code, the ID number of the image, the coordinates of the center of mass and the size of the tolerance area of the image being processed are save in a file.

4.3 Experimental test of the control

The following experiments were carried out only to evaluate the performance of the control scheme for two fundamental aspects: the flow field fluctuations due to the physical imperfections of the flow cell studied in the previous chapter; and to find the most adequate parameter l_{in} for the control stage. So, emphasis is given to the trajectory of the drop more than the deformation. Actually, the capillary number was the same for all experiments, hence, the deformation D_T and orientation θ are also the same.

For these experiments the exterior fluid is a Polydimethylsiloxane oil DMS 25, η = 485 mPa·s with a relative density of 0.971 at 23°C. The drop fluid is a vegetable canola oil, filtered through a 3 µm pore size with η = 72.6 mPa·s and relative density of 0.917 at 23°C. Both liquids have a well defined Newtonian behavior at the interval of shear rate values used. The capillary number for the experiments was Ca = 0.1031 and the values of the slope β of l_{in} were β = 20°, 30°, 40° and 50° and one with a vertical limit, figure 4.7. By adjusting l_{in}, the drifting effects on the τ_c time can be optimized, which is a nonlinear function of the viscosity of the surrounding fluid.
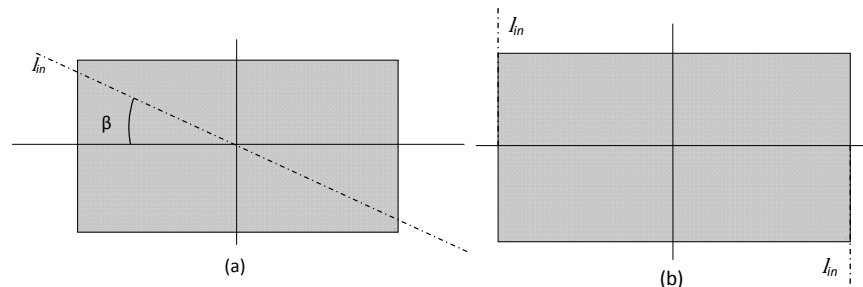

Figure 4.7. Limits taken by the program for turning off the corrective flow. (a) Diagonal limit with an angle β between the x axis and the line l_{in}, (b) vertical limit taken l_{in} at the borders of the tolerance area.

Measurements of the drop deformation parameters are made by processing the files generated during execution of the experiments. The archive for a single run, consists in a list containing: all frames, and the control status and values of the motors parameters for each frame. Thus, this data set contains the

history of the control status active at the moment when the frame was taken and when the control scheme is started or stopped. This data provides the coordinates of the center of mass, the mayor and minor axis L and B, and the orientation angle θ, for every frame. More details about the post processing are given in the chapter corresponding to the experimental results. The following Figs. 4.8 to 4.12 show the deformation, orientation and trajectories of the center of mass of the drop due to variations on the l_{in} parameter.

The plots corresponding to the trajectories of the drop centroid show that these are different from the expected ideal path; all have observable perturbations. Even when the control program keeps the velocity of the cylinders constant, the plots show abrupt and chaotic changes of the trajectories, caused by small changes in the velocity field near the cylinders. These fluctuations in the velocity field are caused by imperfections of the cell and cylinders, which causes small accelerations and decelerations of the cylinders, albeit when these variations are not sufficient to modify the flow field parameters.

However, the average steady state values of the deformation and orientation plots are not affected by the centroid trajectory. Even more, the plots of the deformation parameter seem to have the same values despite the trajectory followed by the drop or the value of l_{in} used in the experiments. The former values remain constant during the time that the experiment lasts, with those parameters essentially being insensitive to the imperfections in the flow cell, and more important, insensitive to the control stage active at that moment. That is, the deformation and orientation induced in the drop is robust, regardless of the fluctuation of the applied flow field, either under nominal (Y_{Nom}) or corrective (Y_{SS} or $-Y_{SS}$). Figure 4.13 shows the time duration of the drop under all stages of the control, for different values of the limit l_{in}, showing that the time under nominal conditions is longer than the time under corrective environment.

The values of l_{in} —used as limits for deactivation of the control in Figs. 5.8 – 5.12— has no effect on the deformation and orientation induced in the drop, but it has a significant influence on the centroid trajectory of the drop around the nominal stagnation point. Cases when the drop carried out the maximum displacements are those corresponding to the $l_{in} = 20^\circ$ (see Fig. 4.8), and with the vertical limit (see Fig. 4.12. Under this condition, the maximum distance of center of mass of the drop respect to the Y_{Nom} is about 0.45mm in the x-axis and 0.12 mm in the y-axis, however in the plots corresponding to $l_{in} = 30^\circ, 40^\circ$ and 50°, the maximum displacement are in the order of 0.35 mm in the x-axis and 0.07 mm in the y axis. Even when this does not affect the deformation and orientation results, and that the control of the drop was effective in all cases, it would be important to keep the center of mass of the drop the closest possible to the nominal stagnation point. The last in order to avoid long distances from the Y_{Nom} which prevent the situation where the drop is so far from the stagnation point that it would be impossible for the control to redirect the drop toward it and in that case to lose the drop from the central region.
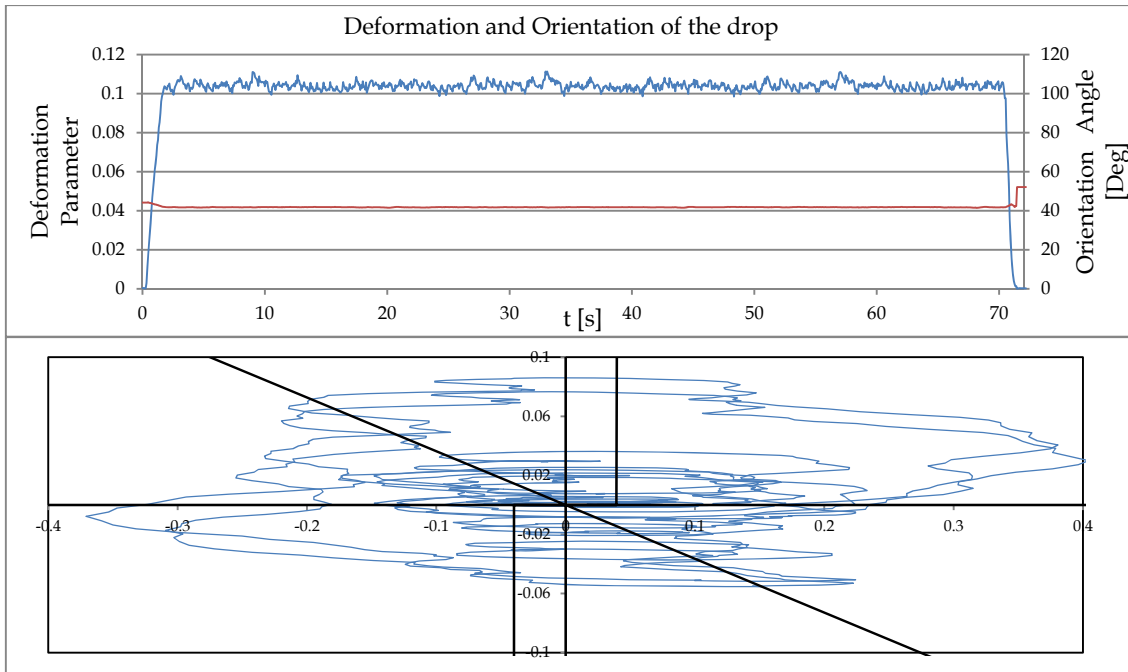
Figure 4.8. **Deformation, orientation and trajectory of the centroid of the drop, using the parameter** l_{in} **= 20º. The mean deformation is** D_T **= 0.1039, STD=0.002 and the mean orientation angle is 41.8º.**
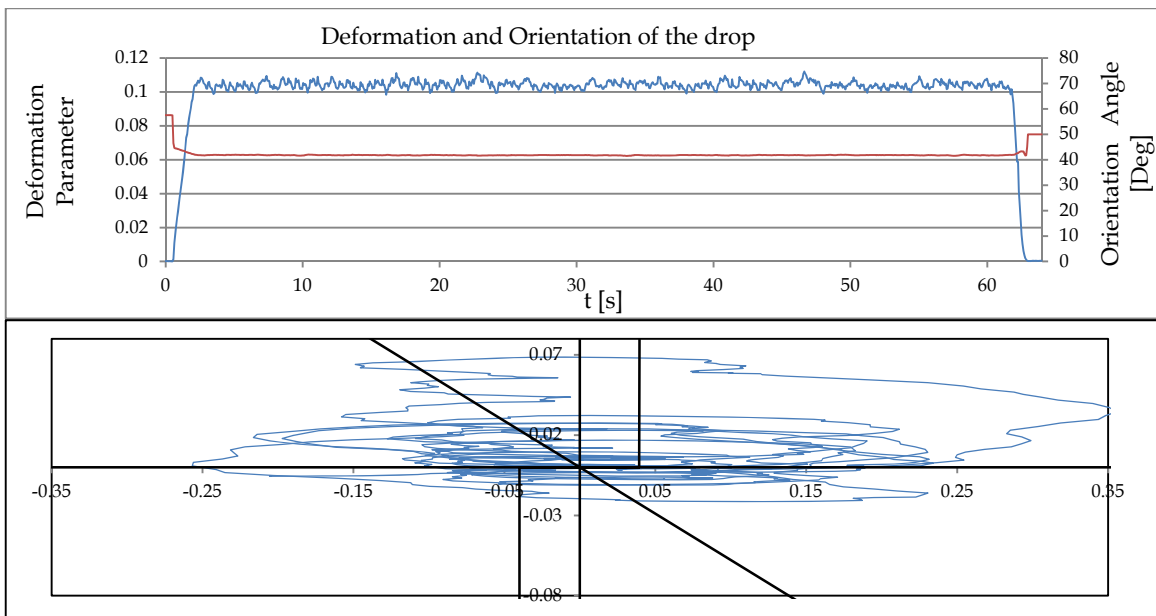

Figure 4.9 **Deformation, orientation and trajectory of the center of mass of the drop, using the parameter** l_{in} **= 30º. The mean deformation is** D_T **= 0.1042, STD = 0.0021, the mean orientation angle is 41.8º.**
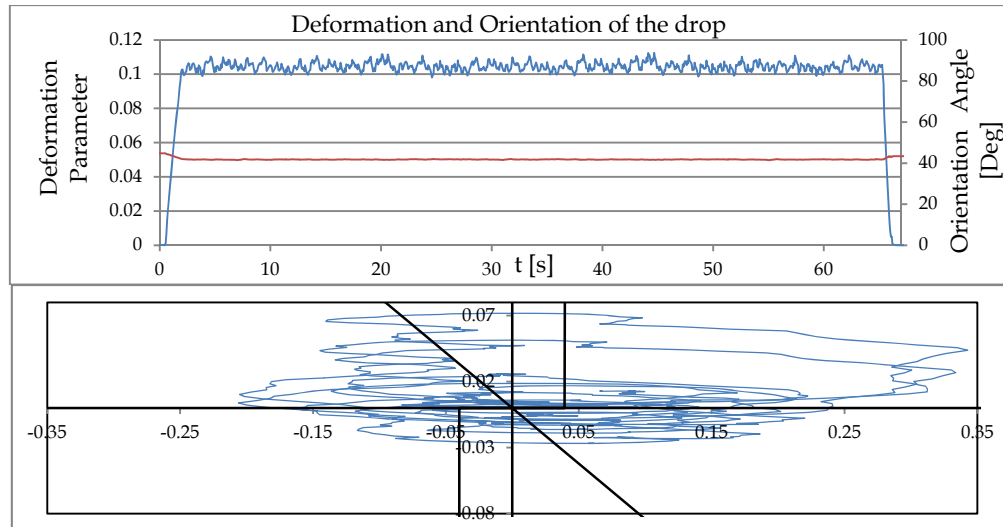
Figure 4.10. Deformation, orientation and trajectory of the center of mass of the drop, using l_{in} = 40º . The mean deformation is D_T = 0.1045, STD = 0.0025, and the mean orientation angle is 41.8º.
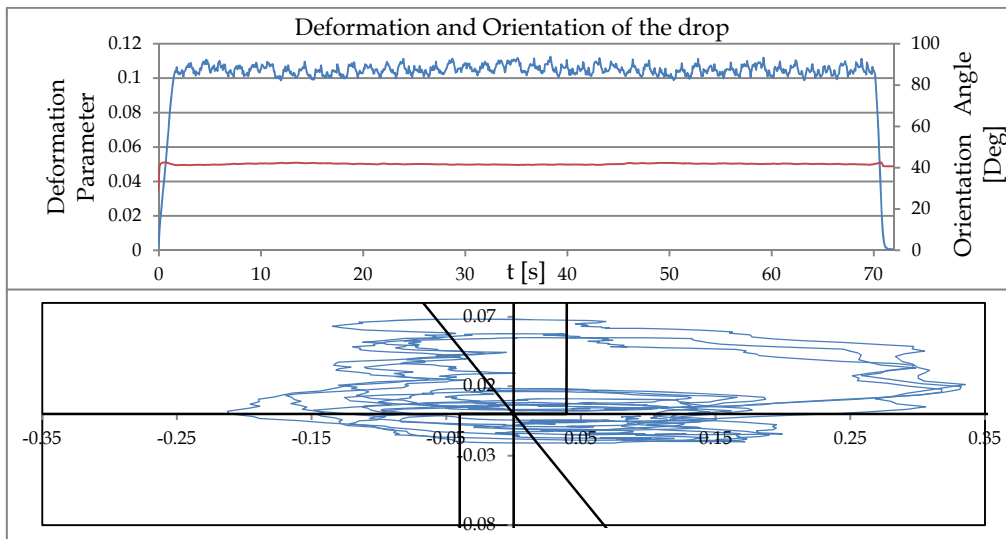

Figure 4.11. Deformation, orientation and trajectory of the center of mass of the drop, using l_{in} = 50º. The mean deformation is D_T = 0.1049, STD = 0.0027, the mean orientation angle is 41.8º.
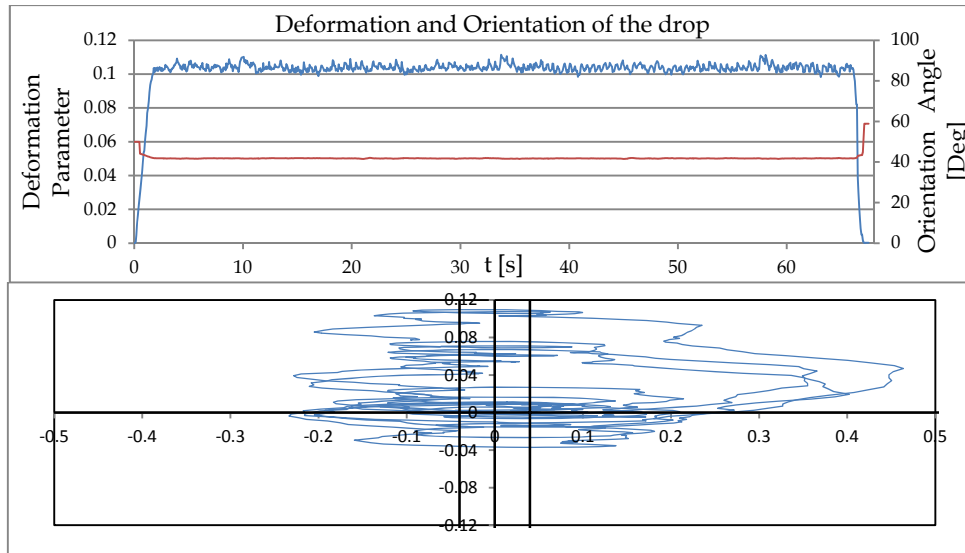
Figure 4.12. Deformation, orientation and trajectory of the center of mass of the drop, using vertical limits. The mean deformation is $D_T = 0.1039$, STD = 0.0020, the mean orientation angle is 41.8º.
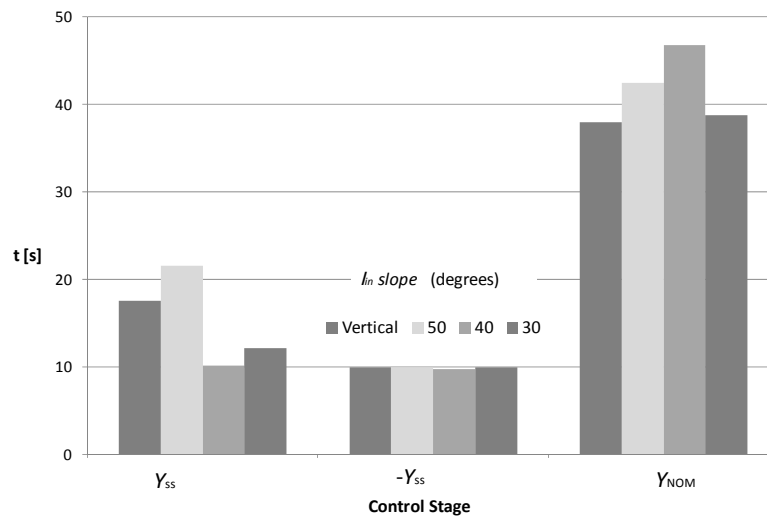

Figure 4.13. Duration of the control stages in a deformation experiment. The plot shows that the time under nominal conditions is larger than the time under corrective conditions.

The control implemented is shown to be successful. At this point, several adverse effect have been evaluated in the implementation. Nevertheless, the control scheme is robust enough to keep the drop inside a region where the parameters of interest have a small variation, for long times; enough to have reliable measures of the relevant parameters. Figures 4.8-4.12 show that, despite the trajectory of the drop, the parameters of the drop dynamics (D_T and orientation angle) are well characterized, thus, the main imperfections have a minimal effect. It is important to mention that even when the comparisons are

made just for only one *flow-type* parameter, the results shown that it is reasonable to expect the same when a different *flow-type* parameter, (a different geometry) is used.

5 Experiments and results

This chapter presents a general description of a typical experiment with the TRM and the results obtained from the experiments performed in this thesis. The chapter is divided in two sections, the first one describes the characteristics of the fluids used and the general procedure followed during the experimentation and the second part corresponds to the experimental results obtained.

5.1 Fluid properties and experimental procedure

5.1.1 Fluid properties

The experiments were carried out for two viscosity ratio systems, a low viscosities ratio system and a high viscosities ratio system, in both cases the suspending fluid used was the DMS T35, a PolyDiMethylSiloxane (PDMS) from Gelest Inc, with a measured viscosity $\mu_1 = 5.1$ Pa·s (51 Poise) and relative density of $\rho_r = 0.973$ at 25 °C filtered through a 3 μm pore size. For the low viscosity ratio system the drop fluid consisted of vegetable canola oil with a measured viscosity $\mu_0 = 62$ mPa·s (0.6 Poise) and a relative density $\rho_r = 0.917$ at 25 °C. The viscosity ratio for this system is $\lambda = 0.012$ and the interfacial tension is 2.7mN/m. For the high viscosity ratio system the drop fluid consisted in PolyIsobutilene by Polysciences Inc., with a viscosity $\mu_0 = 80$ Pa·s (800 Poise) and a relative density $\rho_r = 0.92$ at 25°C. The viscosity ratio for this system is $\lambda = 16$ and the corresponding interfacial tension is 3.5mN/m. All experiments were performed at 25°C ± 0.1°C. Figures 5.1 to 5.3 show the results of the viscosities values for the fluids as a function of the shear rate and for different temperature values.
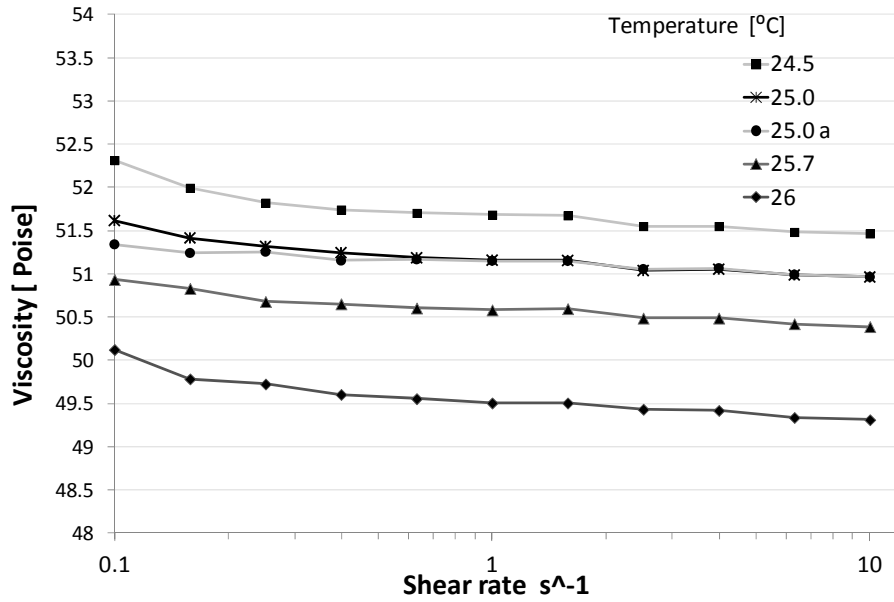
Figure 5.1. Viscosity of the suspending fluid DMS T35 for different temperatures. The viscosity for the temperature of the experiments correspond to 51 Poise @ 25^0 C.
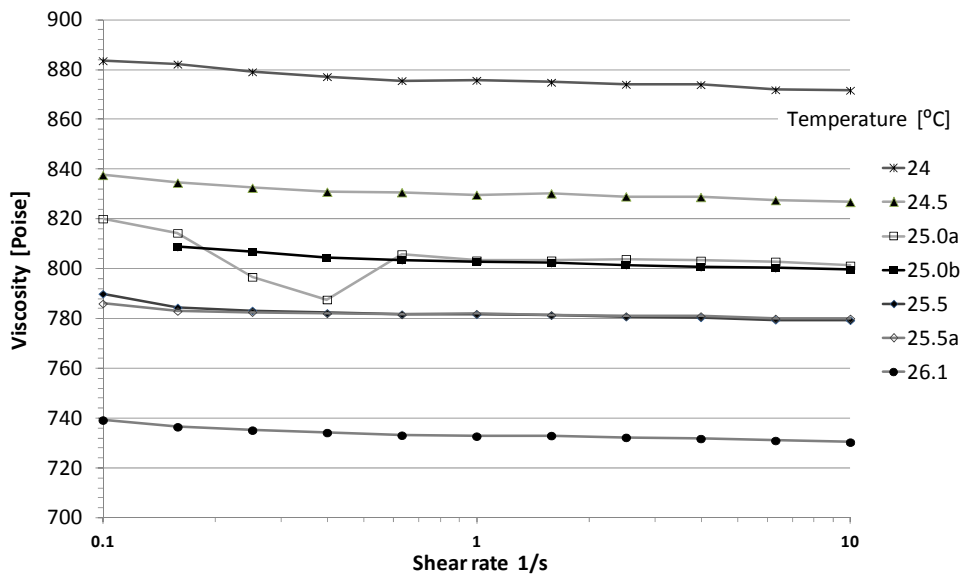

Figure 5.2. Viscosity of the drop fluid PolyIsoButilene for the high viscosities ratio. The viscosity for the temperature of the experiments correspond to 800 Poise @ 25^0 C.
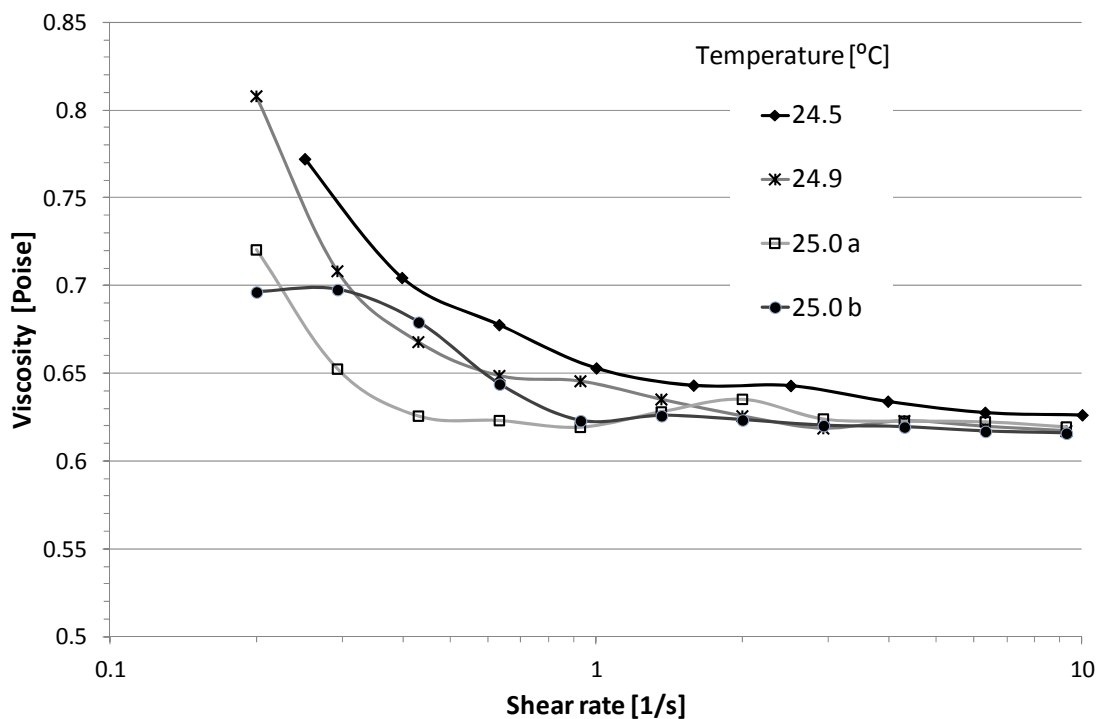
Figure 5.3. Viscosity of the canola oil corresponding to the drop fluid for low viscosities ratio. The viscosity for the temperature of the experiments correspond to 0.62 Poise @ 25^0 C.

5.1.2 Experimental procedure

An experiment consists of introducing a drop into the gap region between the cylinders using a homemade device. Using the computer control under the manual supervision, the drop is positioned so that its centroid is inside the tolerance area. Then, the automatic control is activated and an experiment is carried out, keeping the drop under the pre-established flow conditions (shear rate), while recording all digital images for a posterior analysis. Every drop is deformed under a series of values of shear rate. At first, the shear rate is set at a small value, and once the experiment has lasted long enough —and the drop has reached the steady state deformation— the flow is stopped; subsequently, the deformed drop slowly recovers its spherical form. For a new run, the shear rate is set to a higher value and the procedure is repeated. This procedure is carried out several times until the shear rate is strong enough to cause the drop to breakup. In this way, an archive with the images of the deformation, as a function of the time, for the imposed shear rate is obtained; a set of files of this kind is generated for every drop. Each set of files corresponds to a specific drop, with known diameter. With these data, the parameters of the deformation are obtained by performing an image analysis to the files generated in the experiments.

A file for a single run consists of a list containing: all frames, the control status as well as variables for the motors as a function of time. These data make possible to know when exactly the flow is

started and the deformation process begins, and when exactly the flow stops. The image analysis for evaluation of the deformation parameters is carried out using a program very similar to the image analysis in the control part, Fig 5.4. An averaging filter is preliminarily applied to the image for noise reduction. The contour of the drop is identified by applying the Canny algorithm for edge detection after a threshold corresponding to maximum contrast of the drop with respect to the background. Subsequently, L and B are calculated as the two semi-axes of an equivalent ellipse having the same area and the same first and second moment of area. The program analyses each frame in a file and generates a list with the coordinates of the center of mass, the lengths of the major and minor semi-axes L and B, and the orientation angle θ. The Taylor deformation parameter D_T is also calculated, and, if needed, saves the frame that is displayed with the standard format *.bmp.
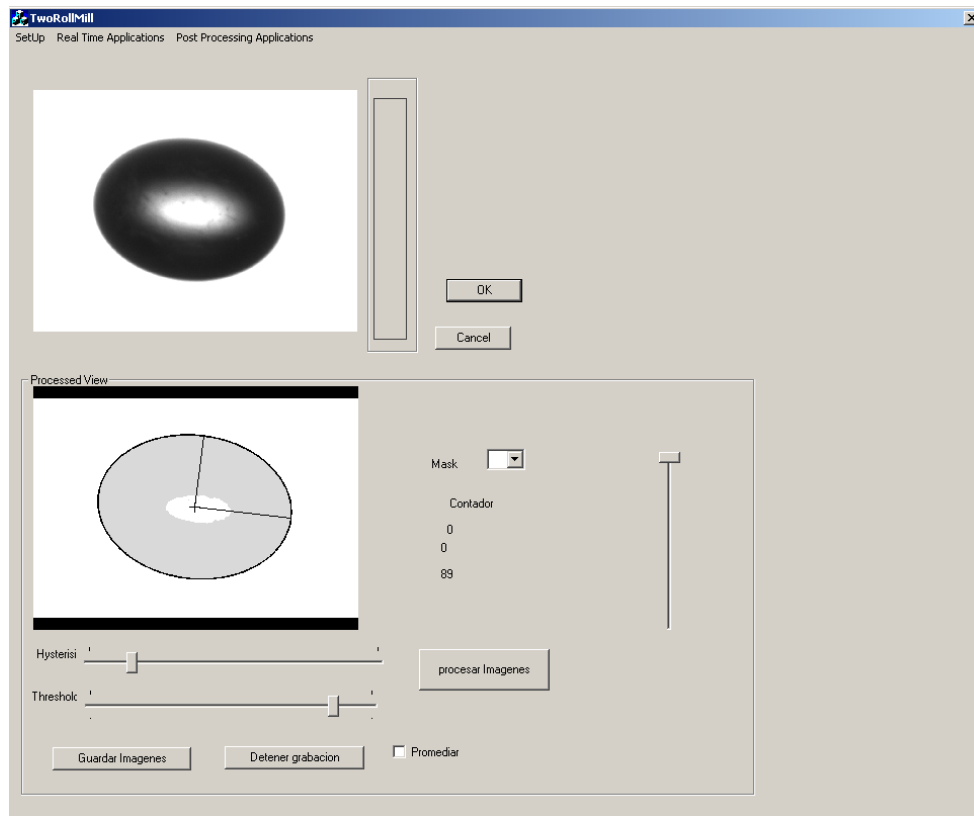

Figure 5.4. GUI of the program used to process the image files from the experiments.

The data obtained during processing of the images are in pixels. But given that a relation between mm and pixels is available and knowing that the video is taken at a rate of 15 fps, it is quite easy to have these data in terms of mm and seconds. Fig. 5.5 shows the plots for the complete image analysis obtained from an experiment with a drop with $r_0 = 0.46$ mm, a viscosities ratio $\lambda = 0.012$ and a flow type $\alpha = 0.03$ under a shear rate of $\dot{\gamma} = 1.0$ s^{-1}: the capillary number is $Ca = 0.86$. Those plots show the

time evolution of the Taylor deformation D_T and the orientation angle θ and can be divided in two parts: the deformation history (after startup of flow), and the relaxation stage (once the flow has been stopped). In this chapter we only focus in the first part, concerning to the onset of deformation, the relaxation stage is analyzed in the interfacial tension chapter.
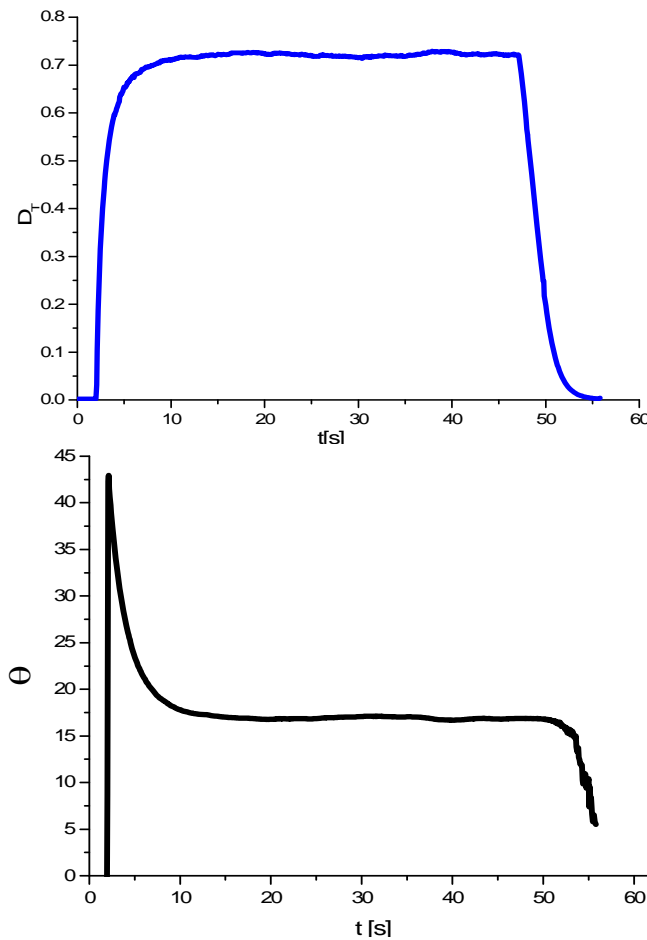

Figure 5.5.   Time evolution of the Taylor deformation D_T and the orientation angle θ for a drop with $r_0 = 0.46$ mm under a flow type with $\alpha = 0.03$ and a shear rate of $\dot{\gamma} = 1.0$ s^{-1}.

5.2 Experimental results

When a drop of one fluid is placed in another fluid under flow conditions, the drop will deform and under specific conditions it might break. The initially spherical drop will deform in response to the stresses exerted by the flow on its surface, $\tau_f = \mu\dot{\gamma}$, which depend on the viscosity of the external fluid and on the shear rate $\dot{\gamma}$. In response to the flow, the drop tries to resist these distorting forces through the action of the interfacial stress, $\tau_d = r_0/\sigma$. This force balance results in an equilibrium shape that is

maintained as long as the flow exists. In general, the response and ultimate form of a drop immersed in a flow field is determined by: (*i*) the capillary number Ca, the ratio between the stresses due to the flow and those due to the interfacial tension, $Ca = \tau_f/\tau_d = \mu\dot{\gamma}r_0/\sigma$; (*ii*) the ratio between the viscosity of the drop and the fluid matrix, λ; and (*iii*) the type of flow field, characterized by α. Experimental studies have found that the behavior of the drop depends in a complicated manner specially on the type of flow and on the viscosities ratio.

In this section the dynamics of drops embedded in flow fields with $\alpha = 0.13$, $\alpha = 0.05$ and $\alpha = 0.03$ are presented. The experiments show the time evolution of drops for two viscosities ratio: $\lambda = 0.012$ and $\lambda = 16$, under different values of capillary numbers Ca. Of primary interest is to visualize the shape that the drop will take up, whether it will deform into a steady shape or whether it will break at some point as the strength of the distorting forces is increased.

5.2.1 Low viscosities ratio

In general, for the case of low viscosities ratio, $\lambda \ll 1$, the breakup of the drop is always possible in any strong flow, despite the parameter α characterizing it. For a given viscosity ratio, the capillary number needed is a function of the type of flow because the vorticity —measured with α— inhibits the drop deformation and therefore retards the breakup. For these drops, the relevant question is determining the magnitude of the capillary number —which depends on the type of flow and the viscosities ratio— that must be applied to ensure breakup. In this way, for equal capillary numbers the stresses over the drop will be different whether it is immersed in a flow with α close to *zero* or in a flow with α close to one. In the first case, the vorticity will cause on the drop a higher rotation and a lower deformation than in the second case; therefore, the drop will be less prone to be broken. With α and λ given, for capillary numbers below a critical value Ca_{crit}, the drop only attains a steady state shape and orientation whereas above Ca_{crit} the stresses of the flow are high enough to cause the drop to break up.

5.2.1.1 Drop deformation

Figs. 5.6, 5.9 and 5.12 show the transient and steady deformation and orientation for initially spherical drops ($D_T = 0$) subjected to a stepwise increment up to subcritical conditions, with constant shear rate. The figures belong to experiments carried out with the same drop —one drop for each type of flow. Each curve shows the deformation and orientation as a function of the time for startup experiments, with different capillary numbers, with the last curve obtained corresponding to a capillary number whose value is slightly above the critical value; because of that, the flow conditions led to the breakup of the drop. For the subcritical conditions in all three flow fields, the interfacial tension dominates and the drop is deformed into

an ellipsoid, reaching the steady state after a monotonic evolution. The typical internal circulation of the drop maintains a stable equilibrium shape, and upon cessation of the flow the drop returns to its original spherical shape after a relaxation process. Figs. 5.7, 5.10 and 5.13 are polar plots of the deformation parameter D_T versus the orientation angle θ for the same experiments as before. This parametric time evolution shows clearly the deformation and orientation of the drop at its final stationary state. The plots concerning to $\alpha = 0.13$ and $\alpha = 0.05$ show that for $Ca > 0.6$, the drop evolves over the same curves, this behavior is not present in the plot corresponding to $\alpha = 0.03$.
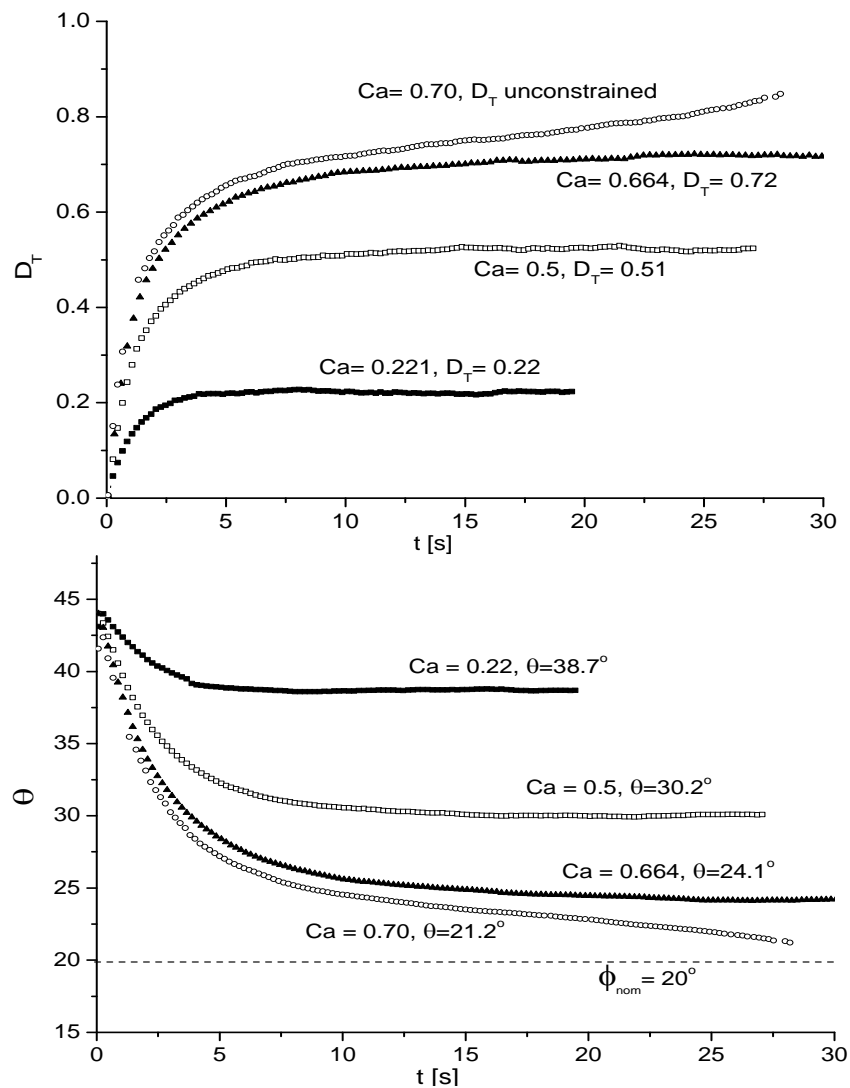

Figure 5.6. Time evolution of the deformation and orientation parameter for $\alpha = 0.13$ and $\lambda = 0.012$ and different capillary numbers.
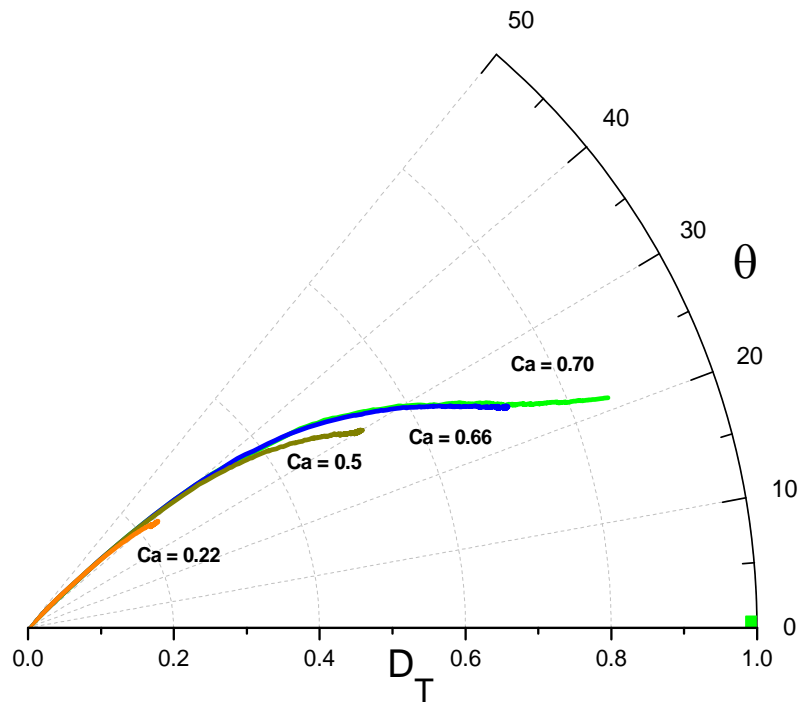
Figure 5.7. Polar plot for different capillary numbers. Parameters obtained for a drop under a flow field with $\alpha = 0.13$ and $\lambda = 0.012$.

As the capillary number increases so do the final deformation, while the orientation angle θ approaches the limiting value ϕ, the characteristic angle of the outgoing axes for each flow. Figs. 5.8, 5.11 and 5.14 show the steady state deformation and orientation as a function of the capillary number for each type of flow. All three flow fields present a linear behavior for low capillary numbers, $Ca < 0.5$, where the slope of the curve fitted to the data has a value close to unity for all them. The flow with $\alpha = 0.13$ maintains this behavior for all ranges of the capillary numbers but for $\alpha = 0.05$ and $\alpha = 0.03$, as Ca increases, the effect of the higher vorticity is manifested with a slight deviation from the linear behavior. Fig. 5.15 is a comparison between the three flow fields and data available from literature (Bentley and Leal 1986b) both for deformation and orientation as a function of the capillary number. It can be seen that for flows with higher vorticity (lower values of α) the critical capillary number increases, and the minimum angle attained by the drop is closer to the angle ϕ, for each flow field. Fig. 5.15 also shows the theoretical linear behavior predicted by the Taylor for $\alpha = 0$ and for the same viscosities ratio. There is a good agreement between Taylor´s theory and the experimental data obtained for $\alpha = 0.1$, over predicting elongation for flow-type parameter values lower than 0.1 and under predicting deformation for the most elongational flow fields. However, Taylor's theory is quite accurate for capillary numbers up to 0.5 for all geometries of the TRM.

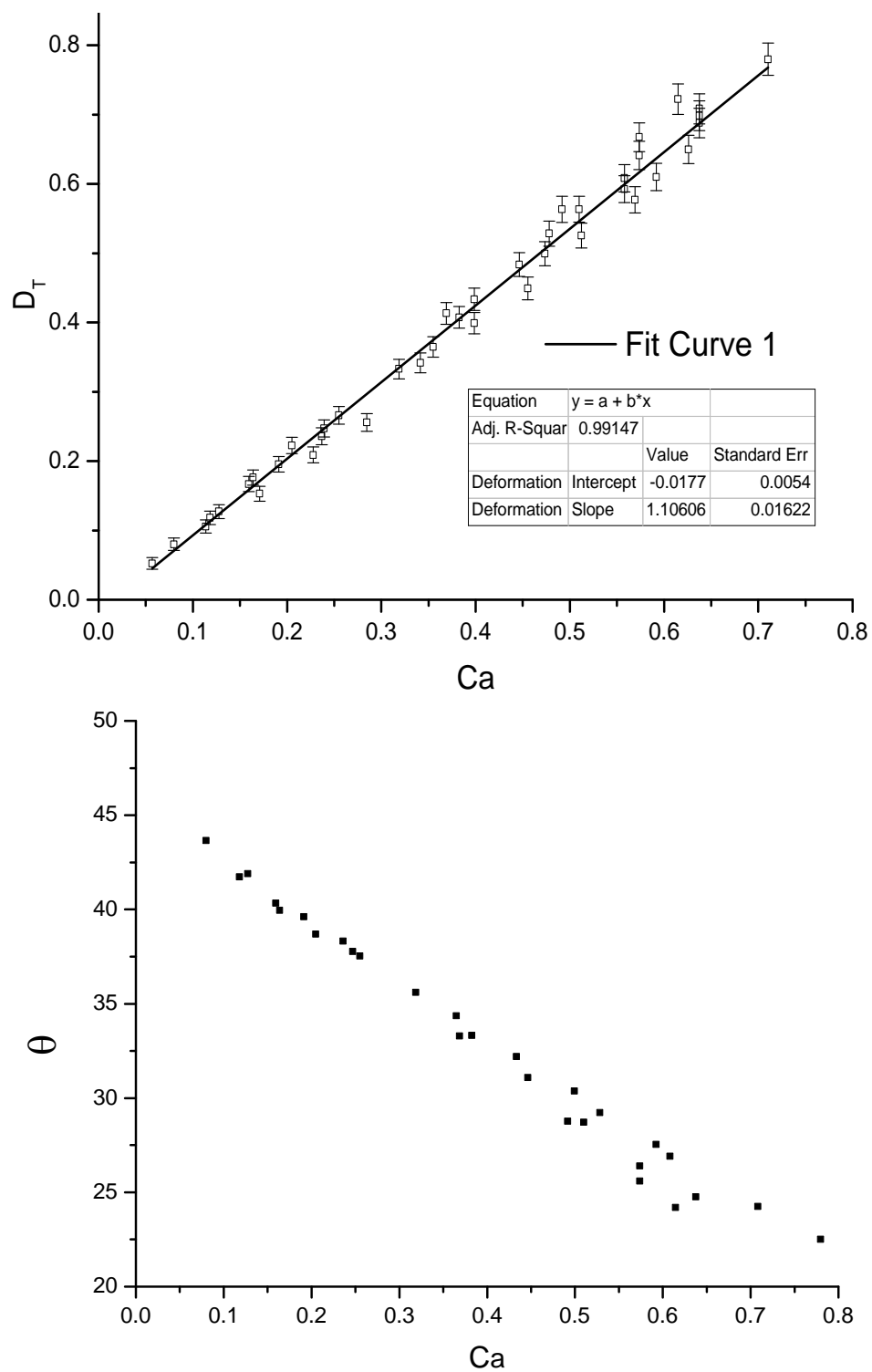| Equation	y = a + b*x	
Adj. R-Squar	0.99147	
	Value	Standard Err
Deformation Intercept	-0.0177	0.0054
Deformation Slope	1.10606	0.01622

Figure 5.8. Steady state drop deformation and orientation for $\alpha = 0.13$ and $\lambda = 0.012$.

Figure 5.9. Time evolution of the deformation and orientation parameters for $\alpha = 0.05$ and $\lambda = 0.012$ and different capillary numbers.

Figure 5.10. Polar plot for different capillary numbers. Parameters obtained for a drop under a flow field with $\alpha = 0.05$ and $\lambda = 0.012$.

Equation	y = a + b*x		
Adj. R-Square	0.99692		
		Value	Standard Error
Deformation	Intercept	-0.00401	0.00242
Deformation	Slope	1.00956	0.01255

Figure 5.11. Steady state drop deformation and orientation for $\alpha = 0.05$ and $\lambda = 0.012.$
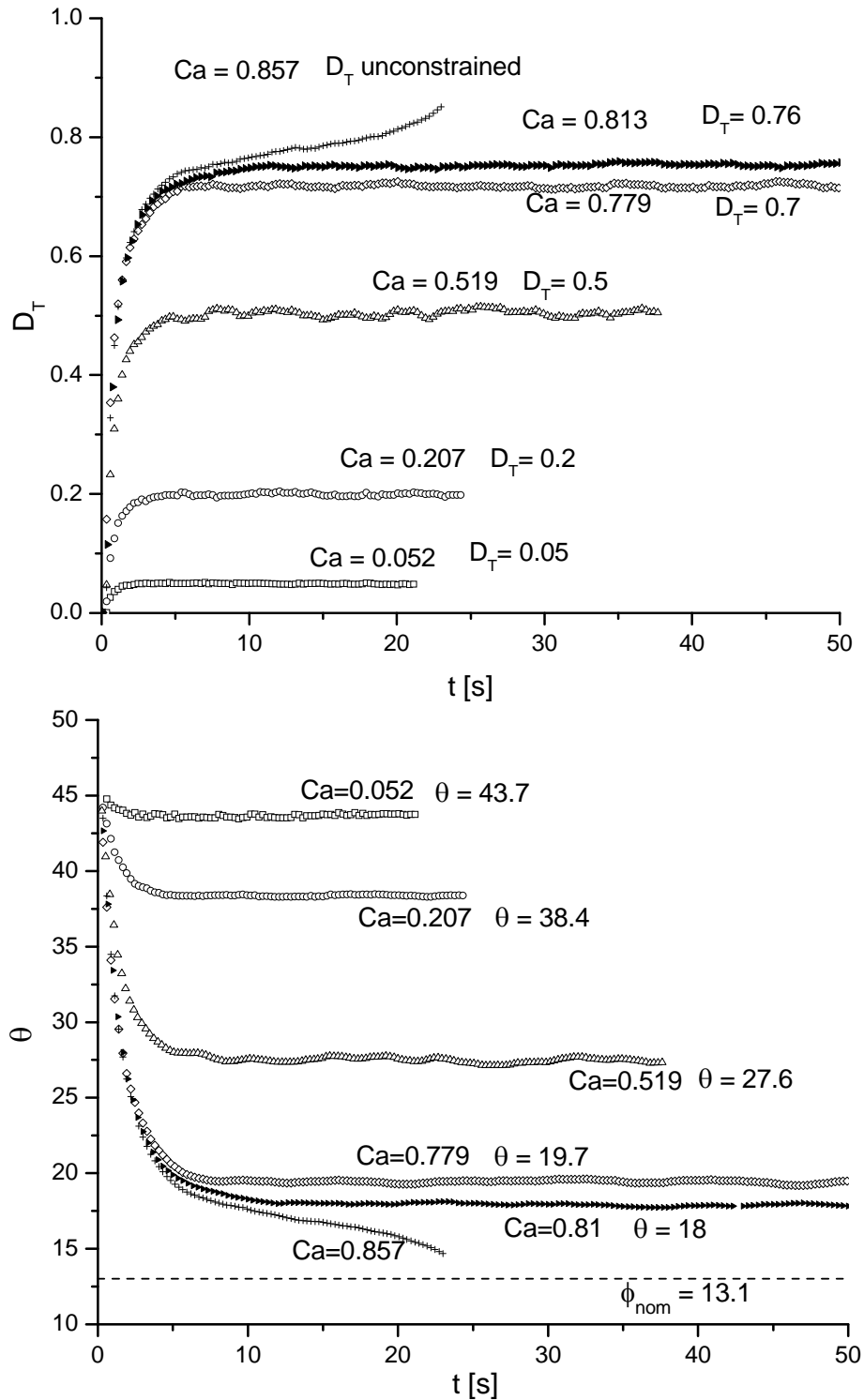
Figure 5.12. Time evolution of deformation and orientation parameters for $\alpha = 0.03$ and $\lambda = 0.012$ and different capillary numbers.
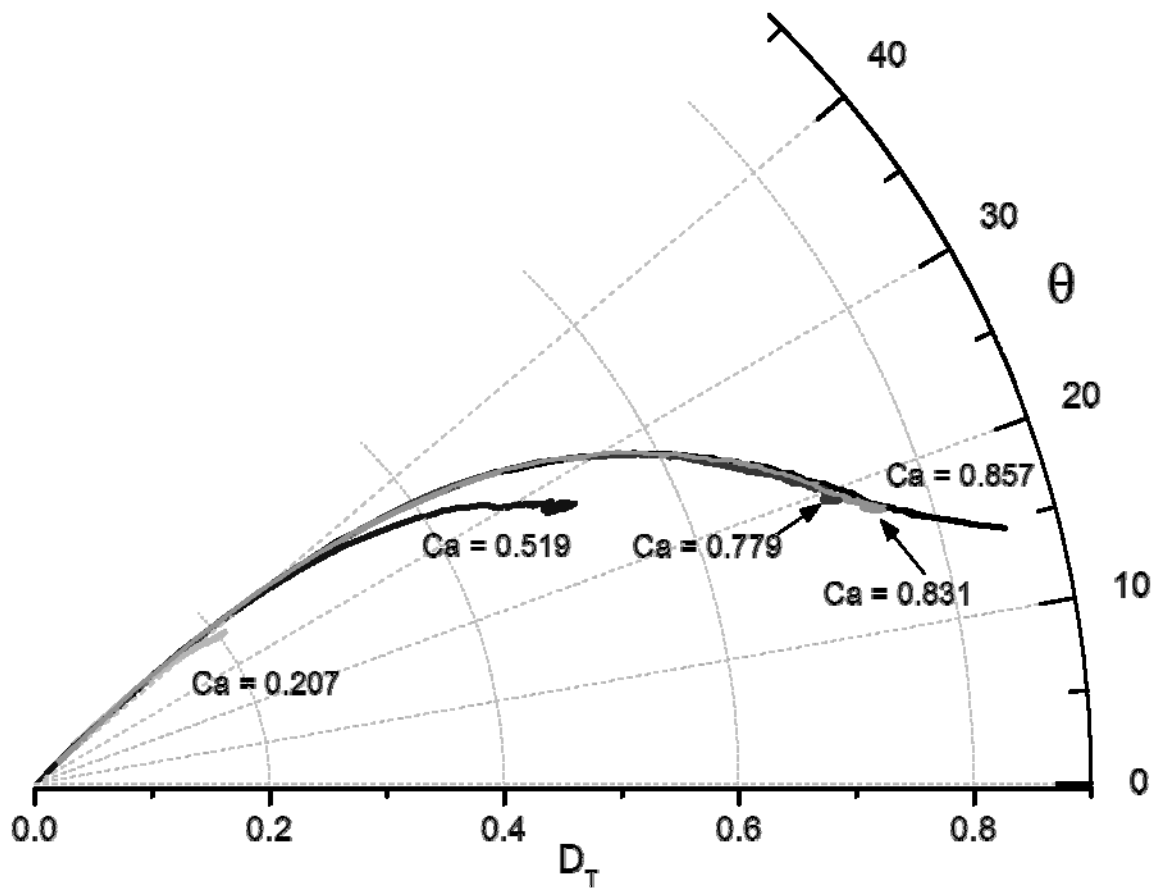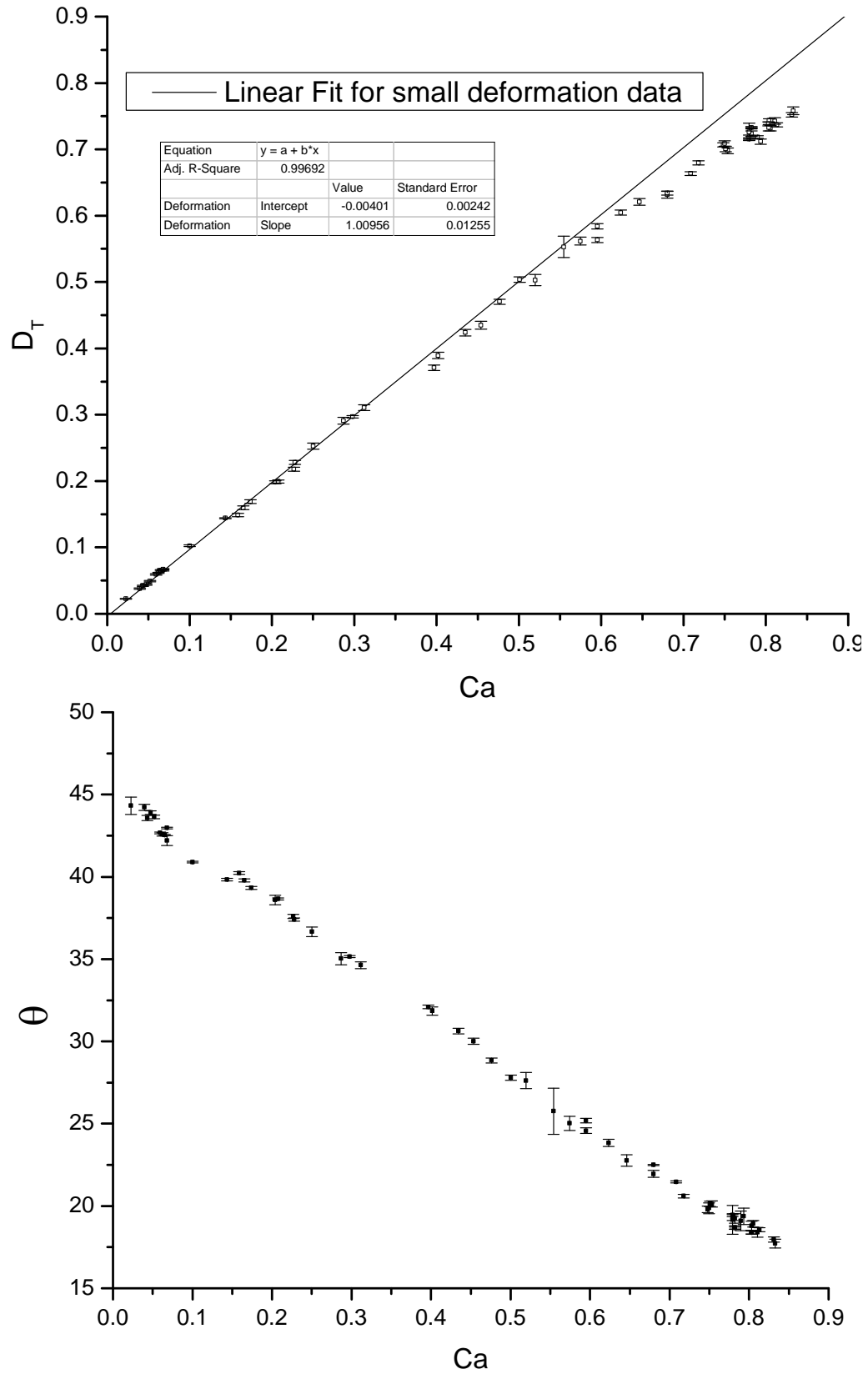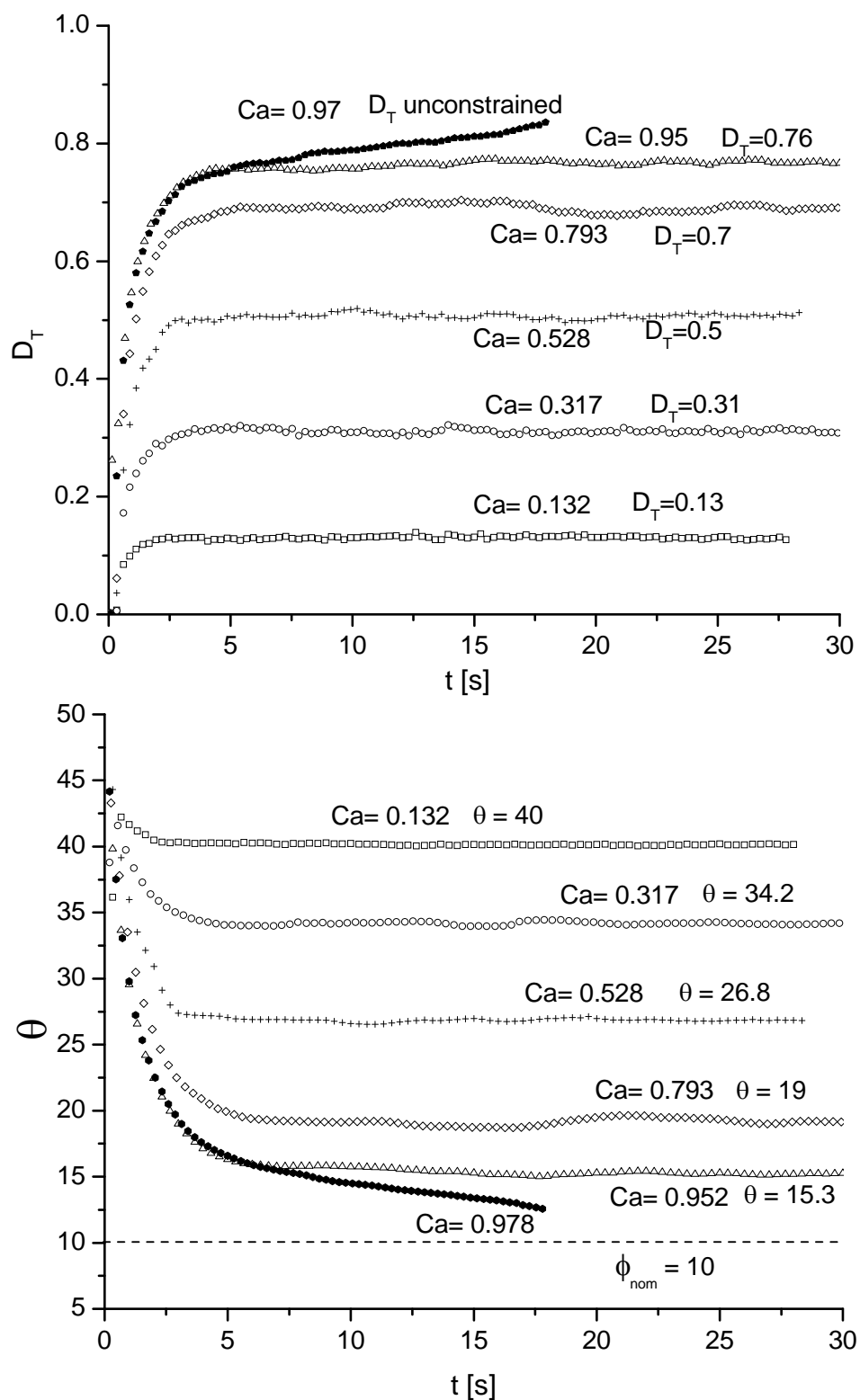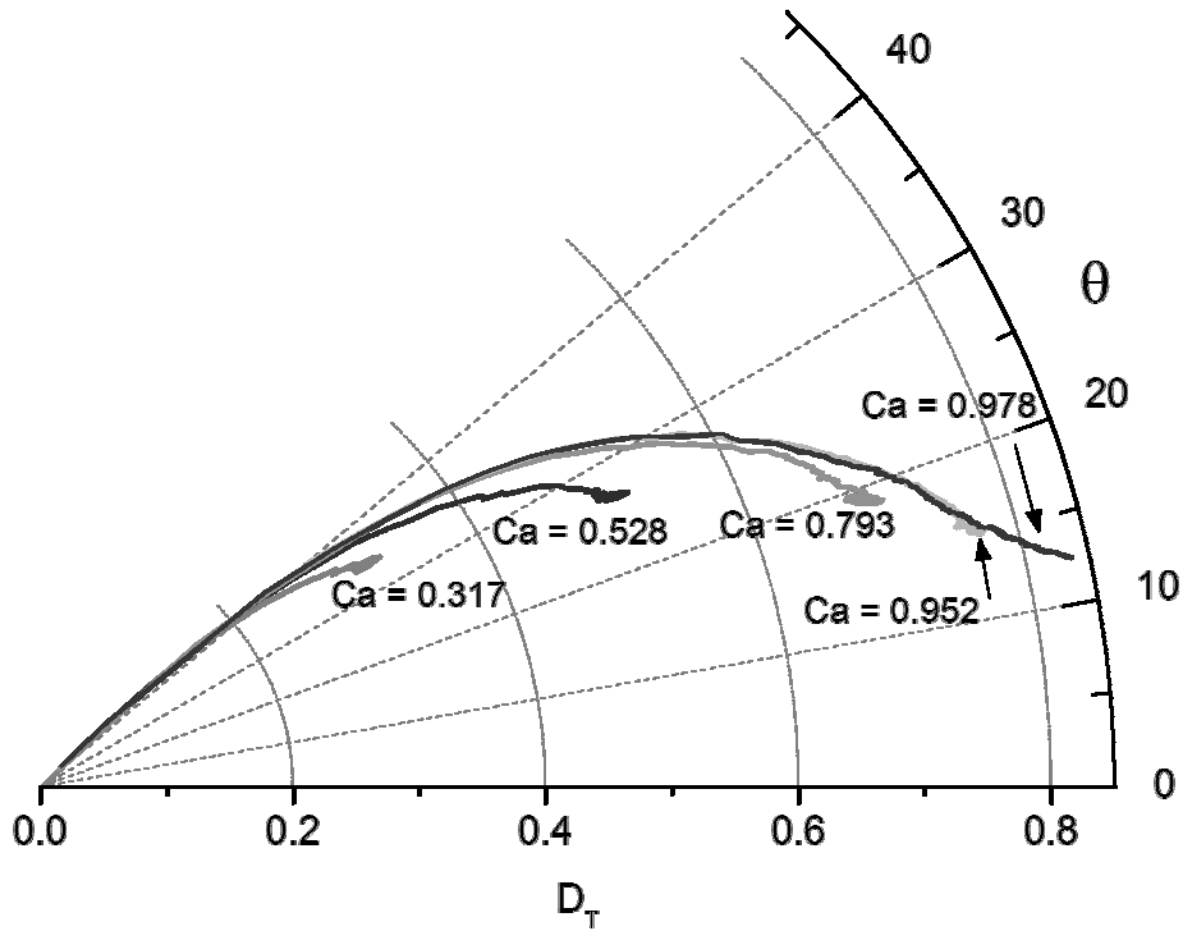
Figure 5.13. Polar plot for different capillary numbers. Parameters obtained for a drop under a flow type α = 0.03 and $\lambda = 0.012$.

The figure contains two plots. The upper plot shows D_T versus Ca with a legend "Linear Fit for small deformation data" and a fit table:

Equation	y = a + b*x		
Adj. R-Square	0.99816		
		Value	Standard Error
Deformation	Intercept	9.13045E-4	0.00246
Deformation	Slope	0.96484	0.00883

The lower plot shows θ versus Ca.

Figure 5.14. Steady state drop deformation and orientation for $\alpha = 0.03$ and $\lambda = 0.012$.

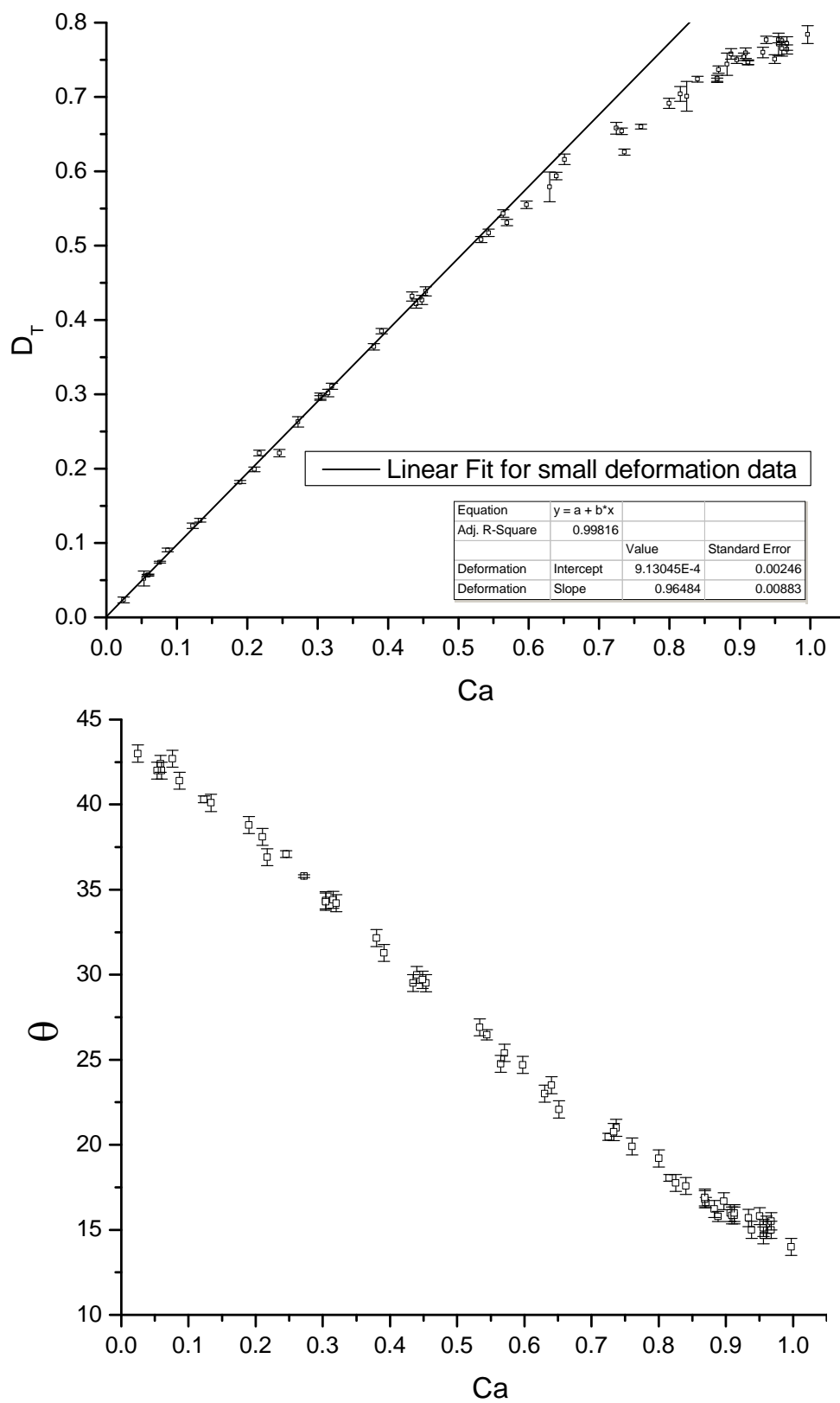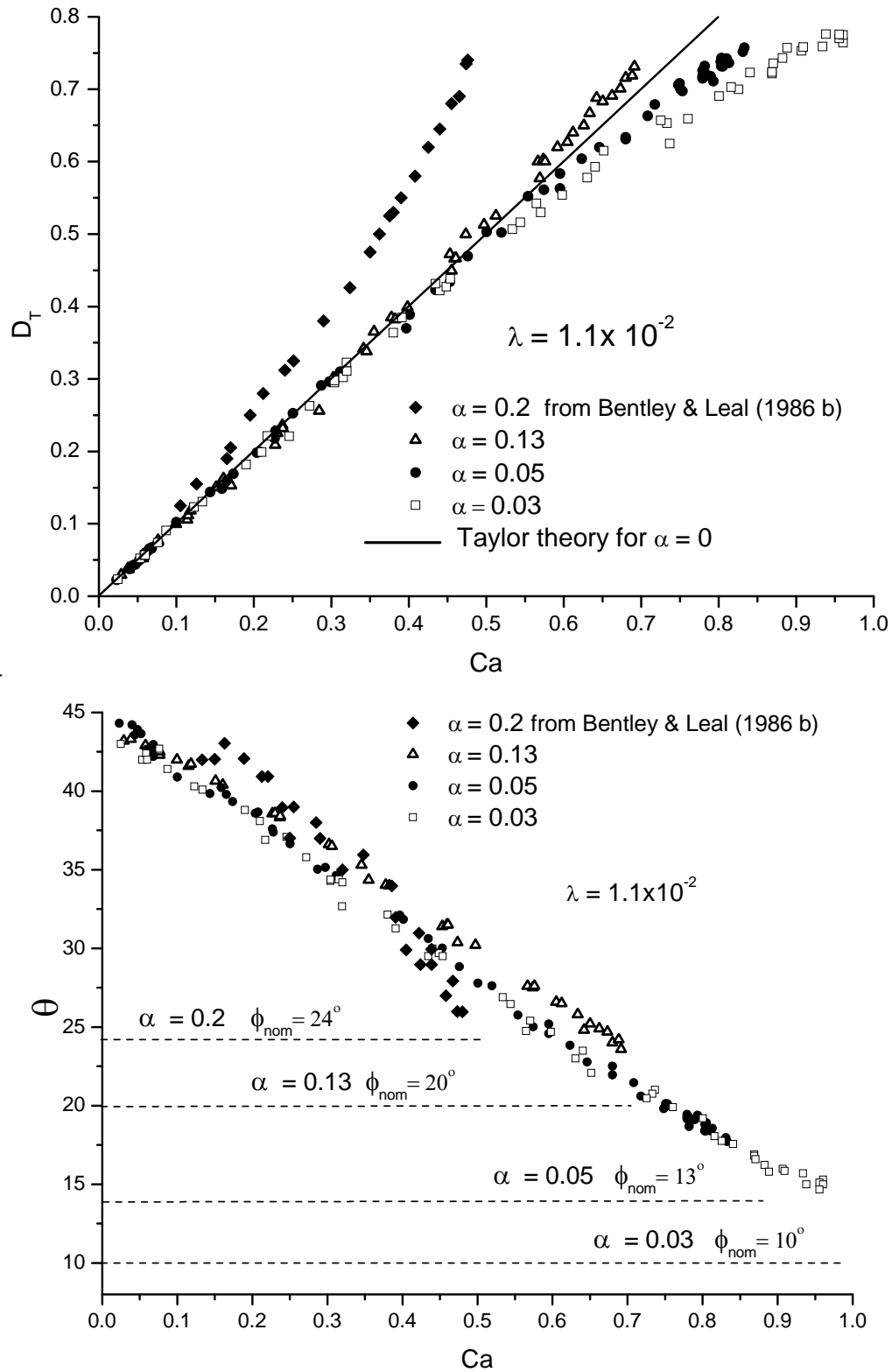**Figure 5.15.** Comparison between the steady states drop deformation and orientation for different flow fields.

5.2.1.2 Critical capillary number

If *Ca* reaches a certain limit, then the stresses due to the flow cannot be supported by the interfacial tension and the drop has reached breakup conditions. The value of this critical capillary number Ca_{crit} strongly depends both on the type of flow and the viscosities ratio. Critical capillary numbers have been determined for a wide range of viscosities ratio and different type of flows, covering the classical simple shear $\alpha = 0$ and elongational $\alpha = 1$ (Grace 1982) as well as intermediate flows in the range of $0.2 < \alpha \leq 1$ (Bentley and Leal, 1986b) but leaving uncovered the range of $0 < \alpha < 0.2$. In this work, the Ca_{crit} is determined for drops under flow conditions; no previous experimental data was available corresponding to a viscosity ratio of $\lambda = 0.012$ nor for flow fields with $\alpha = 0.13$, $\alpha = 0.05$ and $\alpha = 0.03$. The critical capillary number is experimentally determined by slowly increasing the shear rate applied to the drop until no more stable condition of the deformation is obtained. The Ca_{crit} for the flows with $\alpha = 0.13$ is $Ca_{crit} = 0.70$ and for the flows with $\alpha = 0.05$ is $Ca_{crit} = 0.82$, which are the lowest values where no stable conditions were present; see Figures 5.16 and 5.18.

Figure 5.16. Time evolution of the deformation parameter D_T for capillary numbers above critical for a flow field with $\alpha = 0.13$ and $\lambda = 0.012$.

Figure 5.17. Polar evolution of the deformation and orientation parameters for $Ca > Ca_{crit}$ for a flow field with $\alpha = 0.13$ and $\lambda = 0.012$.
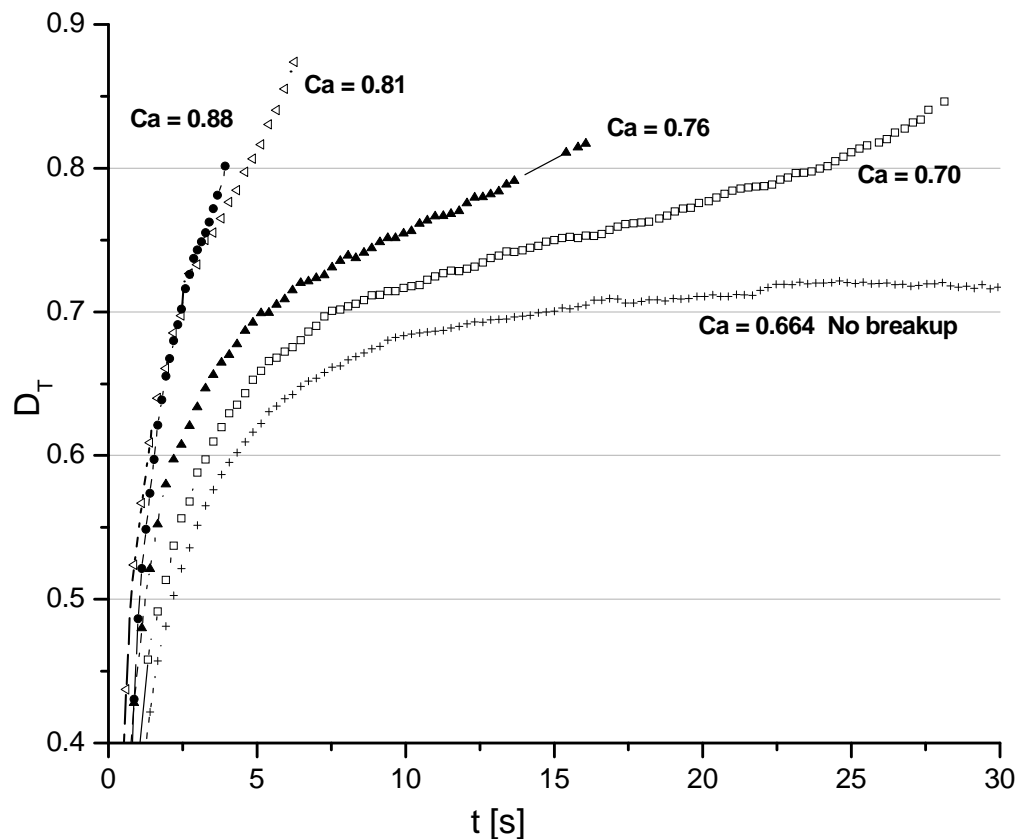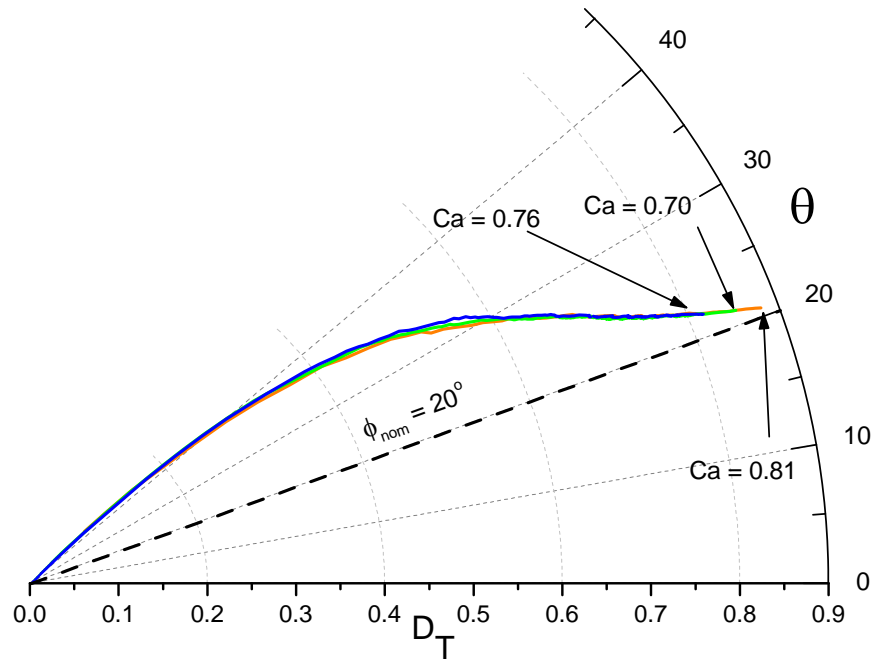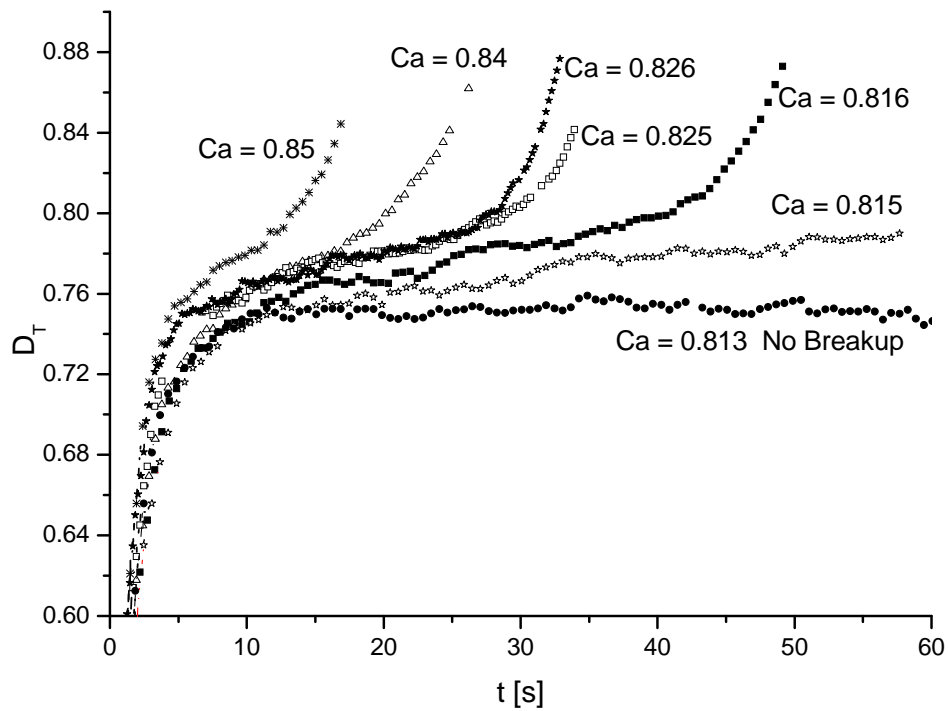

Figure 5.18. Time evolution of the deformation parameter D_T for capillary numbers above critical for a flow field with $\alpha = 0.05$ and $\lambda = 0.012$.

Figures 5.16 and 5.18 show the deformation as a function of the time for conditions in which the forces due to the applied shear rate exceeds the interfacial tension ones. When the drop is subjected to $Ca \geq Ca_{crit}$, it cannot attain a stable shape (supported by the interfacial tension) and the deformation continues increasing unconstrained with a deformation velocity that depends on how much the capillary number applied exceeds critical value. Figures 5.17 and 5.19 are polar plots of the deformation parameter D_T vs the orientation angle θ for $Ca \geq Ca_{crit}$. The dimensionless graphics show that the value of the capillary number does not matters on the evolution of the deformation with respect to the orientation: the path followed by the drop is the same with D_T increasing while θ approaches to the outgoing axis angle ϕ. Regarding the flow with $\alpha = 0.03$, a confinement effects was observed. For simple shear flows the *confinement ratio* is defined as the ratio of the drop diameter, $d = 2r_0$, to the gap spacing, g, separating the walls of the devices used to produce the flow. The same definition of the confinement ratio d/g will be used in this work but taking g as the gap defined for the TRM geometry, (the distance that separates the cylinders surfaces as shown in Fig. 2.1) that for the case of $\alpha = 0.03$ is $g = 3.0$ mm. Accordingly, the degree of confinement seems not to have an appreciable effect on Ca_{crit} when it is lower than 0.3, or for λ values of the order unity; when d/g exceeds a value of 0.3, the Ca_{crit} increases with increasing the degree of confinement for $\lambda < 1$ and reduces for $\lambda > 1$ (Vananroye et al. 2006a).

Figure 5.19. Polar evolution of the deformation and orientation parameters for $Ca > Ca_{crit}$ for a flow field with $\alpha = 0.05$ and $\lambda = 0.012$.
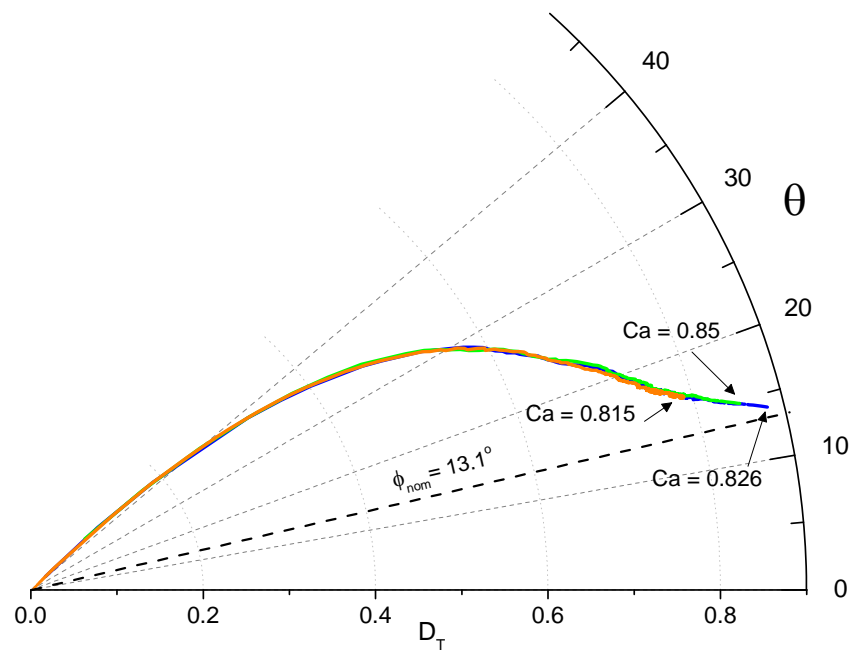
Figure 5.20 shows the deformation evolution for different capillary numbers that led to breakup and its associated d/g value. It can be observed that the lower Ca is 0.96 and corresponds to confinement ratios below 0.3. Hence, it can be said that the critical capillary number for unconfined drops under flow fields with $\alpha = 0.03$ is close to $Ca_{crit} = 0.96$. The same figure shows that as predicted, for a viscosity ratio $\lambda = 1.1 \times 10^{-2}$, Ca_{crit} increases for $d/g = 0.3$, and when $d/g = 0.45$ there is no breakup despite a capillary number close to $Ca = 1.06$, which for lower confinement ratios causes the rupture of the drop. The polar plot in Fig. 5.21 show that as d/g increases, the drop starts to modify its evolution, presenting slight departures from what can be considered the "unconfined evolution", these departures are barely visible for $d/g = 0.3$ and are more evident for $d/g = 0.45$ where the drop attains a deformation and orientation stable in the long run. Fig. 5.22 is a comparison of the trajectories followed by the drops for the three types of flow.
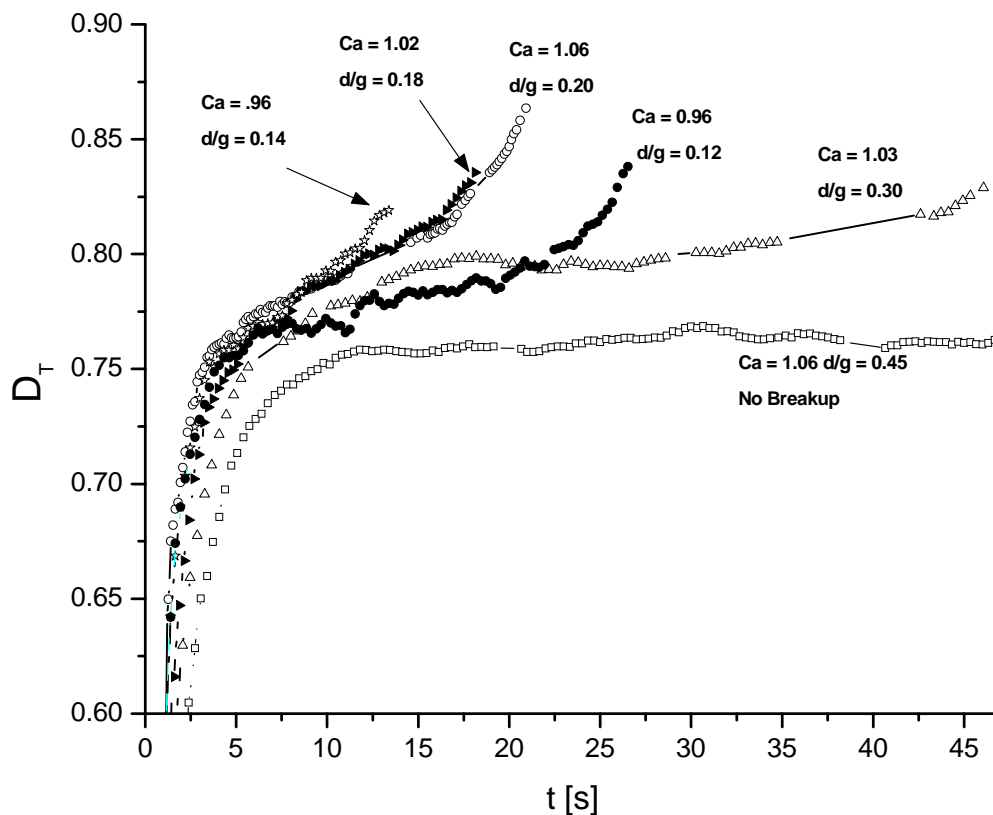
Figure 5.20. Time evolution of drop deformation D_T for critical capillary numbers and for different confinement ratios for a flow field with $\alpha = 0.03$ and $\lambda = 0.012$.

Figure 5.21. Polar evolution of the deformation and orientation parameters for $Ca > Ca_{crit}$ in a flow field with $\alpha = 0.03$ and $\lambda = 0.012$ and for different confinement ratios.
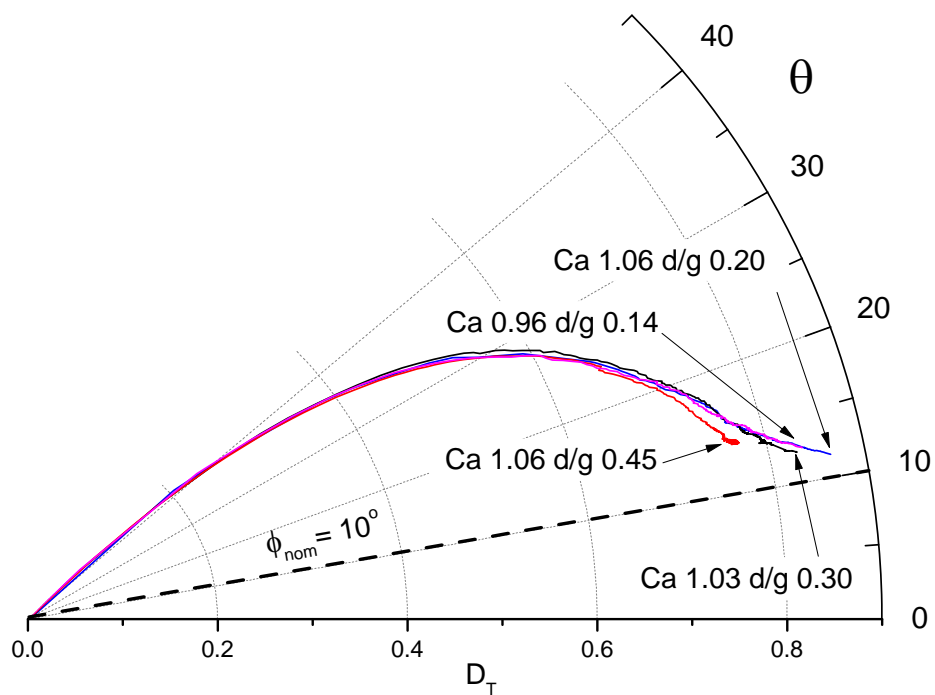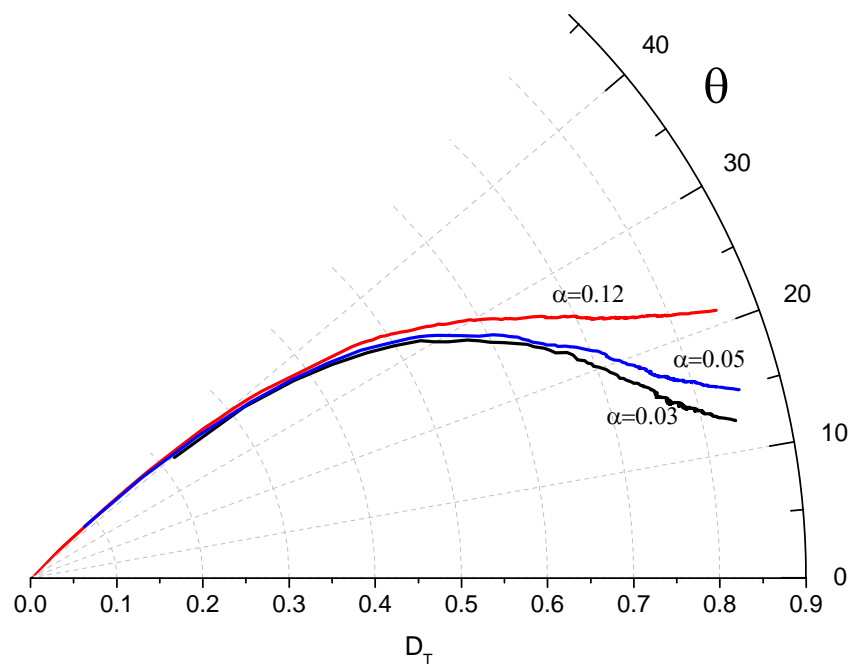

Figure 5.22. Polar evolution of the deformation and orientation for critical capillary numbers for the three types of flow with $\lambda = 0.012$.

74

5.2.1.3 Breakup process

Once the *Ca* exceeds the critical value, the drop starts an unbounded elongation process that continues as long as the flow is kept. If the flow is maintained, the drop will deform until it forms a thread that when is long and thin enough it will breakup by capillary instabilities. If the flow is stopped, driven by the interfacial tension, the drop either will return to its initial spherical shape or it will breakup into smaller fragments depending on the maximum deformation reached. In both cases, the breakup process is similar despite the type of flow used to deform the drop. Its dynamics and the final drop size distribution depend only on the viscosities ratio and the deformation reached by the drop prior to stopping the flow. The effect of the flow is only to modify the time scale for the deformation of the drop (Stone et al. 1986).

For drops that are only slightly deformed, an appropriate measure of deformation is D_T which is strictly applicable only for elliptically deformed drops, being zero for spherical drops and asymptotically approaches unity as the drop became infinitely extended. But beyond a certain degree of deformation, the drop becomes very elongated, $(L \gg B)$, and then, the interfacial tension will make the middle section tubular with a circular cross section (Mikami et al. 1975). This small circular cross section causes a high internal pressure with a slow decay of B, and consequently –given its definition– a slower growth of D_T. Because of that, for highly elongated drops under breakup conditions, it is convenient to characterize the degree of deformation using the dimensionless elongation ratio, L/r_0, as the appropriate parameter of the deformation, being r_0 the radius of the spherical drop.

Figures 5.23 to 5.25 are plots of the deformation measured with the elongation parameter L/r_0 as function of the dimensionless time for subcritical and supercritical *Ca* values. These figures show the maximum possible stable elongation of the drop for this viscosities ratio and the different flow types. These values are: $L/r_0 = 3.25$ for $\alpha = 0.13$, $L/r_0 = 3.5$ for $\alpha = 0.05$ and $L/r_0 = 3.75$ for $\alpha = 0.03$. As mentioned before, if $Ca > Ca_{crit}$ the drop will continue elongating but if the flow is arrested before the drop elongation exceeds a critical value, it will still retract back into a sphere. Stone and Leal (1989b) extensively studied retraction of extended viscous drops and determined the maximum elongation from which a drop still retracts without breaking as function of the viscosities ratio. For a drop with $\lambda = 0.012$, the elongation that the drop needs to reach to be fragmented when it retracts lies in the range of $5.4 < L/r_0 < 6.2$ (Stone and Leal 1989a 1989b).

Figure 5.23. Deformation measured with the elongation parameter L/r_0 as function of the dimensionless time for subcritical and supercritical Ca values for a flow field $\alpha = 0.03$. The plot shows the maximum possible stable elongation.

Figure 5.24. Deformation measured with the elongation parameter L/r_0 as function of the dimensionless time for subcritical and supercritical Ca values for a flow field $\alpha = 0.05$. The plot shows the maximum possible stable elongation.
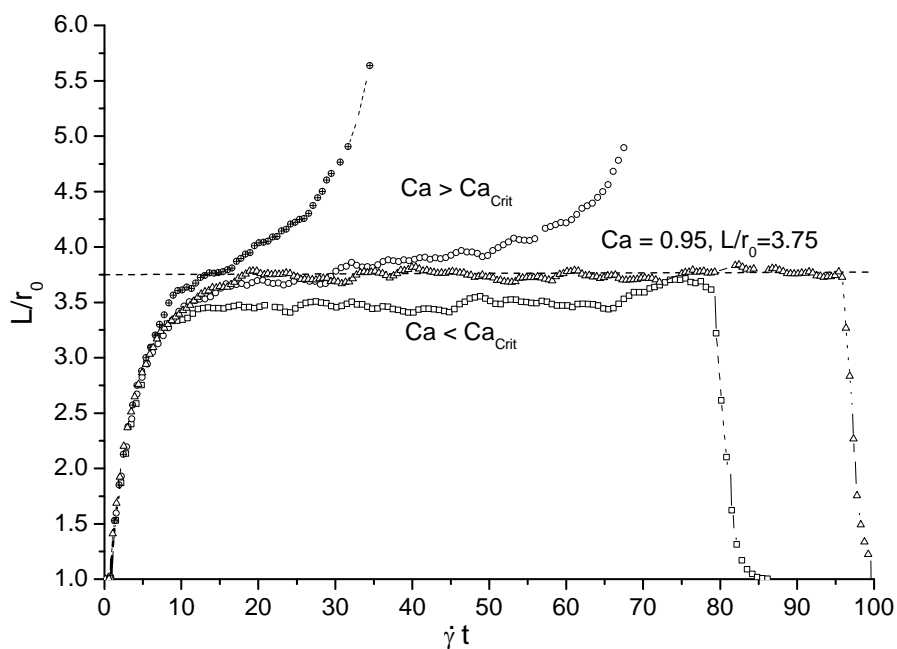
Figure 5.25. Deformation measured with the elongation parameter L/r_0 as function of the dimensionless time for subcritical and supercritical Ca values for a flow field $\alpha = 0.13$. The plot shows the maximum possible stable elongation.

Fig. 5.26 shows different curves of the non-dimensional time evolution of the elongation parameter for a drop under different Ca for $\alpha = 0.03$. The curve A in the plot shows that for $Ca < Ca_{crit}$ the drop attains a stable elongation that is below $L/r_0 = 3.75$, the maximum possible in this flow. When Ca exceeds the Ca_{crit}, the drop elongation is not limited but it continues, surpassing the maximum stable value, but if the flow is stopped and the elongation has not reached the minimum critical value of $L/r_0 = 5.4$, the drop still retracts into a sphere curves B and C on Fig. 5.26. If the flow is maintained so the maximum elongation is allowed to overreach this critical value, the retraction process leads to breakup of the drop via necking, curve D. Fig. 5.27 shows the process of breakup corresponding to the curve D in Fig. 5.26.
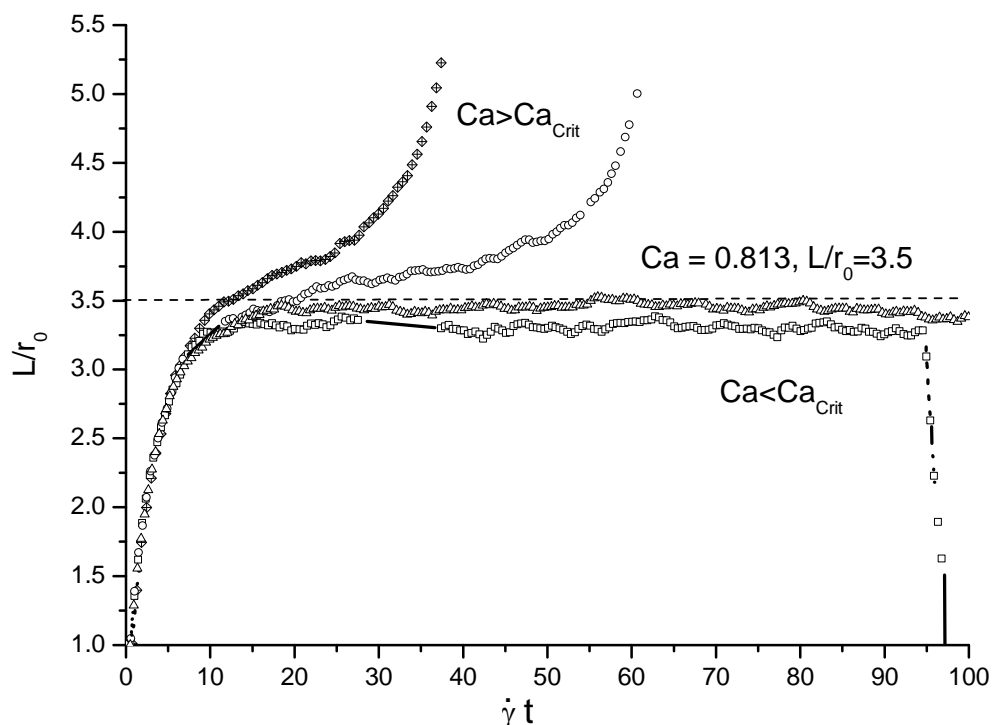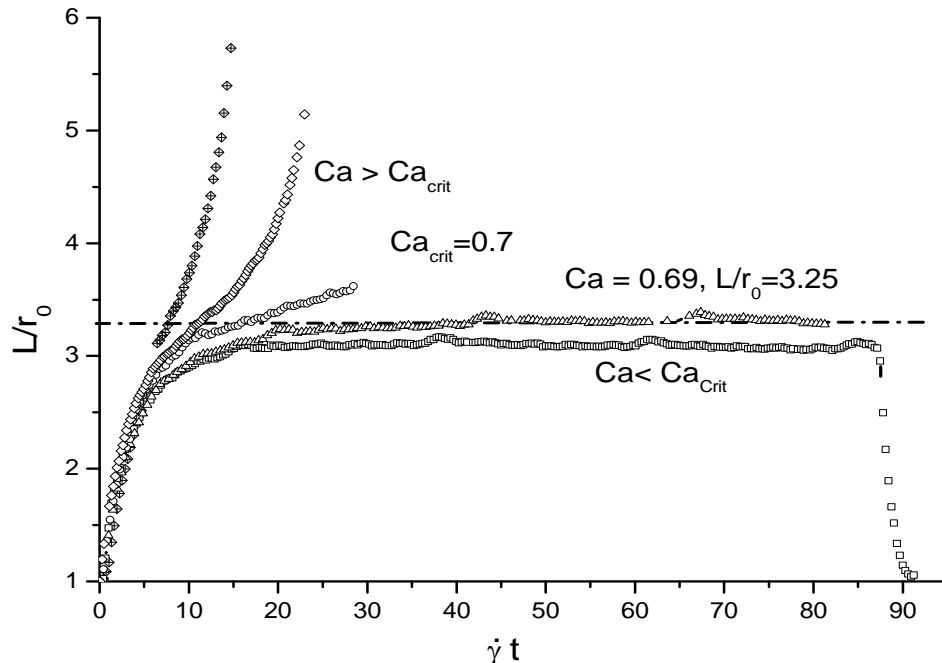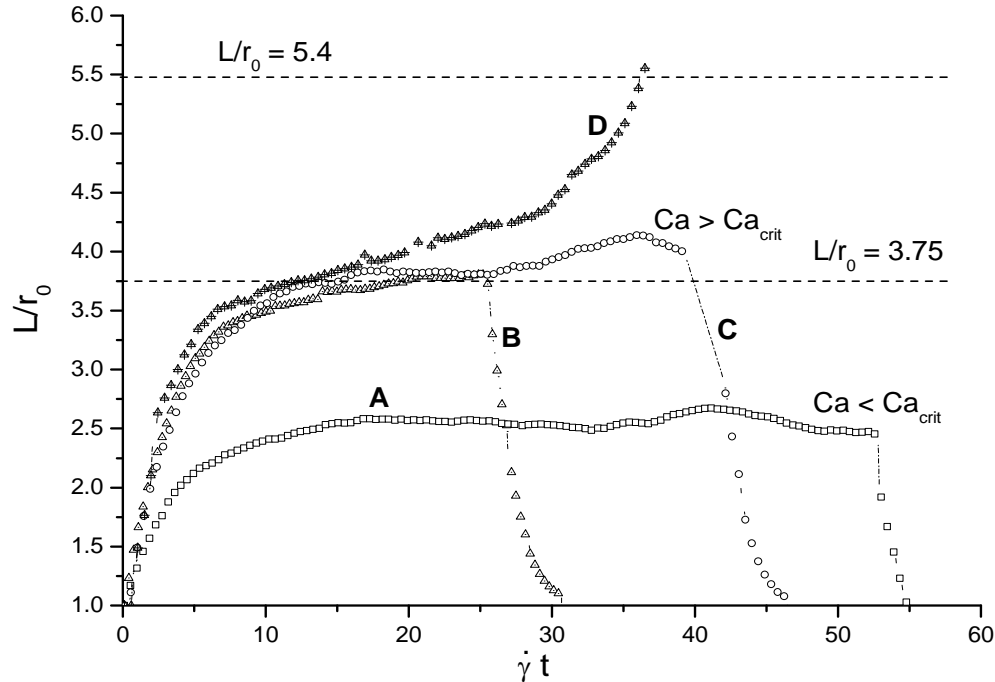
Figure 5.26. Deformation measured with the elongation parameter L/r_0 as function of the dimensionless time for supercritical Ca values. The plots show that if the drop does not reach a minimum elongation, even when there is no stable shape, it still retracts into an sphere. Data from an experiment with a flow field with $\alpha = 0.03$ and $\lambda = 0.012$.

Therefore, the breakup of a drop is possible either by stopping the flow at a determined elongation (that ensures the breakup) or by sustaining the flow, such that the drop is stretched into a long slender viscous thread. In the first case, the mode of breakup depends on the viscosities ratio λ and the deformation reached by the drop at the moment of stopping the flow. If the flow is sustained and the capillary numbers are much higher than the critical value, $Ca \gg Ca_{crit}$, the drop is deformed affinely (negligible interfacial stresses), it is rapidly stretched into a slender fibril, which subsequently breaks up by capillary-wave instabilities. Under those circumstances, the interfacial stresses are overridden by the deforming shear stresses and the drop is deformed with passive interfaces. For Newtonian drops embedded in a Newtonian matrix experiments show that affine deformation occurs for simple shear flow when $Ca/Ca_{crit} \geq 2$ (Elemans et al. 1993) and for plane hyperbolic flow when it is present when $Ca/Ca_{crit} \geq 5$ (Meijer and Janssen 1993). If the Ca number is marginally greater than Ca_{crit}, but $Ca/Ca_{crit} < 2$, in simple shear the drop will also form a long thread and will breakup by capillary instabilities but with a time scale longer than that in affine deformation.

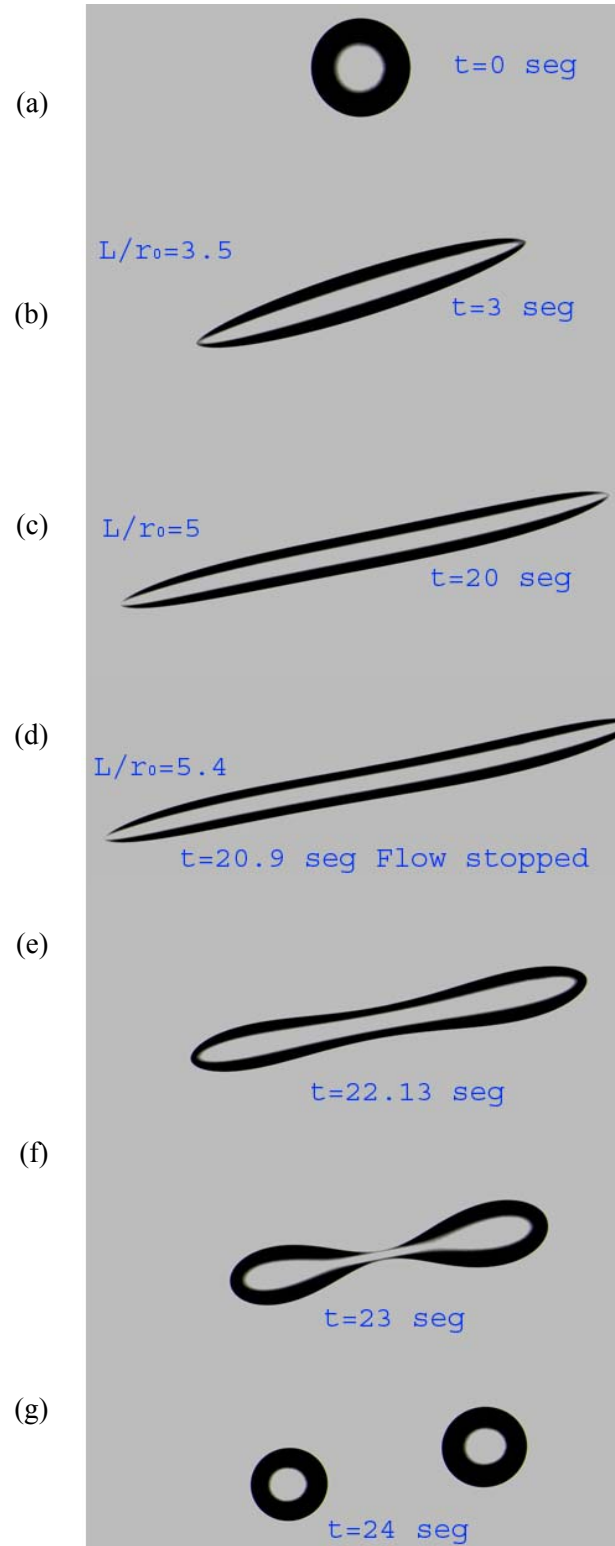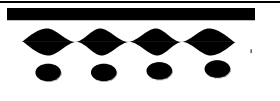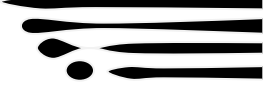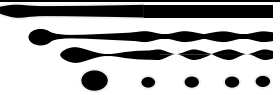**Figure 5.27.** Breakup process via necking of a slightly elongated drop with λ = 0.012 in a flow field with $\alpha = 0.13$.

In general there are three principal breakup mechanisms: necking (also called binary breakup), end-pinching and capillary-wave instabilities. The first two are similar and mainly result after cessation of the flow. The necking, (Fig. 5.27), is present when the drop is deformed slightly beyond a critical length or when the strength of the flow is gradually increased, resulting in the split up of the drop into two equal-sized daughter drops (Rumscheidt and Mason 1961). The end-pinching (Figs. 5.28 and 5.27), occurs when the drop has reached higher elongation values or after step changes in the capillary number and/or the flow type (Stone and Leal 1989a, 1989b). The third mechanism, the capillary-wave instabilities, appears either there is a flow going on or when the flow has been stopped, as long as the drop elongation reached is high enough for each case. In this work only the two first were clearly observed; as for the capillary instabilities, the required elongation for the observation of that phenomenon in absence of flow – and with this viscosities ratio– is L/r_0 $O(15)$ which was not reached. For the case of breakup of the drop in presence of flow the required elongations are even higher, $L/r_0 > O(15)$ (Stone and Leal 1989a, 1989b). Table 5.1 schematizes the principal breakup process of a single drop in linear flows, depending on the elongation ratio L/r_0 (which is a function of the viscosities ratio) and a brief explanation about all three processes is given below.

Table 5.1 Principal Breakup mechanism of single drops.

Breakup conditions		Deformation reached	Principal breakup mode	
Breakup conditions	With Flow	Drop forms very elongated thread	Capillary instabilities	
	Without Flow	L/r_0 barely above the critical value	Necking	
		Moderate L/r_0 values	End-pinching	
		Highly elongated L/r_0	End pinching & capillary instabilities	

5.2.1.3.1 End pinching process

When the drop becomes highly elongated, its shape resembles a cylindrical thread with bulbous ends; see Figs. 5.27e, 5.28e and 5.29c. Observing the axial cross-section of the deformed drop, the cylindrical part has a curvature larger than the one at the bulbous ends and hence (due to the interfacial tension) with the internal pressure being higher than at the ends of the drop. In the regions where the cylindrical part joins the bulbous ends, there is a pressure gradient owed to the change from a high pressure region in the

(a)

t=0 seg

L/r₀=3.2

(b)

t=3seg

(c) L/r₀=4.5

t=5.3seg

(d) L/r₀=6.4

t=7.13 seg Flow stopped

(e) L/r₀=4.5

t=7.73seg
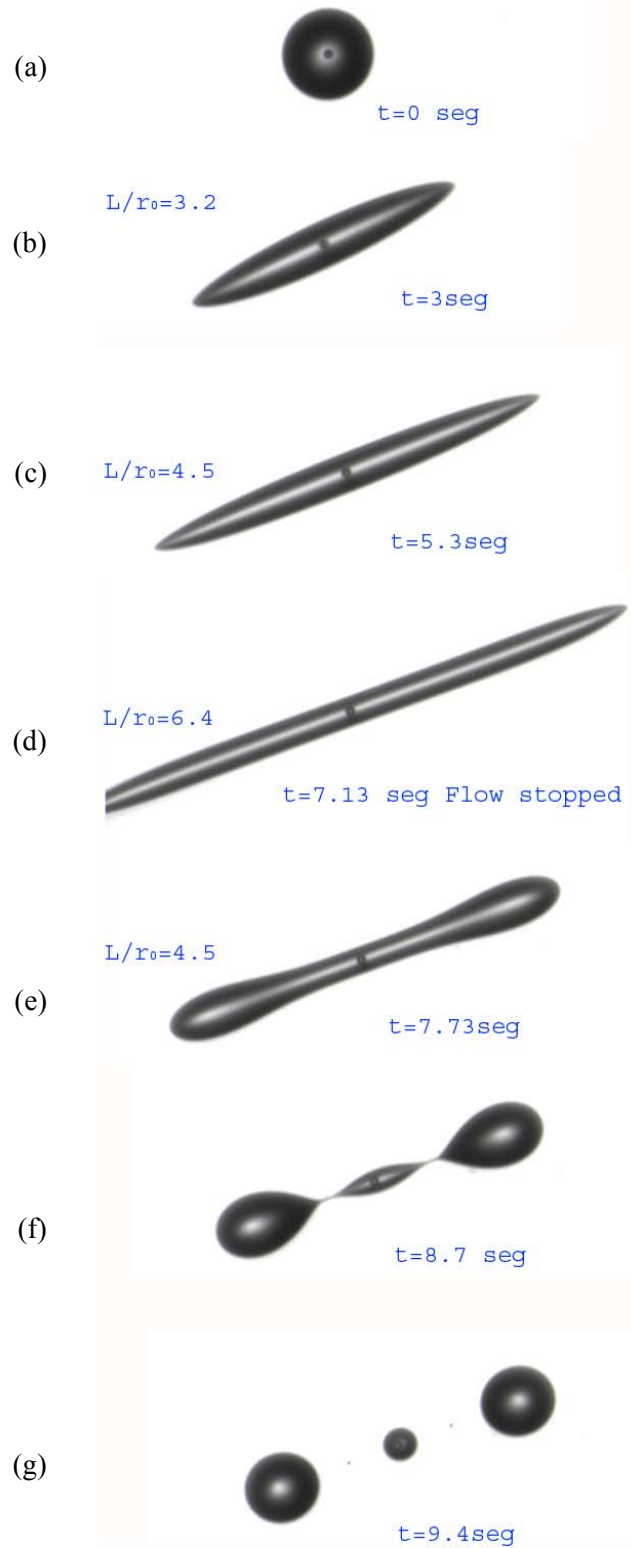
(f)

t=8.7 seg

(g)

t=9.4seg

Figure 5.28. Breakup process via end-pinching process of an elongated drop with $\lambda = 0.012$ in a flow field with $\alpha = 0.13$.
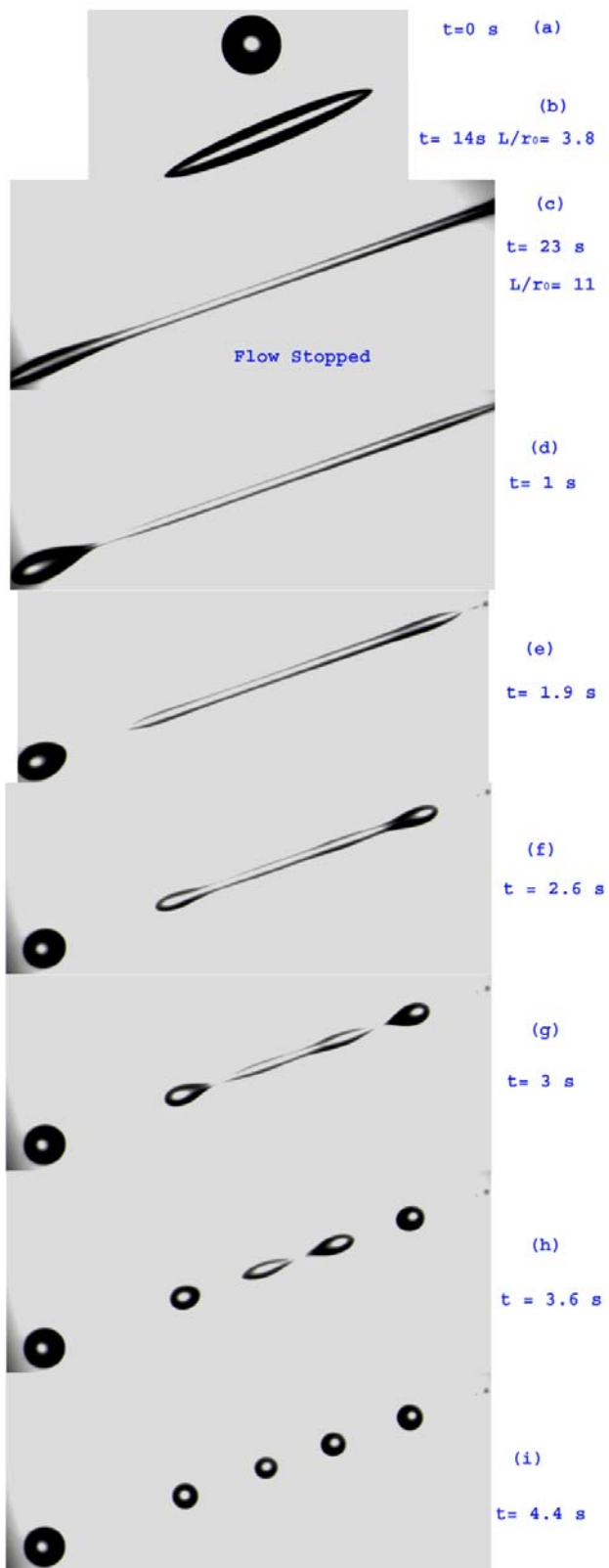
Figure 5.29. Breakup process via end-pinching of an elongated drop with $\lambda = 0.012$ in a flow field with $\alpha = 0.13$.

cylindrical part to a lower pressure region in the bulbous ends. This pressure gradient induces a flow from the central portion of the drop (the cylindrical section) toward the ends (the bulbs). This flow decreases the radius of the circular cross-section in that joining part inducing the formation of a neck and thus the eventual breakup via a capillary pinch-off process, Figs. 5.28f and 5.29d.

After the flow is stopped, all external distorting force vanish. If the curvature at the extremes of the drop is much larger than in the middle section, then a retraction process starts due to a high pressure in those ends with high curvature, creating another pressure gradient. Therefore, a flow field is generated but this time from the ends of the drop toward the center. This flow promotes a reduction in the elongation of the drop and brings the drop back to a more spheroidal shape. This process is evident in the change in shape from Fig. 5.28d (when the flow is stopped and the drop has a elongation ratio of $L/r_0 =$ 6.4) to Fig. 5.28e (where the drop has reduced its elongation ratio to $L/r_0 = 4.5$, but with a shape in which the cylindrical part and the bulbous ends are evident).

Consequently, after the drop has been deformed and suddenly the flow is stopped there will be a competition between those two pressure-driven flows inside the drop. This question is settled by the viscosities ratio. For $\lambda < 1$ the viscosity of the drop is low respect to that in the fluid matrix and therefore there can be large internal velocities and the flow toward the center of the drop cannot inhibit the formation of a neck and the subsequent pinch-off. This environment is shown during the evolution from Fig. 5.28e to Fig. 5.28f; in those pictures, it can be seen that in about one second the change in the length of the drop is just visible, whereas the development of the neck near the bulbous par —and the consequent pinch-off of the extreme— is almost complete. Once that the bulbous ends have been separated, the end-pinching breakup process is self-repeated, because the remaining cylindrical part has pointed ends, Fig. 5.29e. This new shape creates a high internal pressure at the ends with its corresponding flow, subsequently developing a bulbous form; see Fig. 5.29f. Once the bulbous region have been formed, the breakup process is repeated.

For drops with very low viscosities ratio ($\lambda \leq 10^{-2}$), the typical shape for moderate elongation ratios has very sharp ends (Figs. 5.27d and 5.28d). The curvature at these ends is so high that it results in large velocities gradients (due to large pressure gradients) from the ends toward the center and hence a rapid initial reduction in the length of the extremes, but if the drop is sufficiently elongated, it does not shortens fast enough to recover its spherical shape and the ends became bulbous which conduces to a necking breakup following the process mentioned, Fig. 5.27.

5.2.1.3.2 Capillary waves instabilities

Once the drop has been stretched into long slender thread the radius of the cross section decreases in such a way that interfacial tensions become dominant. It tends to minimize the interfacial area, and as a consequence, small perturbations will exist at the interface; these disturbances will grow and eventually bring about the disintegration of the thread into a line of smaller drops. As mentioned before, breakup of drops due to capillary instabilities is present either with or without flow.

Quiescent matrix.

Reviewing first the case of absence of flow, in 1935 Tomotika extended the pioneering work of Raleigh (1879) in the stability of a water jet in air by analyzing the case of an infinitely long viscous cylinder with radius R_0, embedded in a quiescent fluid matrix with viscosity μ_1. He considered small disturbances at the interface, the so called "Raleigh disturbances" or "Raleigh instabilities". To first order, these perturbations are sinusoidal, each one possessing a wavelength ζ with a small amplitude ε; see Fig. 5.30.

$$R(z) = R_m + \varepsilon\, sin(2\pi z/\zeta), \tag{5.1}$$

or

$$R(z) = R_m + \varepsilon\, sin(z\, \chi/R_0), \tag{5.2}$$

with $\chi = 2\pi R_0/\zeta$ as the dimensionless wave number instead of the wavelength amplitude ζ and R_m as the mean radius,

$$R_m = \sqrt{R_0^2 - \frac{\varepsilon^2}{2}}. \tag{5.3}$$

The disturbance amplitude is assumed to grow exponentially in time:

$$\varepsilon = \varepsilon_0 e^{qt}. \tag{5.4}$$

The initial distortion amplitude, ε_0, is given by (Kuhn 1953):

$$\varepsilon_0 = \left(\frac{21\, \kappa\, T}{8\, \sigma\, \pi^{3/2}}\right)^{1/2}, \tag{5.5}$$

T being the absolute temperature, σ the interfacial tension and κ Boltzmann´s constant, $\kappa = 1.38 \times 10^{-23}$ J/K. Thus, the growth rate q is

$$q = \frac{\sigma\, \Omega(\chi,\lambda)}{2\mu_1 R_0}, \tag{5.6}$$

where $\Omega\,(\chi,\lambda)$ is the dimensionless growth rate of the disturbance and is a function of the viscosities ratio λ and the dimensionless wave number χ (Tomotika 1935).
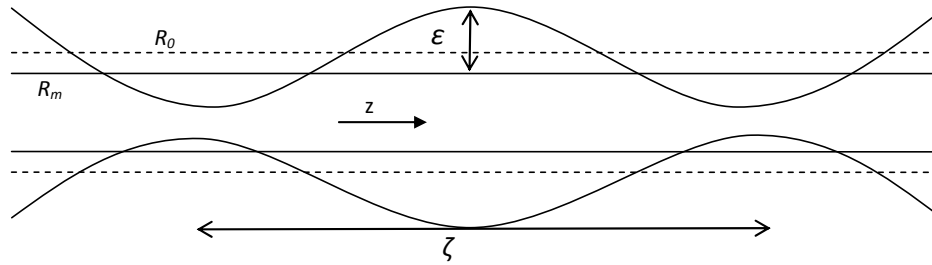

Figure 5.30. Sinusoidal disturbances present on the surface of a viscous cylinder embedded in a quiescent viscous fluid matrix.

At first, disturbances of all wave-numbers χ (or wave-lengths ζ) are present, and depending on the viscosities ratio, one disturbance, χ_m (and its corresponding growth rate Ω_m), will become dominant causing the breakup of the cylinder when its amplitude equals the mean radius, i.e., $\varepsilon_b = R_m = \sqrt{2/3}\,R_0$ (Raleigh 1879; Tomotika 1935; Elmendorp 1986). From Eqs. (5.4) to (5.6), the time for breakup t_b for a Newtonian thread in a Newtonian quiescent matrix can be calculated as:

$$t_b = \frac{1}{q}\ln\left(\frac{\varepsilon_b}{\varepsilon_0}\right) = \frac{1}{q}\ln\left(\frac{0.82\,R_0}{\varepsilon_0}\right) = \frac{\mu_1\,R_0}{\sigma\Omega_m}\ln\left(\frac{10^{23}\sigma R_0^2}{T}\right), \qquad (5.7)$$

where Ω_m is the growth rate of the amplitude of the dominant perturbation. The values of χ_m and its corresponding dimensionless growth rate Ω_m depend only on the viscosities ratio and can be obtained graphically from Fig. 2.7 in Elmendorp (1986). Considering that each spherical drop with radius R_d created after the breakup comes from the division of the initial cylinder with radius R_0 into smaller identical cylinders of length ζ, then, the radius of the resulting drops can be determined from conservation of volume, resulting in:

$$R_d = R_0\left(\frac{3\pi}{2\chi_m}\right)^{\frac{1}{3}}; \qquad (5.8)$$

that is, it is only a function of the dimensionless wave number (or the viscosities ratio) and R_0.

The breakup of a deformed drop after the cessation of the flow is mainly via capillary pinch-off (either necking or end-pinching), for breakup via capillary instabilities it is necessary to reach extremely high elongation ratios —depending also on the viscosities ratio, $L/r_0 \sim \mathcal{O}(15)$, for $\lambda \sim \mathcal{O}(10^{-2})$— because the length of the cylinder must be greater than its cross-sectional circumference (since the amplitude ε of the perturbations grows up only when $\zeta > 2\pi R_0$). Even when the drop is a long thread, the occurrence of

capillary instabilities is not guaranteed. The time-scale for developing the neck due to the interfacial tension is shorter in comparison with that needed for the development of the capillary instabilities, and the end-pinching effect reduce the length of the cylindrical thread and the probability for a perturbation to develop. For this reason, even when the drop has formed a long thread, it will breakup by end-pinching, unless the elongation ratio is very large. Figure 5.29 is a set of time-lapse photos of the breakup process of a very elongated drop, $L/r_0 = 11$. This sequence shows that the degree of elongation is not high enough for the occurrence of breakup via capillary instabilities, because the cylindrical thread disintegrates before the capillary instabilities became dominant.

At the moment the flow is stopped, see Fig. 5.29c, the cylindrical middle part has a radius $R_0 = 1.12 \times 10^{-4}$ m. The interfacial tension of the system is $\sigma = 0.0027$ N/m, the viscosity of the external fluid is $\mu_1 = 5.1$ Pa $\cdot$ s and the temperature is $T = 25°C = 298.15$ K. With a viscosities ratio $\lambda = 0.012$, and from Fig. 2.7 in Elemndorp (1986), the corresponding values of the dimensionless wave number and the dimensionless rate of growth are: $\chi_m = 0.41$ and $\Omega_m = 0.54$. Thus, using Eq. (5.7), the estimated time needed for breakup via capillary instabilities is $t_b \approx 9$ s, and from Eq. (5.8) the radius of the resulting droplets should be around $R_d = 0.25$ mm.

According to Fig. 5.29, the complete disintegration of the deformed drop took only about 4.4 s; that is, half the time t_b; and during this short period of time the instabilities will not fully develop. The perturbations became present at $t = 2.6$ s after the flow cessation, and its amplitude did not grow sufficient to cause the breakup of the cylindrical thread; see Fig. 5.29f. By the time they are evident at $t = 3$ s, as in Fig. 5.29g, the second end-pinching process is almost complete and the pointing ends of the residual cylinder contributes to the formation of the bulbous extremes. This bulbous part accelerates the growth of the neck that initially was formed by the capillary instability and the last remaining part of the cylinder is finally divided in two drops, as shown Fig. 5.29h. Nevertheless, the smaller "daughter" drops created by end-pinching have radii $R_d' = 0.26$ mm, comparable to the value predicted by capillary instabilities.

Deforming matrix.

The stability of a thread in a flowing matrix is more difficult. For instance, under simple shear flow the perturbations may be swept away so its effect will be damped out before being able to cause the thread breakup; see Fig 5.31 (Tomotika 1936; Elemendorp 1986). Mikamy (1975) and later Khakhar and Ottino (1987) extended the theory for breakup of an infinitely long Newtonian cylinder in a quiescent matrix to cylinders in general linear flows and showed that the presence of flow has a stabilizing effect on the thread. For a thread being elongated by a deforming fluid matrix, the wavelengths are continuously stretched, hence at any moment another disturbance wavelength becomes dominant and the breakup of
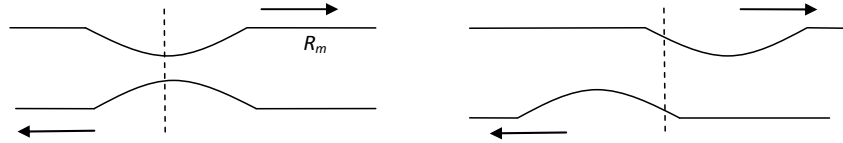
Fig 5.31. The perturbations present in the cylinder are swept away due to the flow present around the cylinder.

the threat is postponed when compared to a thread in a quiescent matrix. Breakup occurs as soon as the amplitude of a disturbance is greater the mean thread radius R_m that continuously decreases in time. In hyperbolic extensional flow, the time for breakup increases slowly with the capillary number (Khakhar and Ottino 1987) :

$$t_b \sim \log(Ca). \tag{5.9}$$

For simple shear flows, the results depend on the initial orientation angle of the thread β_0 in the flow field. The time for breakup is given by:

$$(1 + c\, t_b) \sim (c\, Ca)^\nu, \tag{5.10}$$

where $c = 2 \tan \beta_0$, β_0 is the initial orientation angle of the threat, and $\nu > 0$ (Khakhar and Ottino 1987). The main idea is illustrated in Fig. 5.32. All disturbances with initial wavelengths ζ or dimensionless wave numbers χ, evolve in time. At the same time the wavelengths are stretched and the radius of the cross section is thinned, the amplitude ε of the dimensionless wavelength χ first damps then grows and finally dams again. Breakup is achieved when the amplitude of a disturbance intersects with the continuously decreasing mean threat radius (Tjahjady and Ottino 1991; Janssen and Meijer 1993).

Figure 5.32. Magnification of the disturbances and reduction of the mean radius in a cylinder immersed in a linear flow. The dashed line represents the dimensionless mean radius of the cylinder and the full lines represent the growth of the amplitude of the dimensionlees wave number. The intersection gives the breakup point, occurred at the breakup time t_b. (Tjahjady and Ottino 1991).

5.2.2 High viscosities ratio

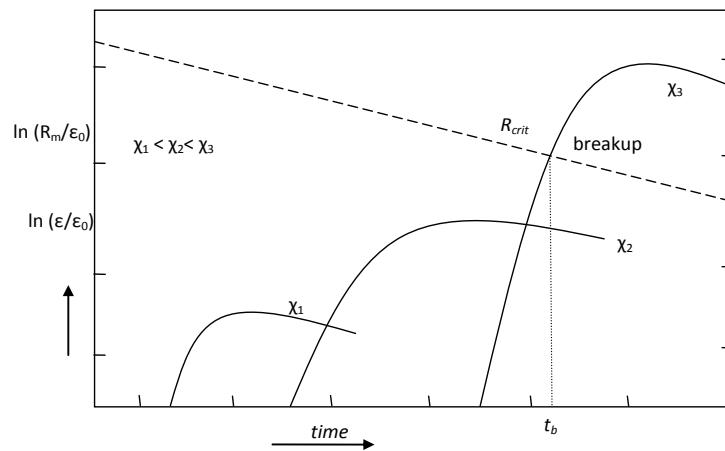For highly viscous drop fluids, with respect to the matrix one, the system evolves differently from cases where the drop viscosity is comparable to that of the matrix or lower. The dynamic of drop deformation under such conditions was first studied by Taylor (1934), who reported the main features of those systems. Taylor main conclusions are: (*i*) for a viscosities ratio high enough, the simple shear flow is unable to cause the drop breakup; (*ii*) the steady state deformation is limited and inversely proportional to the viscosities ratio $D_T = 5/4\lambda$ (Taylor 1934); and (*iii*) the steady state orientation tends to zero $\theta \approx 0°$. Later, Rumscheidt and Mason (1961) carried out more detailed experiments with high viscosities ratios and reported an oscillatory response to start up experiments in simple shear flow. This oscillatory behavior was firstly studied theoretically by Cox (1969) —at least for the case of small drop deformations— providing analytical expressions to evaluate the timeless evolution of a drop with high viscosities ratio that is abruptly subjected to a simple shear flow. The equations provided by Cox for $\lambda \gg 1$ expresses the Taylor´s deformation parameter as

$$D_T = D_S[1 - 2\, e^{-20\dot{\gamma}t/19Ca\lambda}\, cos(\dot{\gamma}t) + e^{-40\dot{\gamma}t/19Ca\lambda}\,]^{\frac{1}{2}}. \tag{5.11}$$

And the steady state deformation D_S given by:

$$D_S = \frac{5(19\lambda + 16)}{4(1 + \lambda)\sqrt{(19\lambda)^2 + (20/Ca)^2}}. \tag{5.12}$$

The orientation of the longest axis of the ellipsoidal drop is given by:

$$\theta' = \frac{\pi}{2} + \frac{1}{2}tan^{-1}\left(\frac{19\lambda[\, e^{-20\dot{\gamma}t/19Ca\lambda}\, cos(\dot{\gamma}t) - 1] + (20/Ca)e^{-20\dot{\gamma}t/19Ca\lambda}\, sin(\dot{\gamma}t)}{(20/Ca)[\, e^{-20\dot{\gamma}t/19Ca\lambda}\, cos(\dot{\gamma}t) - 1] + 19\lambda e^{-20\dot{\gamma}t/19Ca\lambda}\, sin(\dot{\gamma}t)}\right), \tag{5.13}$$

with θ' given in rad. In this case, the steady state orientation can be obtained from Eq. (5.13) by letting $\dot{\gamma}t \rightarrow \infty$. Those equations describe an oscillatory damped behavior were the damping of the oscillations is proportional to $1/(\lambda\, Ca)$ in the dimensionless form, or in dimensional terms proportional to $\sigma/\mu_0 r_0$.

Even when those equations were derived for simple shear flows ($\alpha = 0$), and are not accurate at all, they show the global behavior of the high viscosity ratios systems and can be used as a benchmark for the qualitative behavior of the types of flow studied in this work. Figures 5.32 to 5.35 are a comparison of the predictions of Cox (1969) (that appears to be the only analytical formulas so far) and the experimental results for the flow of $\alpha = 0.03$, the flow closest to simple shear. The comparisons are done with the purpose of

showing the general characteristics in drop deformation under high viscosities ratio conditions. Figs. 5.33 and 5.34 are plots of the dimensionless time evolution of the deformation and the orientation in a system with $\lambda = 16$ and different capillary numbers.

Figure 5.33. Deformation as a function of the dimensionless time for a viscosities ratio of $\lambda = 16$. Left side corresponds to the theoretical prediction of Cox (1969) for $\alpha = 0$ and the right side to experimental results for $\alpha = 0.03$.

Figure 5.34. Deformation as a function of the dimensionless time for a viscosities ratio of $\lambda = 16$. Left side corresponding to theoretical prediction of Cox for $\alpha = 0$ and the right side corresponding to experimental results for $\alpha = 0.03$.

Fig. 5.35 is a parametric plot of the deformation D_T vs the orientation angle θ. It shows the timeless evolution of the drop toward its equilibrium conditions and it can be seen that as Ca increases the drop starts to present cycles that increase in number as Ca rises.

Looking at those figures some characteristics of these systems can be noted:

(a) For large capillary numbers, the steady state conditions are reached after a damped oscillatory transient behavior.

(b) The steady state deformation D_T becomes independent of the capillary number when this is large enough, see Fig. 5.33.

(c) The steady state orientation θ always depends on the capillary number and approaches to zero as Ca increases, see Fig. 5.34.

(d) The maximum amplitude of the oscillations in the transitory state depends on Ca, but its frequency does not.

(e) The number of cycles needed for the drop to reach the stationary states increase with Ca. see Fig. 5.35.

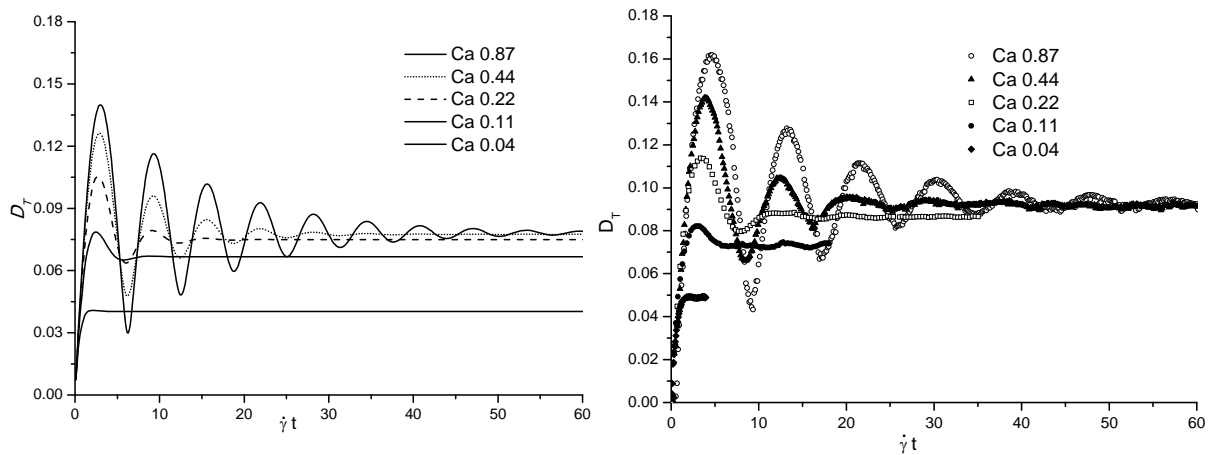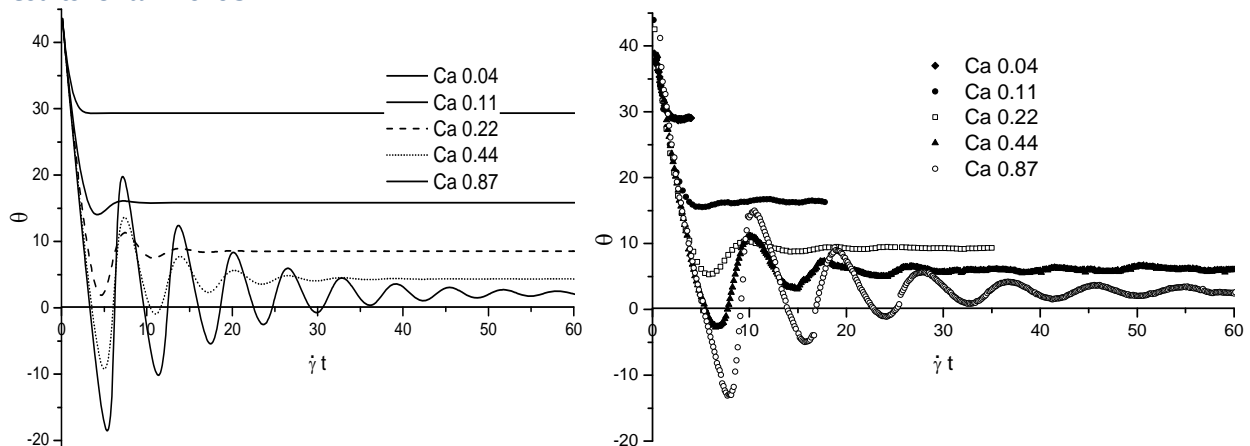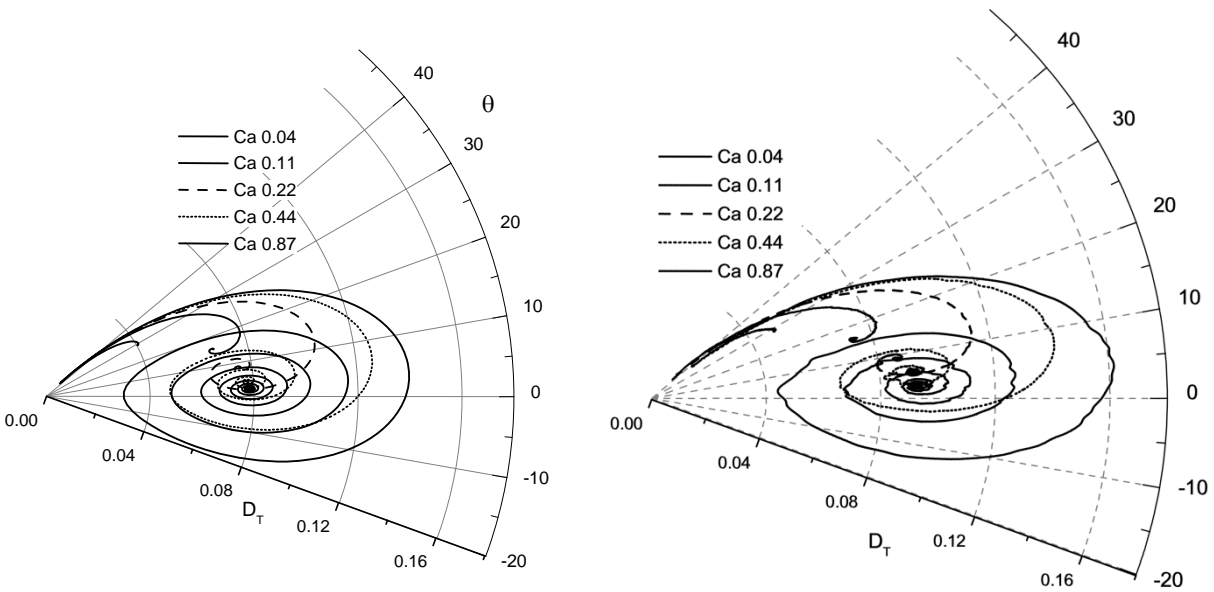**Figure 5.35. Deformation as a function of the dimensionless time for a viscosities ratio of $\lambda = 16$. Left side corresponds to theoretical prediction of Cox (1969) for $\alpha = 0$ and the right side corresponding to experimental results for $\alpha = 0.03$.**

In general and for the system of a low viscosities ratio, the steady states are reached monotonically, and as long as subcritical conditions are maintained, the steady state deformation and orientation depend on the value of Ca. For these systems, the stress field imposed by the external flow is mainly balanced by the interfacial tension, by modifying the drop geometry. For these systems, the vorticity present does not have a significant contribution in stabilizing the drop. However, when $\lambda \gg 1$, the monotonic transient and the dependence of the stationary deformation D_T on Ca are rapidly lost. Unlike systems with low viscosities ratio, the evolution to the steady states is no longer monotonic for high Ca, and stationary conditions are reached after the observed transient oscillatory behavior, as shown in Figs. 5.33 to 5.35. The steady state orientation decreases toward zero as Ca increases and the steady state deformation becomes independent from Ca, reaching the maximum value allowed by the viscosities ratio λ and the type of flow α.

Blawzdziewicz *et al*., (2002, 2003) performed a linear stability analysis of the time-dependent form of the equations describing the deformation of a drop under the effects of an external flow field. Even when this analysis was done for flow fields closer to elongational, they established some points which have a close resemblance to those observed in the experiments. They showed that the deformation equations have, at least, two branches of stable solutions that merge and disappear at critical lines, L_c, drawn where turning-point bifurcations occur. Figure 5.36 schematizes the ideas of stability studied by Blawzdziewicz *et al*., (2003). These two branches (the mechanisms in which the stationary drop shape is achieved) are: (1) drop deformation, due to the interfacial tension stresses and characterized by a low rotation of the drop and (2) drop rotation, due to the vorticity of the external flow and characterized by a low deformation. The limits of the domains of these solutions depend on the viscosities ratio λ, the type of flow α and the capillary number *Ca*. From that point of view Blawzdziewicz *et al*., (2002, 2003) and Young *et al*., (2008) reached the same conclusions than previous experimental works. Considering the instability of the systems as synonym of breakup condition and the stability as the existence of steady states, the system will always have a stable solution when the viscosities ratio exceeds a critical value λ_c, that decreases with α. With λ high enough to ensure the stability, the branch will only depend on the *Ca*, if it is above certain value, the stabilizing mechanism will be the rotation, below that value the mechanism will be the deformation.
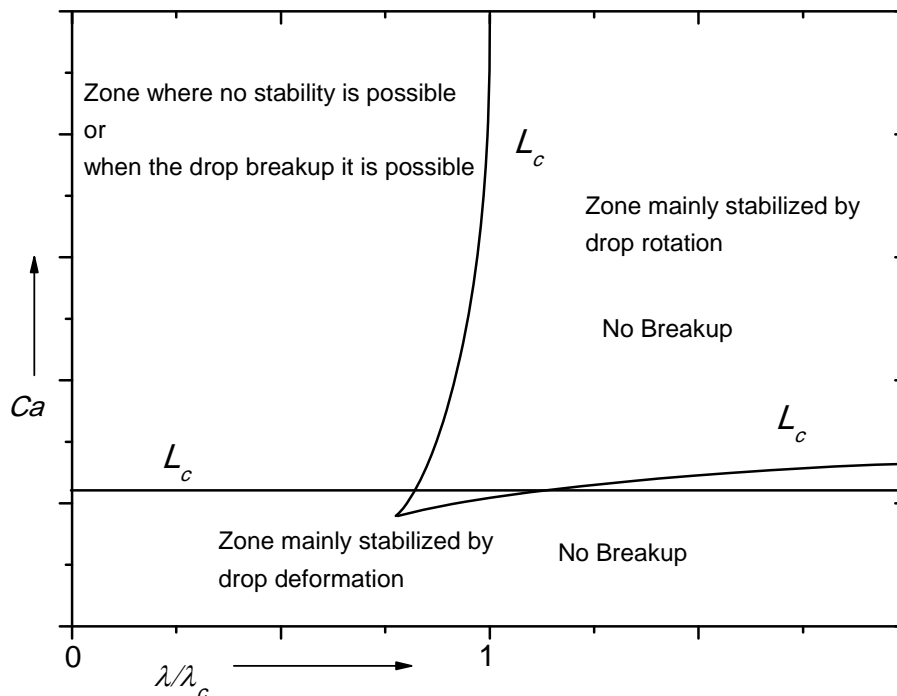

Figure 5.36. Stabilizing mechanisms in drop deformation as function of the viscosities ratio and the capillary number. This figure only represent a typical graphic, the lines separating the stable zones may vary depending on the type of flow.

Drop deformation

The systems with $\lambda \gg 1$ behave different from those with $\lambda \ll 1$. As the viscosity of the drop is increased, it starts to behave more as a rigid body than as a fluid particle. Taking the extreme case of a drop with $\mu_0 \to \infty$, immersed in any flow with vorticity different from zero (simple shear flow for example), it is more or less clear that the particle would not suffer any deformation but only rotation. This behavior would be the same despite the magnitude of shear rate applied; increasing the shear rate would only make the particle to spin faster but never to deform. Hence, the role played by the vorticity increases with λ, whereas the deforming part diminishes. This was first noted by Taylor (1934); he realized that in simple shear flows the contribution of the vorticity becomes dominant enough to inhibit the breakup of drops when $\lambda \approx 4$. Above this value, the drop only attains a small deformations determined only for the viscosities ratio λ and independent of the *Ca* applied.

Then, with λ fixed, the other parameter governing the maximum possible steady state deformation is the parameter of type of flow α. This parameter determines the capacity to induce deformations in the drop. When the drop is deformed under a flow field with vorticity, its particles are continuously extended and at the same time rotated; being the extending part the responsible for the deformation. Consequently, the maximum deformation in steady state depends on the competition between those two components of the flow. The vorticity induces a rotation that causes a continuous redistribution of the particles inside the drop respect to the directions of maximum extension, and depending on the quantity of vorticity present in a flow field, this will be more o less able to cause a reorientation of these particles before they are extended by the deforming component, i.e. the flow inside the drop will be more prone to form a vortex as the vorticity and viscosity increase. In this manner, a flow with zero vorticity can always accomplish the breakup of a drop (no matter the viscosity ratio), given that the reorientation of the particles is nil, and therefore they remain all the time under a continuous deformation that eventually derives in breakup. For flows with vorticity different from zero, there are limits on the viscosity ratios at which they are able to cause the breakup because the contribution of the vorticity (seen as the capacity of particle reorientation or the tendency of the drop to form vortex), increases with λ. Thereby, in a flow with the parameter α fixed, the steady state deformation reduces as λ increases, and for a viscosities ratio λ fixed this steady deformation increases with the flow type parameter α that characterizes the flow field.

The characteristics mentioned above roughly describe the behavior of high viscosity ratio systems. In general, the study of the dynamics of drop deformation is a difficult problem because of the non-linear coupling of the processes involved, and still remains open. Due to this non-linear character, a formal theoretical analysis is not a trivial task and a detailed mathematical description is out of the scope

of this work. So, in order to understand the general role played by the principal factors in the drop deformation, the following descriptions are used assuming sometimes a linearized behavior. However, this are only made with the specific purpose of simplifying the phenomena and having an easier description for its study, and may not have any general character.

In the next lines, the reference plane used is the *x-y* plane with the origin at the center of the drop and where any particle position can be described by a vector $\hat{\mathbf{r}}$ of length *r* and angular orientation β, the angle respect the *x*-axis; see Figure 5.37.
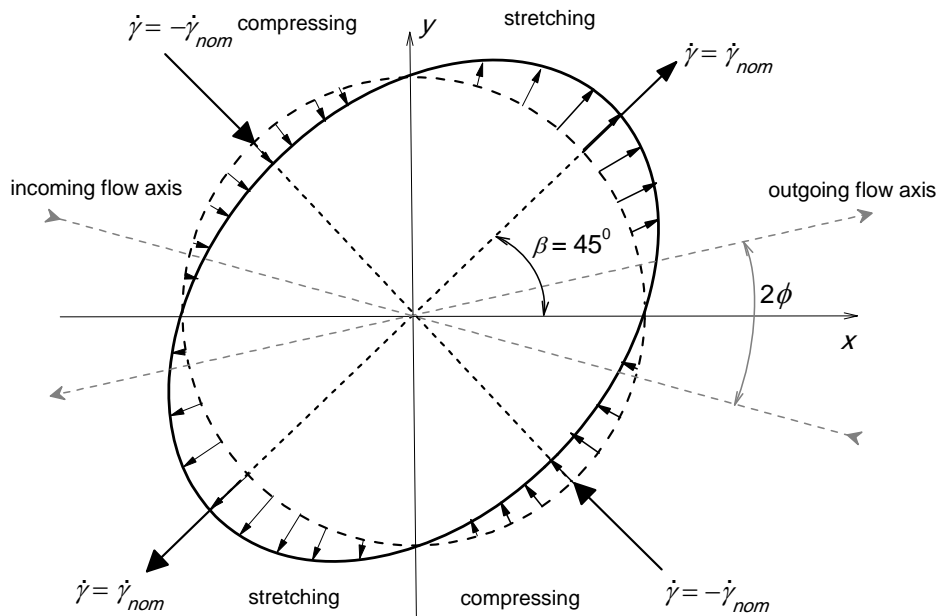
Figure 5.37. Regions of stretching and compression in the flow field. The principal axes of deformation are rotated 45° respect to the reference axes in the *x-y* plane. The magnitude of the rate of deformation varies as function of the angular position, achieving its maximum values at the position of the principal deformation axes.

Summarizing, the three main effects governing the drop behavior are: (*i*) the drop relaxation; (*ii*) the drop deformation; and (*iii*) the drop rotation. The first one depending on the properties of the fluids and the physical characteristics of the drop and the two last depending both on the properties of the fluids and on the of type of flow field.

i.   **The relaxation of the drop.** This is the process by which the drop shape is adjusted by the effect of the interfacial tension σ, in response to changes in the outer pressure field, contracting the drop to a new equilibrium geometry. It acts as an elastic membrane that as soon as the pressure out of the drop is modified so does the geometry. However, this modification is not instantaneous; it has

a time-scale is given by: $t_\sigma = (\mu_0 + \mu_1)r_0/\sigma$, expression that takes in count the viscosities of the drop and the matrix, the drop radius and the interfacial tension.

The relaxation of the drop involves an internal flow, required by the reconfiguration of the geometry; these flows are caused by the pressure gradients due to the interfacial tension. Very viscous fluids, as well as weak interfacial tensions, or large drops will cause the internal fluid to retract slowly, and, therefore, the time taken by readjustment of the drop shape will be long.

ii.   The deformation of the drop, caused by the symmetric part of the velocity gradient tensor. The magnitude of the rate of deformation it is not constant over the drop surface, it depends on the angular position of the particles inside the drop, i.e., $\dot{\gamma} = \dot{\gamma}(\beta)$ (while the rotation does not). The principal directions of deformation are rotated 45° respect to the x-y plane. The axes of maximum rate of elongation are oriented at $\beta = 45°$ and $\beta = 225°$ while axes of maximum rate of compression are oriented at $\beta = 135°$ and $\beta = 315°$; see Figure 5.37. The particles inside the drop, placed in the stretching regions, $0° < \beta < 90°$ and $180° < \beta < 270°$, are advected (pulled from the center of the drop) while those in the compression regions $90° < \beta < 180°$ and $270° < \beta < 360°$, are pushed toward the center of the drop, with an initial spherical form being transformed into an ellipsoid. The time scale for the deformation is that of the flow, given by the shear rate imposed, $t_{flow} = 1/\dot{\gamma}_{nom}$.

iii.   The rotation of the drop is caused by the vorticity tensor, the anti-symmetric part of the velocity gradient tensor. At the same time that the drop deforms it also rotates with an angular velocity proportional to the shear rate applied. The proportionality is a function of the type of flow $\omega \propto \dot{\gamma}_{nom}f(\alpha)$, with $f(\alpha)$ denoting the proportionality of the angular velocity ω to the shear rate applied as function of the parameter of type of flow (for $\alpha = 1$ the vorticity is zero and therefore the angular velocity $\omega = 0$. For $\alpha \neq 1$, ω is different from zero but always varying in the same proportion with $\dot{\gamma}_{nom}$).

The time-scale for the rotation is also that of the flow, $t_{flow} = 1/\dot{\gamma}_{nom}$, but with another important time-scale to take into count: the diffusion of vorticity time-scale. The rotation applied at the interface between the drop and the outer fluid is eventually transmitted (or diffused) to the inner particles. The time scale for this transmission is the characteristic time for the diffusion of the vorticity given by $t_v = r_0^2/v_0$, where v_0 is the kinematic viscosity of the fluid of the drop. This time scale represents the time spent for the vorticity to diffuse from the interface into the interior of the drop. For large values of v_0, or small drops, this time of diffusion is short which means that at the moment the particles on the interface starts to rotate, the vorticity diffuses so fast to the interior that the particles inside the drop start to rotate almost at the same time with nearly the same angular velocity.

The dynamics of the deformation comes from the interplay of the deformation and the rotation. Fluid particles placed at about $\beta = 45°$ are stretched with the maximum rate of deformation and as the angular position changes, so does the magnitude of this rate, decreasing from $\dot{\gamma} = \dot{\gamma}_{nom}$ at $\beta = 45°$ to $\dot{\gamma} = 0$ at $\beta = 0°$, where all particles are not stretched nor compressed. Then at $\beta = 0°$, the direction of the shear rate is reversed, changing from stretching to compression with a magnitude that rises from $\dot{\gamma} = 0$ at $\beta = 0°$ to $\dot{\gamma} = -\dot{\gamma}_{nom}$ at $\beta = -45°$ (or 315°), where the fluid particles are compressed with the maximum rate of deformation. In this way, the shape of the drop changes from spherical to ellipsoidal. But besides this deformation there is a rotation due to the high viscosity of the drop fluid, with the diffusive time for the vorticity being short, meaning that the particles inside the drop start to rotate almost at the same with nearly equal angular velocities.

Since a rotation is nothing but a change in the angular orientation, their position with respect to the principal axes of deformation changes, while the magnitude of its velocity of deformation also does as well. Supposing a clockwise rotation, initially the particles placed at $\beta = 45°$ are being advected from the center of the drop with the maximum velocity, $\dot{\gamma}_{nom}$, but as they rotate and β approaches to 0° their velocity of deforming is reduced and eventually when they are at $\beta = 0°$ this velocity is 0. As the rotation continues, the velocity of deformation of those particles increase, but in the opposite direction; now they are being compressed, and they are no longer pulled but pushed to the drop center. In a similar way, the particles located in an angular position corresponding to compression will change with the rotation to a position of stretching.

Basically, the mechanism that generates the experimental behavior is as follows: the process of elongation and contraction initializes at the moment of the start of the flow, are out of phase for the same fluid particle, and is present as long as the flow is maintained. The time-response of the drop it different, developing oscillations on its shape at the beginning of the flow (or transitory) but keeping a stable shape in the long term (or steady states).

5.2.2.1 Steady states

The steady state deformation can be divided in two main behaviors:

(a) A steady state deformation independent of Ca, only determined by the type of flow α and by the viscosities ratio λ.

(b) A steady state deformation that depends only on the Ca applied, present for small values of Ca.

In order to describe both behaviors, the steady state deformation independent from the capillary number is described first.

Steady state deformation independent from Ca

With α and λ fixed, if the steady state deformation reached by the drop is the same, regardless the value of Ca, it must be only due to the deformation and rotation imposed by the flow. Then, it can be analyzed without taking in count the interfacial tension contribution. During this deformation, the drop attains an elliptical shape with the major semi axis $L > r_0$ and the minor semi axis $B < r_0$ (see Fig. 5.38). Under steady state conditions, the drop shape does not change in dimensions nor orientation and therefore the length r of the vector $\hat{r}$ that follows, say Particle A through time, depends only on the angular position and has specific values at specific angles, $r = L$ at $\beta = 0°$ and $\beta = 180°$ and $r = B$ at $\beta = 90°$ and $\beta = 270°$. But it can be noticed that $L = B + \Delta r$, where Δr is the total change in the length of r when the particle covers an angular displacement $\Delta\beta = \pi/2$. Δr is the sum of the instantaneous increments in the distance r while the particle is passing through an stretching or compression region $\Delta r = \sum dr_\beta$, with dr_β proportional to the instantaneous length $r(\beta)$ times the shear rate $\dot{\gamma}(\beta)$ times the time spent by the particle in that angular position: $dr_\beta \propto r(\beta)\dot{\gamma}(\beta)\Delta t$. It is to say, the total elongation Δr_{elong} (or contraction Δr_{contr}) depends on the magnitude of the shear rate and on the time spent by the particles in the stretching (or compression) regions. Given that the time in the deforming regions (stretching or compression) depends on the angular velocity in the form $\Delta t = \Delta\beta/\omega$, and that the particles are rotating at almost the same angular velocity, then $\Delta r_{elong} \propto r(\beta)\dot{\gamma}(\beta)\Delta\beta/\omega$ and $\Delta r_{contr} \propto r(\beta) - \dot{\gamma}(\beta)\Delta\beta/\omega$ or $\Delta r_{elong} = -\Delta r_{contr}$ resulting in the stationary drop shape.
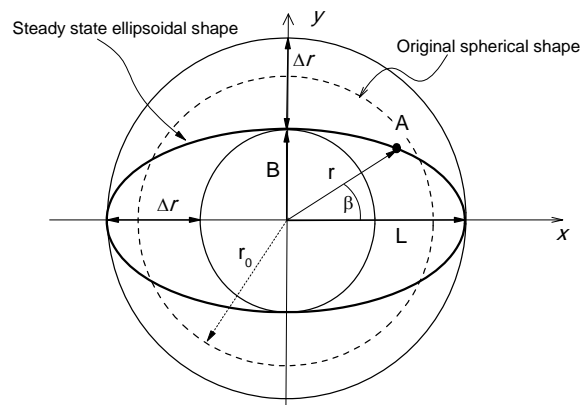
Figure 5.38. Steady state ellipsoidal shape of the drop due to the elongation suffered in the stretching region and the contraction suffered in the compressing region. The magnitude of the elongation Δr is exactly the same to that in contraction $-\Delta r$. The outer circumference has as radius the longest semi axis L and the inner circumference has as radius the shortest semi axis B.

Now, the total extension appears to be function of the shear rate, $\Delta r \propto r(\beta)\dot{\gamma}(\beta)\Delta\beta/\omega$, but the magnitude of the angular velocity also depends on the shear rate and on the type of flow and is assumed

to have the form $\omega = \dot{\gamma}_{nom} f(\alpha)$. Besides, the distribution of the shear rate in the perimeter of the ellipsoid is assumed to be only function of the angular position and proportional to the shear rate applied in the form $\dot{\gamma}(\beta) = \dot{\gamma}_{nom} f(\beta)$. Then, $\Delta r \propto r(\beta)\,\dot{\gamma}(\beta)\,\Delta\beta/\omega = r(\beta)\,\dot{\gamma}_{nom}\,f(\beta)\,\Delta\beta/(\dot{\gamma}_{nom}\,f(\alpha))$ or $\Delta r \propto r(\beta) f(\beta)\,\Delta\beta/f(\alpha)$ which can be written as $\Delta r \propto f_1(r, \alpha, \beta)\,\Delta\beta$.

In this way, it can be seen that the steady state deformation does not depend on the shear rate applied, and is only a function of the type of flow (for λ fixed) that also determines both the distribution of the shear rate on the perimeter of the ellipsoid and the proportion of the angular velocity to the shear rate applied. An increase in the shear rate would imply a large velocity of elongation and contraction but with these increase there is also a proportional rise in ω reflected in a lower time in the regions of stretching and compression and hence the steady state deformation remains constant. The only effect of this increase is a drop spinning faster.

Steady state deformation dependent on the Ca

The equilibrium deformation, independent from Ca, occurs only when the contribution due to the interfacial tension on the drop deformation is not taken into account; as mentioned before, this is only possible for high Ca values. For low Ca, the steady state deformation depends on the applied Ca, this behavior being the result of the time-scales of the deformation mechanisms. The relaxation time-scale (due to interfacial tension) is given by $t_r = \mu_0(1 + \lambda)r_0/\sigma$, which is the time spent by the interfacial tension to modify (retract) the drop geometry. On the other side, the time scale for the deformation (and rotation) by the flow field is given by $t_f = 1/\dot{\gamma}_{nom}$: the time for the elongation (caused by the stretching) and for the contraction (caused by the rotation). Now, the capillary number defined as $Ca = \mu_1 \dot{\gamma} r_0/\sigma$ can be written in the form: $Ca = (t_r/t_f)\lambda/(1 + \lambda)$ or

$$\frac{Ca(1 + \lambda)}{\lambda} = \frac{\text{time for retraction via interfacial tension}}{\text{time of retraction via the flow field}}, \tag{5.14}$$

i.e., a relationship between the characteristic time of relaxation and the characteristic time of the flow. This expression is valid when $\lambda \gg 1$, because the diffusion of the vorticity and, in consequence, the reorientation of the particles (and the retraction via rotation) also depends on ν_0. This relationship means that when $Ca \ll 1$ the rotation of the drop is so slow that the time for the particles to be reoriented is long compared with the time of relaxation. Given this time, the particles inside cannot change of regions of deformation (stretching to compressing) fast enough, then they remain in the same angular position being elongated or contracted for long periods of time. Despite this, an ellipsoid does not arises because it is contained by the interfacial tension with the consequent change in the drop geometry proportional to the

stresses applied by the flow, and in that way the steady state deformation depends on the Ca applied as in the case of low viscosities ratios. When $Ca \gg 1$ then, $t_r \gg t_f$, the time taken by the interfacial tension to change the drop shape becomes slow compared with the time taken by the deformation and rotation to do the same, i.e., the drop particles are rotated (reoriented) so fast that the deformation caused by the flow is canceled by the rotation in the same proportion, and the interfacial tension does not plays any roll in containing that deformation. In this way, the steady state deformation is independent of Ca, and reaches the maximum possible.

The maximum (critical) value of Ca at which the deformation of the drop still depends on Ca is a function of the type of flow, the properties of the fluids, and the drop size, apparently. Now, when $Ca \approx 1$, all characteristics times are of the same order; thus, both contributions are important. This is seen more clearly in the transitory where the drop deformation time curves present overshoots in the deformation parameter D_T and undershoots in the orientation angle θ, but after the transient, the steady state deformation still depends on Ca.

Figures 5.39 to 5.41 present the steady state deformation and orientation values obtained with a TRM. At this point, it is necessary to present a note of caution about the experiments carried out with the flow types $\alpha = 0.05$ and $\alpha = 0.03$. These results behave in an unexpected way, apparently due to effects of the large size of the drops used. The data used for the following discussion are under conditions (explained later in the drop size effects section) considered to be free of "size" effects.

For high viscosities ratio systems and for very small capillary numbers, the steady state deformation depends only on the shear rate applied; for large Ca it depends only on the viscosities ratio λ and on the parameter of the type of flow α values. The steady state orientation, on the other hand, always depends on the applied capillary number, and unlike low viscosities value systems, it is not restricted to the value of the angle ϕ of the outgoing axis of the flow field. Actually, the observed angles attain values below ϕ relatively fast, at very low capillary numbers, when the drop becomes oriented with the x-axis as Ca increases.

Figures 5.39 to 5.41 present each a sequence of photos of the steady states, measured for the three types of flows and different capillary values. The final shape attained by the drop, as well as its orientation, can be observed in those figures; the photos of drops corresponding to the higher capillary values present the same deformation but with different orientation angles. Tables 5.1 to 5.3 present values of Ca and the corresponding parameters D_T and θ of each photo on each image. For a flow with $\alpha = 0.13$, the steady state deformation reached is $D_T = 0.13$. For $\alpha = 0.05$ this value decreases to $D_T = 0.10$ and for $\alpha = 0.03$ it drops to $D_T = 0.092$. These figures show that the Ca value at which the steady

deformation becomes independent from Ca or when the time scale of the flow turns dominant are $Ca \approx 0.5$ for $\alpha = 0.13$, and $Ca \approx 0.3$ for $\alpha = 0.05$ and $\alpha = 0.03$. The orientation angles present different values for each Ca, corresponding to the lowest θ to the highest Ca.

Figure 5.39. Steady state drop shape and orientation attained for different capillary numbers. The drop has a viscosities ratio of $\lambda = 16$ and is deformed under a flow field with $\alpha = 0.13$.

Table 5.2 . Steady state deformation and orientation values corresponding to Figure 5.39.

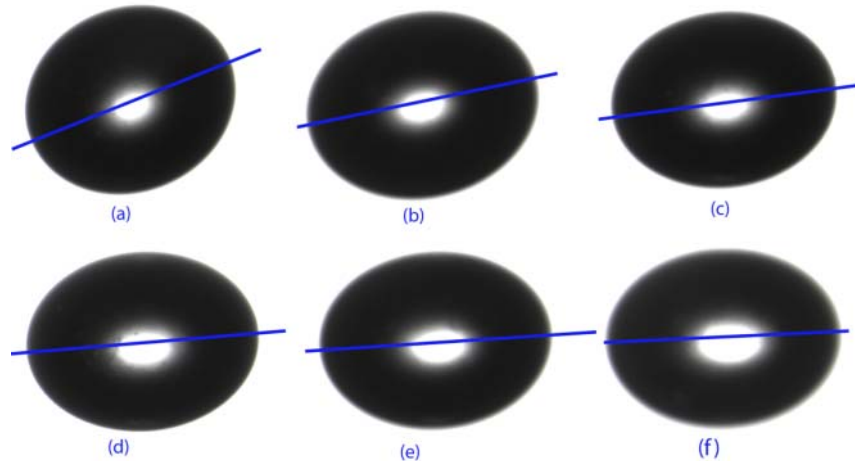|	(a)	(b)	(c)	(d)	(e)	(f)
Ca	0.08	0.2	0.4	0.6	0.8	1.2
D_T	0.075	0.11	0.125	0.13	0.13	0.13
θ	22.8^0	12^0	8^0	4.7^0	3.7^0	3^0

Fig 5.40. Steady state drop shape and orientation attained for different capillary numbers. The drop has a viscosities ratio of $\lambda = 16$ and is deformed under a flow field with $\alpha = 0.05$.

Table 5.3. Steady state deformation and orientation values corresponding to the Figure 5.40.

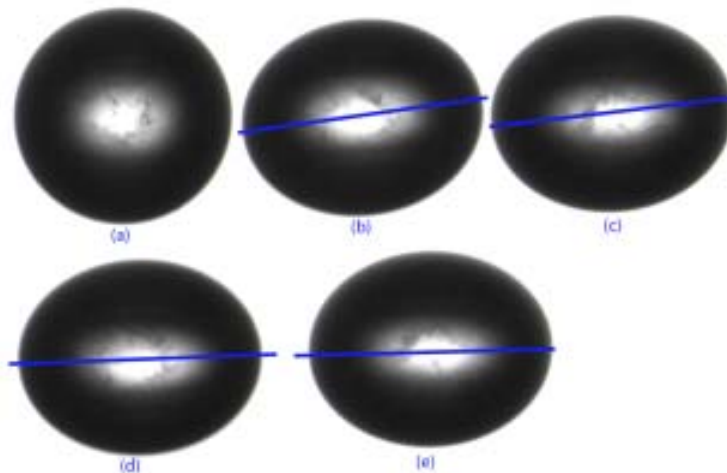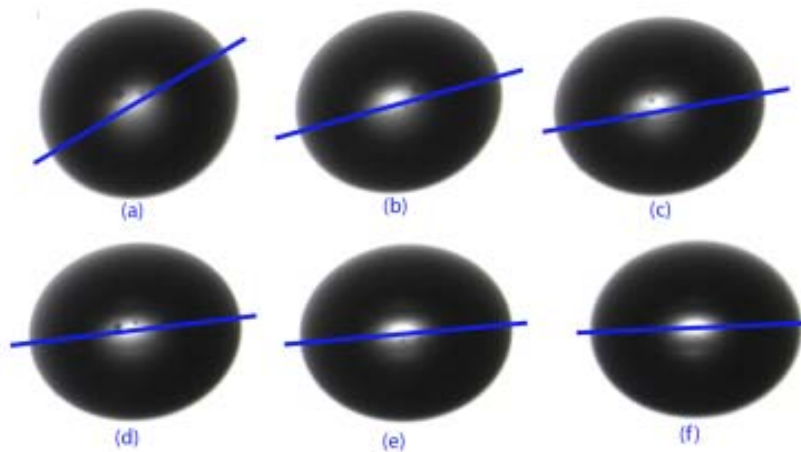|	(a)	(b)	(c)	(d)	(e)
Ca	0	0.26	0.5	1.0	1.2
D_T	0	0.09	0.10	0.10	0.10
θ	-	8.18^0	4.37^0	2.28^0	1.5^0

Figure 5.41. Steady state drop shape and orientation attained for different capillary numbers. The drop has a viscosities ratio of $\lambda = 16$ and is deformed under a flow field with $\alpha = 0.03$.

Table 5.4. Steady state deformation and orientation values corresponding to the Figure 5.41.

	(a)	(b)	(c)	(d)	(e)	(f)
Ca	0.04	0.11	0.22	0.33	0.44	0.87
D_T	0.05	0.07	0.08	0.09	0.092	0.092
θ	29^0	16.3^0	9.3^0	6.1^0	6^0	2.6^0

Figure 5.42 is a comparison of the steady state orientation angle as a function of the capillary number, for the flow types of this work and experimental data for $\alpha = 0.2$ from Bentley and Leal (1989b). The orientation does not appear to be very sensitive to the parameter of type of flow α. For the same capillary number, only small differences are observed in the steady state orientation, with the θ values a little higher for the most elongational flow ($\alpha = 0.13$). The plot shows that the angle also becomes independent from Ca but at higher values, $Ca > 1.75$, approaching the limit $\theta = 0°$ when $Ca >> 1$. This value seems to be common for all three flow types. In general, all three flow fields have the same qualitative behavior. In fact, the experimental data for the less elongational flows, $\alpha = 0.05$ and $\alpha = 0.03$, are in good agreement with the theoretical predictions of Cox (1969) for $\alpha = 0$. The discrepancies with respect to the angles for $\alpha = 0.2$ can be due to the fact that this flow field is capable of breaking the drop up; in other words, it is unable to produce an effective reorientation which inhibits the deformation.
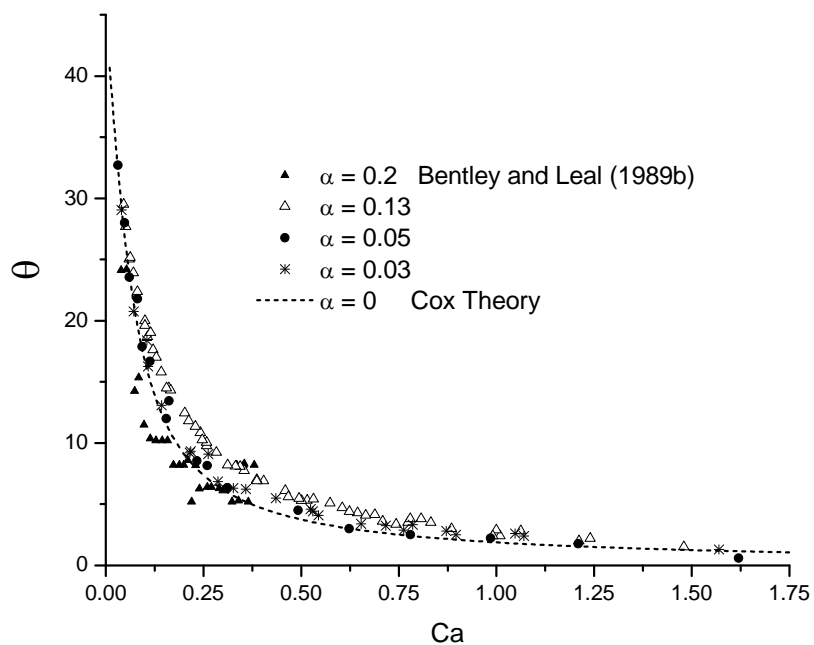
Figure 5.42. Steady state orientation achieved by the deformed drop under different capillary values for a viscosities ratio $\lambda = 16$. The orientation angle appears to have an asymptotic behavior toward $0°$ when $Ca \gg 1$. The dotted line is the steady orientation predicted by Cox (1969) and it has a remarkable coincidence with the experimental values for $\alpha = 0.05$ and $\alpha = 0.03$.

Figure 5.43 is a plot of the steady state deformation as function of the capillary number for different parameters of the type of flow and a viscosities ratio of the same order. The data for $\alpha = 0.13$, $\alpha = 0.05$ and $\alpha = 0.03$ belong to this work, while those for $\alpha = 0.4$ and $\alpha = 0.2$ are those of Bentley and Leal (1989b). Also the maximum steady state deformation for $\alpha = 0$ corresponding to $D_T = 0.085$ is shown (Rumscheidt and Mason 1961). The figure shows that for this value of the viscosity ratio, only flows stronger than $\alpha = 0.13$ are capable of breaking up drops, while flows with a parameter α lower than that only achieve moderate deformation, which remains constant regardless the Ca applied. As expected, with λ fixed, the only way to achieve higher deformations is with a stronger flow, i.e., increasing the flow type parameter α.

5.2.2.2 Transitory states

As mentioned before, the transient phase of systems with $\lambda \gg 1$ is well known to present a complex damped oscillatory behavior, but further than that, the detailed characteristics of such a particular response and its specific dependence on the properties of the fluids are barely known. Besides, since the earliest theoretical approach of Cox (1969) until numerical and experimental works nowadays, this oscillatory behavior has been only studied for simple shear flows given that until now there was not any device able to produce a flow field with constant and specific values of the parameter α different

from zero but close to simple shear. With that, most features of the transitory stages in flow fields other $\alpha = 0$ are still unknown. In this section, the transient response of a spherical drop, at rest to an impulsively started flow field different from simple shear flow, is described.
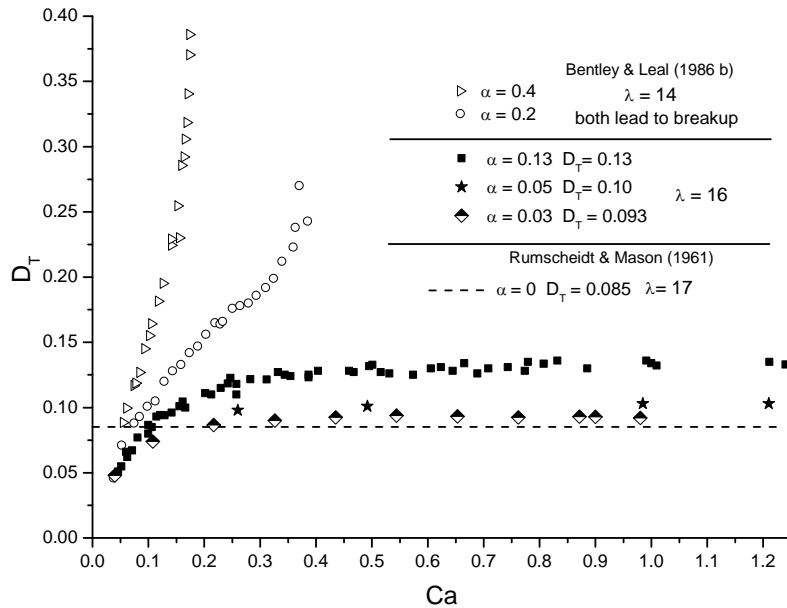

Figure 5.43. Steady state deformation achieved by the drop under different capillary values. Flow fields with $\alpha < 0.2$ are unable to cause breakup with this viscosities ratio instead the deformation becomes independent from Ca very fast and when $Ca \gg 1$ attains the limit value that only depends on the flow type parameter.

Drop oscillations

The drop shape oscillations come from the combined effects of deformation and rotation, that together with the initial spherical shape of the drop, cause an unbalanced state. Nevertheless, this unbalance is reduced slowly by the interfacial tension with the drop attaining its equilibrium shape or the steady state deformation.

When the flow is suddenly applied and the drop start to be elongated, this deformation begins to transform the drop into an ellipsoid. Those particles situated in the stretching region will be pulled away from the center of the drop and those in the compressing region will be pulled back to the center of the drop, generating the elongation of the drop in the stretching regions and a contraction in the compression ones. But at the same time, the drop is being rotated and the particles are continuously changing its angular position, passing from a stretching to a compression region and vice versa. Analyzing the path of two particles placed in the perimeter of the spherical drop, one particle placed in the point a at $\beta_a = 90°$ with a distance $r_a = r_0$ from the center of the drop, and the other particle placed in the point b at $\beta_b = 0°$

and with $r_b = r_0$ Fig. 5.44. When the flow starts and the drop begins to deform and rotate in the clock wise direction; these particles move from their original points, changing their angular position β and their distance r from the center. On one hand and given its position in the stretching region, the particle at a traces an elliptical path going away from the center of the drop and eventually when it rotates a $\Delta\beta = 90°$ reaches the position a' at $\beta_{a'} = 0°$. The distance from the center at that point is now $r_{a'} = r_0 + \Delta r_{a'}$. On the other hand, the particle at b is in the compressing region; therefore, it traces an elliptical toward the center of the drop. And because both particles are rotating at the same speed, when the particle at a reaches a' the particle at b reaches b', at $\beta_{b'} = 270°$, and with a distance relative to the center $r_{b'} = r_0 - \Delta r_{b'}$.

Now, Δr is the total displacement of the particles while they rotate 90°; $\Delta r = \sum dr_\beta$, with dr_β proportional to the instantaneous length $r(\beta)$, along with the shear rate $\dot\gamma(\beta)$ and the time spent by the particle in each angular position, $dr_\beta \propto r(\beta)\dot\gamma(\beta)\Delta t$. Even when the particles in a and b start with the same initial distance $r = r_0$, when the flow begins, the particle in a is placed in the stretching region and then r_a starts a continuous growing while the particle in b is placed in the compressing region and then r_b starts a continuous reduction. Given that dr is proportional to the instantaneous distance, dr_a, it becomes bigger while dr_b becomes smaller with time. After a rotation of 90° of the particles, $\Delta r_{a'} > \Delta r_{b'}$. This is seen as an over-deformation of the drop shape which turns into an ellipsoid with a major semi axis L larger than that of steady state and a minor semi axis B smaller than that of steady state. Using the Taylor parameter, this initial deformation is reflected in a rapid increase in D_T that overshoots the steady state and reaches its maximum value D_{Tmax}. It is worth mentioning that this rotation is not reflected upon the orientation of the major axis L, that is measured with the angle θ, that is independent from the angular position β of the particles inside the drop. As the fluid elements in the drop continue rotating, they describe the remaining portion of the ellipsoidal movement previously carried out; i.e., due to the last rotation, the particle at a' moves through the compression region and the particle in b' traverses the stretching one. Then, after another 90° rotation they reach the position a'' at $\beta(a'') = 270°$ and b'', at $\beta_{b''} = 180°$ with $r_{a''} = r_{a'} - \Delta r_{a''} = r_0$ because of $\Delta r_{a'} = -\Delta r_{a''}$, and $r_{b''} = r_{b'} + \Delta r_{b''} = r_0$, because of $\Delta r_{b'} = -\Delta r_{b''}$. Now, $L = r_0 = B$, and the drop shape returns to its original spherical shape. This is reflected on the D_T value that falls to zero. In the absence of the interfacial tension action, the deformation parameter would be oscillating in time continuously, between a maximum value D_{Tmax} and zero.
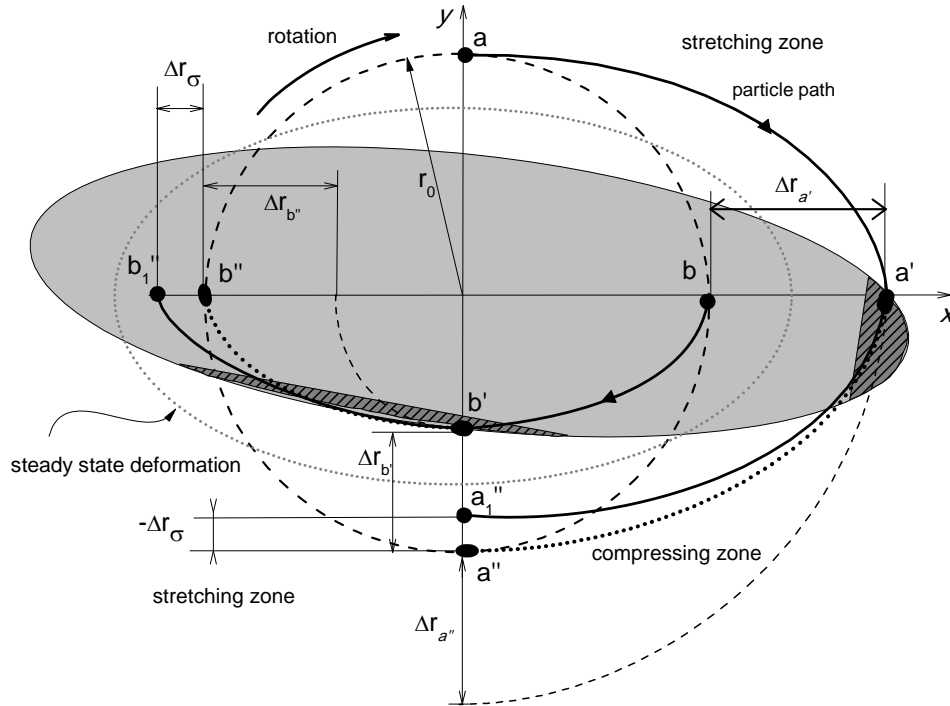
Figure 5.44. Maximum deformation suffered at the start-up flow. The drop is immediately deformed and starts to rotate in the clockwise direction. Particles placed in the compression region are elongated and those in the compressing region are contracted. As the drop rotates and the particles are reoriented, the deformation is reduced and the drop tries to return to its initial spherical shape, but at the same time, the interfacial tension adjust the shape and takes the drop to the steady state deformation.

Now, this oscillatory behavior is not permanent: oscillations are damped and eventually disappear. The interfacial tension σ is responsible for such a damping. The interfacial tension seen as an elastic membrane, compress the particles inside the drop with a internal pressure p_i proportional to the curvature of the surface (or inversely proportional to the radius of the geometry): $p_i = \sigma/r$. When the drop is at rest, having a spherical shape, its surface has a constant radius r_0 and the pressure inside the drop is also constant $p_i = \sigma/r_0$. But when a flow is present, it deforms the drop, with zones of maximum curvatures (small radius at the ends of L) and zones of minimum curvatures (maximum radius at the ends of B).

If the ellipse were fixed (without rotation) and there were variations in the outer pressure field p_o, it would result in the unbalance between the outer pressure and the inner pressure that would be compensated by the interfacial tension adjusting the drop geometry. For example, an increase in the outer pressure in the extreme of L, p_{oL}, is reflected in a modification in the drop shape because the higher curvature in L creates a high inner pressure at the extreme of L, p_{iL}, respect to the inner pressure in B, p_{iB}, this pressure gradient generates a retraction process in which the fluid inside the drop flows from the L

zone to the B zone resulting in the oblateness of the ellipsoid. In that way, the equilibrium between the outer pressure and the inner pressure is reached again (see Fig. 5.45).
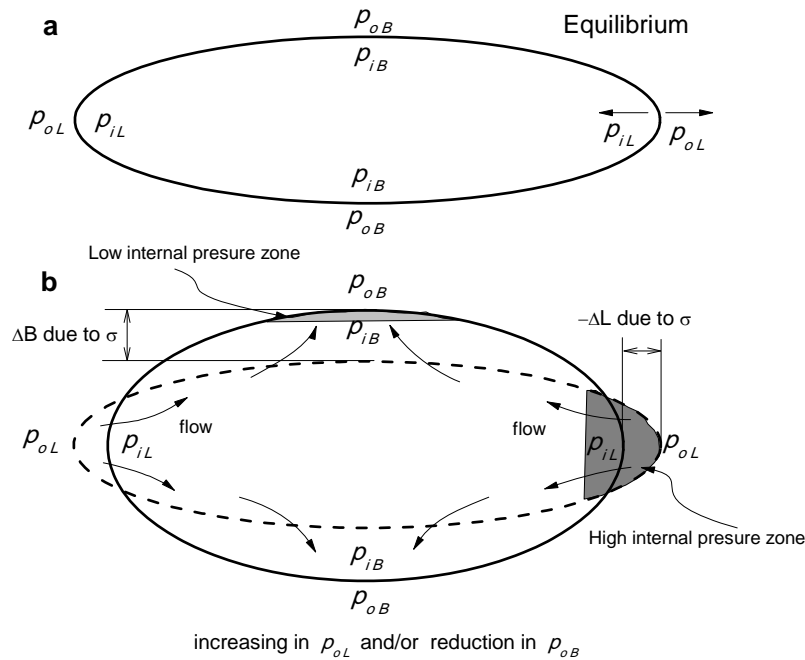

Figure 5.45. Contraction process due to the action of the interfacial tension. When the pressure out of the drop changes, the interfacial tension modifies the drop shape to reach a new equilibrium state.

In the case of the presence of oscillations described earlier, the changes in the pressure are not due to variations in the flow field but because of the angular movement of the particles. When they rotate and the parts in the ellipse with maximum curvatures (ends of the semi axis L) formed during the elongation passes to compression regions, the retraction of the drop will have two components, that of the flow and that of the interfacial tension. In the same way, when the zones of minimum curvature (ends of semi axis B) passes to the stretching region they will be more elongated because of the interfacial tension contribution. This contributions modify the trajectory of the particles in a' and b', as mentioned before, the particles initially at a and b after a rotation of 90° are in the positions at a' and b' with $r_{a'} = r_0 + \Delta r_{a'}$ at $\beta_{a'} = 0°$ and $r_{b'} = r_0 - \Delta r_{b'}$ at $\beta_{b'} = 270°$. The point a' is placed in a zone of high curvature and as the particle continues rotating, this high curvature zone passes to a compression region and when the particle describes another 90° rotation, it is compressed (pushed) to the center of the drop by two independent mechanisms:

i)   the retraction caused by the compression region in the flow, which causes a reduction in $r_{a'}$ of magnitude $-\Delta r_{a''}$; and

ii)   the retraction caused by the interfacial tension σ due to the high curvature zone passing to a high pressure region, this retraction has a magnitude $-\Delta r_\sigma$.

At the end, with these effects combined, the particle at a' describes an ellipsoidal trajectory toward a'' different from that previously described. With the contribution of the interfacial tension the particle reaches the point a_1'' with $\beta_{a''1} = 270°$ and a distance respect to the center of the drop $r_{a''1} = r_{a'} - \Delta r_{a''} - \Delta r_\sigma$, which is not the radius of the drop, but a smaller distance in the proportion $r_0 = r_{a''1} + \Delta r_\sigma$. The same applies to the particle in b' that describes a trajectory to b_1''. The particle at b' is stretched (pulled) from the center of the drop by:

i)   the elongation caused by the stretching region in the flow, which causes an increase in $r_{b'}$ of magnitude $\Delta r_{b''}$; and

ii)   the expansion caused by the interfacial tension σ and due to the low curvature zone passing to a low pressure region, this expansion has a magnitude $-\Delta r_\sigma$.

With those contributions the distance of the particle at b_1'' (with $\beta_{b''1} = 180°$) with respect to the center of the drop is $r_{b''1} = r_{b'} + \Delta r_{b''} + \Delta r_\sigma$, which is not the radius of the drop but a larger distance in the proportion $r_0 = r_{b''1} - \Delta r_\sigma$.

In that way, the final shape of the drop after a rotation of the particles of 180° from the beginning is not spherical but ellipsoidal, and each time that the particles rotates 90° the contractions of L_{max} are increased by a quantity Δr_σ and the elongation of the B_{min} are increases in the same quantity Δr_σ in such a way that at $\Delta r_a - \Delta r_\sigma \rightarrow \Delta r$ and $\Delta r_b + \Delta r_\sigma \rightarrow \Delta r$, the total deformation in the steady state. With this adjustments, the deformed ellipse approaches to that of the stationary state in which at $\beta = 0°$ and 180°, $r_a = r_b = L$ and at $\beta = 90°$ and 270°, $r_a = r_b = B$. Given that those compensations in deformation are carried out by the interfacial tension they have the characteristic times of relaxation t_r which depends only on the properties of the fluids and on the drop size. Thus, the duration of the transitory is independent of the flow conditions and depends on how fast the interfacial tension takes the drop to the equilibrium shape, or how fast the interfacial tension modifies the geometry from an sphere to an ellipsoid with the steady state deformation. Modifying any of the properties that define the relaxation time will increase or reduce the transitory duration; i.e., as the interfacial tension values diminishes —with the viscosities and the radius of the drop fixed— the relaxation time increases, and therefore the duration of the transitory. In the extreme case of an interfacial tension $\sigma = 0$, the damping will be nil and then the oscillations will remain for as long as the flow is maintained. As well for the viscosities and the interfacial tension fixed, bigger drops will imply a longer transitory. Fig 5.46.
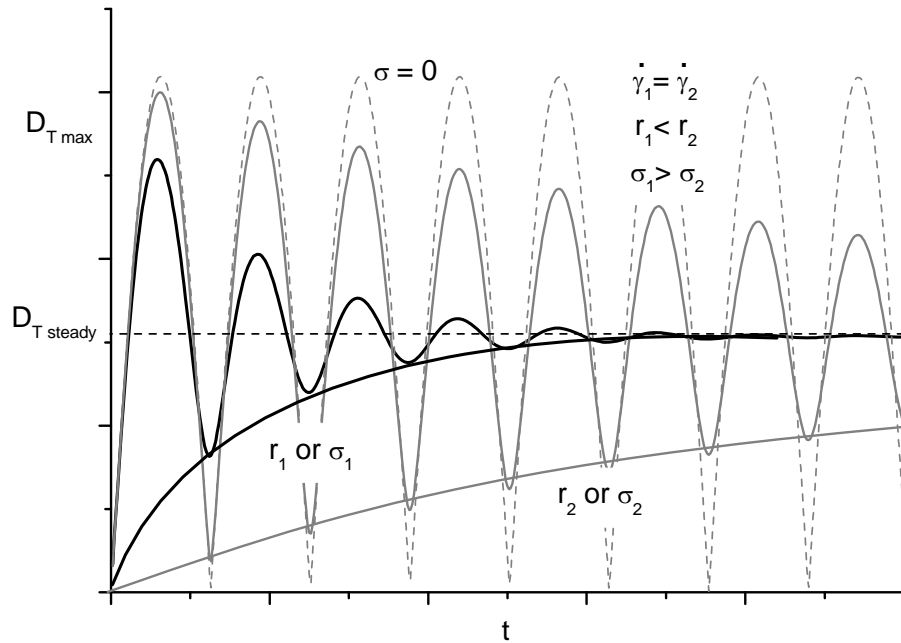
Figure 5.46. Damping curves only as function of the drop size and the fluids properties. As pointed by Torza et al. (1972), in the absence of interfacial tension there would not be damping and the oscillations would last all the time the flow was on.

Although the 2-D analysis presented would appear limited it turns out to be appropriate, given that it is on the *x-y* plane where the mayor deformations take place; actually, the oscillations are present only in this plane. Even when at this moment the experimental setup only allows the visualization of the *x-y* plane and therefore only the cross section of the drop in that plane can be measured, the missing *W* minor semi-axis of the ellipsoid is easily calculated. Considering that the drop is deformed in an ellipsoid, valid for small deformations, the semi-axis *W* can be computed from the volume conservation of the original drop. The volume of the drop is given by $V_0 = 4\pi r_0^3/3$ and it must be the exactly the same volume of the ellipsoidal shape at all times: $V_0 = 4\pi \, LBW/3$. Thus, the value of the *W* is given by $W = r_0^3/LB$. Figure 5.47 shows the evolution of the lengths of the three semi-axes of the deformed ellipsoid *L, B* and *W,* showing that the oscillations develop only in the semi-axes *L* and *B*; increments on *L* are compensated by reductions on *B*, and in that way, *W* remains almost constant, with a value close to the original radius $W \approx r_0$. Also, the plot shows that initially, increments on the *L* semi-axis are bigger than reductions on the *B* semi-axis i.e. $\Delta r_{a'} > \Delta r_{b'}$.

The following Figures 5.48 to 5.70, show the transient oscillatory behavior observed in the experiments of drop deformation carried out for three TRM geometries and $\lambda = 0.13, 0.05$ and 0.03. The plots presented are those corresponding to the deformation and orientation of the drop measured in terms of D_T and θ.
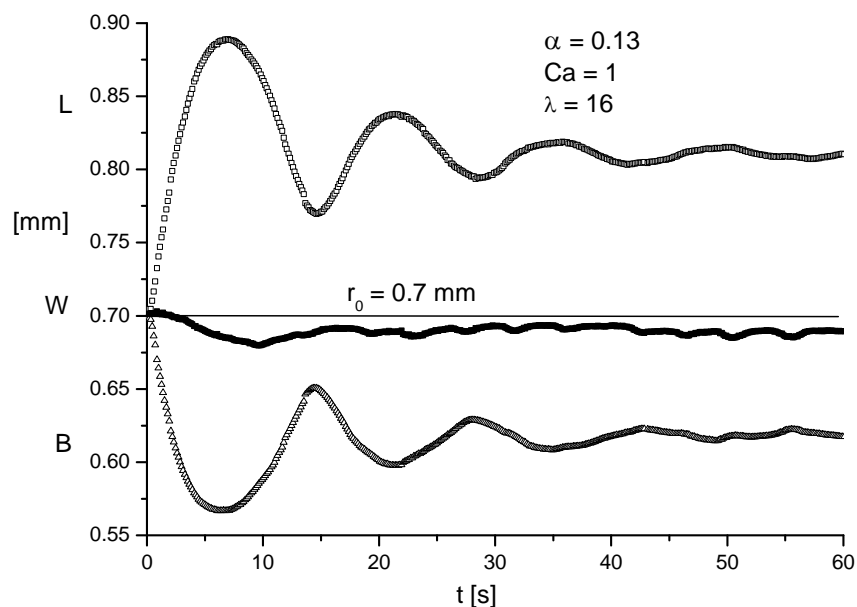
Figure 5.47. Evolution of the three semi axes of the ellipsoidal shaped of a drop originally spherical with r_0 = 0.7mm subjected to star up flow. The oscillations are mainly present in the semi-axes *L* and *B*, while *W* remains almost constant and with a value close to the original radius of the drop r_0.

Figs. 5.48 and 5.63, show the time evolution of the deformation parameter for low capillary numbers. In these cases, the stresses imposed by the flow are only balanced by the interfacial tension with a proportional change in the drop shape and therefore the steady state deformation depends on the *Ca* applied. In order to achieve a low *Ca*, low shear rates were applied (with the same drop), so low that compared with the characteristic time of the flow, t_{flow} (deformation and rotation), the characteristic relaxation time t_σ is smaller. Hence, the interfacial tension modifies (adjusts) the geometry on time, in a way that there is no overshoot in the curves of deformation nor undershot in the orientation ones, and therefore the transient has a monotonic evolution to the steady state.

This behavior corresponds to the stability of the drop via the deformation mechanism mentioned by Blawzdziewicz et al. (2003) and Young et al. (2008) —see Fig. 5.36— and was found to occur approximately for *Ca* < 0.1. As *Ca* increases, the characteristic time of the flow becomes of the order of the relaxation time $t_\sigma \approx t_{flow}$, and the vorticity competes with the interfacial tension in the retraction of the drop. Then, the overshoots in the deformation curves appears (the manifestation of the contraction via rotation), this happens approximately when *Ca* > 0.1. And if *Ca* increases, the overshoots become bigger, with undershoots following later. Nevertheless, at long times in the stationary state, D_T still depends on *Ca*. But, this time even when the stresses over the drop are mainly counteracted by the interfacial tension, there starts to be a contribution due to the vorticity. This would represent the transition to the rotation stabilizing mechanism shown in Fig 5.37, but given that the time scales of the processes involved are of the same order, there is not a well defined division as that drawn in Fig 5.36. Once *Ca* reaches certain

value, the overshoots and undershoots in the deformation curves are now damped oscillations and the stationary state deformation reached is the same, irrespective of Ca; see Figs. 5.49, 5.56 and 5.64. These conditions were mentioned by Blawzdziewicz et al. (2003) and Young et al. (2008): if Ca achieves a characteristic value (which depends on the type of flow), the mechanism of stabilization changes from drop deformation to drop rotation, and higher Ca will not generate higher deformations in the drop but instead it will spin faster around its centroid. The values of the characteristic capillary numbers for this transition for the different types of flow have been found to be $Ca \sim 0.5$ for $\alpha = 0.13$, $Ca \sim 0.3$ for $\alpha = 0.05$, and $Ca \sim 0.25$ for $\alpha = 0.03$, even though more detailed experimental studies could be of assistance to determine these values with better precision. Further increments in the capillary number are not reflected in the stationary deformation –because the rotation counteracts the elongation– but it is in the transitory stage.

Figs. 5.49, 5.56 and 5.64 show that by increasing Ca, the maximum amplitude in the oscillations and its frequency also increases. The increase in Ca is done by augmenting the shear rate and higher shear rates means faster deformations, but due to the coupling of elongation and rotation this is rapidly contained; the higher the shear rate, the faster the rotation and the shorter the time of particle reorientation. The result is that by increasing the shear rate the frequency is also increased. Table 5.5 presents the maximum amplitude D_{Tmax} and the frequency of the oscillations for the three flow fields with a low and a high Ca value.

Table 5.5 Maximum amplitudes and frequencies for the three flow types for low and high Ca values.

Figure	Type of flow α	Low Ca			High Ca		
		Ca	D_{Tmax}	f [1/s]	Ca	D_{Tmax}	f [1/s]
5.50	0.13	0.5	0.18	0.03	1.5	0.23	0.1
5.57	0.05	0.5	0.16	0.07	1.2	0.18	0.16
5.65	0.03	0.44	0.14	0.12	0.87	0.16	0.23

The data show that the higher frequencies belong to lower values of α. The Figures also show that despite the value of Ca, the duration of the transitory is the same, because the compensations to the deformation made by the interfacial tension does not depends on the shear rates applied. Or in other words, the characteristic time of the envelope curve of damping depends only the properties of the fluids and on the drop size. The plot of Fig. 5.49 belongs to a drop with radius $r_0 = 0.7$ mm and the transitory phase last about 60s. Figure 5.56 corresponds to a drop with $r_0 = 0.5$ mm, and the damping time is about 45s, while the smallest drop corresponding to Fig. 5.64 with $r_0 = 0.33$ mm and with the shortest time of about 25s. The effect of the drop size is also present in the plots presented in the drop size effects section.

The same behavior as for the damped oscillations is observed on the orientation angle curves but the stationary state always depends on Ca, approaching to zero as Ca increases. Fig 5.50, 5.57 and 5.65 are plots of the time evolution of the orientation of the mayor semi-axis L of the ellipsoid. Those Figures show the continuous reconfiguration of the shape suffered in the path toward the stationary state. This angle is always observed to depend on Ca because it is the remaining contribution of the interfacial tension that even when it does not modify the final drop shape, it still affects the distribution of the magnitude of the shear rate. That is, it re-orientates the actual principal directions of deformation. When Ca becomes large enough, this contribution is diminished and eventually when $Ca \gg 1$ the effect disappears and the drop orientates with the x-axis. In those figures it can be noticed that after the first undershot in the orientation angle, the θ value changes very fast. This does not means a rapid rotation of the drop but a very fast contraction process and hence a rapid reconfiguration of the shape. Given that the deformation and reconfiguration are not independent, the frequency in the angle oscillations is the same to that corresponding to the deformation parameter.

Plotting those curves in dimensionless time $\dot{\gamma}t$, Figs. 5.50, 5.52, 5.58,5.60 5.66 5.67 it can be seen that the frequency in each plot is very similar (not exactly the same), only depending on the type of flow (for λ fixed) because the oscillations are the result of the coupling of deformation and rotation and the rotation is reduced by increasing the flow type. The theoretical predictions of Cox (1969) describes dimensionless oscillations that have exactly the same frequency i.e. all the curves has its maximum amplitude at exactly the same dimensionless time and subsequent peaks in the oscillations occurs also at the same time. Even when the experimental plots show very similar frequencies these are not the same; it can be noticed that the frequency does depend on Ca as well, or on the shear rate (it is the same drop). The maximum amplitude is reached in longer dimensionless times when the shear rates increases; besides, the dimensionless frequency becomes a little lower with for longer times. Those changes are the result of changes in the velocity of reorientation, implying a change in the vorticity to deformation ratio (that it was supposed to be constant for a fixed value of α) showing the complexity of the dynamics of deformation. Table 5.6 shows the maximum amplitude D_{Tmax}, the dimensionless time $\dot{\gamma}t$ of these maximum, and the dimensionless frequency f^* for low and high Ca for the three types of flow.

Table 5.6 Maximum amplitudes and frequencies for the three flow types for low and high *Ca*

Fig.	Type of flow α	Low Ca				High Ca			
		Ca	D_{Tmax}	$\dot{\gamma}t$	f^*	Ca	D_{Tmax}	$\dot{\gamma}t$	f^*
5.54	0.13	0.5	0.18	5.8	0.07	1.5	0.23	7.3	0.06
5.61	0.05	0.5	0.16	5	0.1	1.2	0.18	4.3	0.09
5.69	0.03	0.44	0.14	3.8	0.12	0.87	0.16	4.5	0.11

The history of deformation may be better visualized using polar plots of the deformation parameter D_T and the orientation angle θ; see Figures 5.53, 5.54, 5.60, 5.61, 5.68 and 5.69. Figure 5.53 and 5.68 show that only for values of the capillary numbers lower than 0.05 a true monotonic evolution is observed toward the stationary state. When $Ca > 0.05$ the curves present overshoots in the deformation; this behavior also can be noticed in the dimensionless time evolution plots. In Figures 5.53, 5.60 and 5.68 it can be seen the as Ca increases, the curves belonging to low capillary numbers only present one overshoot. For larger values of Ca, the curves begin to present a spiral structure that illustrates the magnitude and nature on the damped oscillations. This parametric representation shows that the number of cycles needed for the drop to reach the equilibrium conditions increase with Ca, reaching higher amplitudes in deformation and orientation but eventually falling to the same deformation state. Note that these plots are a timeless evolution, and even when the drop deformation parameter develops more oscillations, the steady state is reached in the same time. The figures show that in the oscillations developed, the drop reaches its maximum deformation when its orientation angle is barely above the stationary value. Figs. 5.54, 5.61 and 5.69 are the polar plots for the highest capillary number of each experiment and where the number of cycles developed is the maximum. The letters in those Figures correspond to the set of pictures in Figs. 5.55, 5.62 and 5.70 respectively. Those pictures show the drop deformation and orientation at the points marked by the letter in the transient evolution. The values of the deformation and orientation parameter at that instant are listed in the Table below each figure.
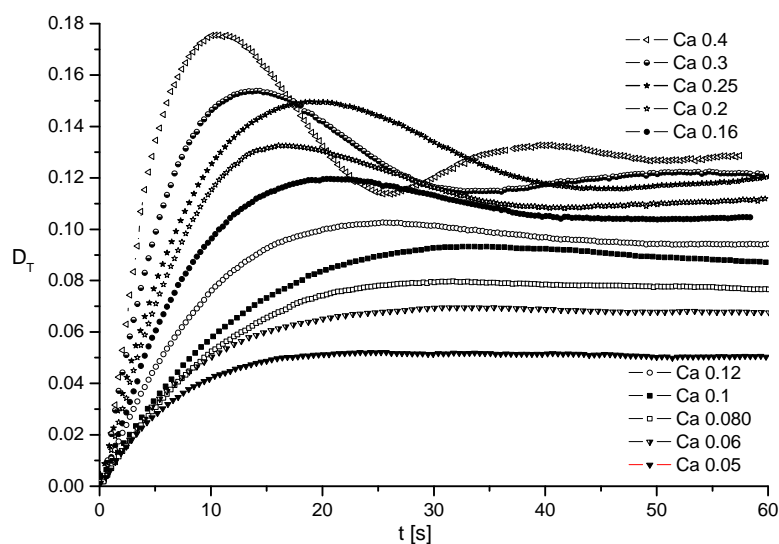

Figure 5.48. Deformation evolution of a drop with $\lambda = 16$ and $\alpha = 0.13$ under low capillary numbers. For very low Ca the curves present a monotonic evolution toward the steady state but as Ca increases, the curves star to develop overshoots which eventually becomes oscillations.
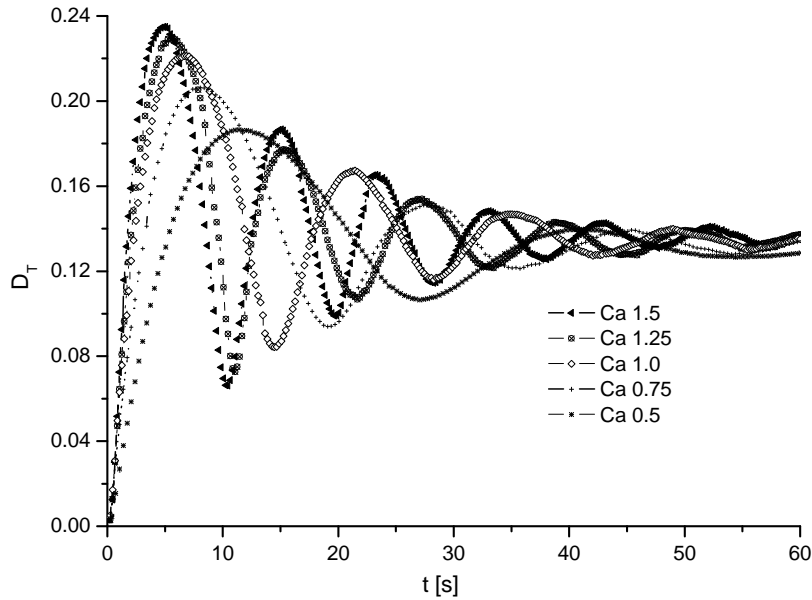
Figure 5.49. Deformation evolution of a drop with $\lambda = 16$ and $\alpha = 0.13$ under high capillary numbers. The curves present a damped oscillatory behavior. The effect of *Ca* it is only to modify the frequency and amplitude of the oscillations but the steady state deformation reached is the same. Besides, the envelope damping curve it is the same given that is the same drop and the damping of the oscillations is only function of the relaxation time.
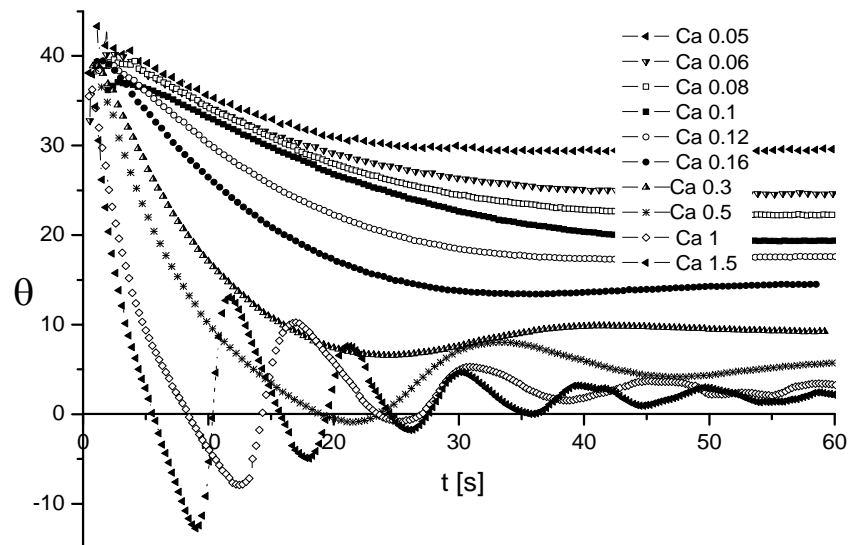

Figure 5.50. Orientation angle evolution of a drop with $\lambda = 16$ under a flow field with $\alpha = 0.13$ and different capillary numbers. The effect of *Ca* it is the same as in the deformation curves, by increasing *Ca*, higher frequencies and larger amplitudes are obtained but unlike the steady deformation, the steady orientation depends on the *Ca* value and approaches to $0°$ as *Ca* rises.
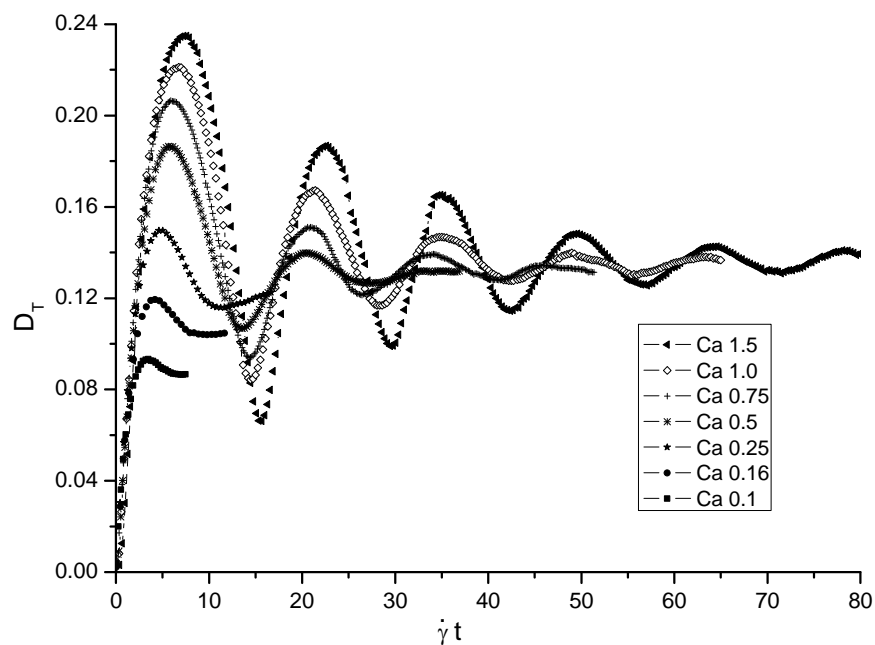
Figure 5.51. Dimensionless time evolution of the deformation of a drop with $\lambda = 16$ under a flow field with $\alpha = 0.13$ and different capillary numbers. In this plot, the damping time and the amplitude of the oscillations depend on *Ca*, but the frequency is almost the same for all curves. As well, the steady state deformation is the same for the higher *Ca*.
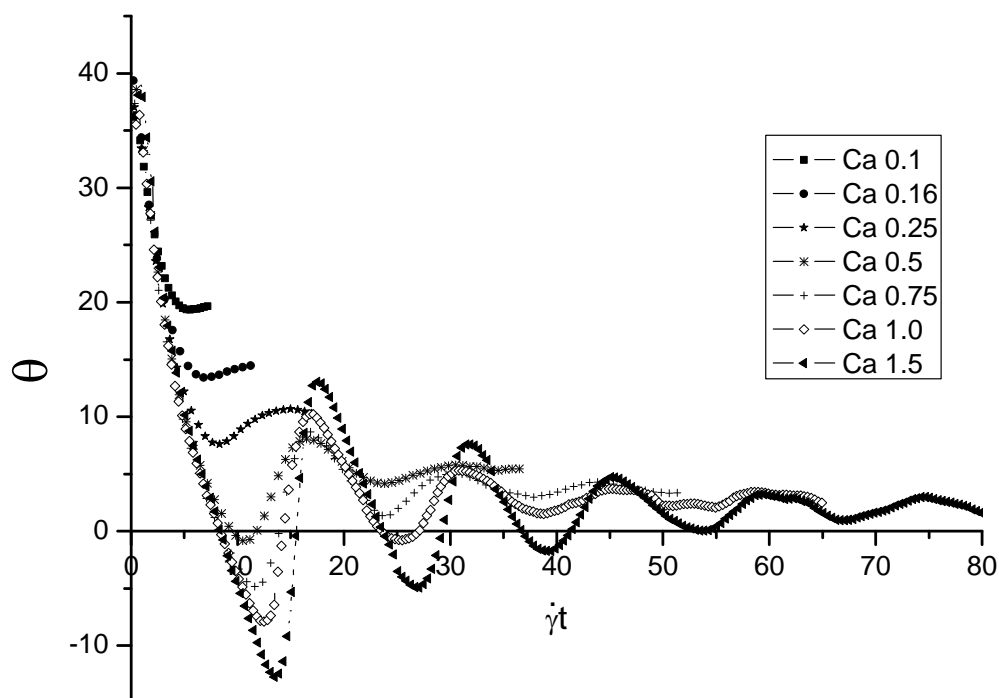

Figure 5.52. Dimensionless time evolution of the orientation angle of a drop with $\lambda = 16$ under a flow field with $\alpha = 0.13$ and different capillary numbers. In this plot, the amplitude of the oscillation also depends on *Ca* as well as the steady orientation. The frequency is almost the same for all curves.
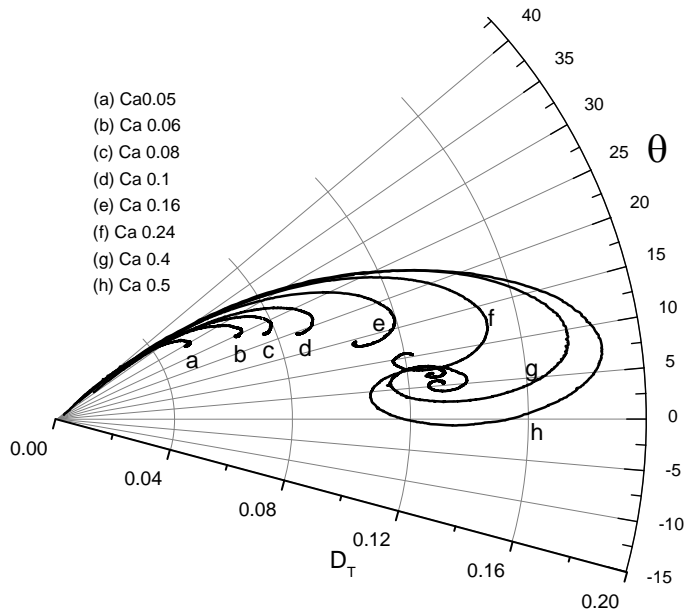
Figure 5.53. Polar plot of the deformation D_T vs the orientation angle θ for $\alpha = 0.13$, $\lambda = 16$ and low capillary numbers. This plot illustrates the oscillatory behavior that becomes present as Ca increases. The curves start to show a spiral structure and the final states begin to be closer each time until for the higher Ca the curves have almost the same steady state.
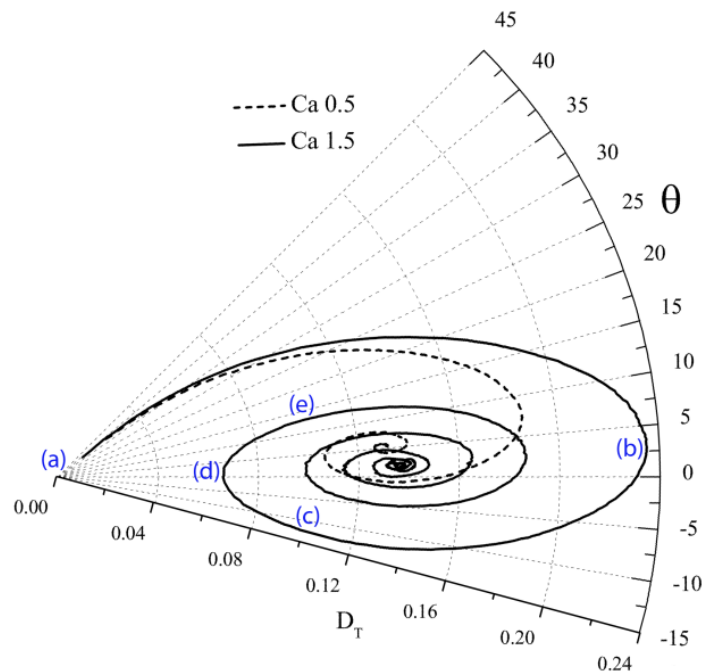

Figure 5.54. Polar plot of the deformation D_T vs the orientation angle θ for $\alpha = 0.13$, $\lambda = 16$ and high capillary numbers. This plot illustrates that by increasing Ca the number of cycles needed for reaching the steady state also increases. It must be observed that even when these curves present different paths, the time taken to reach the final state it is exactly the same. The letters in the curve for $Ca = 1.5$ correspond to the images in Fig. 5.55.
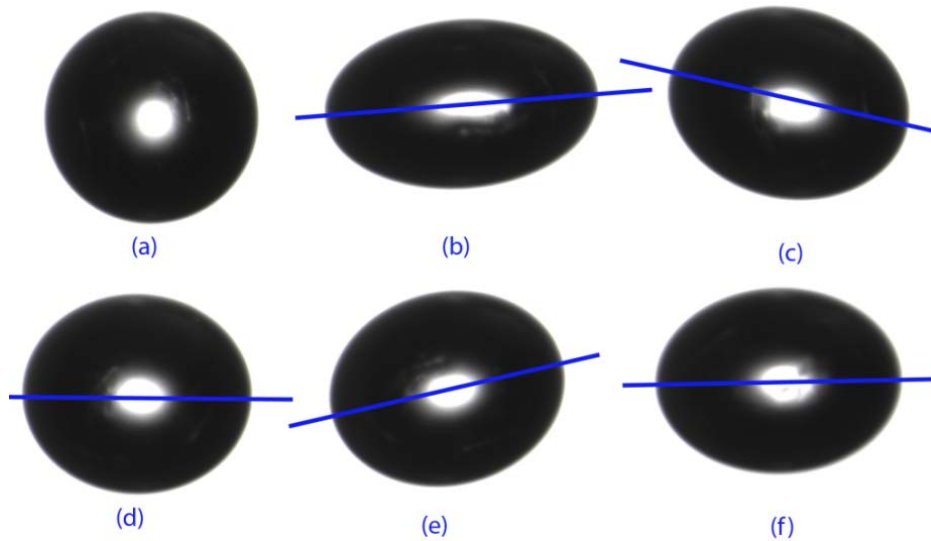
Figure 5.55. Images of the drop deformation and orientation at the instants pointed in the transient behavior ploted in Fig. 5.54. The values of the parameter of deformation and orientation of these images are listed in Table 5.7.

Table 5.7. Parameters of the drop evolution at the instants marked by letters in Figs. 5.54 and 5.55.

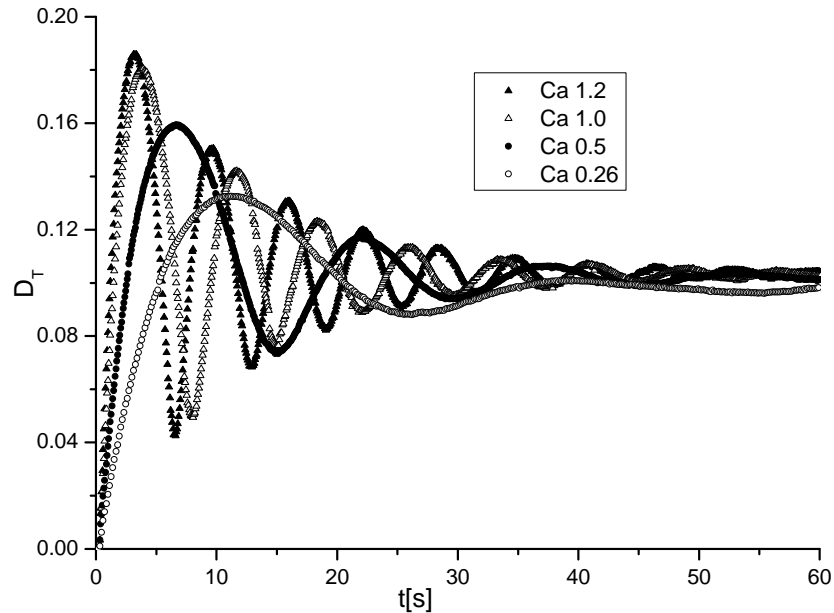|	(a)	(b)	(c)	(d)	(e)	(f)
	Initial shape	Maximum deformation	Minimum angle	Minimum deformation	Maximum angle	Steady state
t [s]	0	4.6	9	10.33	11.6	t > 70
D_T	0	0.23	0.11	0.066	0.10	0.13
θ	--	4.5^0	-12.7^0	-0.4^0	13^0	1^0

Figure 5.56. Deformation evolution of a drop with $\lambda = 16$ **under high capillary numbers and a flow field with** $\alpha = 0.05$**. The curves present a damped oscillatory behavior. The effect of** *Ca* **it is only to modify the frequency and amplitude of the oscillations but the steady state deformation reached is the same for all** *Ca***. Besides the envelope damping curve it is the same given that is the same drop and the damping of the oscillations is only function of the relaxation time.**
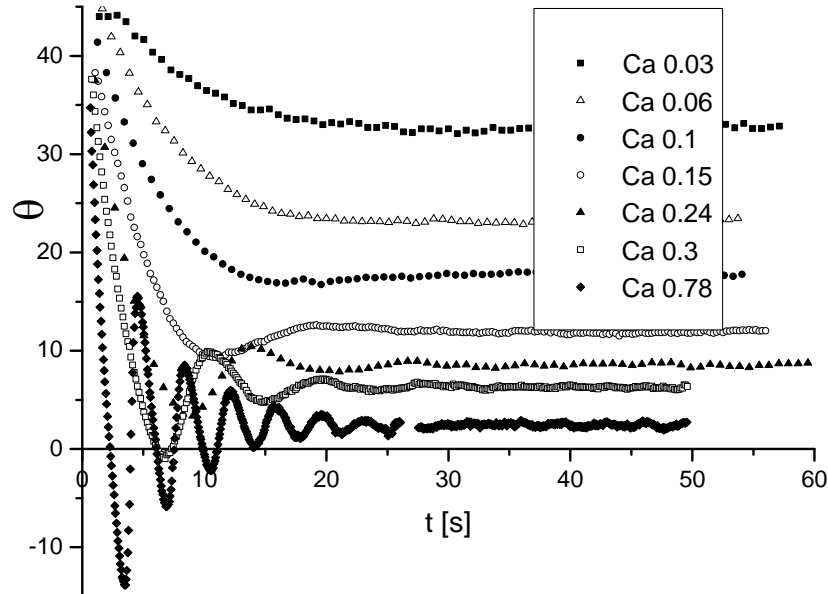

Figure 5.57. Orientation angle evolution of a drop with $\lambda = 16$ **under a flow field with** $\alpha = 0.05$ **and different capillary numbers. The effect of Ca it is the same as in the deformation curves, by increasing Ca, higher frequencies and larger amplitudes are obtained but unlike the steady deformation, the steady orientation depends on the** *Ca* **and approaches to** $0°$ **as** *Ca* **rises.**
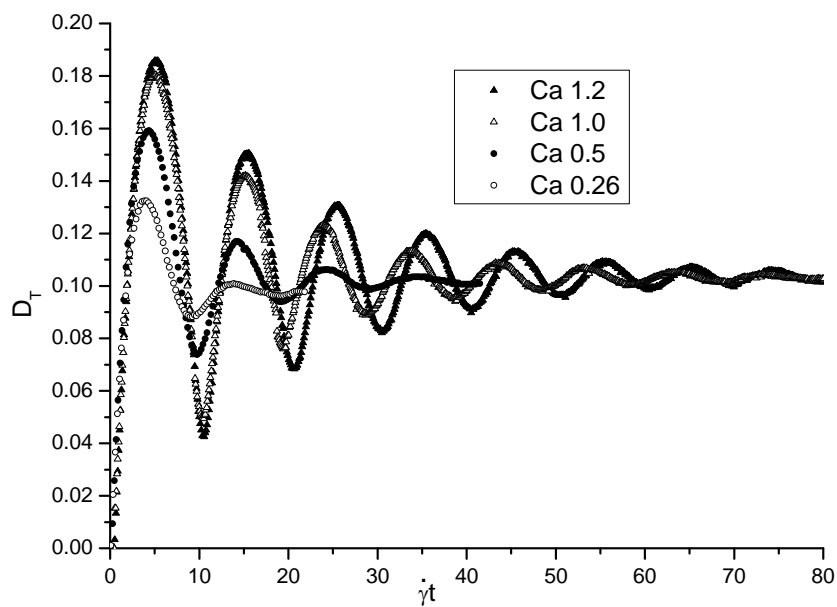
Figure 5.58. Dimensionless time evolution of the deformation of a drop with $\lambda = 16$ under a flow field with $\alpha = 0.05$ and different capillary numbers. In this plot, the damping time and the amplitude of the oscillations depend on *Ca*, but the frequency is almost the same for all curves. As well, the steady state deformation is the same.
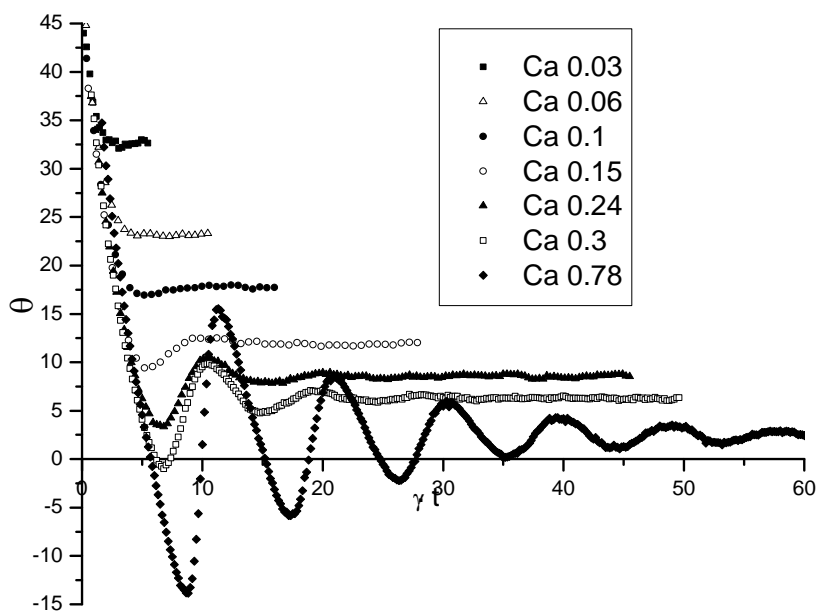

Figure 5.59. Dimensionless time evolution of the orientation angle of a drop with $\lambda = 16$ under a flow field with $\alpha = 0.05$ and different capillary numbers. In this plot, the amplitude of the oscillation also depends on *Ca* as well as the steady orientation. The frequency is almost the same for all curves
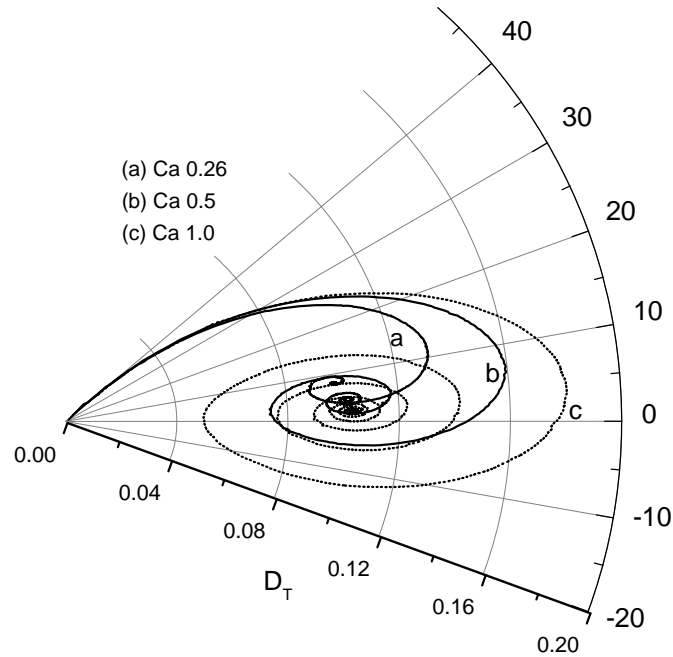
Figure 5.60. Polar plot of the deformation D_T vs the orientation angle θ for $\alpha = 0.05$, $\lambda = 16$ and low capillary numbers. This plot illustrates the oscillatory behavior that becomes present as *Ca* increases. The curves start to show a spiral structure and the final states begin to be closer each time until, for the higher *Ca*, the curves have almost the same steady state.
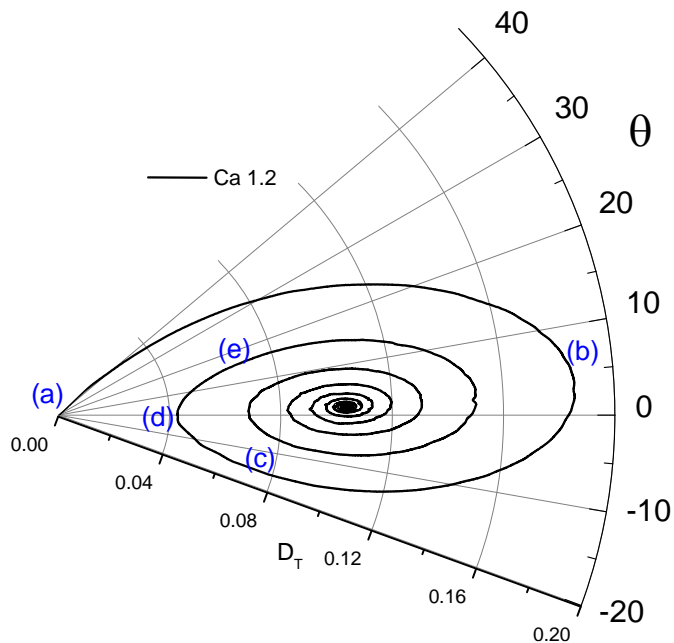

Figure 5.61. Polar plot of the deformation D_T vs the orientation angle θ for $\alpha = 0.05$, $\lambda = 16$ and a *Ca* = 1.2. This plot illustrates how by increasing *Ca* the number of cycles needed for reaching the steady state also increases. The letters in the curve correspond to the images in Fig. 5.62.
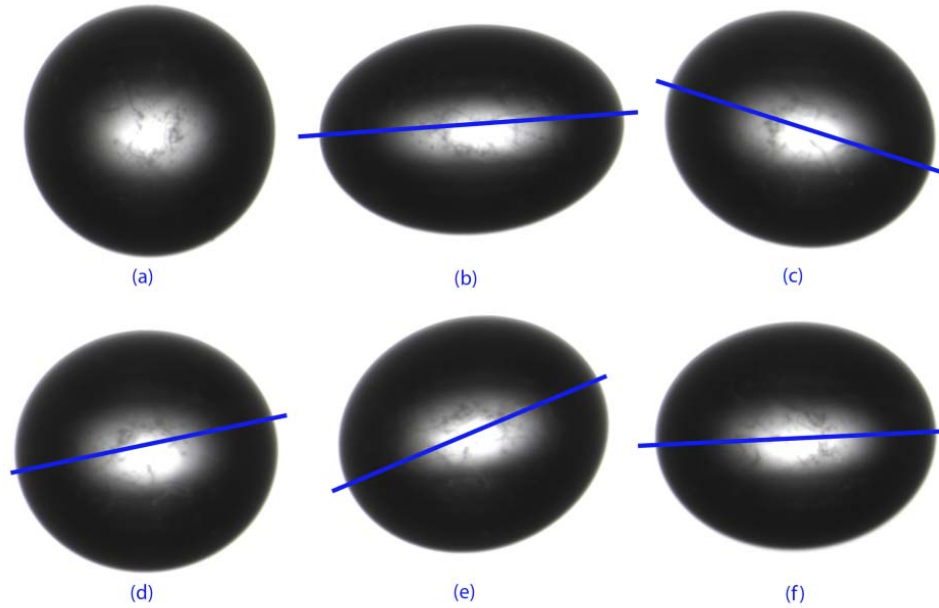
Figure 5.62. Images of the drop deformation and orientation at the instants pointed in the transient behavior plotted in Fig. 5.61. The values of the parameters of deformation and orientation of these images are listed in Table 5.8.

Table 5.8. Parameters of the drop evolution at the instants marked by letters in Figs. 5.61 and 5.62.

	(a)	(b)	(c)	(d)	(e)	(f)
	Initial shape	Maximum deformation	Minimum angle	Minimum deformation	Maximum angle	Steady state
t [s]	0	3.1	5.8	6.6	7.4	t > 30
D_T	0	0.186	0.077	0.043	0.078	0.10
θ	--	3.9^0	-15.8^0	1.89^0	16.5^0	1.5^0

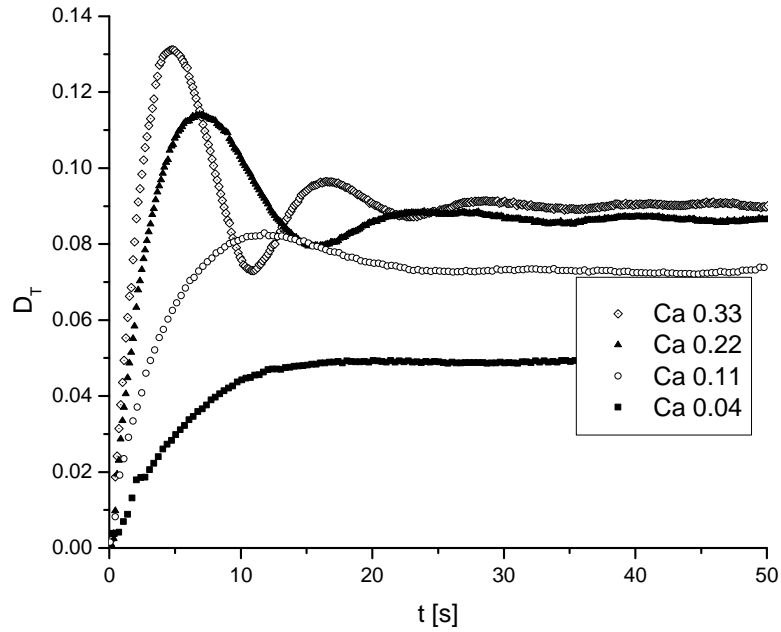**Figure 5.63.** Evolution of the deformation parameter of a drop with $\lambda = 16$ and $\alpha = 0.03$ under low capillary numbers. For very low *Ca* the curves present a monotonic evolution to the steady state but as *Ca* increases, the curves star to develop overshoots which eventually becomes oscillations.
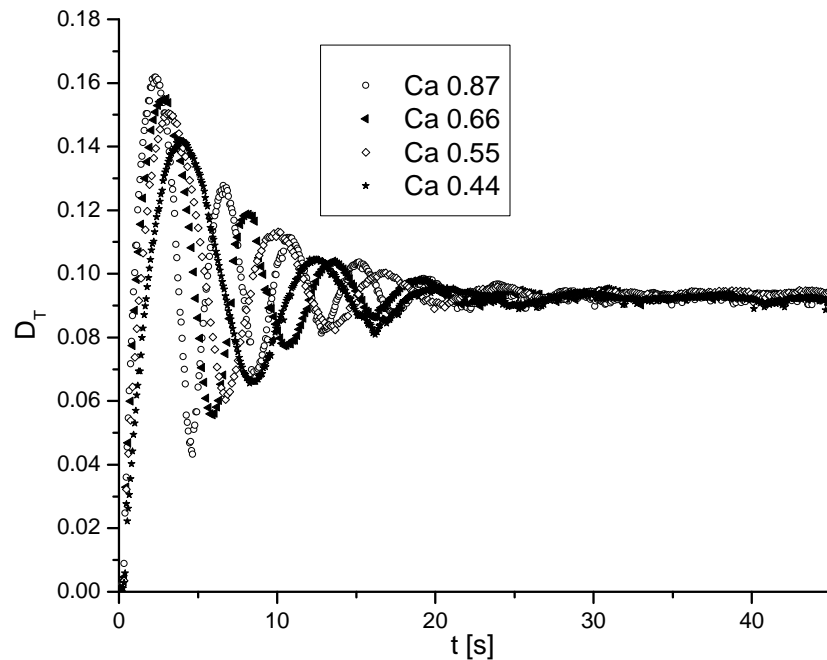
Figure 5.64. Deformation evolution of a drop with $\lambda = 16$ and $\alpha = 0.03$ under high capillary numbers. The curves present a damped oscillatory behavior. The effect of *Ca* it is only to modify the frequency and amplitude of the oscillations but the steady state deformation reached is the same. Besides the envelope damping curve it is the same given that is the same drop and the damping of the oscillations is only function of the relaxation time.

120
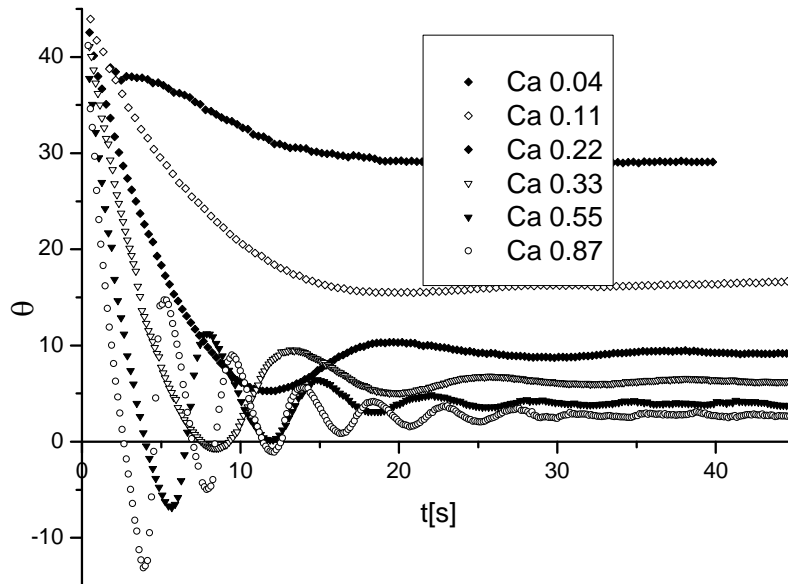
Figure 5.65. Orientation angle evolution of a drop with $\lambda = 16$ and $\alpha = 0.03$ under different capillary numbers. The effect of *Ca* it is the same as in the deformation curves, by increasing *Ca*, higher frequencies and larger amplitudes are obtained but unlike the steady deformation, the steady orientation depends on the *Ca* and approaches to $0°$ as *Ca* rises.
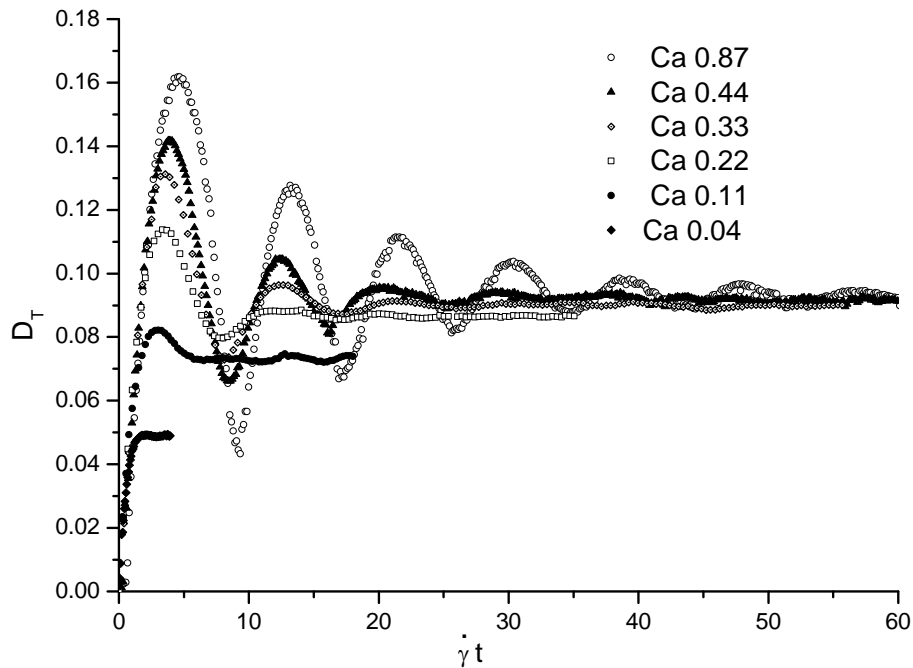
Figure 5.66. Dimensionless time evolution of the deformation parameter of a drop with $\lambda = 16$ and $\alpha = 0.03$ under a flow field with and different capillary numbers. The damping time and the amplitude of the oscillations depend on *Ca*, but the frequency is almost the same for all curves. As well, the steady state deformation is the same for the higher *Ca*.
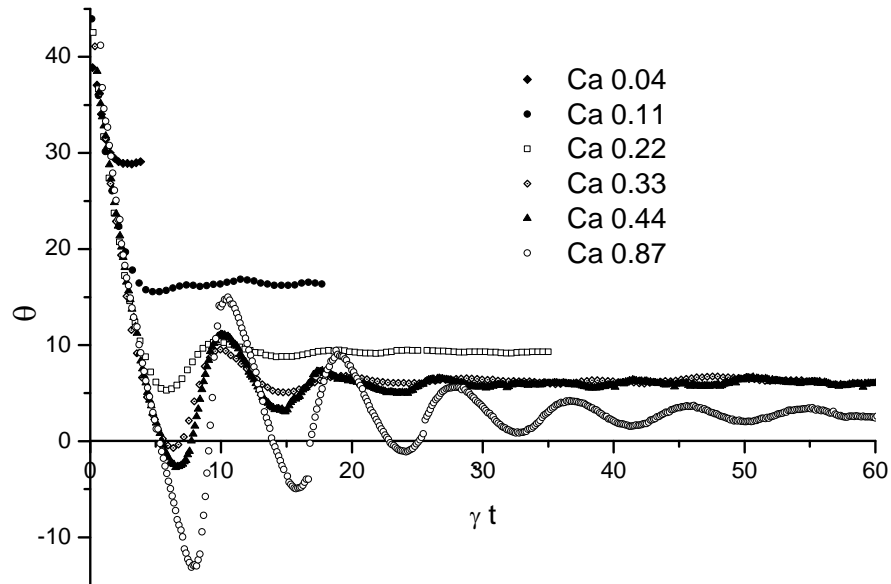
Figure 5.67. Dimensionless time evolution of the orientation angle of a drop with $\lambda = 16$ and $\alpha = 0.03$ and different capillary numbers. In this plot, the amplitude of the oscillation also depends on Ca as well as the steady orientation. The frequency is almost the same for all curves.
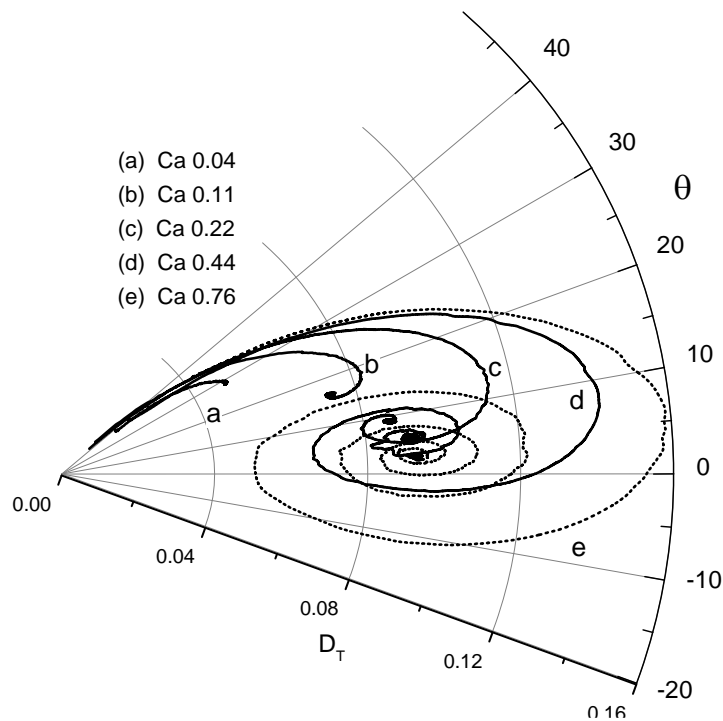
Figure 5.68. Polar plot of the deformation D_T vs the orientation angle θ for $\alpha = 0.03$, $\lambda = 16$ and different capillary numbers. This plot illustrates the oscillatory behavior that becomes present as Ca increases. The curves start to show a spiral structure and the final states begin to be closer each time until for the higher Ca the curves have almost the same steady state
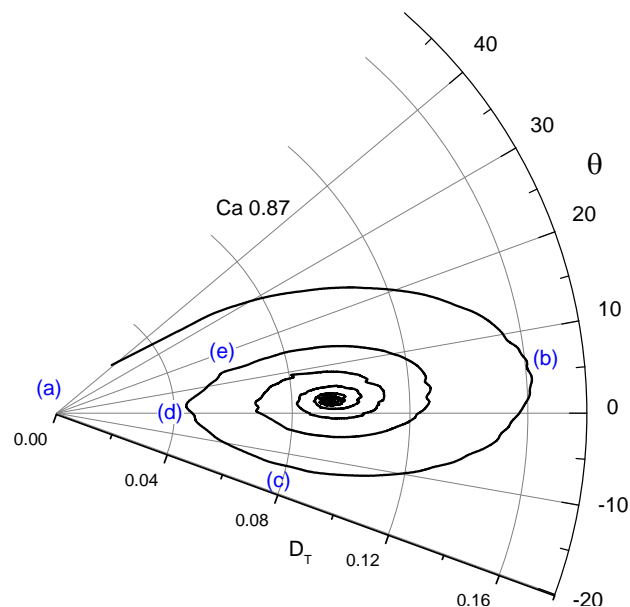
Figure 5.69. Polar plot of the deformation D_T vs the orientation angle θ for $\alpha = 0.03$, $\lambda = 16$ and the highest capillary numbers. This plot illustrates that by increasing Ca the number of cycles needed for reaching the steady state also increases. The letters in the curve correspond to the images in Fig. 5.70.
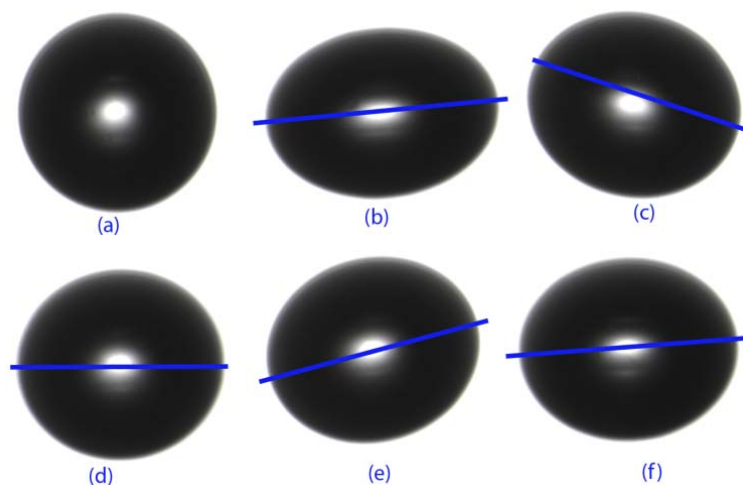
Figure 5.70. Images of the drop deformation and orientation at the instants pointed in the transient behavior ploted in Fig. 5.69. The values of the parameter of deformation and orientation of these images are listed in Table 5.9.

Table 5.9. Parameters of the drop evolution at the instants marked by letters in Figs. 5.69 and 5.70.

	(a)	(b)	(c)	(d)	(e)	(f)
	Initial shape	Maximum deformation	Minimum angle	Minimum deformation	Maximum angle	Steady state
t [s]	0	2.26	3.86	4.66	5.26	t > 30
D_T	0	0.162	0.09	0.043	0.08	0.092
θ	--	4.6^0	-13.1^0	-3.3^0	15^0	2.6^0

The effects of vorticity on the deformation dynamics are seen in the following Figures, which are comparisons between the transient phases of the three flow field types. The effect of the flow type on the deformation and orientation is independently seen in the dimensionless time evolution curves of Figs. 5.71 to 5.75. Observing Fig. 5.71, it can be seen that, as previous results show, the maximum amplitude of the oscillations on the deformation parameter as well as the steady state deformation reached are proportional to the parameter of type of flow α. The oscillations have larger dimensionless periods, because the angular reorientation of the particles is slower and hence, the particles remain more time being elongated or contracted. This period of the oscillations can be considered a characteristic of each flow field, given that by changing Ca the frequency is barely altered (Figs 5.51, 5.58 and 5.66). Figure 5.72 is a plot of the parameter of deformation re-scaled with the steady state deformation $D_T/D_{Tsteady}$ for each flow. This figure shows that despite the flow type, the dimensionless time for reaching the equilibrium state is the same. As predicted by Cox (1969), the damping of the oscillations in dimensionless form is independent from α and proportional to $1/(\lambda\,Ca)$, or in dimensional form it is given by the relaxation time of the drop. This case is analogous to an experiment with: a drop size fixed, and where changes made to the shear rate value —in order to obtain different capillary numbers— are reflected as change in the frequency of the oscillations.

Now, Figure 5.73 shows the effect of the type of flow in the orientation angle. Whereas flows with less vorticity have the highest amplitudes in the oscillations of the deformation parameter, they also have the minimum amplitudes in the oscillations of the orientation angle. The effect of the flow type on both the deformation and orientation is better illustrated in polar plots. Figure 5.74 is a polar plot of the scaled deformation parameter $D_T/D_{Tsteady}$ vs the orientation angle θ, showing that flows with more vorticity increase the number of cycles needed for the drop to reach the steady state. But besides the difference in the number of cycles there is also a change in the form of the curves: Fig. 5.75 shows higher amplitudes in deformation combined with lower amplitude in angle orientation giving as a result a flattening in the path of the drop toward the stationary states, with curves more peaked at the extremes where the elongation of the drop process changes to retraction. These effects of the type of flows have been also noticed by Reyes (2005) who performed numerical simulations for highly viscosities ratio and different values of the parameter of type o flow. The results of Reyes were obtained for a viscosity ratio $\lambda = 25$ and his plots show curves with less pronounced differences, which might indicate that the effect of the flow type reduces with increments of the viscosities ratio. The latter scenarios agree well, given that for each flow type there is a critical value of λ at which breakup is possible; that is, in which an oscillatory behavior is not present.
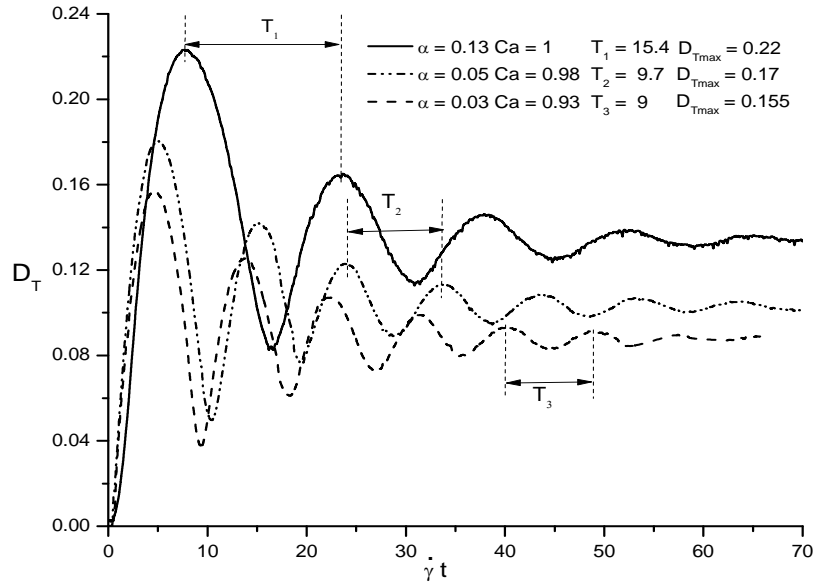
Figure 5.71. Evolution of the deformation parameter D_T for the three types of flow. The effect of the increase in the flow type parameter in the transient phase, it is to increase the amplitude and period of the oscillations developed. In the stationary state it is seen that flow fields with less vorticity (higher values of α) can achieve higher steady state deformations.

Figure 5.72. Evolution of the scaled deformation parameter $D_T/D_{Tsteady}$ for the three types of flow. This plot shows the duration of the transient phase is not affected by the flow type because in dimensionless time it only depends on the capillary number and the viscosities ratio.
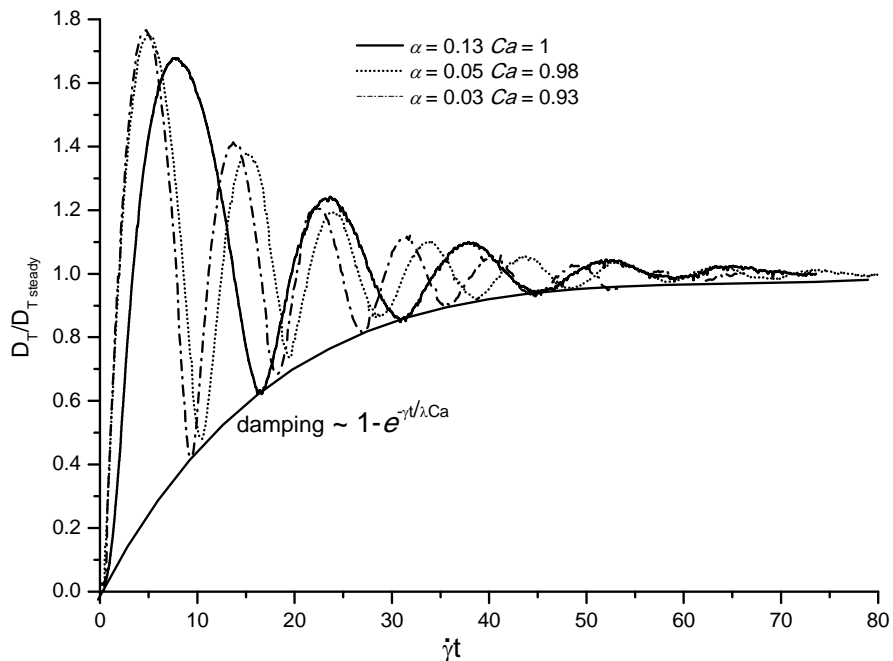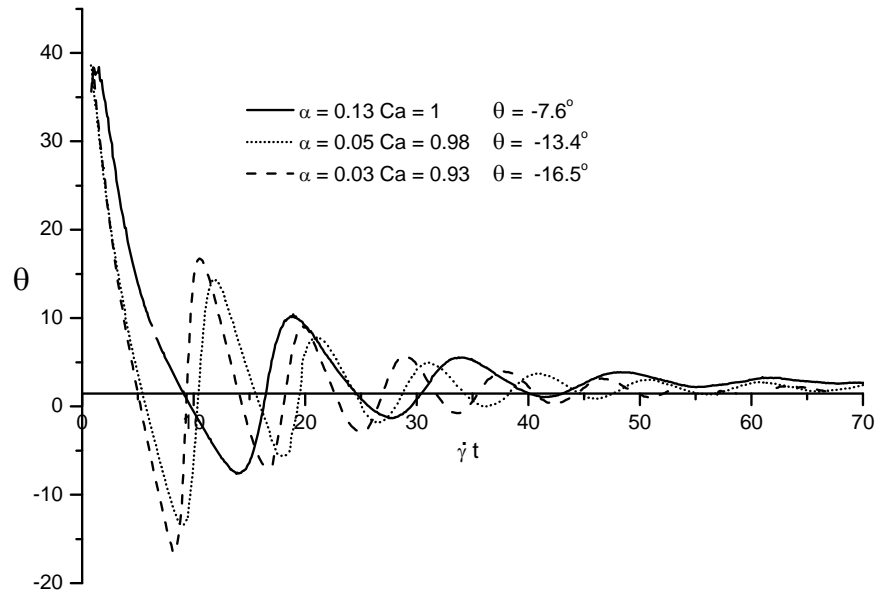
Figure 5.73. Evolution of the orientation angle θ for the three types of flow. The plot shows that as in the deformation parameter, the flow type also affects the amplitude and period of the oscillations during the transient, but unlike the deformation parameter, the amplitude of the oscillations reduces as α increase and the flows with more vorticity present the maximum undershoots (or the minimum angles), besides the plots also shows that the steady state orientation only depends on *Ca.*

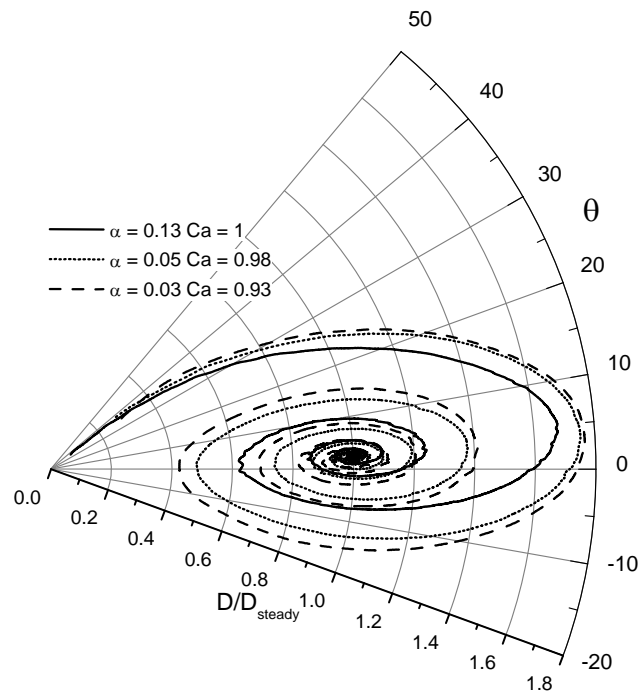**Figure 5.74.** Polar plot of the scaled deformation parameter $D_T/D_{Tsteady}$ vs the orientation angle for the three types of flow. This plot shows that even the duration of the transient phase does not depends on the flow type, the number of cycles needed to reach the steady state increases for flows with more vorticity.
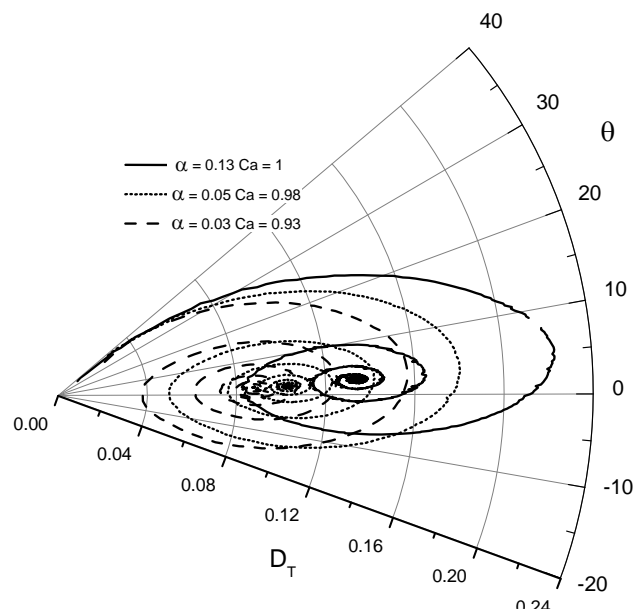
Figure 5.75. Polar plot of the deformation parameter D_T *vs* the orientation angle θ, for the three types of flow. This plot shows more clearly the effect of the flow type parameter in both the orientation and deformation, higher values of α imply higher amplitudes in the deformation but lower amplitudes in the orientation which derives in more flattened curves. The plot also shows that in the steady state, the flow type parameter affects only the deformation and has a minimum effect on the orientation.

5.2.2.3 Drop size effects

Even when there is no exact solution for the dynamics of the deformation of drops immersed in flows with vorticity and with high viscosities ratios, the general features of these systems are known and they can be used as a benchmark for experimental studies. Is in this way that, once the raw data of the experiments for the flows fields with $\alpha = 0.03$ and $\alpha = 0.05$ were analyzed, some discrepancies were noted in relation to the maximum steady state deformation. The results are not consistent with respect to those expected. Since for high viscosities ratio, D_T only depends on λ and α, it was expected that with λ fixed, each flow type had one characteristic maximum steady state deformation. However, a different value was observed of this parameter for each experiment carried out; i.e., the drop deformation, under the same conditions (λ, α and Ca), attains different steady state deformation values. On the other hand, the steady state orientation appears consistent for all experiments.

When the experiments for the flow types with $\alpha = 0.03$ and $\alpha = 0.05$ were carried out, the corresponding to the flow type with $\alpha = 0.13$ had already been performed because this flow was used for the equipment testing. With that, a reference had been established and it was expected that the experiments with the other flow types behave in a similar manner, except of course, by the differences

associated with the change of flow type. Three main features of the expected results are recalled in order to establish the discrepancies and similarities found; the results obtained for the flow type with $\alpha = 0.13$ are used to establish the reference. In this manner, for the experiments in flow fields with vorticity different from zero, it is expected that:

- When λ exceeds a critical value, the flow is unable to cause breakup and then the drop attains a maximum steady state deformation D_T that is only a function of the type of flow and of the viscosities ratio. With λ fixed, the deformation is lower in flows with higher vorticity. For these flows ($\alpha = 0.03$ and $\alpha = 0.05$), the maximum stationary deformation must be below $D_T = 0.13$ —the value found for $\alpha = 0.13$ and $\lambda = 16$—, and above $D_T = 0.085$ —the value found for $\alpha = 0$ and $\lambda = 17$ by Rumscheidt and Mason (1961).

- The steady state orientation angle approaches zero as Ca increases. In this point, there is no specific values expected but a similar behavior with respect to the stationary angle of $\alpha = 0.13$.

- When Ca reaches certain value, the stationary deformation is achieved after a damped oscillatory behavior, its value is the maximum possible and is no longer dependent on Ca. For $\alpha = 0.13$ this happens when $Ca \sim 0.5$ and a similar value is expected with other flow types.

The above characteristics were all observed, except for the one corresponding to the maximum steady state deformation as a function of λ and α only. In a deformation experiment with the same drop and where the shear rate was stepwise increased in order to achieve higher Ca values, it was expected that eventually, for some shear rate the transient oscillatory behavior to be observed, and the steady state deformation reached after this transitory was the maximum possible, independent from the shear rate and common for all the experiments (for the same type of flow). However, even when the general behavior was accomplished (damped oscillations, stationary angles closer to zero and a maximum value in the stationary deformations), it was found that the maximum stationary deformation was different for each experiment, i.e., for each drop.

Thus, this difference must be an effect of the drop size. Consequently, it is necessary, and is the aim of this part, to evaluate maximum steady deformations. That is, to study the maximum steady state deformation for the flows with $\alpha = 0.03$ and $\alpha = 0.05$, and to seek a better understanding of its dependence on the size of the drop. Figure 5.76 shows two plots of the time evolution of the deformation of experiments with the flow type $\alpha = 0.13$, the plot to the left corresponds to a drop with $d = 0.72$ mm and the plot to the right to a drop with $d = 1.4$ mm. These drop evolution shows the expected behavior: the maximum steady state deformation for both diameters is $D_T = 0.13$, regardless the Ca applied. The only difference between these plots is the damping time which depends on r_0. But for the experiments

with the smaller flow types, this behavior does not occur.   That is, the results are different depending on the diameter of the drop.

The effect of the drop size will be analyzed using the parameter of *the confinement ratio d/g* defined in the low viscosities ratio section as the ratio of the drop diameter $d = 2r_0$ to the gap g in the TRM geometry. The gap corresponding to the geometry for $\alpha = 0.05$ is $g = 5$ mm and for the geometry with $\alpha = 0.03$ is $g = 3$ mm. Figure 5.77 shows two plots of the time evolution of the deformation experiments with the flow type $\alpha = 0.03$, the plot to the left corresponds to an drop with $d = 0.62$ mm, $d/g = 0.2$, and the plot to the right to a drop with $d = 1.1$ mm, $d/g = 0.36$.   The only difference between those plots should be the damping time of the oscillations because it depends on the drop radius. Beyond that, the stationary deformation should be the same. Observing the plots it is noted that there is a remarkable difference in the values achieved in both experiments, the plot with $d/g = 0.2$ presents a maximum steady state deformation of $D_T = 0.92$ while in the plot with $d/g = 0.36$ this value appears to be $D_T \approx 0.105$.   Fig. 5.78 show the same case for the flow type $\alpha = 0.05$, the plot to the left corresponds to a drop with $d = 0.44$ mm, $d/g = 0.09$, and the plot at the right to a drop with $d = 1.78$ mm, $d/g = 0.36$, the plot with $d/g = 0.09$ presents a maximum steady state deformation of $D_T = 0.08$ and in the plot with $d/g = 0.09$ $D_T \approx 0.11$. These figures show that the behavior is qualitatively similar in all three flow fields but with a maximum steady state deformation proportional to the drop size. Figs. 5.79 and 5.80 are plots of steady state deformation and orientation as function of the capillary number for low, medium and high confinement ratios for the flow types $\alpha = 0.05$ and $\alpha = 0.03$, respectively. The figures show that the stationary angle is not affected by the drop size (except for the lowest value of d/g in the plot for $\alpha = 0.03$) and that the stationary deformations depend on the drop size characterized by the parameter d/g.

Figure 5.76. Evolution of the deformation parameter for two drops under a flow field with $\alpha = 0.13$ and different capillary numbers.   The plot to the left corresponds to a drop with $d = 0.72$ mm and the plot to the right to a drop with $d = 1.4$ mm, in both plots the steady state deformation is the same $D_{Tsteady} = 0.13$ for all the capillary numbers.

Figure 5.77. Evolution of the deformation parameter for two drops under a flow field with $\alpha = 0.05$ and different capillary numbers. The plot to the left corresponds to a drop with d = 0.62 mm —d/g = 0.2— and reaches a steady deformation $D_{Tsteady}$ = 0.92. The plot to the right corresponds to a drop with d = 1.1 mm or, d/g = 0.36, and has a steady deformation $D_{Tsteady}$ = 0.105.
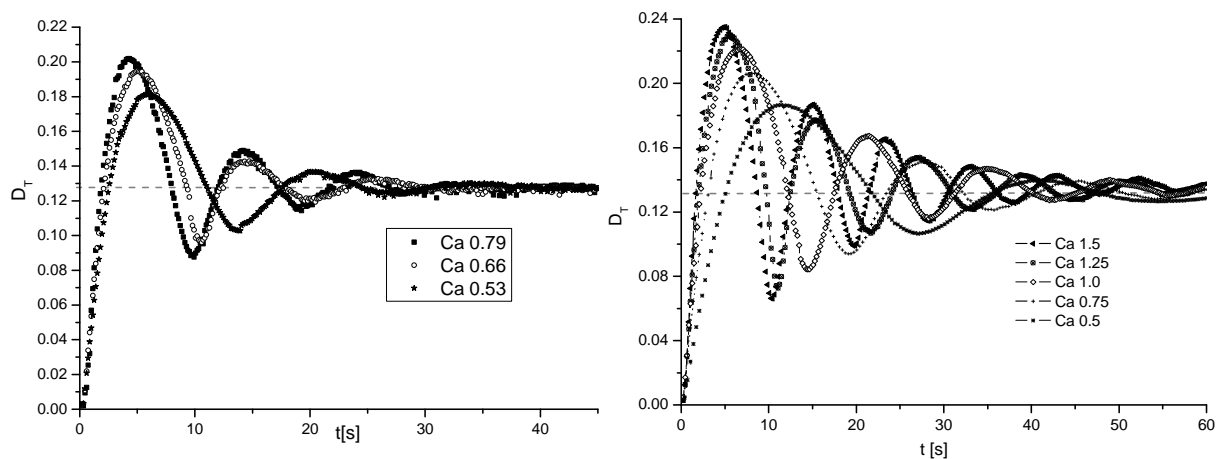

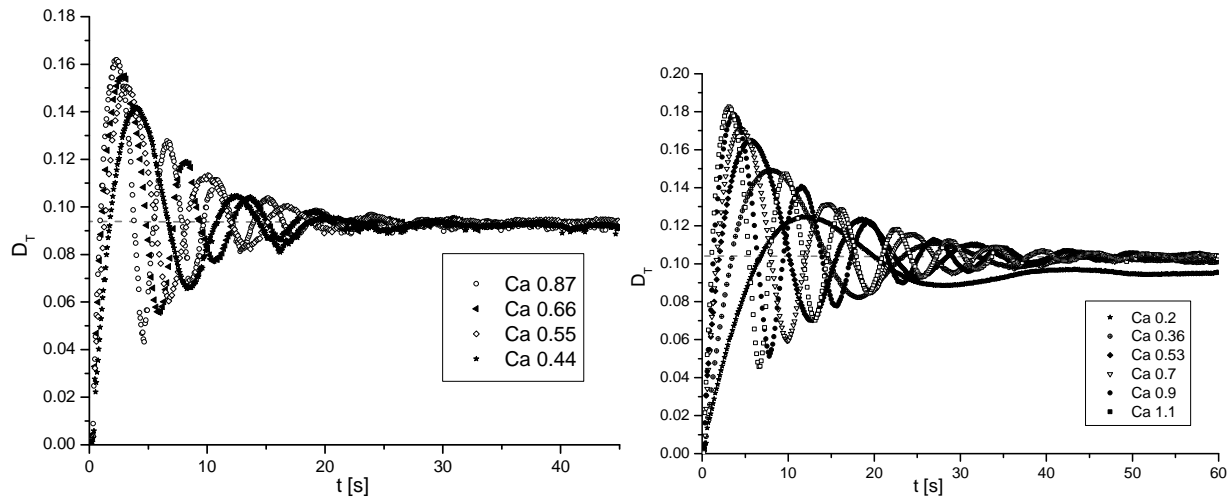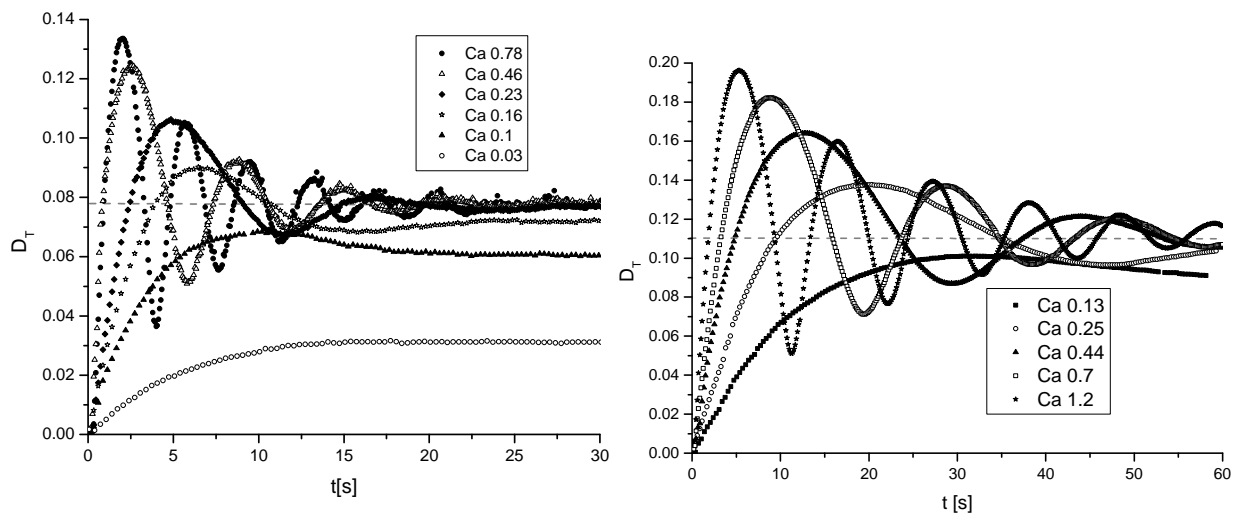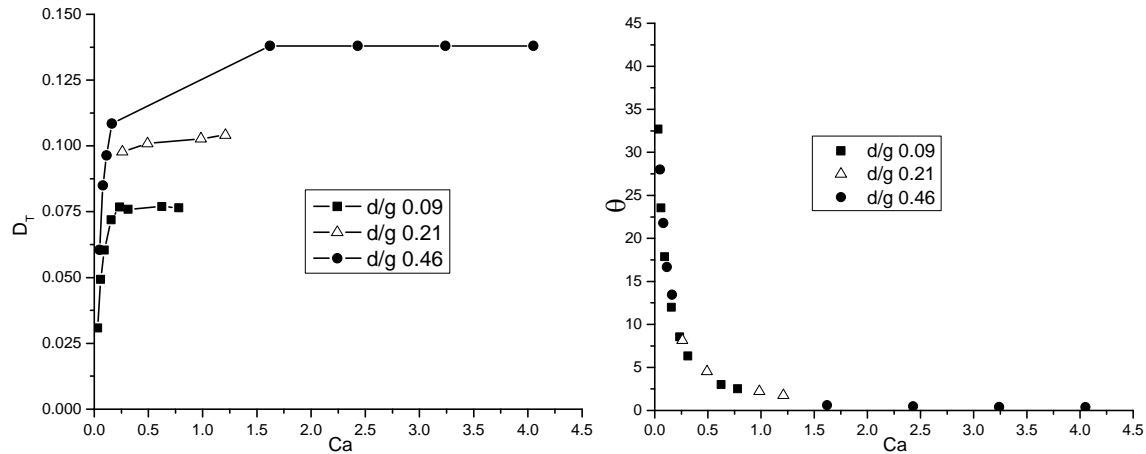**Figure 5.78.** Evolution of the deformation parameter for two drops under a flow field with $\alpha = 0.05$ and different capillary numbers. The plot to the left corresponds to an drop with d = 0.44 mm, d/g= 0.09, and the plot at the right to a drop with d = 1.78 mm, d/g=0.36, the plot with d/g=0.09 presents a maximum steady state deformation of D_T = 0.078 and in the plot with d/g = 0.36 $D_T \approx 0.11$.

Figures 5.79. Steady state deformation and orientation as function of the capillary number for low, medium and high confinement ratios for the flow types $\alpha = 0.05$. The plot shows that the stationary angle is not affected by the drop size and that the stationary deformations depend on the drop size characterized.
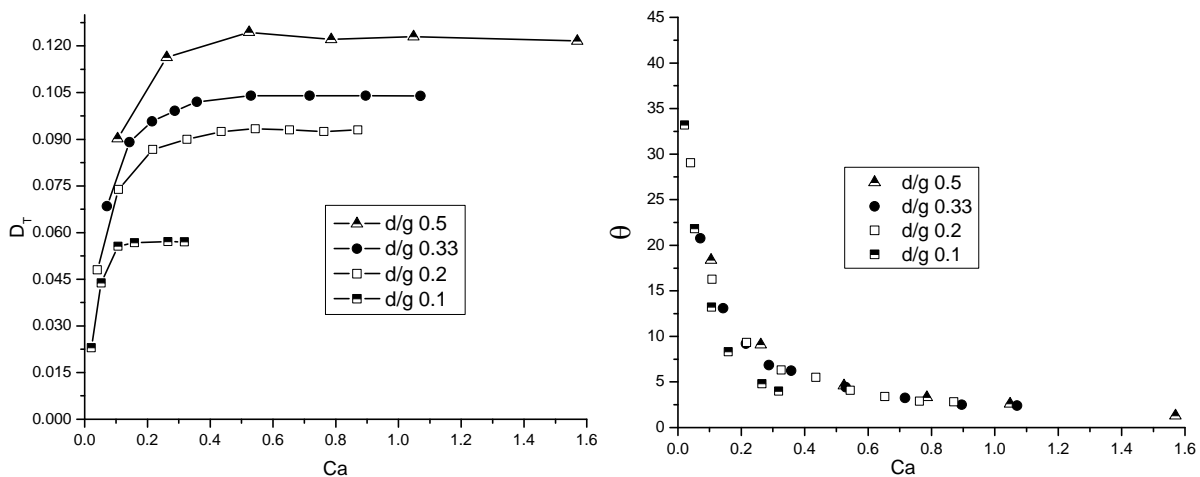
Fig 5.80. Steady state deformation and orientation as function of the capillary number for low, medium and high confinement ratios for the flow types $\alpha = 0.03$. The plot shows that the stationary angle is only affected by the drop size for the confinement ratio *d/g* = 0.1 while the stationary deformations depend on the drop size for all *d/g*.

In some ways, this behavior is not unexpected. Not at all at least, if the effect of the drop size with respect to the distance separating the frontiers in experimental devices is taken into account. Shapira and Haber (1990) considered theoretically drops immersed in simple shear flows with nearby boundaries. Their analysis concludes that close walls exacerbates the drop deformation. The deformation as a function of the *confinement degree* shows that it increases as a cubic order and given by:

$$D_T = D_{T,bulk}\left[1 + 5.7\frac{1 + 2.5\lambda}{1 + \lambda}\left(\frac{r_0}{g}\right)^3\right], \tag{5.15}$$

where D_T is the deformation suffered by the confined drop and $D_{T,bulk}$ is the deformation reached without confinement effects. Even when this equation establishes that only very small drops are not affected by close boundaries, literature points out that the confinement effect is relevant when $d/g > 0.3$ (Vananroye et al. 2006a). Shapyra and Haber (1990) showed as well, that the effect is always to raise the values of the deformation in a continuous way i.e., $d^2(D_T)/d(d/g)^2 > 0$ for all d/g values.

Consequently, drop-size effects should only be reflected by a continuous increase in the drop deformation, ruled by a cubic behavior. Fig. 5.81 is a plot of the maximum steady state deformation data as function of the confinement parameter for the two flows, it shows that the dependence of the maximum stationary deformation is not a linear function of the drop size and the best fitted curve is a cubic order polynomial, which at first instance agrees with general theory.
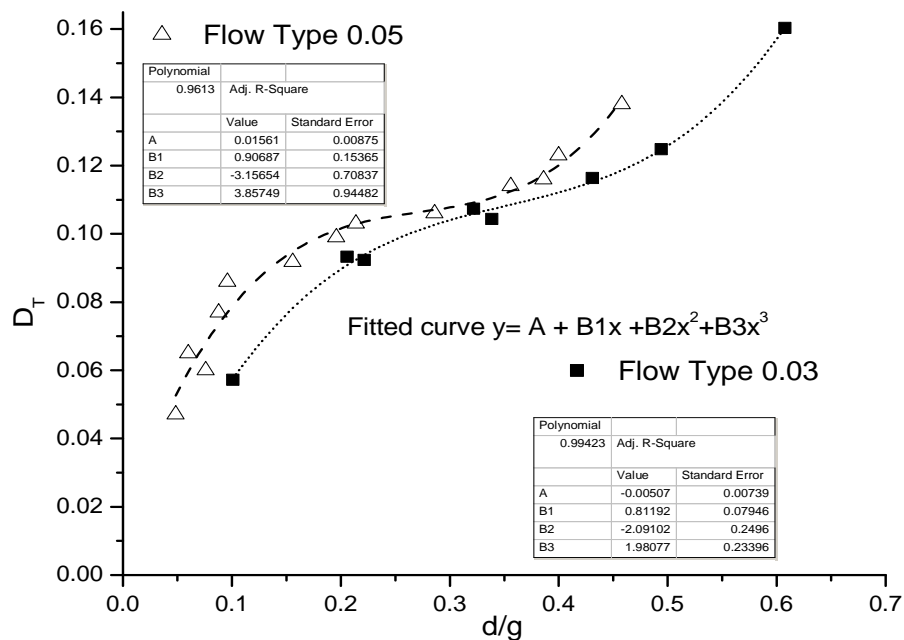
Figure 5.81. **Maximum steady state deformation data as function of the confinement ratio for $\alpha = 0.03$ and $\alpha = 0.05$. It shows that the dependence of the maximum stationary deformation is not a linear function of the drop size and the best fitted curve is a cubic order polynomial.**

But the fitted curves on the plot are not at all as predicted: those curves have a zone with $d^2(D_T)/d(d/g)^2 < 0$, and unlike expected results, the deformation is not independent from d/g. That is, for a typical experimental curve of confinement effects, that derivative has a value very close to zero in the range of $0 < d/g < 0.3$ approximately. According to Fig. 5.81, $d(D_T)/d(d/g) = 0$ when the confinement parameter d/g has a value close to 0.3, that means that in that point the deformation suffered by the drop is only due to the flow conditions or that $D_T = D_{T,bulk}$. The plot shows that when $d/g \sim 0.3$,

the deformations of the two flow types are almost the same; even more, for $\alpha = 0.03$ the deformation seems to be higher than that for $\alpha = 0.05$, which cannot be possible (in absence of confinement effect).

Then, it is necessary to make some other considerations. Fortunately, there are some previous useful experimental results that can be used as reference parameters. Thus, knowing that: the maximum steady state deformation in absence of confinement effects, $D_{T,bulk}$, is a value that only depends on the viscosities ratio λ and on the type of flow α; and that for the same λ, $D_{T,bulk}$ rises as α increases while for the same α $D_{T,bulk}$ diminishes as λ rises. The considerations made in order to decide the value of maximum steady state deformation for the parameters of type of flow $\alpha = 0.03$ and $\alpha = 0.05$ without effect of the drop size, are:

➢ $D_{T,bulk}$ for $\alpha = 0.05$ must be higher than $D_{T,bulk}$ for $\alpha = 0.03$ for the same viscosities ratio.

➢ Rummscheid and Mason (1961), reported a value of $D_{T,bulk} = 0.085$ for a drop with $\lambda = 17$ deformed under simple shear flow, $\alpha = 0$. Therefore, for flows with $\alpha = 0.03$ and $\alpha = 0.05$ with a viscosities ratio $\lambda = 16$, $D_{T,bulk}$ might be higher than $D_T = 0.085$.

➢ Since a flow with $\alpha = 0.13$ and $\lambda = 16$ has a $D_{T,bulk} = 0.13$, in flows with $\alpha = 0.03$ and $\alpha = 0.05$ and the same viscosities ratio, the $D_{T,bulk}$ must be lower than $D = 0.13$.

➢ Cox theory (Cox 1969) predicts a $D_T = 0.079$ and even when it has been showed here that its predictions have an excellent qualitative agreement with experiments, it is well know that Cox deformation values are below the experimental ones, which supports the lower limit taken from Rummscheidt and Mason (1961).

➢ In general, the literature report that the confinement effects are important when $d/g > 0.3$ and therefore the values of $D_{T,bulk}$ for $\alpha = 0.03$ and $\alpha = 0.05$ must belong to values where $d/g < 0.3$.

Under those considerations, it was decided that the values taken as the maximum steady drop deformation for the types of flow are: $D_{T\,bulk} = 0.092$ for $\alpha = 0.03$, and $D_{T\,bulk} = 0.10$ for $\alpha = 0.05$; see Fig. 5.82.

The increase in the drop deformation is explained by the near-walls effect and is consistent with the behavior reported in the literature, but the observed decrease is unexpected and, in fact, a behavior that theoretically should not happen. Then, a plausible explanation could be due to the experimental device, and goes as follows. It was established that for $\lambda \gg 1$, the drop deformation is only determined by the value of the parameter of type of flow; and the only option left is a change in the parameter of the type of flow α linked to the drop size.
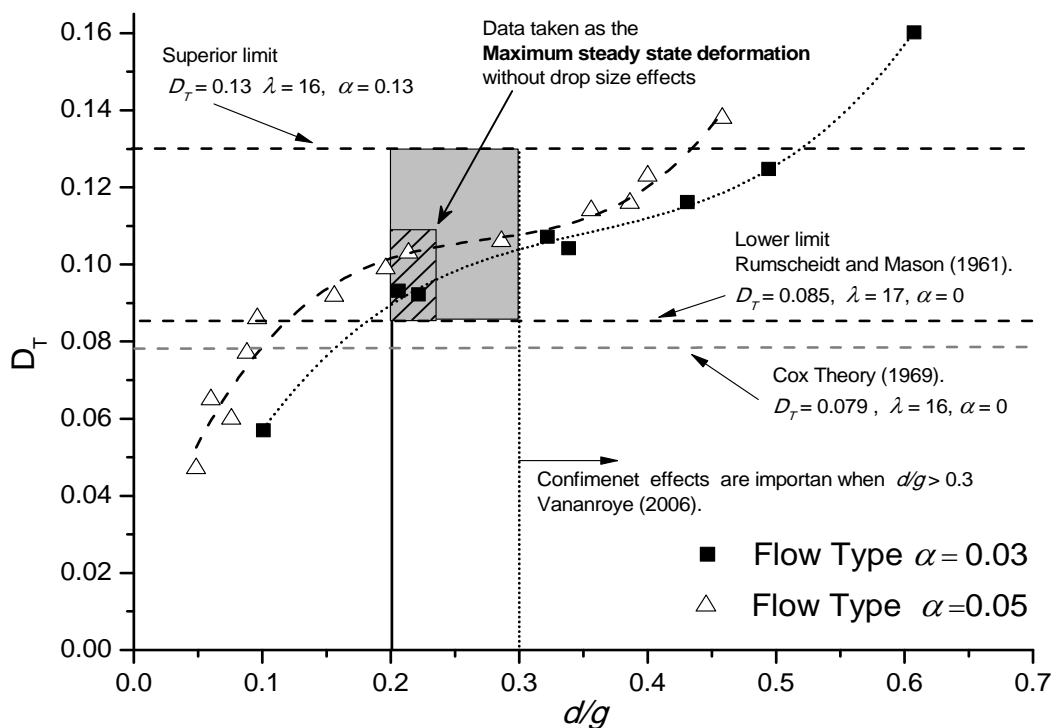
Figure 5.82. Considerations made to decide the values corresponding to non confinement conditions. The values taken as the maximum steady drop deformation are: $D_{T,bulk}$ = 0.092 for $\alpha = 0.03$ and $D_{T,bulk}$ = 0.10 for $\alpha = 0.05$, which are pointed in the plot.

This change can be explained in terms of an average or effective value of α in the flow field acting to deform the drop. The capillary number is defined as $Ca = \dot{\gamma}\, r_0\, \mu_1/\sigma$, with μ_1 and σ fixed. The only way to control Ca is by modifying the product $\dot{\gamma}\, r_0$. Thus, it is clear that the smallest drops require the highest values in the shear rate to achieve moderate values in the capillary number. High shear rates imply high angular velocities in the flow cell cylinders and therefore in the bulk velocity of the drop movements. Due to these higher velocities, and even when the implemented control scheme has proven to be very robust, the trajectories followed by any drop during its wandering about the stagnation point are slightly longer. As well, the time under nominal conditions is slightly less when compared with those for low shear rates. The control scheme tracks only the center of mass of the drop and therefore these trajectories are independent of the drop size and depend only on the shear rate applied; when the trajectories of two drops with the same shear rate are compared, the maximum displacements of the drop centroid are of the same order of magnitude. But if the trajectories are scaled in terms of the drop diameter, smaller drops will have longer trajectories while bigger drops will have the shorter ones.

When the drop is big enough, this is not a mayor problem –actually, the testing of the equipment during the control implementation showed that the drop deformation is insensitive to the relocation of the center of mass of the drop–, but when the drop is very small, the length of this trajectory is so large that at

some instants the drop is far away from the stagnation that it lies out of the drop circumference. In consequence, the drop is no longer under the action of the value of the nominal type of flow but instead a lower value (strictly speaking, the value of this parameter is only definite at the stagnation point of each flow field.).

Figure 5.83 is a diagram of the visual field of the flow field corresponding to the maximum magnification of the equipment, 1.46×1.09 mm^2. The figure shows the recorded experimental trajectories followed by the center of mass of two drops in experiments carried out with a flow field with $\alpha = 0.03$ and with the same shear rate of 1 s^{-1}. The drops are proportionally depicted. The smaller drop has a diameter of $d = 0.3$ mm and corresponds to the smallest value of d/g in Figs. 5.81 and 5.82: $d/g =$ 0.1. The larger drop has a diameter of $d = 0.615$ mm and corresponding to a $d/g = 0.2$, and whose deformation value was taken to determine the $D_{T,bulk}$ in this flow.
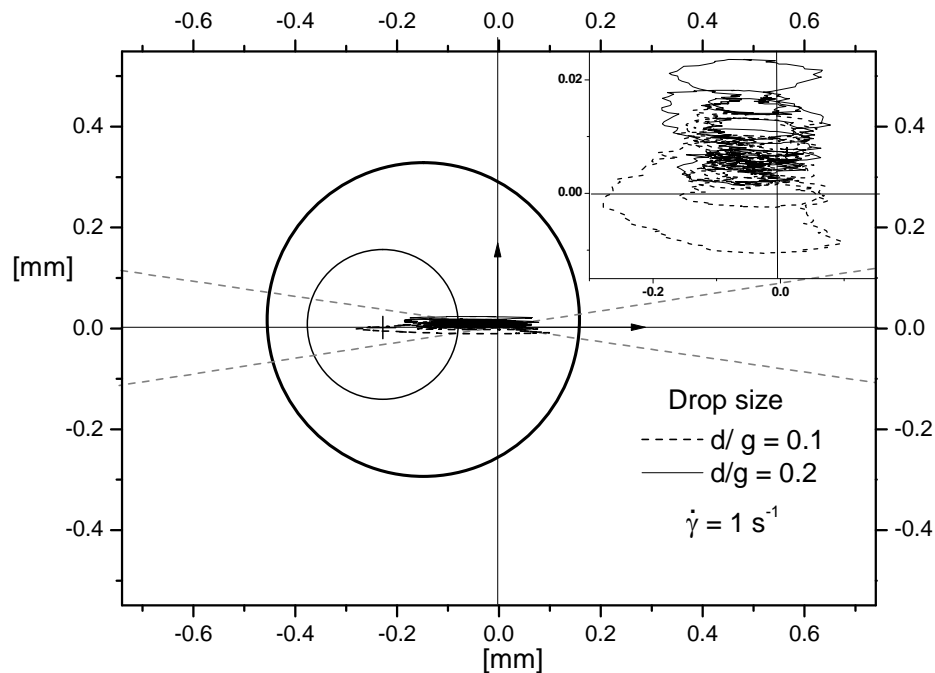
Figure 5.83. Scheme of the visual field of an experiment, the recorded experimental trajectories followed by the center of mass of two drops. The represented drops are proportionally drawn, the smaller has a diameter of $d= 0.3$ mm and the bigger one has a diameter of $d = 0.615$mm. When the drop center is made to coincide with the farthest distance from the stagnation point marked by its trajectory, the smaller drop is completely out of the stagnation point whereas the bigger drop it is not.

It can be seen in the Figure that for the same shear rate, when the drop center is made to coincide with the farthest point from the stagnation point marked by its trajectory, the stagnation point is completely outside the domain of the smaller drop, whereas the bigger drop case still contains it. These different environments imply *different mean values* for the flow parameters; these environments should

be reflected upon the drop deformation. Of course, due to the size, the capillary number of the smaller drop is half the value of the Ca for the bigger one, if the same capillary were required, then higher shear rates would be necessary with the consequent effect in the drop deformation. Given this situation, for future experiments it is highly recommended to use drops with a d/g value in the range of $0.2 < d/g < 0.3$, for the geometries with $\alpha = 0.03$ and $\alpha = 0.05$.

5.2.2.4 Confinement effects

This section present experimental data on the transient behavior for a *confined drop*, induced by a suddenly imposed flow field, with $\alpha = 0.03$. The confinement effect is due to the presence of nearby walls that modify the nominal external stress field upon the drop. This confinement effect in transient phases has barely been studied, with most of the works carried out using simple shear flows: $\alpha = 0$. Because of the difficulty to achieve well defined and continuous strong flow fields, the only previous study on *confined drop deformation*, under flows other that simple shear, are the numerical simulations performed by Reyes (2005). Beyond that –albeit only for simple shear flows– the experimental data are rather few.

Now, given the non-linearity of two-phase flows, the transient phases are complicated enough by themselves and adding the inherent complexities of near wall effects make them particularly difficult and a detailed analysis is also out of the scope of this work. However, the following figures reveal some interesting features worth to investigate in a more detailed and systematic study and they are presented with the purpose of underlying the capabilities of the experimental setup.

In order to study the dynamics of drop deformation in confined flows, many single drop experiments have been carried out in simple shear flows (Vananroye et al 2006b, 2007; Sibillo et al 2006). Those experiments have exposed some specific effects of confinement on drop deformations for high viscosities ratios and are important when the confinement ratio exceeds values of 0.3: that is, a drop size about a third the size of the flow gap. This coincides with the results presented by Reyes (2005) who reported that for a confined drop with $\lambda = 25.8$ immersed in a flow filed with $\alpha = 0.1$, the deformation and orientation parameters are affected when $d/g > 0.25$.

In general the effect of confinement, when $\lambda > 1$, enhances the deformation and reduces the critical Ca. Besides, under confinement conditions in shear flows, the breakup of a drop can be achieved for viscosities ratios that exceed the critical value for non-confined conditions ($\lambda > 4$). For viscosities ratios ranging from 0.3 to 5, confinement induces both an increase in the steady state deformation and a stronger alignment towards the flow direction (Sibillo et al 2006; Vananroye et al 2007). For viscosities

ratios both below and above unity, the steady state deformation parameter is in agreement with the predictions of the theory by Shapira and Haber (1990) (Sibillo et al. 2006; Vananroye et al. 2007), but these theories are limited to small deformations and yield a constant orientation angle of $\theta = 45°$.

Data on the transient dynamics of confined drops are scarce in the literature. On the other hand, numerical simulations have been capable of predicting the complete shape of highly confined drops in simple shear flows (Janssen and Anderson, 2007; Renardy, 2007). Sibillo et al. (2006) performed an experimental study of confinement drop in simple shear flows with a viscosity ratio of unity and reported complex oscillating transients and very elongated drop shapes. More recently, Vananroye et al. (2008), studied the transient dynamics of drops in simple shear flows with different viscosities ratios and under different confinement ratios. Their main conclusions are that: for high viscosities ratios, a deformation enhancement as well as an increased orientation towards the flow direction is seen for $d/g > 0.3$; and in confinement conditions, the steady state regime is reached after a longer time period respect to unconfined cases. They also showed that the confinement ratio affects the overshoots developed in the transient stages but their conclusions are less clear in this topic.

Figure 5.84 shows the dimensionless time evolution of the deformation parameter for different confinement ratios. It can be seen that the degree of confinement affects the amplitude and the dimensionless period of the oscillations. Also, the steady state deformation reached is enhanced. This effect is more accentuated on the curve corresponding to a confinement ratio $d/g = 0.66$. With regards to the orientation angle, Fig. 5.85 shows that confinement reduces the amplitude of the oscillations and delays the undershoots during the transients phase, but the steady state orientation seems to be less sensitive to the confinement and still depends mostly on the applied Ca. Fig 5.86 shows the plot of the evolution of the deformation parameter scaled with the steady state deformation $D_T/D_{Tsteady}$, and contrary to the conclusion of Vananroye et al. (2008), the transitory phase duration is independent from the confinement ratio or from the flow conditions and only depends on the Ca (for the same λ). The behavior described by those plots is very similar to that found in the plots corresponding to the comparisons between the transient phases for different type of flows.

Figure 5.84 can be compared with Fig. 5.71, in both plots the amplitude as well as the period of the oscillations increase and the steady state deformation is larger. Fig. 5.85 can be compared with Fig. 5.73 where the amplitude of the oscillations in the angle are reduced and the undershoot is delayed; besides in both plots the steady state orientation depends only on Ca. Comparing Fig. 5.86 with Fig. 5.72, it can be observed that the duration of the transient phase does not depends on the characteristics of the flow fields but only on the Ca (or in dimensional time, on the properties of the fluids and on the drop

size). Then, the increase of the confinement ratio has the same effect that the increase of the parameter of the type of flow. It means that even when the quantity of vorticity in the flow is not changed, for $\lambda \gg 1$ the confinement inhibits its action and in consequence, the capability of the flow to re-orient the particles diminishes. This explains why the drop breakup is possible for viscosities ratios above the critical values in unbounded conditions. Fig 5.87 is the analogous to Fig. 5.75; this polar plot shows the coupling between the drop deformation and the drop orientation and it can be seen that with the increase in the confinement ratio the curves develop less cycles on its evolution toward the steady state. As in the case of Fig 5.75, its trace becomes narrowed at the ends with smaller amplitudes in the angle. Those plots (Fig. 5.87 and 5.75) show that a reduction or increment in the vorticity (either by changing the quantity via modifying the type of flow or by inhibiting its action via confinement effects) is more evident in the drop deformation, whereas the drop orientation is scarcely affected.
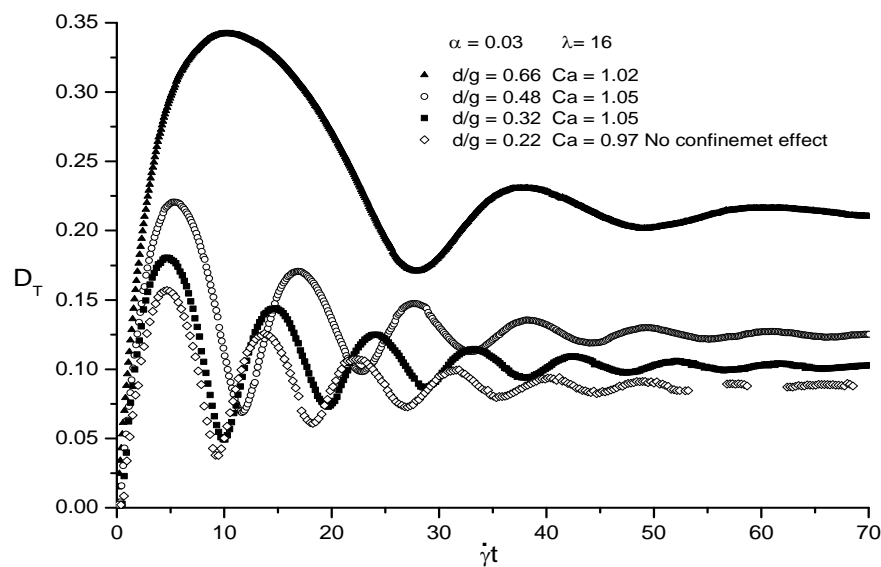
Figure 5.84. Dimensionless time evolution of the deformation parameter for different confinement ratios. The degree of confinement increases the amplitude and period of the oscillations during the transient, and enhances the steady state deformation reached. This effect is accentuated as the confinement ratio increases.
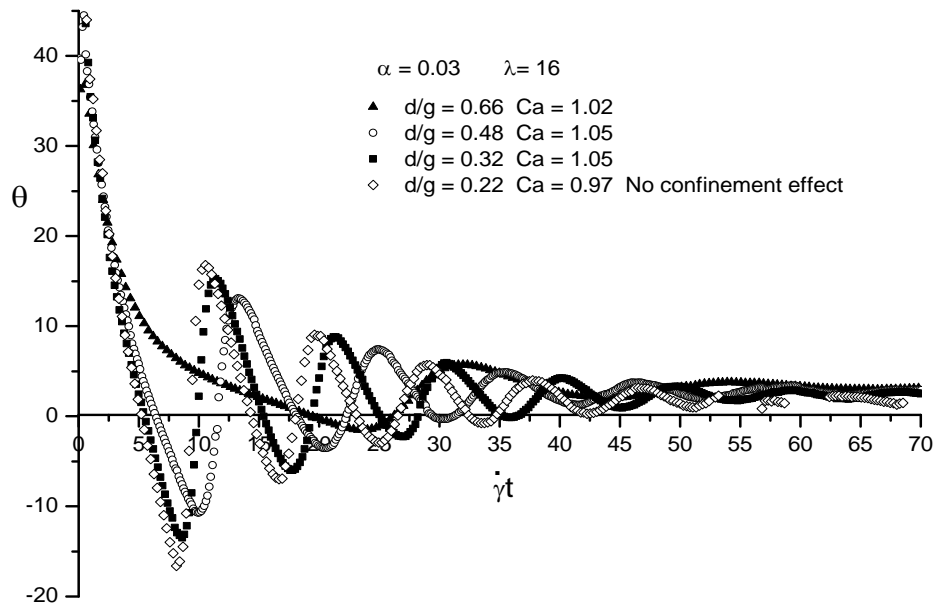
Figure 5.85. **Dimensionless time evolution of the orientation parameter for different confinement ratios. The confinement reduces the amplitude of the oscillations and delays the undershoots in the transients stages but the steady state orientation seems to be less sensitive to the confinement of the drop and still depends almost only on the *Ca* applied.**
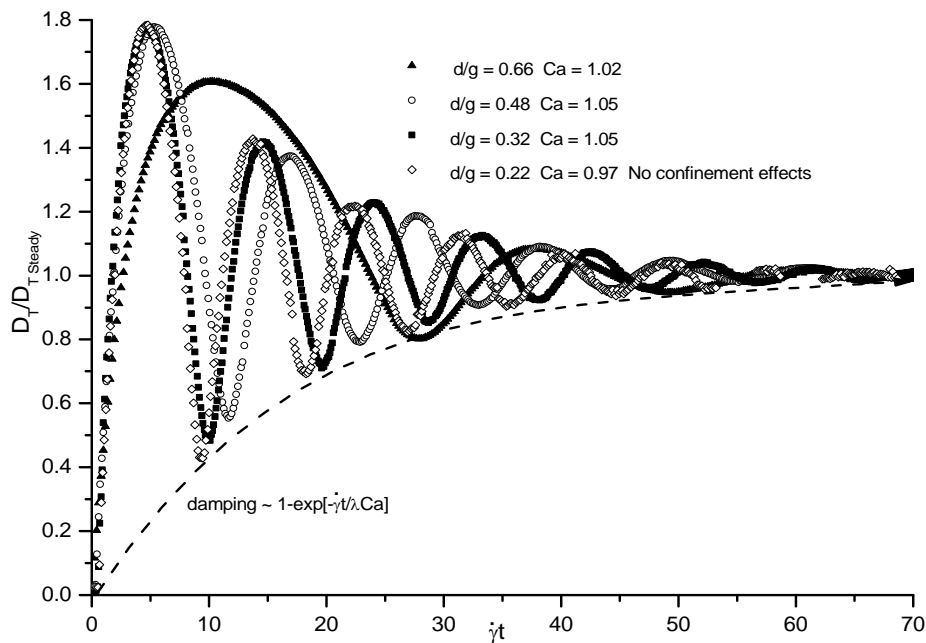
Figure 5.86. **Dimensionless time evolution of the deformation parameter scaled with the steady state deformation. The transient phase duration is independent from the confinement ratio or from the flow conditions and only depends on the *Ca* (for the same λ).**

Figure 5.87. **The polar plot of deformation parameter vs the orientation angle for different confinement ratios.** **It shows the coupling between the drop deformation and the drop orientation.** **With the increase in the confinement ratio the curves develop less cycles on its evolution toward the steady state and as in the case of Fig. 5.75 its form becomes narrowed at the ends with smaller amplitudes in the angle.**

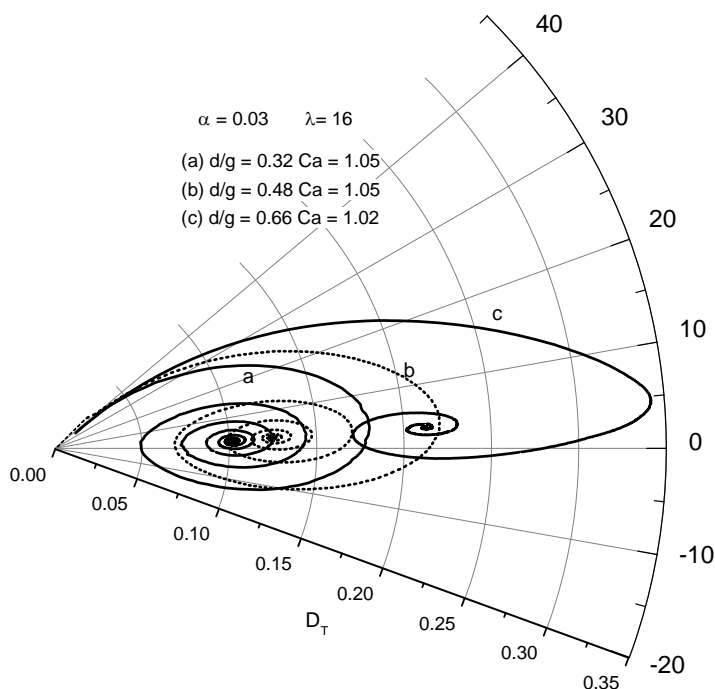Figs. 5.88 to 5.91 show the evolution of the deformation and orientation parameters for different values of the capillary number for the two highest confinement ratios achieved in the experiments $d/g =$ 0.63 and d/g=0.66. Even though they are very similar, the effect on the drop behavior presents important differences. In both cases the main effects of the confinement ratio are present during the first oscillation, and as Vananroye (2008) mentions, the effect increases when Ca rises. This is clearly shown in the highest capillary numbers in Figs. 5.88 and 5.89 with $Ca = 2.1$ for $d/g = 0.63$ and $Ca = 1.57$ for $d/g = 0.66$ where actually, the breakup of the drop is achieved. The orientation angle behavior is also mainly affected in the first oscillation. Fig. 5.90 shows that unlike unbounded conditions (Fig. 5.65), in this case the curves of the evolution for the higher Ca values, crosses the zero value almost at the same time at $t \approx 15s$ for the plot with $d/g = 0.63$ and $t \approx 25s$ for the plot with $d/g = 0.66$. But, still as in Fig. 5.65, the minimum values of each curve is reached faster for the higher Ca. Fig. 5.91 shows the orientation angle evolution in dimensionless time and as in the previous plot, and unlike the unbounded conditions (Fig. 5.67), the curves crosses the zero at different dimensionless times. And as in Fig. 5.67, the minimums are reached at longer dimensionless times.
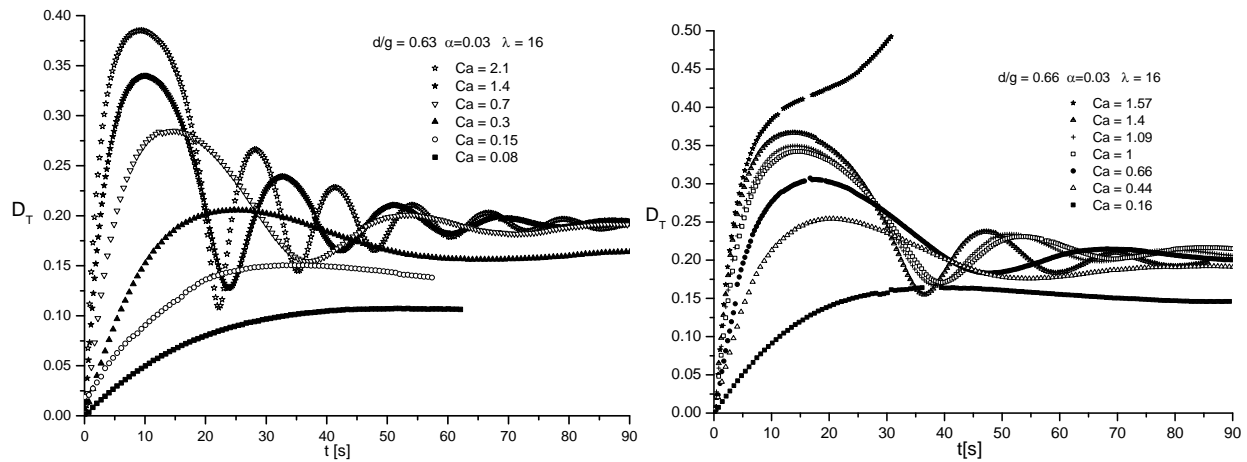
Figure 5.88. **Evolution of the deformation parameter for different values of the capillary number for the two highest confinement ratios achieved in the experiments *d/g* = 0.63 and *d/g* = 0.66. Even when they are very similar, the effect on the drop behavior has important differences. In both cases the main effects of the confinement ratio are present during the first oscillation and as Vananroye (2008) mentions, the effect increases with *Ca*.**
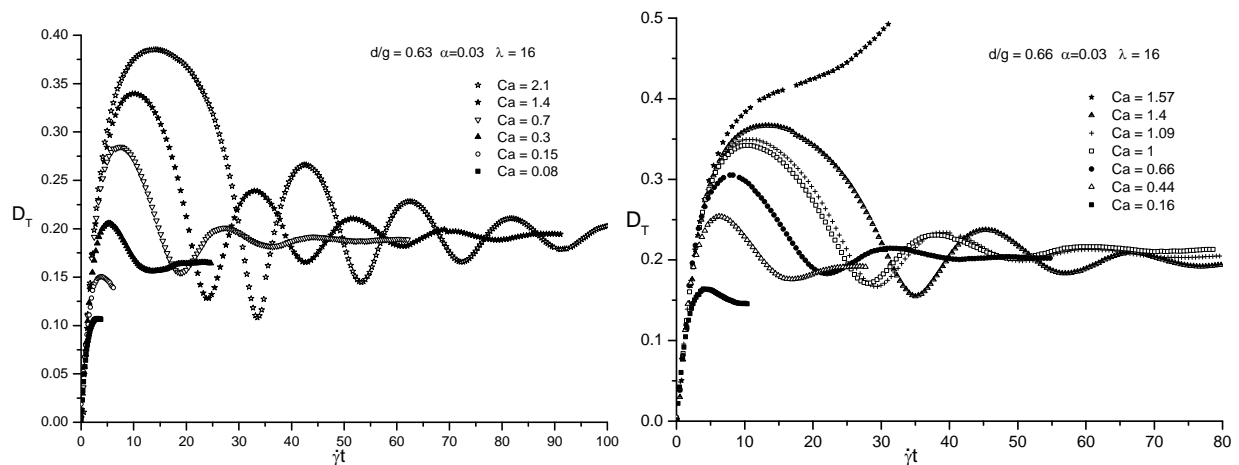
Figure 5.89. Dimensionless time evolution of the deformation parameter for different values of the capillary number for the two highest confinement ratios achieved in the experiments *d/g* = 0.63 and *d/g* = 0.66. The plot shows that contrary to unconfined conditions, the period of the first oscillation is not the same than the following oscillations but longer and this effect increases with *Ca* and the confinement ratio.
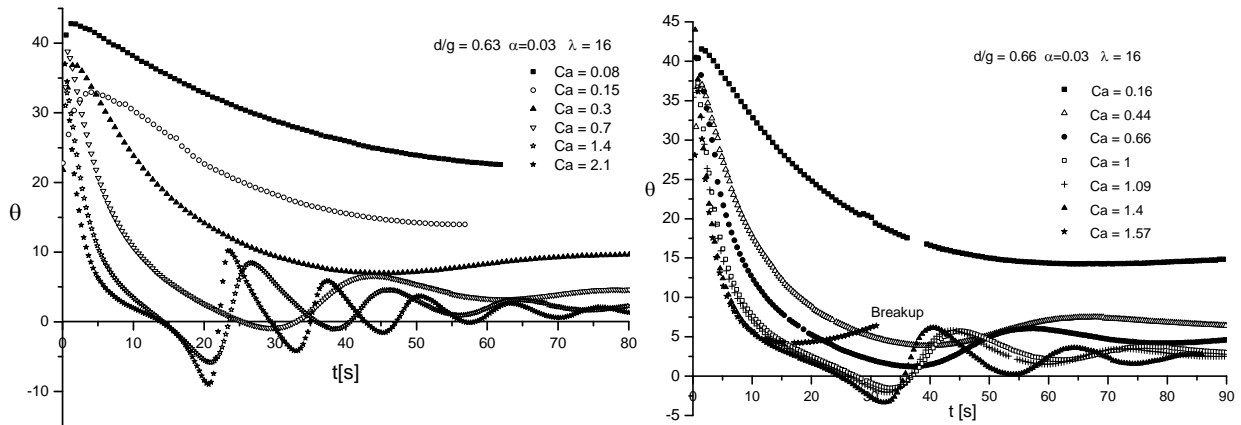
Figure 5.90. **Evolution of the orientation angle parameter.** The curves are also mainly affected in the first oscillation and unlike unbounded conditions (Fig. 5.67), the curves for the higher *Ca*, crosses the zero value almost at the same time at $t \approx 15s$ for the plot with *d/g* = 0.63 and $t \approx 25s$ for the plot with *d/g* = 0.66. The inflexion points in the curves for the highest *Ca* values are clearly shown.
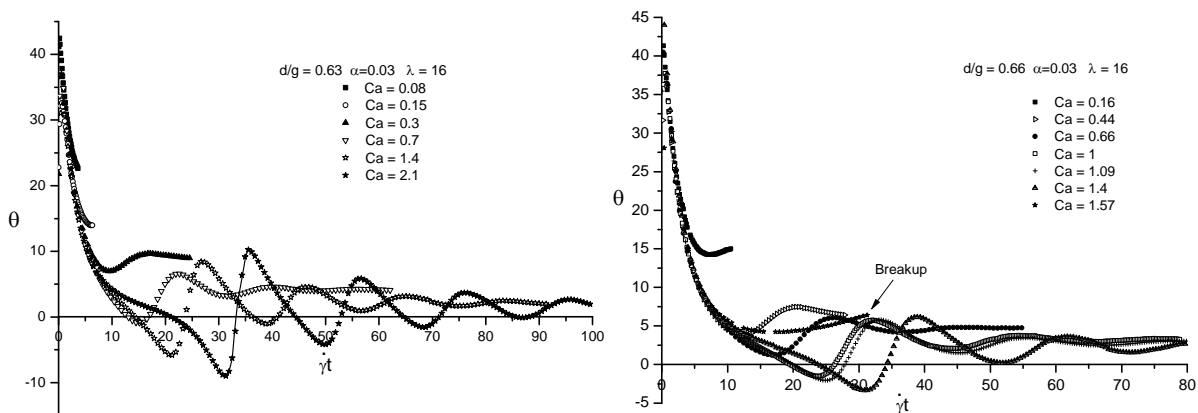
Figure 5.91. **Dimensionless time evolution of the orientation angle parameter.** The angle curves are also mainly affected in the first oscillation and unlike unbounded conditions (Fig. 5.67), the curves crosses the zero at different dimensionless times and as in Fig. 5.67 the minimums are reached at longer dimensionless times. Also as in the previous figure, the inflexion points in the curves for the highest *Ca* values are clearly shown.

The evolution of the orientation angle is plotted in detail in Fig. 5.92, where the effect of the *Ca* and *d/g* in the first oscillation is shown. By observing the curves corresponding to *Ca* = 1.4 for the two confinement ratios, for (a) *d/g* = 0.63 the minimum value is achieved at $\dot{\gamma}t \approx 21$, with an orientation angle of $\theta = -5.8°$ and (b) in the plot for *d/g* = 0.66, the curve has a minimum values of $\theta = -3.4°$ and is reached after $\dot{\gamma}t \approx 31$. But once the first oscillation has developed, all subsequent oscillations reduce their period and become the same, which is almost constant for all *Ca* values and for the same confinement ratio.
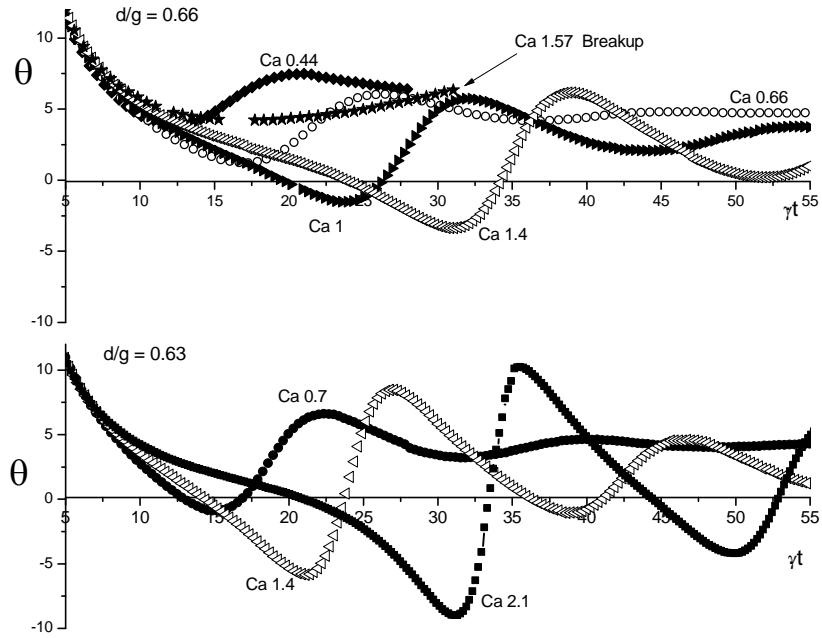
Figure 5.92. Detail of the evolution of the orientation angle showing the effect of *Ca* and *d/g* in the first oscillation. The curves corresponding to *Ca* = 1.4 in the plot for *d/g* = 0.63 achieves the minimum value at $\dot{\gamma}t \approx 21$ with an orientation angle of $\theta = -5.8°$ whereas and the plot for *d/g* = 0.66, the minimum value is $\theta = -3.4°$ and is reached at $\dot{\gamma}t \approx 31$. But once the first oscillation has developed, the subsequent oscillations reduce its period and all they have the same (which is almost constant) for all *Ca* values in the same confinement ratio.
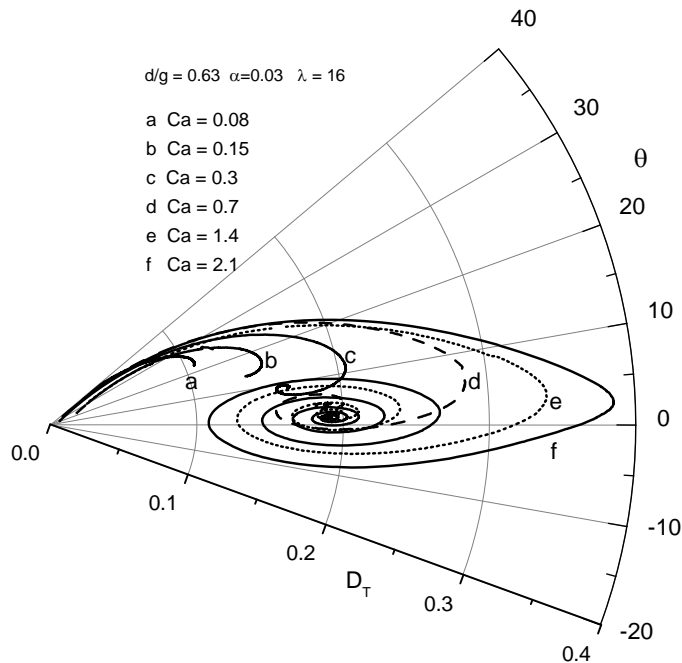
Figure 5.93. Polar plot of D_T vs the orientation angle θ for a confinement ratio *d/g* = 0.63 and different capillary numbers. The breakup was not achieved even with a *Ca* = 2.1, where although the curve present a very peaked, the vorticity is enough to stop the growth of the deformation the oscillatory behavior makes present, taking to the drop to the same steady state.
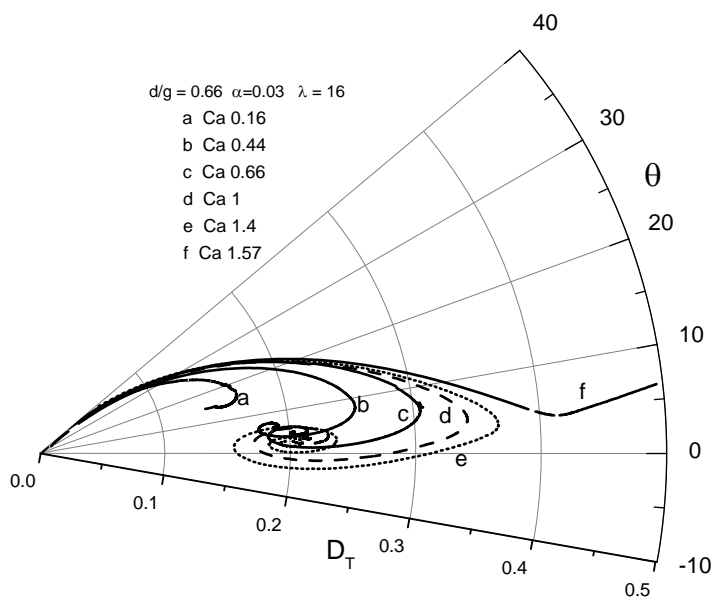
Figure 5.94. Polar plot of D_T vs the orientation angle θ for a confinement ratio d/g = 0.66 and different capillary numbers. The inhibition of the vorticity is enough to disable the reorientation of the particles for Ca=1.57 and hence the curve shows an evolution that appears develop an spiral but suddenly it shows an abrupt inflexion, meaning that the drop is not going to be contracted but will continue elongating and eventually will break up.

An interesting characteristic that can be notice about the curves of the orientation for the highest capillary numbers in Figs 5.90 to 5.92 is an inflexion point that occurs before the first oscillation, the curves for those Ca have an evolution that, when approaching $\theta = 0$, it appears that they are reaching the minimum, i.e., $d\theta/dt = 0$, but suddenly, in those points they develop an inflexion in the trajectory and the angle continues falling, reaching negative values.

Also and on one hand, for the plots corresponding to d/g = 0.63, the breakup of the drop was not achieved even with a Ca = 2.1, where although the curve presents a very peaked form in the polar plot in Fig. 5.93, the vorticity is enough to stop the growth of the deformation and once this reach a maximum values, about 0.39, the drop is rapidly reconfigured with a fast retraction and a subsequent oscillatory behavior, but taking the drop to the same steady state deformation reached for a lower Ca. On the other hand, the plots corresponding to d/g = 0.66 show that by increasing the confinement degree by a small amount, the behavior is completely different: so different that the breakup is reached with a capillary number Ca = 1.57 (even lower that the maximum Ca in the plot for d/g = 0.63). At this Ca value, the inhibition of the vorticity is enough to disable the reorientation of the particles; hence, the curve in Figs 5.88 and 5.89 for that Ca show a continuously increasing deformation that eventually leads to breakup. In Figs 5.90, 5.91 and 5.92, the curve for Ca = 1.57 seems to follow a typical evolution almost equal to that

for $Ca = 1.4$, but the inflexion point does not occurs and hence the angle reaches a minimum about $\theta = 4°$ and begins to rise. This is more clear in the polar plot in Fig. 5.94 where the curve for $Ca = 1.57$ shows an evolution that initially appears to develop an spiral path but suddenly, when D_T surpasses a value about 0.4 and seems that is reaching its maximum deformation, the curve shows an abrupt inflexion, meaning that the drop is not going to be contracted but will continue elongating. With that, it is shown that in a flow field with $\alpha = 0.03$ the critical capillary number for the breakup of a drop with $\lambda = 16$ is lower than $Ca = 1.57$ and higher than $Ca = 1.4$ when $d/g =0.66$ (a more exact value of Ca would require a more systematic experimentation). It is possible that with $d/g = 0.63$ the breakup occurs, but then Ca must be higher than $Ca = 2.1$. A characteristic noted that is worth emphasizing, is that the oscillatory behavior was never suppressed; i.e., it was not observed a transition from a damped oscillatory behavior to a monotonic evolution or even to a transient evolution with just one overshoot.

6 Interfacial tension

In this chapter the methodology to measure the interfacial tension of the fluids based on drop deformation is presented. The measuring principle is the interplay between shear-induced viscous stresses acting to deform drop shape and the restoring effect of interfacial tension. Experimental data on drop shape under both steady-state and transient deformation were compared to classical theories of drop deformation, being the interfacial tension the only fitting parameter.

6.1 Interfacial tension measurement

Interfacial tension is an important physical property that characterizes the interfacial free energy between two immiscible liquids. It plays a dominant role in multi-phase systems, such as polymer blends and alloys, found in many scientific and industrial applications. Many attempts have been made to develop accurate and convenient techniques to measure the interfacial tension (Guido et al. 2002; Megias-Alguacil et al. 2004; Mo et al. 2000). The general principle of these techniques is based on a balance between a driving force (Brownian forces, gravitational and inertia forces, or viscous forces) and a resistance due to the interfacial force that tends to minimize the contact area between the phases. The different techniques can generally be divided in two catalogues: equilibrium methods or steady states and dynamic methods or drop retraction. With equilibrium methods the interfacial tension value is obtained by measuring the shape of the liquid-liquid interface when it is equilibrated by some external force. Dynamic methods make it possible to determine the interfacial tension from the time evolution shape of a distorted fluid particle toward its equilibrium form. The latter are based on the shape evolution of fluid drop from a non-equilibrium state to an equilibrated state.

6.1.1 Interfacial tension from steady states

Conventional equilibrium methods (Drelich et al 2002), require the accurate measurement of the density difference between two liquids; however, in many cases the density difference is very small or inexistent. Additionally these conventional methods are not recommended for high viscous liquids because of the long time required for the system to reach the equilibrium. For such cases, the equilibrium methods, like steady state deformation (Guido et al. 2002; Megias-Alguacil et al, 2004, 2006) and steady state orientation (Guido et al. 2002; Megias-Alguacil et al. 2004, 2006; Rust and Manga 2002), constitute an alternative to the traditional ones. Existing theories on drop deformation under simple shear flow were employed for calculating the interfacial tension. Even though the TRM flow type it is not simple shear flow, it is very close to it and those theories represents an excellent benchmark, as well as a test for the fluid mechanics of two-phase flows under a novel set of deformation-orientations.

The measuring principle is the interplay between flow-induced viscous stresses, acting to deform drop shape, and the restoring effect of interfacial tension. An initial spherical drop placed in a low Reynolds number flow, deforms with a time-dependent shape and orientation until it reaches a steady-state geometry. For a simple shear flow, the steady drop shape and orientation depends on the viscosities ratio and the capillary number Ca. The steady state deformation of the drop was first analyzed by Taylor (1932, 1934) and can be described using the following well-known equation:

$$D_T = Ca \frac{19\lambda + 16}{16\lambda + 16} = \dot{\gamma} \, r_0 \frac{\mu_1}{\sigma} \frac{19\lambda + 16}{16\lambda + 16} = K_{Slope}^T \, \dot{\gamma} \, r_0, \tag{6.1}$$

from this Equation, the interfacial tension is then given by the slope of D_T *vs* $\dot{\gamma} r_0$ in the form:

$$\sigma = \frac{\mu_1}{K_{Slope}^T} \frac{19\lambda + 16}{16\lambda + 16} , \tag{6.2}$$

where K_{Slope}^T is the constant value (of the slope) for Taylor's theory. Associated with the deformation of the drop under flow conditions, there is an orientation process which makes the deformed drop reach a certain angle θ with respect to the flow direction. This angle depends on the capillary number and decreases as the applied shear rate increases and the drop becomes more and more aligned with the flow direction. An equation relating the angle θ to the capillary number under steady state conditions was derived by Chaffey and Brenner (1967),

$$\theta = \frac{\pi}{4} - \frac{(19\lambda + 16)(2\lambda + 3)}{80(1 + \lambda)} Ca = \frac{\pi}{4} - \frac{(19\lambda + 16)(2\lambda + 3)}{80(1 + \lambda)} \frac{\mu_1}{\sigma} \dot{\gamma} \, r_0, \tag{6.3}$$

with θ in radians. From Eq. (6.3) the interfacial tension is also given by the slope of $(\theta - \pi/4)$ *vs* $\dot{\gamma} r_0$ in the form:

$$\sigma = -\frac{\mu_1}{K_{Slope}^{ChB}} \frac{(19\lambda + 16)(2\lambda + 3)}{80(1 + \lambda)} \,.$$ (6.4)

where K_{Slope}^{ChB} is the slope constant for Chaffey and Brenner model. Cox (1969) also developed a theoretical analysis and provided expressions for the steady state deformation parameter and the steady state orientation angle θ as a function of Ca and λ for simple shear flows. It is important to point out that the most appropriate range of applicability of Cox theory is at $\lambda \gg 1$ valid for small Ca vs. D_T and any value of Ca for θ. The equations obtained from Eqs. (5.12) and (5.13) are:

$$D_T = \frac{5(19\lambda + 16)}{4(1 + \lambda)\sqrt{(19\lambda)^2 + \left(\frac{20}{Ca}\right)^2}} \,,$$ (6.5)

and

$$\theta = \frac{\pi}{4} + \frac{1}{2} tan^{-1}\left(\frac{19}{20} Ca \,\lambda\right),$$ (6.6)

with θ in rad. Eq (6.6) can be written as:

$$tan\left(2\theta - \frac{\pi}{2}\right) = \frac{19}{20} Ca \,\lambda = \frac{19}{20} \frac{\mu_1 \,\lambda}{\sigma} \,\dot{\gamma} \,r_0 = K_{Slope}^{C} \,\dot{\gamma} \,r_0 \,,$$ (6.7)

which presents a linear relation and then, as in previous cases, the interfacial tension can be computed as

$$\sigma = \frac{19}{20} \frac{\mu_1 \,\lambda}{K_{Slope}^{C}} \,.$$ (6.8)

6.1.2 Interfacial tension from drop retraction

Dynamic methods are more convenient, especially when carried out under the conditions above mentioned. In our case, an additional disadvantage, important to mention, is the fact that these methods do not have an explicit dependence on the flow type, but only on the properties of the fluids.

Here Three main approaches are studied in the context of flow generated by TRMs: Breaking Thread method (BT) (Guillermo and Demarquette 2005), Imbedded Fiber Retraction method (IFR) (Carriere and Cohen 1991) and Deformed Drop Retraction method (DDR) (Mo et al. 2000; Luciani et al. 1997; Guido and Villone 1999; Son and Yoon 2001; Son and Migler 2002; Liu et al. 2005; Megias-Alguacil et al. 2006) are included in this catalogue. BT method (based on Tomotika's (1935) equation) has the inconvenient that the conditions needed for carrying it out are not easy to attain in practical experiments (Son and Migler 2002). IFR method, although it does not have the limitations of BT method, the mathematical model used requires some extra empirical parameters (Son and Migler 2002). Fortunately, the DDR method, as proposed firstly by Luciani et al. (1997) and Guido and Villone (1999)

overcome the limitations of BT and IFR methods. The principle of DDR is to measure the dimensions of an ellipsoidal drop deformed in its evolution to a sphere shape.

Luciani et al. (1997) and Guido and Villone (1999) measured the interfacial tension by observing the shape evolution of a drop initially deformed by an external shear force. From a general equation derived by Rallison (1984), they get the following equation describing the evolution of a deformed drop —after the flow has stopped— towards an equilibrium spherical form:

$$D_T = D_{T0}\, e^{-t/\tau}, \tag{6.9}$$

where

$$\frac{1}{\tau} = \frac{\sigma}{\mu_1 r_0} \left[\frac{40(\lambda + 1)}{(2\lambda + 3)(19\lambda + 16)} \right]. \tag{6.10}$$

An equivalent equation is obtained by Mo et al., (2000), from the evolution equation proposed by Maffetonne et al., (1998). In this method the drop shape is described by a symmetric, positive-definite, second rank tensor S whose eigenvalues Λ represent the square semi-axes of the ellipsoid that represents the deformed drop. Hence to describe de drop relaxation, the shape parameter $\Lambda_1 - \Lambda_2$ is used (Mo et al. 2000):

$$\Lambda_1 - \Lambda_2 = (\Lambda_1 - \Lambda_1)_0 \exp\left(-\frac{f_1}{k} t \right), \tag{6.11}$$

with

$$\frac{f_1}{k} = \frac{\sigma}{\mu_1 r_0} \left[\frac{40(\lambda + 1)}{(2\lambda + 3)(19\lambda + 16)} \right] = \frac{1}{\tau}. \tag{6.12}$$

According to the definition of S, $\Lambda_1 = L^2$, $\Lambda_2 = B^2$; which are the semi-axes of the ellipsoidal deformed drop. In both cases, the retraction process is characterized by a relaxation time τ, and can be expressed as:

$$\frac{Instant\ shape}{Initial\ shape} = \left[e^{\frac{-t}{\tau}} \right], \tag{6.13}$$

again with

$$\tau = \frac{\mu_1 r_0}{\sigma} \left[\frac{(2\lambda + 3)(19\lambda + 16)}{40(\lambda + 1)} \right]. \tag{6.14}$$

Using Luciani and Guido method, the shape is described by the Taylor deformation parameter D_T Eq. (1.18), and using Mo et al., method, the shape is described by

$$D_M = (L^2 - B^2) \tag{6.15}$$

In the process of a drop retraction, λ, μ_1, σ and r_0 are constant, then we have that σ can be calculated using Eq. (6.13) in the form:

$$ln\,(D/D_0)\ =\frac{-1}{\tau}\,t\ =\frac{-\sigma}{\mu_1\,r_0}\left[\frac{40(\lambda+1)}{(2\lambda+3)(19\lambda+16)}\right]t\,. \tag{6.16}$$

from the slope of the linear plot. The interfacial tension then is given by

$$\sigma=-\ K_{Slope}^{R}\ \mu_1\ r_0\left[\frac{(2\lambda+3)(19\lambda+16)}{40(\lambda+1)}\right]. \tag{6.17}$$

6.2 Interfacial tension for low viscosities ratio

Figure 6.1 is an example of the deformation and orientation data obtained for an experiment of a drop with low viscosities ratio $\lambda=0.012$. The transitory and steady states can be observed in the plots. Steady-state conditions are maintained as long as the flow is applied and once the flow is stopped the drop recovers its spherical shape (region of retraction in Fig. 6.1).
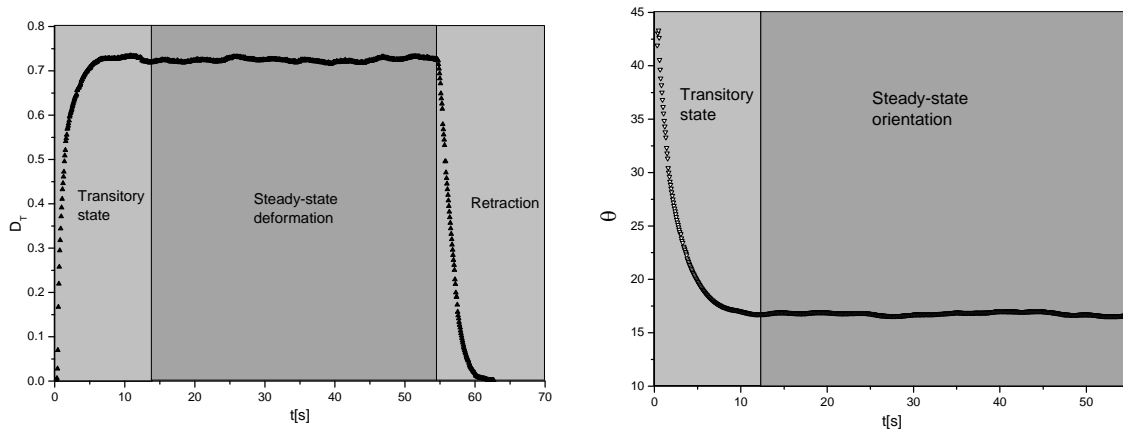
Figure 6.1. Deformation and orientation parameters evolution. The plots corresponds to an experiment with a drop with r_0 = 0.41 mm and under a shear rate $\dot{\gamma}=1.0$ s^{-1} , the viscosities ratio of the system is $\lambda=0.012$ and the flow type is $\alpha=0.13$.

Steady-state deformation

Figure 6.2 shows a plot for the experimental data of the steady state deformation D_T as function of the applied shear rate for the three types of flow and for $\lambda=0.012$. The figure shows a straight line with the slope of a linear fit from which the value of interfacial tension can be obtained using Eq. (6.2) with $\mu_1=5.1\,\text{Pa}\cdot\text{s}$, . For these plots, only the values of $D_T<0.2$ were use —in order to ensure the validity of Taylor's theory— and the condition of $D_T=0$ at $\dot{\gamma}=0$ was imposed in the linear fitting. As expected the slope for the linear fit of $\alpha=0.13$ is slightly higher than the ones for the other two flow types $\alpha=0.05$ and $\alpha=0.03$, which are the closest to simple shear flow and whose slopes almost overlaps. Table 6.1 shows the values of the interfacial tension calculated from the slope of this plots as:

$$\sigma = \frac{5.11}{\text{slope}} \tag{6.18}$$

Table 6.1 Values of the interfacial tension for the canola oil and the PDMS T35.

Flow Type α	Interfacial Tension [mN/m]
0.13	2.71
0.05	2.79
0.03	2.78
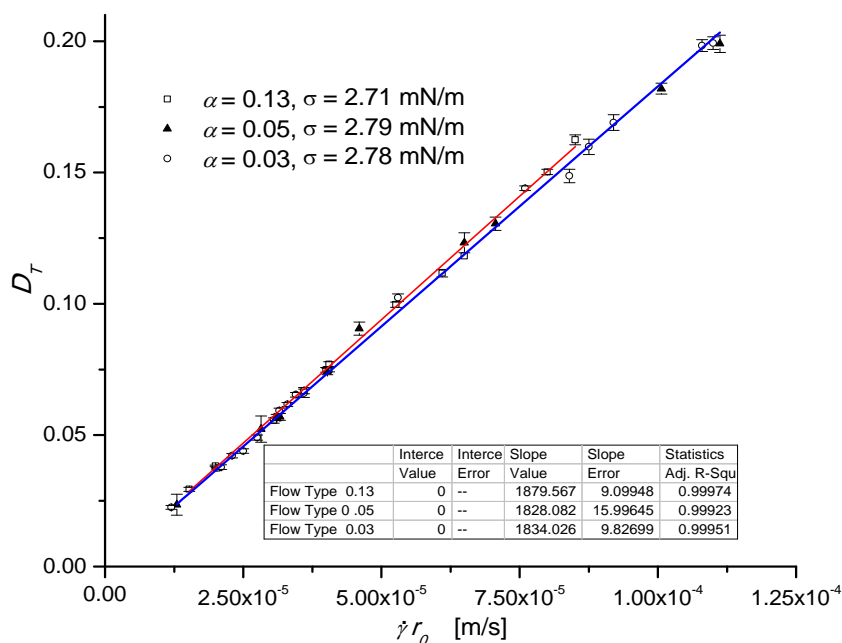
Figure 6.2. Steady-state deformation as function of the shear rate applied and the drop size.

Steady-state orientation

Considering that drop orients under the action of the flow, and that the orientation angle depends on the capillary number, it is also possible to calculate the interfacial tension from the experimental data available. By observing the plots of θ as function of the shear rate applied, it is clear that the most appropriate theory for calculating the interfacial tension is that from Chaffey and Brenner (1967) that presents a linear relationship between the orientation angle and the shear rate applied. Fig. 6.3 shows a plot for the experimental data of the steady-state orientation as a function of the shear stress applied for the three flow types and $\lambda = 0.012$. The value of interfacial tension can be calculated from the slope of a linear fit and using Eq. (6.4).   For these plots —and due to large experimental uncertainties in measuring the orientation when the shape of the drop is close to a sphere— only values of θ between $\pi/9$

and $2\pi/9$ ($20° < \theta < 40°$) were used; and the condition of $\theta = \pi/4$ at $\dot{\gamma} = 0$ was imposed. In this case the difference in the drop orientation due to the flow type is more evident as can be seen in the linear fit of $\alpha = 0.03$ where the slope is slightly higher than the other two. Table 6.2 shows the values of the interfacial tension calculated from this plot using Eq. (6.4) with $\mu_1 = 5.1$ Pa s.
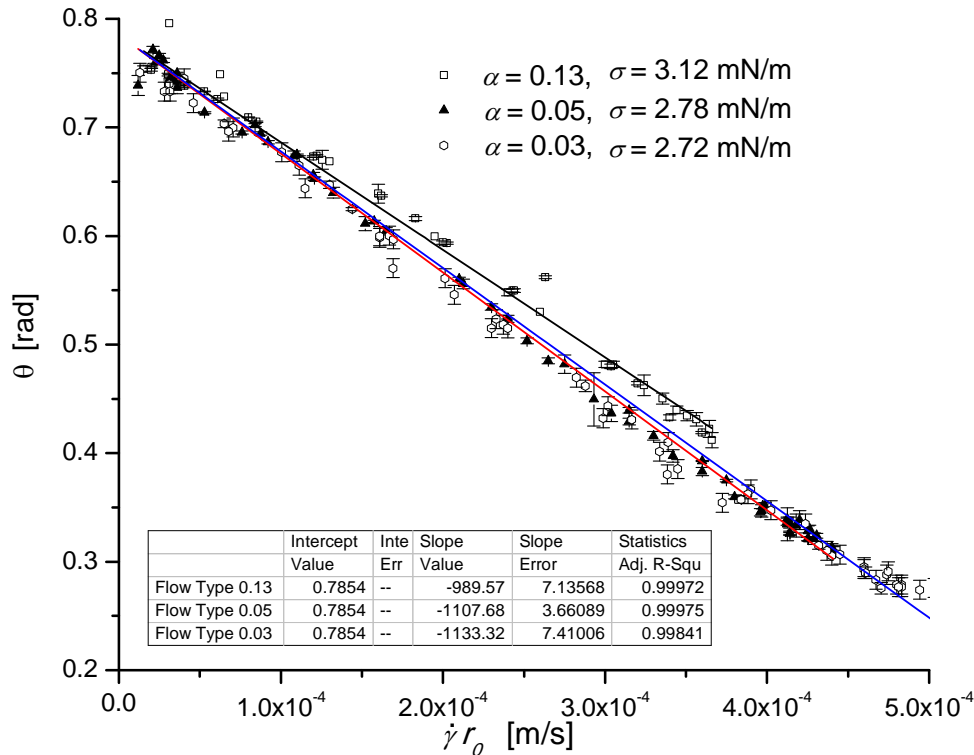
Figure 6.3. Steady-state orientation as function of the shear rate applied and the drop size

	Intercept	Inte	Slope	Slope	Statistics
	Value	Err	Value	Error	Adj. R-Squ
Flow Type 0.13	0.7854	--	-989.57	7.13568	0.99972
Flow Type 0.05	0.7854	--	-1107.68	3.66089	0.99975
Flow Type 0.03	0.7854	--	-1133.32	7.41006	0.99841

Table 6.2. Values of the interfacial tension for the canola oil and the PDMS T35 from drop orientation.

Flow Type parameter α	Interfacial Tension [mN/m]
0.13	3.12
0.05	2.78
0.03	2.72

Drop retraction

Given that the retraction process is independent from the deformation process, the data for all experiments can be used regardless the flow type. Unlike previous methods, in this case, it is possible to obtain a value of the interfacial tension every time the drop is deformed. Each retraction process has a characteristic curve for the exponential relaxation.

When the deformation is large enough and since the deformation parameter used is only a two dimensional parameter, at this point it is difficult to describe the degree of distortion due to 3-D effects. Fig. 6.4 shows the retraction process for the longest and shortest axis of a drop, for different initial deformations. Measuring the deformation with the Taylor parameter, the assumption for equal-short-axis is made ($B = W$); however, perhaps for large deformations, this condition it is not necessarily present. Deformed drops with unequal-short-axis *vs.* equal-short axis, may have different retraction traces, although they have the same interfacial tension. Many authors used the Taylor deformation parameter D_T as a measure of the deformation in the retraction process, however, that this is not always the best choice, instead, the use of D_M in Eq. (6.15) appears to be a better option. Figs. 6.5 and 6.6 show that after plotting the data for $ln(D/D_0)$, one can see that the distortion from a straight line increases as the initial deformation increases, and this effect is attenuated when the D_M parameter is taken rather than Taylor parameter. Nevertheless, Taylor parameter gives acceptable results when the initial Taylor deformation $D_T < 0.2$; if this condition is fulfilled, there is not much difference in taking any parameter (see Fig. 6.7). If not the latter case, D_M, has been proved to give acceptable measures of the interfacial tension Liu et al. (2005).
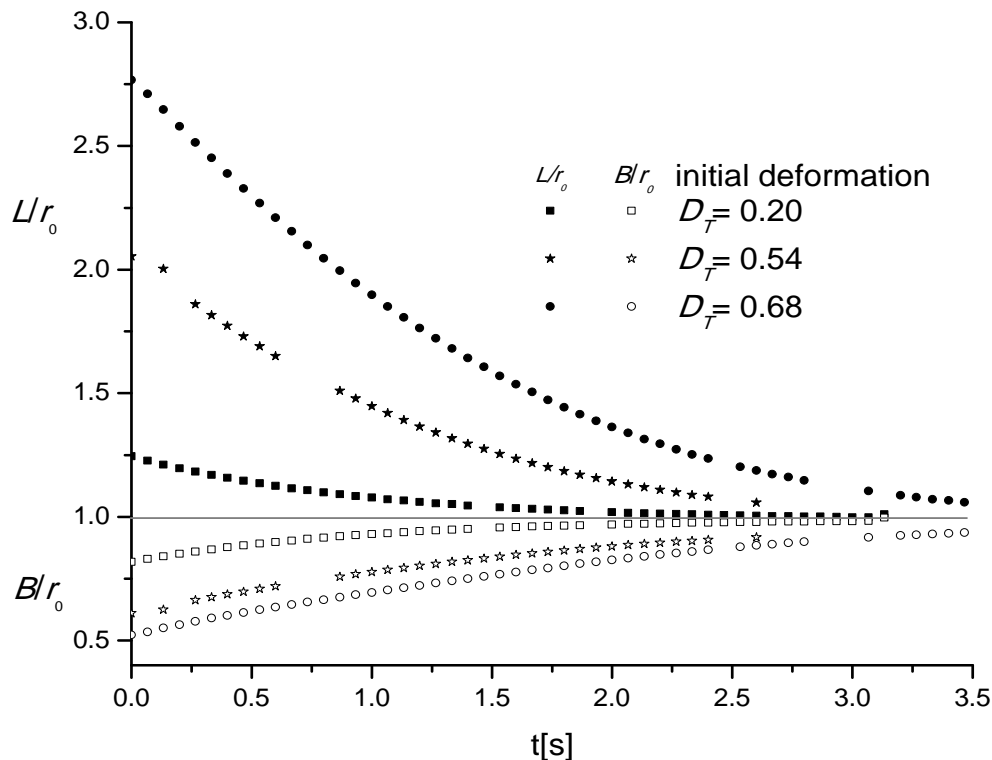
Figure 6.4. Retraction process of the longest and shortest axes for different initial Taylor deformations of the same drop, r_0 = 0.4 mm and $\lambda = 0.012$.
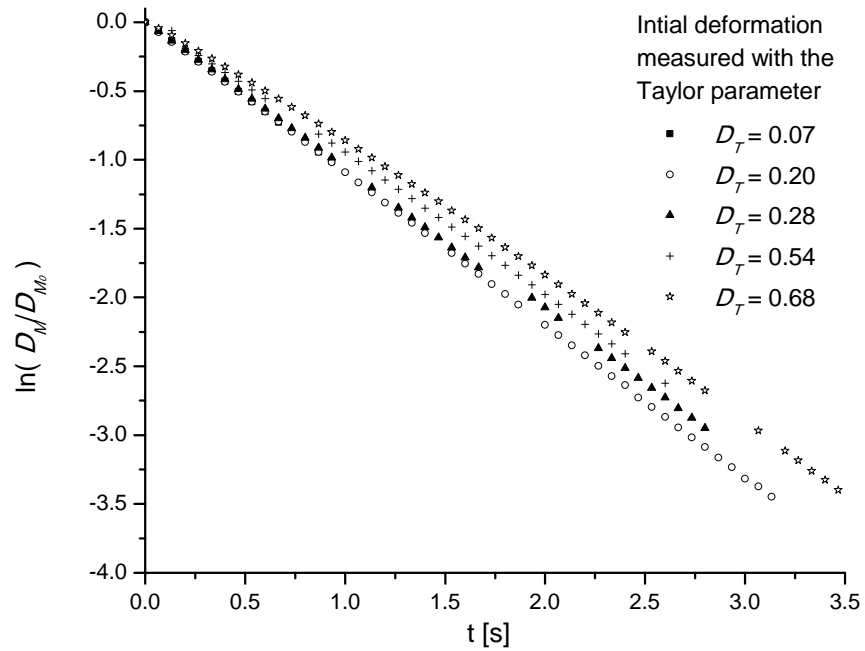
Figure 6.5. Retraction of the drop taking Mo parameter D_M for characterizing the drop shape r_0 = 0.4mm and λ = 0.012. The initial deformation is measured with the Taylor parameter D_T.
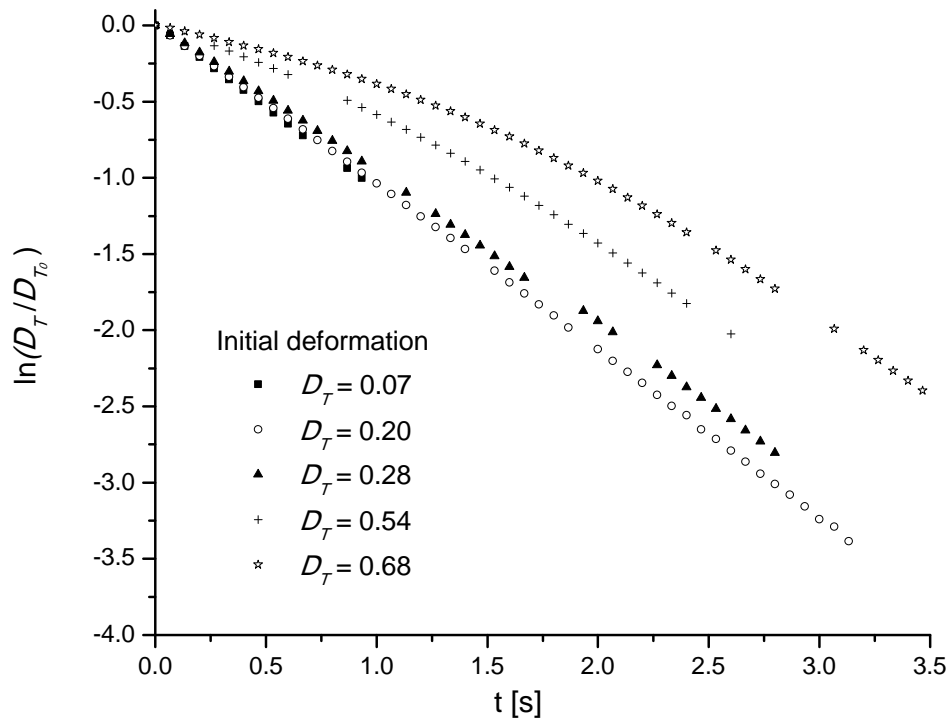
Figure 6.6. Retraction of the drop taking Taylor parameter for characterizing the drop shape r_0 = 0.4mm and λ = 0.012.

Figure 6.7. Comparison of the Taylor and Mo parameters for characterizing the drop shape r_0 = 0.2 mm and λ = 0.012

If the conditions for the experiments are μ_1 and λ are constant, then only one common value for the interfacial tension in all the measurements is obtained. Liu et al. (2005) carried out an extensive revision for the calculation of the interfacial tension using the DDR method, and compared their results with those form available in literature (obtained by diffe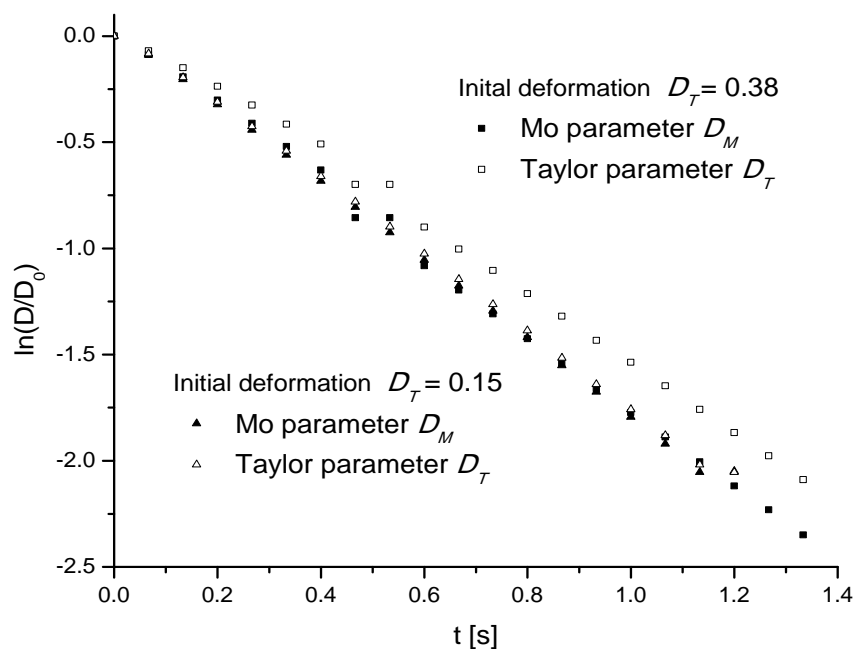rent methods). They found that the retraction scale—or the initial deformation D_0— is important for an accurate determination of the interfacial tension. Liu and coworkers also found that when taking values for $D_T < 0.2$ produces acceptable measures (i.e. error < 10 %).

In order to calculate a more reliable value, the optimum retraction scale is $D_T \cong 0.15$. They also found that by choosing this scale, the effects for unequal-short-axis are small. Figs 6.8 and 6.9 show the retraction process for two different drops and for different initial deformations. It can be seen that the value for the interfacial tension calculated from the slope is different even for the same drop depending on the initial deformation. Table 6.3 shows the value for the interfacial tension taken different values of the initial deformation D_0 measured with the Taylor parameter.

Table 6.3. Interfacial tension between the Canola Oil and the PDMS T35 calculated from different initial deformations measured in terms of Taylor deformation.

Values for D_0	Interfacial tension [mN/m]	Standard deviation [mN/m]
$D_0 = 0.15$	2.72	0.023
$0.10 < D_0 < 0.20$	2.65	0.095
$D_0 < 0.50$	2.73	0.27
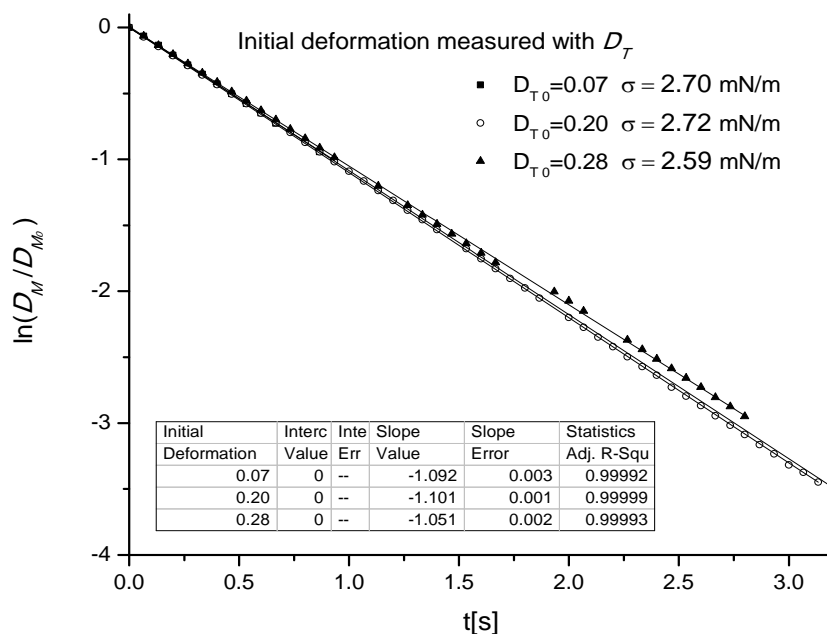
Figure 6.8. Drop retraction for $r_0 = 0.4$ mm and $\lambda = 0.012$. The interfacial tension is computed from deformation data measured with the Mo parameter D_M.
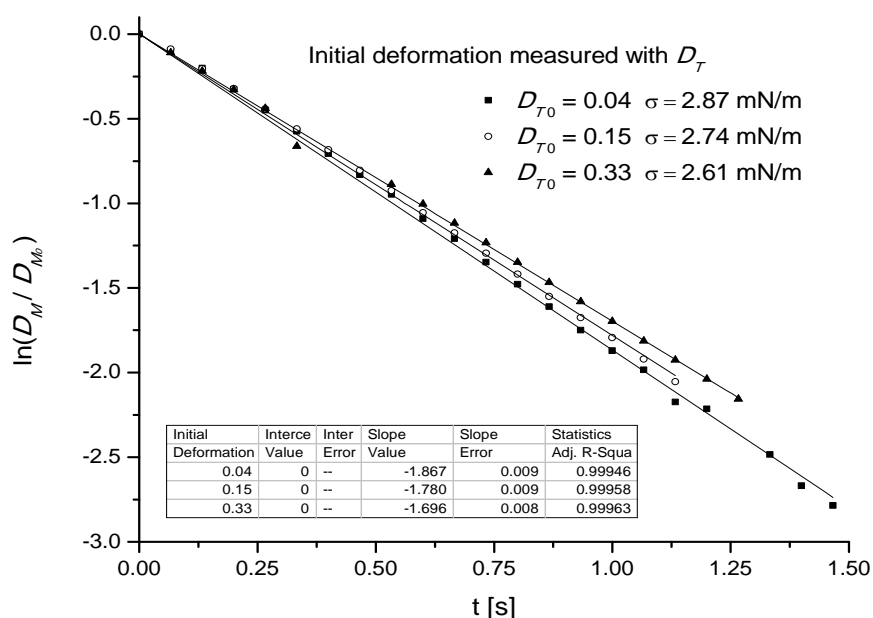
Figure 6.9. Drop retraction for $r_0 = 0.25$ mm and $\lambda = 0.012$. The interfacial tension is computed from deformation data measured with the Mo parameter D_M.

6.3 Interfacial tension for high viscosities ratio

In the case of high viscosities ratio when a drop is under stresses due to a flow, the behavior for deformation is different from that with $\lambda \ll 1$: the steady state deformation is reached after a transitory which has an oscillatory behavior. If the viscosity of the drop is very large, interfacial tension has a

negligible effect in the drop deformation that only depends on the ratio of viscosities and the flow field type, and the steady deformation is reached at relatively low capillary numbers. On the other side, the drop orientation has a wider range in which depends on the *Ca* number, which means that the interfacial tension plays an important role and therefore it can be used to calculate σ; see Fig. 6.10.
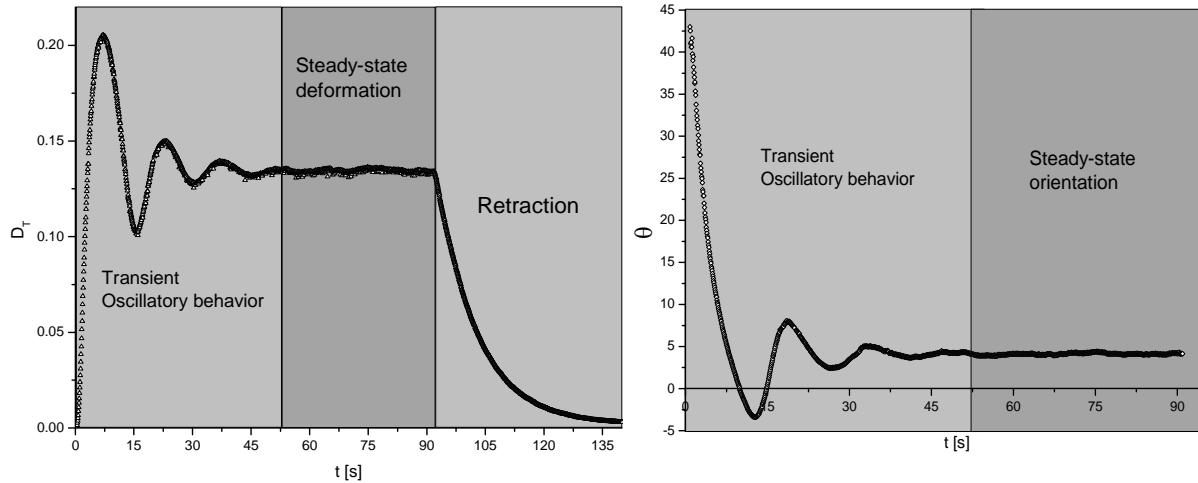
Figure 6.10. Deformation and orientation parameters evolution. Plots corresponding to an experiment with a drop with r_0 = 0.47 mm under a shear rate $\dot{\gamma}$ =1.0 s^{-1}, the viscosities ratio of the system is $\lambda = 16$ and the flow field type is $\alpha = 0.13$.

Steady-state orientation

Having $\lambda = 16$, the most appropriate way to calculate the interfacial tension is through Eq. (6.7) where the orientation of the drop is strongly related with the capillary number as well as the viscosities ratio. Figure 6.11 shows the values of the orientation angle for the three types of flow and the linear fitting for each one as well as the values for the interfacial tension obtained using Eq. (6.8) with the slopes of each fitted line. In these case, the differences between them are remarkable large, even for the closest ones $\alpha = 0.03$ and $\alpha = 0.05$.
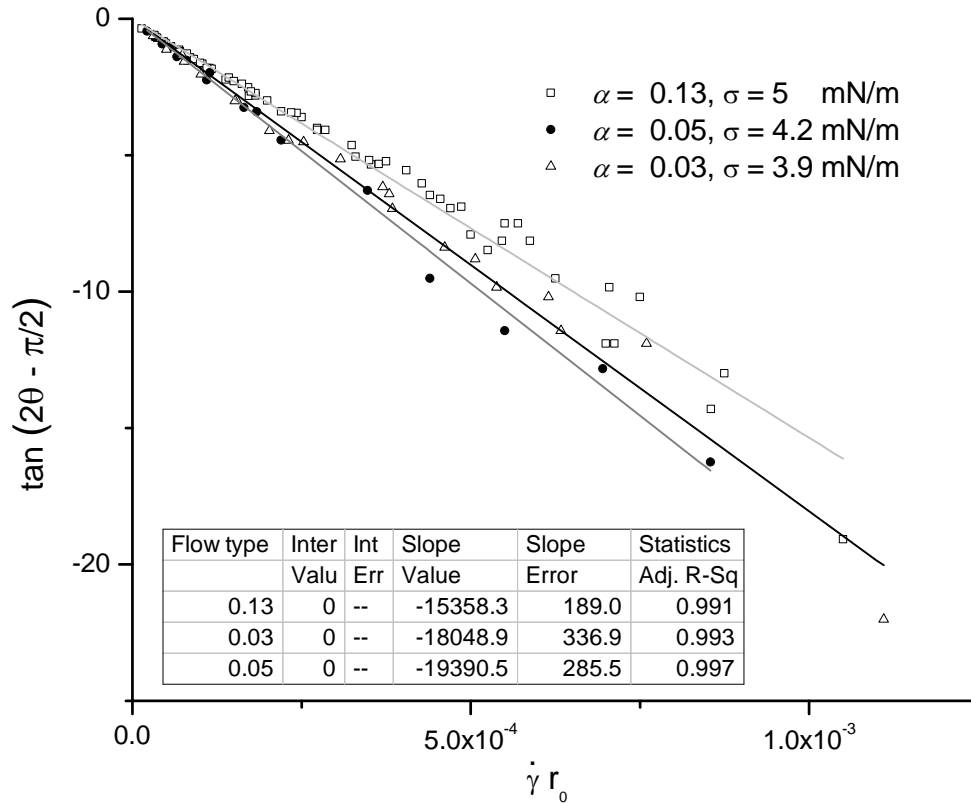
Figure 6.11. Steady-state orientation for different flow types and λ = 16.

Drop retraction

As mentioned before, when the viscosities ratio is high, the maximum deformation of a drop depends on the value of α and λ only when the drop surface is far enough from any frontier. Since the gap in the geometries for the flow types $\alpha = 0.03$ and $\alpha = 0.05$ is small and because of the drop size effects mentioned in Chapter 5, the retraction process may also be affected by the presence of nearby frontiers. So in order to avoid mistakes in the calculation of the interfacial tension due to drop size effects, only the retraction process obtained for the flow field type with $\alpha = 0.13$ were used. In these case, the maximum deformation reached for the drops was $D_T = 0.13$. Fig. 6.12 shows a plot for the data obtained during the retraction processes of a drop and the linear fit for each one, as well as the interfacial tension obtained from them. From that plot the average value for the interfacial tension is 3.5 mN/m ±0.13 mN/m.

All initial deformations are $D_T = 0.13$

Interfacial tension values

□	1	$\sigma = 3.68$ mN/m
○	2	$\sigma = 3.65$ mN/m
+	3	$\sigma = 3.53$ mN/m
▲	4	$\sigma = 3.57$ mN/m

Retraction	Interce Value	Interce Error	Slope Value	Slope Error	Statistics Adj. R-Sq
1	0.0081	0.001	-0.1007	2.06155E	0.99918
2	-0.044	0.001	-0.0993	1.91099E	0.99927
3	-0.004	9.056	-0.09659	1.09985E	0.99974
4	0.0073	0.001	-0.09756	1.91651E	0.99928

Figure 6.12. Drop retraction for $r_0 = 0.47$ and $\lambda = 15.9$

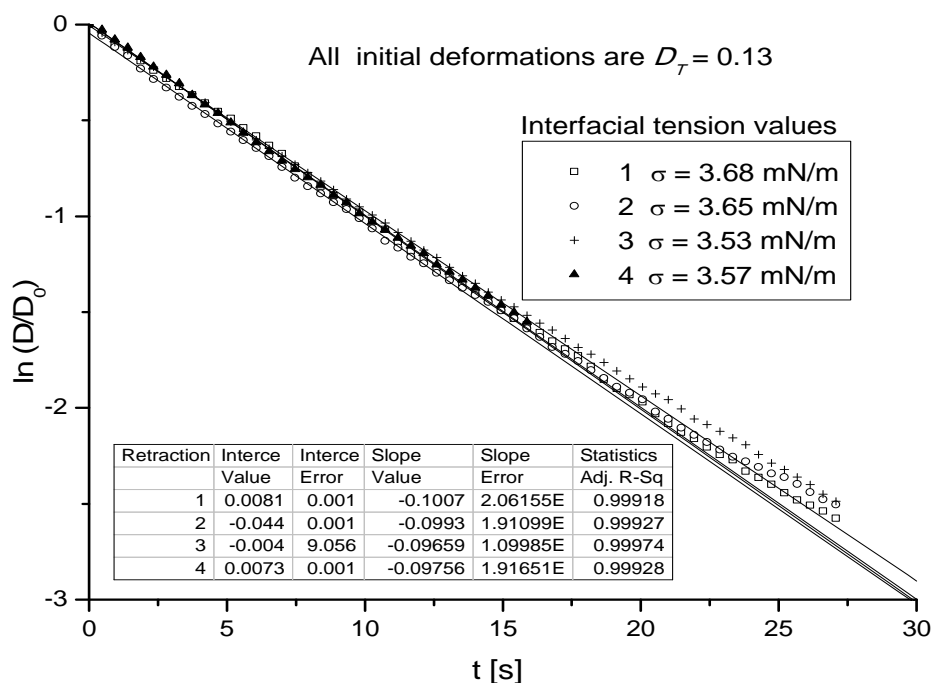Summarizing, the theories used in equilibrium methods were developed for simple shear flow. Thus, the values obtained using them were only expected to be a benchmark. Nevertheless, for low viscosities ratio $\lambda \ll 1$, all methods have proven to produce acceptable values for interfacial tension even when there are differences in the values calculated. Steady state deformation appeared to be more reliable than steady state orientation given that the differences found due to the flow field type are less strong than those for the orientation methods where the values are more dependent on the flow type. For high viscosities ratio $\lambda \gg 1$, steady-state orientation was the only equilibrium method that could be implemented and the values founded do not seem to be very accurate. The dynamic methods are most suitable and have some advantages over the equilibrium methods, they do not have the restriction in regard to the flow field type or the viscosities ratio and, on the other hand, only one experiment would be sufficient to obtain a useful value for the interfacial tension, whereas in equilibrium methods a considerable amount of data are needed for calculating a reliable value of the interfacial tension. Table 6.4 summarizes the results of the values of the interfacial tension for the low and high viscosities ratio used in this work.

Table 6.4. Interfacial tension values calculated for the two viscosities ratio used in thes work. The values taken for the computing of the capillary number are those in the shaded cells.

Viscosities ratio	Measurement method		Flow Field Type	Interfacial Tension [mN/m]
$\lambda=0.012$	Equilibrium	Steady state Deformation	0.13	2.71
			0.05	2.78
			0.03	2.79
		Steady state Orientation	0.12	3.12
			0.05	2.78
			0.03	2.72
	Dynamic	Drop retraction	----------------	2.72 ± 0.02
$\lambda=16$	Equilibrium	Steady state Orientation	0.13	5
			0.05	4.2
			0.03	3.9
	Dynamic	Drop retraction	----------	3.5 ± 0.13

7 Conclusions

In this work, studies of drop embedded in a fluid are carried out with a novel flow device —the Two-Roll Mill, capable of a wide range of flow similar to simple shear flow up to elongational flow with significant vorticity— that produces a history of deformations not accessible with viscometric flow or elongational flow of the type of four-roll mills. The experimental implementation of a computer controlled TRM is firstly described. In Chapters 2-4 the computer-controlled Two-Roll Mill flow cell is presented, requiring of a highly accurate device, and the implementation of the control algorithm for the position and maintaining of a drop under well characterized kinematic conditions. In the second part of this work —Chapters 5-7— experimental results of a single drop deformation in flow fields generated with the TRM are presented.

The computer-controlled TRM flow cell, presented allows studies of drop and particle dynamics in flow fields with values of the flow type parameter α not accessible for any other device. The flow parameter type indicates the relative strength of the vorticity of the flow relative to the rate of deformation. With this device, flows with a vorticity 6 percent less than those present simple shear flows are possible, up to elongational flows with a reduction of vorticity larger 60 percent. The experimental characterization performed of the TRM geometries showed that the flow fields generated have a well defined and constant value of the flow type parameter in at the stagnation point. The continuous real-time control process, based on the non-linear control algorithm implemented (whose feedback is provided by the real-time digital image analysis) along with the computer-controlled servo motors, has proven to be robust enough to retain a drop in the desired region for long experimental times and under the specified flow conditions; besides, the results shown that this control has no effect on the deformation dynamics. This control process together with the high performance components of the setup, make it possible to perform long-time deformation experiments of drops with high accuracy.

The results presented show the dynamics of deformation of drops embedded in flow fields with $\alpha = 0.13$, $\alpha = 0.05$ and $\alpha = 0.03$ for two extreme values of viscosities ratio $\lambda = 0.012$ and $\lambda = 16$. The results for the low viscosities ratio present a smooth transition with respect to previous data available for $\alpha = 0$ and $\alpha = 0.2$, with the expected critical capillary numbers values, lower than those found in simple shear flows and higher than the corresponding to more elongational flows. The transient phases for the three flow fields present a monotonic evolution toward the steady state deformation and orientation. The plots of the steady states as function of Ca show that those states are always linearly proportional to the Ca applied. In those plots, a remarkable agreement between the experimental results for $\alpha = 0.13$ and the Taylor theory for $\alpha = 0$ was found. For the high viscosities ratio the behavior was completely different. For very low capillary numbers the transient stages presented a monotonic evolution with a final steady sate deformation proportional Ca, whereas for high capillary numbers, this transients are characterized by a complex damped oscillatory behavior and the steady states do not depend on the Ca anymore. Those behaviors are consequence of the non linear coupling between the drop rotation caused by the vorticity tensor and the elongation caused by the rate of deformation tensor. A precise division between one behavior and the other is not well defined and theoretically has been only studied for simple shear flows and the computer-controlled TRM flow cell is an excellent experimental device which brings a unique opportunity for the study of these highly complex transient stages where the transition from one behavior to another can be experimentally studied in detail for different flow fields and under well controlled flow conditions. Another relevant feature of the TRM device is the feasibility to perform detailed experimental studies on drop deformation under confinement conditions in flow fields other than simple shear for both steady and transient stages. This topic has recently gained importance and the experimental of the transitory behavior are rather inexistent.

Another important characteristic of the TRM is that the experiments allow the measure of the interfacial tension, a very important parameter needed to characterize the flow conditions. Given that there was not available data for the interfacial tension in the fluids used, it was possible to calculate it with high accuracy from the relaxation stage through Deformed Drop Relaxation DDR method using the data provided by the TRM experiments. This method is easily applicable in the TRM and overcomes the problems that appear in other methods when high viscous fluids are used or when very low difference of densities are present.

The present flow cell can be used to perform numerous experiments including the study of drop deformation and breakup for a wider range of viscosities under flow fields covered by the TRM —not feasible until now— or with non-Newtonian fluids. Other possible experiments include the dynamics of drops near walls with elongational conditions —conditions not amenable to study with earlier flow

devices— and with the presence of surfactants or other polymeric additives, which are of technological relevance. Drop phenomena analyzed with this experimental setup, are similar kinematically, from the point of view of the applicable boundary conditions, as well as dynamically to the slow flow hydrodynamics of two-phase flows trough pores and fractures.

References

[1] Acrivos, A. and Lo, T.S., (1978). Deformation and breakup of a single slender drop in an extensional flow, *J. Fluid Mech.*, **86**:641.

[2] Acrivos, A., (1983). The breakup of small drops and bubbles in shear flows, *Ann. NY Acad. Sci.*, **404**:1.

[3] Astarita, G, (1979). Objective and generally applicable criteria for flow classification, *J. Non-Newtonian Fluids Mech.*, **6**:69.

[4] Atobe, T., (1997). Lagrangian chaos in the Stokes flow between two-eccentric rotatin cylinders, *Int. J. Bifurcation & Chaos,* **7**:1007.

[5] Barthes-Biesel, D. and Acrivos, A., (1973). Deformation and burst of a liquid droplet freely suspended in a linear shear field, *J. Fluid Mech.,* **61**:1.

[6] Bentley, B.J. and Leal, L.G., (1986a). A computer-controlled four-roll mill for investigations of particle and drop dynamics in two-dimensional linear shear flows, *J. Fluid Mech.,* **167**:219.

[7] Bentley, B.J. and Leal, L.G., (1986b). An experimental investigation of drop deformation and breakup in steady two-dimensional linear flows, *J. Fluid Mech.,* **167**:241.

[8] Birkhoffer, B.H. et al., (2005). Computer-controlled flow cell for the study of particle and drop dynamics in shear flow fields, *Ind. Eng. Chem. Res.,* **44**:6999.

[9] Blawzdziewicz, J., Cristini, V., Loewenberg, M., (2002). Critical behavior of drops in linear flows: I. Phenomenological theory for drop dynamics near critical stationary states. *Physics of Fluids,* **14**(8):2709.

[10] Blawzdziewicz, J., Cristini, V., Loewenberg, M., (2003). Multiple stationary states for deformable drops in linear Stokes flows, *Physics of Fluids,* **15**(5):L37.

[11] Boonen, E., Van Puyvelde, P., Moldenaers, P., (2010). Single droplet Break-up in controlled mixed flows, *ACS App. Matt. & Int.,* **2**:2140.

[12] Briscoe, B. J., Lawrence, C.J. and Mietus, W.G.P., (1999). A Review of immiscible fluid mixing, *Advances in colloid and interface science,* **81:**1.

[13] Carriere, J. and A. Cohen, (1991). Evaluation of the interfacial tension between high molecular weight polycarbonate and PMMA resins with the imbedded fiber retraction technique, *J. Rheol.,* **35**(2):205.

[14] Chaffey, C. E., Brenner H., (1967). A second-order theory for shear deformation of drops, *J. Colloid Interface Sci.,* **24**:258.

[15] Chong M.S., Perry A.E., Cantwell B.J., (1990). A general classification of three dimensional flow fields, *Phys. Fluids A,* **2**:765.

[16] Cox R.G., (1969). The deformation of a drop in a general time-dependent fluid flow, *J. Fluid Mech.,* **37**:601.

[17] de Bruijin, R.A., (1989). *Deformation and break-up of drops in simple shear flows . PhD. thesis.* Eindhoven Univ. Technol., The Netherlands,

[18] Drelich, J., Ch. Fang, C.L. White, (2002). Measurement of interfacial tension in fluid-fluid systems, *Encyclopedia of Surface and Colloid Science.*

[19] Elemans, P.H.M., Bos, H.L., Janssen, J.M.H., Meijer, H.E.H., (1993). Transient phenomena in dispersive mixing, *Chemical Engineering Sci.,* **48**:267.

[20] Elmendorp, J.J., (1986). *A study on polymer blending microrheology, PhD thesis,* Delft University of Technology, The Netherlands.

[21] Geffroy E. and Leal L.G., (1992). Flow Birefringence of a concentrated polystyrene solution in a Two Roll-Mill 1. Steady Flow and Start-Up of Steady Flow, *J. Polym. Sci. B: Polym. Phys*., **30**(12):1329.

[22] Grace, H.P., (1982). Dispersion phenomena in high viscosity immiscible fluid systems and application of static mixers as dispersion devices in such systems, *Chem. Eng. Commun.,* **14**:255.

[23] Guido S. and Villone, M., (1998). Three-dimensional shape of a drop under simple shear flow, *J. Rheol.,* **42**:395.

[24] Guido S. and M. Villone, (1999). Measurement of interfacial tension by drop retraction analysis, *J. Colloid Interface Sci.,* **209**:247.

[25] Guido, S., Greco, F., Villone, M., (1999). Experimental determination of drop shape in slow steady shear flow, *J. Colloid Interface Sci.,* **219**:298

[26] Guido, S., Minale M., Maffetone, P.L., (2000). Drop shape dynamics under shear-flow reversal, *J. Rheol.* **44**:1385.

[27] Guido, S. and Greco F., (2001). Drop shape under slow steady shear flow and during relaxation. Experimental results and comparison with theory*, Rheol. Acta.,* **40**:176.

[28] Guido, S., Simeone, M., Alfani, A., (2002). Interfacial tension of aqueous mixtures of Na-caseinate and Na-alginate by drop deformation in shear flow, *Carbohydrate Polymers,* **48**:143.

[29] Guillermo, P. and N. R. Demarquette, (2005). New procedure to increase the accuracy of interfacial tension measurements obtained by breaking thread method, *Polymer* **44**:3045.

[30] Hinch, E.J. and Acrivos, A., (1979). Steady long slender droplets in two-dimensional straining motion, *J. Fluid Mech.,* **91**:401.

[31] Hinch, E.J. and Acrivos, A., (1980). Long slender drops in a simple shear flow, *J. Fluid Mech.,* **98**:305.

[32] Huilgol R.R. and Phan-Thien N. 1998. *The fluid mechanics of viscoelasticity.* Elsevier, The Netherlands.

[33] Jana, S.C., Metcalfe, G., Ottino, J.M., (1994). Experimental and computational studies of mixing in complex stokes flows: the vortex mixing flow and multi-cellular cavity flow, *J. Fluid Mech.,* **269**:199.

[34] Janssen J.M.H., Meijer, H.E.H., (1993). Droplet breakup mechanism: Stepwise equilibrium versus transient dispersion, *J. Rheol.* **37**(4):597.

[35] Janssen, P.J.A., and Anderson, P.D., (2007). Boundary integral method for drop deformation between parallel plates, *Phys. Fluids* **19**:043602.

[36] Khakhar, D.V. and Ottino, J.M., (1987). Breakup of liquid threads in linear flows, *Int. J. Multiphase Flow,* **13**:71.

[37] Kuhn, W., (1953). Spontane Aufteilung von Flüssigkeitszylindern in kleine Kugeln, *Kolloid Z.* **132**:84.

[38] Liu Y., B. Kong, X. Yang, (2005). Studies on some factors influencing the interfacial tension measurement of polymers, *Polymer,* **46**:2811.

[39] Luciani A., M. F. Champagne, L. A. Utracki, (1997). Interfacial tension coefficient frop the retraction of ellipsoidal drops, *J. Polym Sci. B: Polym. Phys.* **35**:1393.

[40] Maffettone P.L. and M. Minale, (1998). Equation of change for ellipsoidal drops in viscous flow, *J. Non-Newtonian Fluid Mech.*, **78**:227.

[41] Megias-Alguacil, D., P. Fischer, E.J. Windhab, (2004). Experimental determination of interfacial tension by different dynamical methods under simple shear flow conditions with a novel computer-controlled paraller band apparatus, *Journal of Colloid and Interface Science,* **274**:631.

[42] Megias-Alguacil, D., et al., (2005). Droplet deformation under simple shear investigated by experiment, numerical simulation and modeling, *J. Non-Newtonian Fluid Mech.***, 126**:153.

[43] Megias-Alguacil, D., P. Fischer, E. J. Windhab, (2006). Determination of the interfacial tension of low density difference liquid-liquid systems containing surfactants by droplet deformation methods. *Chemical Engineering Science,* **61**:1386.

[44] Mikami, T. Cox, R.G., Mason, S.G., (1975). Breakup of extending liquid threads, *Int. J. Multiphase Flow,* **2**:113.

[45] Mo, H., C. Zhou, W. Yu, (2000). A new method to determine interfacial tension from the retraction of ellipsoidal drops, *J. Non-Newtonian Fluid Mech.,* **91**:221.

[46] Olbricht W.L, Rallison, J.M. and Leal, L.G., (1982). Strong flow criteria based on microstructure deformation, *J. Non-Newtonian Fluid Mech.,* **10**:291.

[47] Rallison, J. M., and Acrivos, A., (1978). A numerical Study of the deformation and burst of a viscous drop in an extensional flow, *J. Fluid Mech.,* **89**:191.

[48] Rallison, J. M., (1980). Note on the time-dependent deformation of a viscous drop which is almost spherical, *J. Fluid Mech.,* **98**:625.

[49] Rallison, J. M., (1984). The deformation of small viscous drops and bubbles in shear flows, *Ann. Rev. Fluid Mech.*, **16**:45.

[50] Rayleigh, Lord, (1879). On the Capillary phenomena of jets, *Proc. Roy. Soc. London* **29**:71.

[51] Renardy, Y., (2007). The effects of confinement and inertia on the production of droplets, *Rheol. Acta* **46**:521.

[52] Reyes, M.A.H. and Geffroy, E., (2000a). A co-rotating two-roll mill for studies of two-dimensional, elongational flows with vorticity, *Phys. Fluids* **12**(10):2372.

[53] Reyes, M. A. H. and E. Geffroy, (2000b). Study of low Reynolds number hydrodynamics generated by symmetric co-rotating two-roll mills, *Revista Mexicana de Física* **46**(2):135.

[54] Reyes, M.A.H., (2005). *Hydrodynamics of deformable objects in creeping flows. PhD thesis.* UNAM. Mexico.

[55] Reyes, M.A.H., Minzoni A.A., Geffroy E., (2011). Numerical study of the effect of nonlinear control on the behavior of a liquid drop in elongational flow with vorticity, *Journal of Engineering Mathematics,* **71**(2):185.

[56] Rumscheidt, F.D. and Mason, S.G., (1961). Particle motions in sheared suspensions. XII. Deformation and burst of fluid drops in shear and hyperbolic flow, *J. Colloid Sci.* **16**:238.

[57] Rust, A.C. and M. Manga, (2002). Bubble shapes and orientations in low Re simple shear flow, *Journal of Colloid and Interface Science,* **249**:476,

[58] Shapira, M., and Haber, S., (1990). Low Reynolds number motion of a droplet in shear flow including wall effects, *Int. J. Multiphase Flow,* **16**:305.

[59] Sibillo, V., Pasquariello, G., Simeone, M. Cristini, V., Guido, S., (2006). Drop deformation in microconfined shear flow, *Phys. Rev. Lett.* **97**:054502.

[60] Singh, P. and Leal L.G., (1996). Computational studies of the fene dumbbell model with conformation-dependent friction in a corotating two-roll mill. *J. Non-Newtonian Fluid Mech.* **67**:137.

[61] Son Y. and J.T. Yoon, (2001). Measurement of interfacial tension by a deformed drop retraction method, *Polymer* **42:**7209.

[62] Son Y. and K. B. Migler, (2002). Interfacial tension measurement between immiscible polymers:improved deformed drop retraction method, *Polymer,* **43**:3001.

[63] Stone H.A., Bentley B.J. and Leal, L.G., (1986). An experimental study of transient effects in the breakup of viscous drops, *J. Fluids Mech.,* **173**:131.

[64] Stone, H.A. and Leal, L.G., (1989a). Relaxation and breakup of a n initially extended drop in an otherwise quiescent fluid, *J. Fluid Mech.,* **198**:399

[65] Stone, H.A. and Leal, L.G., (1989b). The influence of initial deformation on drop breakup in subcritical time-dependent flows at low Reynolds numbers, *J. Fluid Mech.,* **206**:223.

[66] Stone, H. A., (1994). Dynamics of drop deformation and breakup in viscous fluids, *Ann. Rev. Fluid Mech.,* **26**:65.

[67] Taylor, G. I., (1932). The viscosity of a fluid containing small drops of another fluid. Proc. *R. Soc. London, Ser. A* **146**:41.

[68] Taylor, G. I., (1934). The formation of emulsions in definable fields of flow, *Proc. R. Soc. London, Ser. A* **146**:501.

[69] Tjahjadi B., and Ottino, J.M., (1991). Stretching and breakup of droplets in chaotic flows, *J. Fluid Mech.,* **232**:191.

[70] Tomotika, S., (1935). On the instability of a cylindrical thread of viscous liquid surrounded by another viscous fluid, *Proc. Roy. Soc. London, Ser. A* **150**:332.

[71] Tomotika, S., (1936). Breaking up of a drop of viscous liquid immersed in another viscous fluid which is extending at uniform rate, *Proc. Roy. Soc. London, Ser. A* **153**:302.

[72] Torza S., Cox, R.G., Mason, S.G., (1972). Particle motions in shear suspensions, *J. Colloid and Interface Sci.,* **38**(2):395.

[73] Vananroye, A., Van Puyvelde, P., Moldenaers, P., (2006a). Effect of confinement on droplet breakup in sheared emulsions, *Langmuir*, **22**:3972.

[74] Vananroye, A., Van Puyvelde, P., Moldenaers, P., (2007). Effect of confinement on the steady-state behavior of single droplets during shear flow, *J. Rheol.*, **51**: 139.

[75] Vananroye, A., Cardinales, R., Van Puyvelde, P., Moldenaers, P., (2008). Effect of confinement and viscosity ratio on the dynamics of single droplets during transient shear flow, *J. Rheol.,* **52**:1459.

[76] Young, Y-N., Blawzdziewicz, J., Cristini, V., Goodman, R.H., (2008). Hysteretic and chaotic dynamics of viscous drops in creeping flows with rotation, *J. Fluid Mech.*, **607**:209.